



National Library
of Canada

Acquisitions and
Bibliographic Services Branch

395 Wellington Street
Ottawa, Ontario
K1A 0N4

Bibliothèque nationale
du Canada

Direction des acquisitions et
des services bibliographiques

395, rue Wellington
Ottawa (Ontario)
K1A 0N4

Your file *Votre référence*

Our file *Notre référence*

NOTICE

The quality of this microform is heavily dependent upon the quality of the original thesis submitted for microfilming. Every effort has been made to ensure the highest quality of reproduction possible.

If pages are missing, contact the university which granted the degree.

Some pages may have indistinct print especially if the original pages were typed with a poor typewriter ribbon or if the university sent us an inferior photocopy.

Reproduction in full or in part of this microform is governed by the Canadian Copyright Act, R.S.C. 1970, c. C-30, and subsequent amendments.

AVIS

La qualité de cette microforme dépend grandement de la qualité de la thèse soumise au microfilmage. Nous avons tout fait pour assurer une qualité supérieure de reproduction.

S'il manque des pages, veuillez communiquer avec l'université qui a conféré le grade.

La qualité d'impression de certaines pages peut laisser à désirer, surtout si les pages originales ont été dactylographiées à l'aide d'un ruban usé ou si l'université nous a fait parvenir une photocopie de qualité inférieure.

La reproduction, même partielle, de cette microforme est soumise à la Loi canadienne sur le droit d'auteur, SRC 1970, c. C-30, et ses amendements subséquents.

Canada

The Feasibility of Separating Concurrent Sources in Cardiac Magnetic Field and Body Surface Potential Maps

by

M.J. Reina Lamothe

Submitted in partial fulfillment
of the requirements for the degree of
Doctor of Philosophy

at

Dalhousie University
Halifax, Nova Scotia, Canada

February, 1994

©Copyright by M.J. Reina Lamothe, 1994



National Library
of Canada

Acquisitions and
Bibliographic Services Branch

395 Wellington Street
Ottawa, Ontario
K1A 0N4

Bibliothèque nationale
du Canada

Direction des acquisitions et
des services bibliographiques

395, rue Wellington
Ottawa (Ontario),
K1A 0N4

Your file Votre référence

Our file Notre référence

The author has granted an irrevocable non-exclusive licence allowing the National Library of Canada to reproduce, loan, distribute or sell copies of his/her thesis by any means and in any form or format, making this thesis available to interested persons.

L'auteur a accordé une licence irrévocable et non exclusive permettant à la Bibliothèque nationale du Canada de reproduire, prêter, distribuer ou vendre des copies de sa thèse de quelque manière et sous quelque forme que ce soit pour mettre des exemplaires de cette thèse à la disposition des personnes intéressées.

The author retains ownership of the copyright in his/her thesis. Neither the thesis nor substantial extracts from it may be printed or otherwise reproduced without his/her permission.

L'auteur conserve la propriété du droit d'auteur qui protège sa thèse. Ni la thèse ni des extraits substantiels de celle-ci ne doivent être imprimés ou autrement reproduits sans son autorisation.

ISBN 0-315-93783-1

Canada

Name M.J. Reina Lamotte

Dissertation Abstracts International is arranged by broad, general subject categories. Please select the one subject which most nearly describes the content of your dissertation. Enter the corresponding four-digit code in the spaces provided.

0760

U·M·I

SUBJECT TERM

SUBJECT CODE

Subject Categories

THE HUMANITIES AND SOCIAL SCIENCES

COMMUNICATIONS AND THE ARTS

Architecture 0729
 Art History 0377
 Cinema 0900
 Dance 0378
 Fine Arts 0357
 Information Science 0723
 Journalism 0391
 Library Science 0399
 Mass Communications 0708
 Music 0413
 Speech Communication 0459
 Theater 0465

EDUCATION

General 0515
 Administration 0514
 Adult and Continuing 0516
 Agricultural 0517
 Art 0273
 Bilingual and Multicultural 0282
 Business 0688
 Community College 0275
 Curriculum and Instruction 0727
 Early Childhood 0518
 Elementary 0524
 Finance 0277
 Guidance and Counseling 0519
 Health 0680
 Higher 0745
 History of 0520
 Home Economics 0278
 Industrial 0521
 Language and Literature 0279
 Mathematics 0280
 Music 0522
 Philosophy of 0998
 Physical 0523

Psychology 0525
 Reading 0535
 Religious 0527
 Sciences 0714
 Secondary 0533
 Social Sciences 0534
 Sociology of 0340
 Special 0529
 Teacher Training 0530
 Technology 0710
 Tests and Measurements 0288
 Vocational 0747

LANGUAGE, LITERATURE AND LINGUISTICS

Language
 General 0679
 Ancient 0289
 Linguistics 0290
 Modern 0291
 Literature
 General 0401
 Classical 0294
 Comparative 0295
 Medieval 0297
 Modern 0298
 African 0316
 American 0591
 Asian 0305
 Canadian (English) 0352
 Canadian (French) 0355
 English 0593
 Germanic 0311
 Latin American 0312
 Middle Eastern 0315
 Romance 0313
 Slavic and East European 0314

PHILOSOPHY, RELIGION AND THEOLOGY

Philosophy 0422
 Religion
 General 0318
 Biblical Studies 0321
 Clergy 0319
 History of 0320
 Philosophy of 0322
 Theology 0469

SOCIAL SCIENCES

American Studies 0323
 Anthropology
 Archaeology 0324
 Cultural 0326
 Physical 0327
 Business Administration
 General 0310
 Accounting 0272
 Banking 0770
 Management 0454
 Marketing 0338
 Canadian Studies 0385
 Economics
 General 0501
 Agricultural 0503
 Commerce-Business 0505
 Finance 0508
 History 0509
 Labor 0510
 Theory 0511
 Folklore 0358
 Geography 0366
 Gerontology 0351
 History
 General 0578

Ancient 0579
 Medieval 0581
 Modern 0582
 Black 0328
 African 0331
 Asia, Australia and Oceania 0332
 Canadian 0334
 European 0335
 Latin American 0336
 Middle Eastern 0333
 United States 0337
 History of Science 0585
 Law 0398
 Political Science
 General 0615
 International Law and
 Relations 0616
 Public Administration 0617
 Recreation 0814
 Social Work 0452
 Sociology
 General 0626
 Criminology and Penology 0627
 Demography 0938
 Ethnic and Racial Studies 0631
 Individual and Family
 Studies 0628
 Industrial and Labor
 Relations 0629
 Public and Social Welfare 0630
 Social Structure and
 Development 0700
 Theory and Methods 0344
 Transportation 0709
 Urban and Regional Planning 0999
 Women's Studies 0453

THE SCIENCES AND ENGINEERING

BIOLOGICAL SCIENCES

Agriculture
 General 0473
 Agronomy 0285
 Animal Culture and
 Nutrition 0475
 Animal Pathology 0476
 Food Science and
 Technology 0359
 Forestry and Wildlife 0478
 Plant Culture 0479
 Plant Pathology 0480
 Plant Physiology 0817
 Range Management 0777
 Wood Technology 0746
 Biology
 General 0306
 Anatomy 0287
 Biostatistics 0308
 Botany 0309
 Cell 0379
 Ecology 0329
 Entomology 0353
 Genetics 0369
 Limnology 0793
 Microbiology 0410
 Molecular 0307
 Neuroscience 0317
 Oceanography 0416
 Physiology 0433
 Radiation 0821
 Veterinary Science 0778
 Zoology 0472
 Biophysics
 General 0786
 Medical 0760

Geodesy 0370
 Geology 0372
 Geophysics 0373
 Hydrology 0388
 Mineralogy 0411
 Paleobotany 0345
 Paleocology 0426
 Paleontology 0418
 Paleozoology 0985
 Palynology 0427
 Physical Geography 0368
 Physical Oceanography 0415

HEALTH AND ENVIRONMENTAL SCIENCES

Environmental Sciences 0768
 Health Sciences
 General 0566
 Audiology 0300
 Chemotherapy 0992
 Dentistry 0567
 Education 0350
 Hospital Management 0769
 Human Development 0758
 Immunology 0982
 Medicine and Surgery 0564
 Mental Health 0347
 Nursing 0569
 Nutrition 0570
 Obstetrics and Gynecology 0380
 Occupational Health and
 Therapy 0354
 Ophthalmology 0381
 Pathology 0571
 Pharmacology 0419
 Pharmacy 0572
 Physical Therapy 0382
 Public Health 0573
 Radiology 0574
 Recreation 0375

Speech Pathology 0460
 Toxicology 0383
 Home Economics 0386

PHYSICAL SCIENCES

Pure Sciences
 Chemistry
 General 0485
 Agricultural 0749
 Analytical 0486
 Biochemistry 0487
 Inorganic 0488
 Nuclear 0738
 Organic 0490
 Pharmaceutical 0491
 Physical 0494
 Polymer 0495
 Radiation 0754
 Mathematics 0405
 Physics
 General 0605
 Acoustics 0986
 Astronomy and
 Astrophysics 0606
 Atmospheric Science 0608
 Atomic 0748
 Electronics and Electricity 0607
 Elementary Particles and
 High Energy 0798
 Fluid and Plasma 0759
 Molecular 0609
 Nuclear 0610
 Optics 0752
 Radiation 0751
 Solid State 0611
 Statistics 0467
 Applied Sciences
 Applied Mechanics 0346
 Computer Science 0984

Engineering
 General 0537
 Aerospace 0538
 Agricultural 0539
 Automotive 0540
 Biomedical 0541
 Chemical 0542
 Civil 0543
 Electronics and Electrical 0544
 Heat and Thermodynamics 0348
 Hydraulic 0545
 Industrial 0546
 Marine 0547
 Materials Science 0794
 Mechanical 0548
 Metallurgy 0743
 Mining 0551
 Nuclear 0552
 Packaging 0549
 Petroleum 0765
 Sanitary and Municipal 0554
 System Science 0790
 Geotechnology 0428
 Operations Research 0796
 Plastics Technology 0795
 Textile Technology 0994

PSYCHOLOGY

General 0621
 Behavioral 0384
 Clinical 0622
 Developmental 0620
 Experimental 0623
 Industrial 0624
 Personality 0625
 Physiological 0989
 Psychobiology 0349
 Psychometrics 0632
 Social 0451

EARTH SCIENCES

Biogeochemistry 0425
 Geochemistry 0996



To Derek

Contents

List of Figures	xi
List of Tables	xv
Abstract	xvii
Symbols and abbreviations	xviii
Acknowledgements	xxiv
Preface	1
1 Body Surface Potential and Magnetic Field Mapping	5
1.1 BSPM and MCG instrumentation	5
1.2 Comparison of instrumentation and protocols	7
1.2.1 Simultaneous versus sequential measurements	7
1.2.2 Recording bandwidths	12
1.3 Recording protocol, averaging and data display	16
1.3.1 A BSPM and MCG recording	16
1.3.2 Noise reduction by averaging	20
1.3.3 Standard post-average processing	24
1.3.4 General-purpose software for data analysis and display	27
2 The Cardiac Sources and Volume-conductor Problem	36
2.1 The current dipole as a source model	36
2.2 Volume-conductor models	37
2.2.1 Infinite homogeneous conductor	37

2.2.2	Bounded inhomogeneous volume-conductor	38
2.3	The forward and inverse problems	38
2.3.1	The forward problem	40
2.3.2	The inverse problem	41
2.3.3	Implementation of the inverse solution	43
2.3.4	Special cases of source and volume conductor	43
2.3.5	Effects of boundaries	46
2.3.6	Validity of the current-dipole source model	50
2.3.7	Validity of a standard volume-conductor model	54
3	Signal Extraction Techniques	56
3.1	Introduction	56
3.2	Temporal averaging technique	57
3.3	Correlation technique	58
3.4	Orthogonal Expansions	59
3.4.1	Singular Value Decomposition	60
3.4.2	Karhunen-Loève Transform	62
3.5	Simulations of extraction techniques	64
3.5.1	Results: Characterisation of background source	65
3.5.2	Results: Extraction of a superimposed source	69
3.5.3	Discussion: Background source characterisation	73
3.5.4	Discussion: Extraction of superimposed source	74
4	PR-interval Mapping	76
4.1	Introduction	76
4.2	Methods	77
4.2.1	Data processing	77
4.2.2	Baseline correction	77
4.2.3	Data analysis	78
4.3	Results	79

4.3.1	Isofield contour maps	79
4.3.2	Signal durations, peak amplitudes and locations	86
4.4	Discussion	90
4.4.1	P-wave onset and the pacemaker complex	90
4.4.2	Spatial discrimination of LD and RR	91
4.4.3	Sensitivity of MFM to atrial activation	92
4.4.4	Atrial repolarisation	93
4.4.5	Final comments	94
5	Extraction Techniques Applied to PR-segment Events: I. His-Purkinje System	96
5.1	Introduction	96
5.2	Method	100
5.3	Results	101
5.3.1	Interpretation of results	111
5.3.2	HPS signal amplitude at body surface	111
5.3.3	Expected spatial distribution of HPS maps	116
5.3.4	Atrial repolarisation and PR-segment eigenmaps	117
5.3.5	Orthogonality of Ta and HPS	118
5.3.6	Recording bandwidths	119
5.3.7	Comparison of extraction techniques	119
5.3.8	Summary	121
5.4	Discussion	122
5.4.1	Variance maps of Horan et al.	123
5.4.2	Isolation of His-Purkinje system signal from magnetic field maps	125
5.4.3	Peper's time-shift method	127
5.5	Conclusions	129
6	Extraction Techniques Applied to PR-segment Events: II. Wolff-Parkinson-White Syndrome	131

6.1	Introduction	131
6.1.1	Non-invasive localisation of AP	134
6.1.2	Limitations of non-invasive AP localisation criteria	136
6.1.3	Enhancement of early δ -wave signal	137
6.2	Recording protocol and WPW study group	137
6.3	Development of the enhancement protocol	138
6.3.1	Method	140
6.3.2	Results	142
6.3.3	Discussion	144
6.4	Method of WPW-signal enhancement	145
6.5	Examples	147
6.5.1	Left-sided pathways	147
6.5.2	Right-sided pathways	148
6.5.3	Small or short δ waves	153
6.6	12-lead ECG localisation of AP	155
6.7	BSPM and MFM as a function of AP site	160
6.8	SMD localisation of AP from BSP and MF maps	166
6.8.1	Method	166
6.8.2	Results and discussion	168
6.9	Discussion	178
6.9.1	Success of δ wave enhancement	178
6.9.2	Map features	179
6.9.3	Single-current-dipole inverse solutions	181
6.10	Conclusions	184
	Conclusions	186
	Appendices	190

A	MCG and BSPM Recording Procedures	190
A.1	Before participant arrives	190
A.2	Have the following available in the shielded room	190
A.3	Participant arrives	191
A.3.1	BSPM	191
A.3.2	MCG	192
A.4	End of session	192
B	Averaging and DALECG	193
B.1	The averaging process	193
B.1.1	Beat detection	194
B.1.2	Family assignment and beat alignment	195
B.1.3	Averaging	195
B.1.4	Specific programs, their functions and output data format	198
C	Peper's time shift method	199
C.1	The shift operator	199
C.2	Application to cardiac traces	199
D	Gradiometer Design	203
D.1	The measured fields	203
D.2	Simulations	204
E	Heart and torso anatomy	207
E.1	Anatomy of the heart and ECG trace nomenclature	207
E.2	Heart and torso coordinate systems	207
F	Case study: WPW syndrome patient with two accessory pathways and atrial pacemakers	214
F.1	Introduction	214
F.2	Method	214

F.2.1	BSPM and MFM recording systems	215
F.3	Results	215
F.3.1	BSPM data	215
F.3.2	MFM data	219
F.4	Discussion	219
F.5	Conclusion	222
	Bibliography	224

List of Figures

1.1	Schematic of the MCG and BSPM combined recording system.	7
1.2	MCG noise spectra.	8
1.3	BSPM noise spectra.	9
1.4	Heart-rate variability as a function of time during an MCG recording.	11
1.5	56-lead AC BSP recording.	14
1.6	56-lead AC-DC BSP recording.	15
1.7	The BSPM electrode locations.	17
1.8	MCG measuring grid.	19
1.9	Plots of the RMS noise vs.number of complexes averaged.	22
1.10	Demonstration of the noise reduction by averaging.	23
1.11	Flowchart of steps in MCG and BSPM averaging.	25
1.12	Post-average processing.	26
1.13	Display of MCG temporal data.	29
1.14	Display of BSPM temporal data leads 4-64.	30
1.15	Display of BSPM temporal data leads 1-3 and 65-120.	31
1.16	Example of an MCG RMS map.	33
1.17	Example of a BSPM RMS map.	34
1.18	Display convention for magnetic field and body surface potential maps.	35
2.1	Anterior view of the human torso model with lungs and intracavitary blood masses.	40
2.2	MF and BSP maps for a source in an infinite homogeneous volume-conductor.	45
2.3	Demonstration of a situation which may give rise to electrically silent sources.	46

2.4	MF and BSP maps for a source in a homogeneous volume conductor.	47
2.5	MF and BSP maps for a source in an inhomogeneous volume conductor.	48
3.1	The time relationship between the background and superimposed sources.	57
3.2	Simulation of a dipole with changing amplitude.	66
3.3	Simulation of a dipole with changing location.	67
3.4	TAT residual maps, \mathbf{R} , for the moving dipole.	68
3.5	Simulated maps generated by a combined source.	70
3.6	Residual maps, \mathbf{R} , for combined-source simulation.	71
3.7	Superimposed signal extraction errors for the SVD and TAT methods.	72
4.1	PR-interval isofield maps for subject RF108.	80
4.2	PR-segment isofield maps for subject RF108.	81
4.3	PR-interval isofield maps for subject CP95.	82
4.4	Sketches of the locations of extrema during the PR interval.	83
4.5	Isofield contour maps of early P wave for subject RK156.	86
4.6	Locations of peak magnetic fields and potentials during the P wave. .	87
4.7	Sketch of the timing of atrial activation.	91
5.1	BSPM residuals for subject RF108.	102
5.2	MFM residuals for subject RF108.	103
5.3	BSPM residuals for subject RF108, using a late Ta representation. . .	104
5.4	MFM residuals for subject RF108, using a late Ta representation. . .	105
5.5	BSPM (1000 Hz sampling frequency) residuals for subject RF108. . .	107
5.6	BSPM and MFM residuals for subject RK156.	108
5.7	BSPM and MFM SVD eigenmaps \mathbf{u}_1 and \mathbf{u}_2 for RF108.	109
5.8	BSPM and MFM SVD eigenmaps \mathbf{u}_1 and \mathbf{u}_2 for HS25, TH175 and RK156.	110
5.9	BSPM and MFM HPS model maps.	116
6.1	Accessory pathway locations and Gallagher 12-lead localisation scheme.	132

6.2	Conduction mechanism in WPW syndrome.	133
6.3	Normal and accessory pathway ECG leads for subject CM186.	140
6.4	Enhanced δ -wave maps for the different methods studied.	143
6.5	Unenhanced PR-segment and early QRS-complex maps for subject CN197.	149
6.6	Enhanced PR-segment and early QRS-complex maps for subject CN197.	150
6.7	Unenhanced PR-segment and early QRS-complex maps for subject VP190.	151
6.8	Enhanced PR-segment and early QRS-complex maps for subject VP190.	152
6.9	Unenhanced PR-segment and early QRS-complex maps for subject BS184.	154
6.10	Enhanced PR-segment and early QRS-complex maps for subject BS184.	156
6.11	MF and BSP ventricular excitation maps at 20 ms into the δ wave as a function of AP location.	162
6.12	MF and BSP ventricular excitation maps at 40 ms into the δ wave as a function of AP location.	163
6.13	Torso models for two WPW patients.	167
6.14	DSLs recovered at 20 ms in the standard torso.	169
6.15	Recovered DSL projected onto MR transverse images of subject MS193.	172
6.16	The recovered DSL projected onto the torso model of subject MS193.	174
B.1	Baseline adjustment of candidate beat.	196
C.1	Simulation of Peper's signal separation technique.	200
D.1	Location of extrema for various gradiometer designs.	205
E.1	Anatomy of the heart.	208
E.2	Electrocardiographic nomenclature of the heart cycle.	209
E.3	Sketch of heart with accessory connection at A-V ring.	210
E.4	Anterior view of torso model and ventricular epicardial surface.	211

E.5	Transverse view of torso model and ventricular epicardial surface.	212
E.6	Plots of the epicardial surface.	213
F.1	Raw data traces of leads aVL and aVF.	216
F.2	BSPM isocontour plots of 4 different beats for subject DI189.	218
F.3	MFPM isocontour plots of beat D for subject DI189.	219
F.4	Sketch of timing of events in the 4 pre-excitation complexes.	221

List of Tables

1.1	MCG and BSPM instrumentation specifications and recording parameters.	6
2.1	Average of the extrema ($max+ min $)/2 for seven test sites in the heart.	49
2.2	Inverse solution localisation errors averaged over 7 sites.	51
2.3	Localisation errors of the inverse solution for site G6 (LPP) as a function of excitation time.	53
2.4	Change in recovered MFM DSL as a function of grid height.	55
3.1	Percent errors of fit represented by the rms of the residuals.	68
4.1	Comparison of MCG and BSPM P-wave signal amplitudes.	86
4.2	Normal durations and potential peak amplitudes.	88
6.1	WPW patient group summary.	139
6.2	Inverse solutions compared to theoretical solution.	144
6.3	Locations of WPW accessory pathway.	157
6.4	Comparison of results obtained by 12-lead Gallagher classification.	158
6.5	Self-fit test of the Gallagher 12-lead scheme.	159
6.6	Average distance and standard deviation of the recovered DSL to the correct AP location in a standard torso model.	168
6.7	Average distance of the recovered DSL to the correct AP location in a homogeneous, standard torso model at $t=20$ ms.	170
6.8	Relative differences in recovered DSL for subject MS193.	173
6.9	Average difference (S.D.) between MFM and BSPM recovered DSL in various volume conductor models.	175

6.10 Difference (cm) between recovered DSL in unenhanced and enhanced data. 177

Abstract

117-lead body surface potential maps (BSPM) and 56-point magnetic field maps (MFM) of human cardiac electrical activity were recorded and analysed to establish the feasibility of spatially separating concurrent electrophysiological events of the heart cycle.

The present study focusses on events in the PR interval and was broken up into 4 parts: development and evaluation of signal-extraction protocols; characterisation of atrial activation; detection and isolation of the His-Purkinje system (HPS) signal from atrial repolarisation during the late PR segment; and, finally, enhancement of the δ -wave maps and localisation of accessory pathways associated with ventricular pre-excitation in patients suffering from Wolff-Parkinson-White (WPW) syndrome. The atrial activation and WPW studies included a comparative analysis of the BSPM and MFM patterns.

The signal-extraction protocols studied were orthogonal expansion techniques (SVD, KLT), a correlation technique, and a simple averaging method. We conclude that the orthogonal expansion and correlation techniques have inherent difficulties, primarily associated with their mathematical constructs. The signal averaging method, though it does present some limitations, can be used successfully in the WPW problem.

The dominant dipole direction associated with atrial activation is tangential to the atrial blood masses, resulting in a higher sensitivity of the magnetic field, than the potential measurements, to atrial electric events. Results show that atrial repolarisation starts immediately after P-wave offset and is not delayed until ventricular activation, as has been suggested by some authors. We determined that no HPS signal is present in the extracted maps of the PR segment. Further, the spatial patterns and ramps in the PR segment that were previously associated with the conduction system, actually reflect the continuous changes in the electric source due to atrial repolarisation as a function of time in both magnetic and electric signals.

On the other hand, the decreased sensitivity to atrial repolarisation in BSPM measurements the detection of the early δ -wave signal in patients with left-sided accessory pathways (AP). We used pattern-matching techniques (12-lead ECG, BSPM distributions) and inverse-solution localisation of AP to confirm the successful extraction of the atrial repolarisation signal. With identified limits to the present accuracy of localisation procedures based on inverse solutions, we make suggestions for improved 12-lead and BSPM pattern-matching criteria and present a basis for the development of MCG criteria to locate the site of the AP.

Symbols and abbreviations

A matrix A

\mathbf{A} matrix of expansion coefficients associated with the eigenvectors \mathbf{U}

\mathbf{B} matrix of expansion coefficients associated with the eigenvectors \mathbf{V}

\underline{B} magnetic flux density [T]

\mathbf{C} KLT expansion coefficients

d dipole depth in the thorax[m]

dS differential surface area

δ separation of extrema [m]

δl distance separating a pair of current source and sink [m]

$|\Delta \underline{R}|$ three-dimensional magnitude of the difference of dipole source location coordinates [m]

ΔX X -component of difference of coordinates [m]

ΔY Y -component of difference of coordinates [m]

ΔZ Z -component of difference of coordinates [m]

E expectation value

ϵ mean-square error function

\mathbf{F} KLT orthonormal basis set

I current source or sink [A]

\underline{I} identity matrix

g_i correlation fraction

K covariance matrix
 λ_i eigenvalues of **K**
 μ_0 permeability of free space [Wb (A·m)⁻¹]
N number of samples (i.e. heartbeats)
p number of MF grid points or BSP leads
 \underline{P} current dipole moment [A·m]
 P_{neg} peak negative signal
 P_{pos} peak positive signal
 ϕ electric potential [V]
 Φ potential matrix
r rank of matrix **X**
 \underline{r} source coordinate [m]
 \underline{r}' observation coordinate [m]
 $\left| \frac{R_{max}}{P_{max}} \right|$ ratio of maximum R-wave to P-wave signals
 R_{prim} primary source characterisation error
 R_{sec} secondary source extraction error
 \mathbf{R}^{CT} correlation technique residual matrix
 \mathbf{R}^{KLT} Karhunen-Loève expansion residual matrix
 \mathbf{R}^{SVD} Singular Value Decomposition residual matrix
 \mathbf{R}^{TAT} temporal averaging technique residual matrix
 σ conductivity [mho m⁻¹]

S/N signal to noise ratio

S_{HPS}/S_{Ta} ratio of HPS to Ta signals

t time [ms]

$t_{P_{neg}}$ time of peak negative signal

$t_{P_{pos}}$ time of peak positive signal

U orthonormalised eigenvectors of \mathbf{XX}^*

V orthonormalised eigenvectors of $\mathbf{X}^*\mathbf{X}$

W non-negative square-root of the eigenvalues of \mathbf{XX}^*

ω solid angle matrix

Ω deflated solid angle matrix

w_i^2 common eigenvalues of \mathbf{XX}^* and $\mathbf{X}^*\mathbf{X}$

X primary source matrix

X* transpose of primary source matrix

\mathbf{x}_i column of matrix **X**

$\bar{\mathbf{x}}$ average of columns of matrix **X**

Y secondary source matrix

Z combined source matrix

AP accessory pathway

A-V atrio-ventricular

aVF augmented left foot ECG lead

aVL augmented left arm ECG lead

aVR augmented right arm ECG lead

BB bundle branch

BSP(M) body surface potential (mapping)

CT Correlation Technique

DALECG Dalhousie ECG Analysis Program

DSL dipole source location

δ **wave** ECG preexcitation waveform in WPW syndrome

ECG electrocardiogram

EPS electrophysiological study

HB His bundle

HPS His-Purkinje system

HR heart rate

HV His-to-ventricular

KLT Karhunen-Loève Transform

LA left anterior AP location OR left arm ECG lead OR left atrium

LAL left antero-lateral AP location

LAP left anterior paraseptal AP location

LD left depolarisation

LL left lateral AP location OR left leg ECG lead

LP left posterior AP location

LPL left postero-lateral AP location

LPP left posterior paraseptal AP location

LR left repolarisation

MCG magnetocardiogram

MF(M) magnetic field (mapping)

QRS complex ventricular depolarisation ECG waveform

PR interval ECG interval from P-wave onset to QRS-complex onset

PR segment ECG interval from P-wave offset to QRS-complex onset

P wave atrial depolarisation ECG waveform

RA right anterior AP location OR right arm ECG lead OR right atrium

RAL right antero-lateral AP location

RAP right anterior paraseptal AP location

RD right depolarisation

RL right lateral AP location OR right leg ECG lead

RP right posterior AP location

RPL right postero-lateral AP location

RPP right posterior paraseptal AP location

RR right repolarisation

SA sino-atrial

S.D. standard deviation

SQUID Superconducting QUantum Interference Device

STT ECG interval from end of QRS-complex to end of T wave

SVD Singular Value Decomposition

Ta atrial repolarisation

\overline{Ta} average atrial repolarisation map

TAT Temporal Averaging Technique

Ta wave atrial repolarisation ECG waveform

T wave ventricular repolarisation ECG waveform

WCT Wilson central terminal

WPW Wolff-Parkinson-White (syndrome)

Acknowledgements

First, a special thank you is extended to my supervisor Gerhard Stroink. His patience and encouragement, despite some very difficult periods, were instrumental toward completing this work. Thank you GS.

Dr. Martin Gardner was instrumental in referring all patients to us for the WPW and HPS studies. He has also participated in development of research protocols and, as a clinician, has provided valuable advice about clinical aspects of this work. Without his participation, this work would not have been possible and his contributions are gratefully acknowledged.

Particular appreciation is extended to Dr. Milan Horáček for the very interesting discussions throughout my years at Dalhousie, for providing the pre-excitation simulation maps, and in particular, for his useful comments in the editing of this manuscript. Paul MacInnis often provided crucial assistance in software development, and particularly, understanding DALECG and averaging of the data. Earlier aspects of the His-Purkinje system study were performed in parallel with Dr. Carol Kafer's development of the model of the HPS. During this time, we had very profitable discussions, leading to mutual progress in unravelling this mystery. Her sincere friendship was especially valued.

Although this study is a result of my own research efforts, the use of the term 'we' throughout this thesis is particularly appropriate because of the contributions made by many others. Through the years many people have been a part of this effort, and all are thanked first for their friendship and then for their contributions, small or large to this work: Chris Purcell, Rob Merritt, G.A. Tan, John Lant, David Vardy, Phil Elliott, Doug Milsom, Stewart Ferguson, Graham Bateman, Rok Hren, Helen Tremayne, Dorothy Marshall, Gail Blackmore, Rob MacLeod, Brian Hoyt, Bob Potter and numerous summer students.

Finally, thank you to all my friends and colleagues in the physics department for their friendship. In particular, I must thank my best friend, colleague and husband, Derek Lawther, for his devotion and belief in my abilities. I could not have completed this work without him.

Financial support for this work was provided by the Heart and Stroke Foundation of Nova Scotia, the Medical Research Council of Canada, the Eliza Ritchie Doctoral Scholarship fund and the Walter C. Sumner Memorial Fellowship fund.

Preface

The history of electrocardiography predates magnetocardiography by some 75 years. The first electrocardiogram (ECG) was recorded by Waller [1] in 1887, while the first magnetocardiogram (MCG) was published by Baule and McFee [2] in 1963. Both the electric potentials and magnetic fields at the body surface are due to the movement of ions across cell membranes in the myocardium. Through the years, there was a widespread belief that the different nature of the electric and magnetic fields and ECG and MCG recording systems would provide independent, complementary information about the cardiac electrical processes. To date, very few studies deal with ECG and MCG data recorded from the same subjects. So far, these studies have not shown conclusively that any significant differences, leading to clinical application for the MCG, can be found in the information obtained from these signals. Because of its shorter history, and a significantly higher cost, the MCG has remained primarily a research tool. Nevertheless, some research directions in the biomagnetism community (i.e. inverse solutions) have contributed to new directions in clinical electrocardiography and research. In addition, there are technical advantages of magnetic over potential mapping techniques. With multi-channel MCG systems, a recording session would be faster and easier than ECG mapping, since no equipment (electrode paste) or patient preparation (e.g. skin rubbing, shaving) is required. The cost of the MCG technology is also becoming much lower than in previous years, reducing financial detractions.

This work will represent one of the few studies involving both magnetic field mapping (MFM) and body surface potential mapping (BSPM). Subject data presented in this study consist of both MFM and BSPM data recorded during the same session for most subjects. This complete set permits parallel MFM and BSPM studies, which

allows not only conclusions about the individual data sets, but also a comparative analysis. Further, the data sets are found to be truly complementary in that comparison of the two data sets can lead to observations and conclusions which might be otherwise missed.

The direction of this study was inspired by an increasing effort in both the bio-magnetism and body surface potential mapping communities to identify, extract and localise signals in the heart which one might label as superimposed sources. This terminology is chosen to identify a number of signals generated by the heart which are distorted by larger background signals.

The His-Purkinje system (HPS) signal, the δ wave associated with Wolff-Parkinson-White Syndrome (WPW), late QRS potentials and the U wave are all superimposed signals. The HPS and δ wave occur during the PR segment, which (although classically considered isoelectric) reflects the repolarisation of the atria (Ta wave) as a background source. Late potentials are superimposed on the STT segment, and the U wave, whose origins remain controversial, often rides on the tail of the much larger T wave.

WPW syndrome and late potentials are both of eminent clinical interest because they can cause life-threatening ventricular arrhythmias. The ability to detect the HPS signal at the body surface was initially thought to be clinically useful but has evolved more as an exercise in testing and developing high-resolution mapping techniques and, to validate inverse solutions. The source of the U wave is still plagued with controversy, and as such has not been of any clinical interest. As a result, studies on U waves still focus on unravelling its origins.

The questions which will be explored in the following pages relate specifically to mapping techniques, and will focus on events in the PR segment (Ta, HPS and WPW). In the author's M.Sc. thesis [3] dealing with the extraction of the HPS signal from MF maps, questions were raised about the reliability of the numerical techniques used and validity of assumptions required. Most important is the question of the physiological significance of the extracted maps. The same or similar techniques

were in use by other groups to isolate the HPS source. After initial confidence in these methods was established, most groups proceeded to use similar methods to extract and then validate the localisation of the accessory pathways in the hearts of WPW patients. In the present study, some of our previous questions are answered. We then proceed to apply this experience to a comparative study of the MF and BSP maps of a group of patients with WPW syndrome.

A review of the Dalhousie combined mapping systems, data averaging and display is presented in Chapter 1. Reference in this chapter will be made to 3 appendices. Appendix A presents an itemised guide to the recording session. Appendix B is a brief description of DALECG (the ECG/MCG averaging program) and post-average file handling.

A brief theoretical presentation of the forward and inverse problems in electrocardiography and magnetocardiography, with simulations of particular interest in this study, are presented in Chapter 2.

A second part of theory and simulations, for various extraction techniques, are presented in Chapter 3. These simulations are crucial to the extraction and interpretation of HPS data.

The first part of results from recorded data is in Chapter 4. The comparative analysis of BSP and MF maps of atrial excitation and recovery during the PR interval, in a group of 30 subjects, is presented. This analysis provided an important basis for understanding the results of the HPS and WPW studies.

The next two chapters deal with the application of the signal extraction techniques. In Chapter 5, an attempt to isolate the superimposed HPS source from the background atrial repolarisation signal is described. The relevance of these results, and their relationship to previously published work, are discussed. Appendix C is a brief presentation of the time-shift technique used by another group [4].

Chapter 6 is a study of a group of WPW syndrome patients. The characteristic δ wave associated with this syndrome is larger than the HPS signal, but at onset it is also distorted by atrial signals. The ability to accurately localise the source of

the δ wave is of clinical interest. For some subjects with small δ waves, present non-invasive ECG techniques have limited value. In addition, MFM and BSPM inverse solutions will most accurately reflect the site of pre-excitation early in the δ wave. The extraction techniques are applied to this group with an interest to enhancing the early δ wave, simultaneously addressing both these limitations.

Appendix D is a short discussion and simulations examining the dependence of magnetic field patterns on gradiometer design. Appendix E is a review of cardiac anatomy, and the relative orientation of the heart in the torso; as well, the standard nomenclature applied to ECG and MCG traces is summarised. Appendix F is a case study of a WPW patient, whom we could not include in the main WPW group because of the presence of 2 accessory pathways and 2 different atrial pacemaker sites.

1 Body Surface Potential and Magnetic Field Mapping

The first MCG at Dalhousie was recorded in 1976, but research effort in the laboratory's earliest years was directed primarily toward technological advances and design of a low-noise environment for magnetocardiographic recordings [5,6,7]. Eventually, through the 80's, efforts turned more toward recordings and data analysis. In the mid 80's a BSPM system was built and installed for the Biomagnetism Laboratory and it became routine to obtain both MCG and BSPM recordings on all participants.

There is a vast array of literature available covering the topics of electric and magnetic field mapping of the myocardium in general [8,9,10,11,12,13,14,15] and at Dalhousie in particular [3,5,6,7,16,17,18,19,20,21,22,23,24]. A detailed review is beyond the scope of this work. So after a general overview, only those features of the recording system and protocols that are of particular interest to this study, will be described.

1.1 BSPM and MCG instrumentation

Presently, the MCG and BSPM instrumentation form one complete integrated recording system, of which the schematics are shown in Figure 1.1 and the details of the instrumentation specifications listed in Table 1.1. The subject is placed in an eddy-current shielded room which reduces the 60 Hz magnetic noise and its harmonics in both the MCG and BSPM signals. The output from the magnetic and electric sensors are both recorded by a common data acquisition system based on a PDP-11/24 micro-computer. Both the hardware and software for the data acquisition system have been designed in the Dept. of Physiology and Biophysics. The asymmetric 2nd order RF SQUID gradiometer Model SQP-400 and superinsulated dewar with quartz tail was

Instrumentation specifications and recording parameters

	MCG	BSPM
Noise ^[1]		
• instrumentation	30 fT/Hz ^{1/2}	70 nV/Hz ^{1/2} ^[2]
• patient	30 fT/Hz ^{1/2}	140 nV/Hz ^{1/2}
Sensor	2nd order asymmetric gradiometer - 2.5 cm front end coil - 4 cm baseline	Ag/AgCl electrodes referenced to Wilson Central Terminal
No. channels	56 sequential	120 simultaneous
Total gain	1.3/ <i>n</i>	2000
Bandwidth	DC–125 Hz	.05–125 Hz
Sampling frequency	500 Hz	500 Hz
Sampling time	30 s	30 s
12-bit ADC range	± 150 pT × <i>n</i>	± 5 mV
Bit resolution	75 fT × <i>n</i>	2.5 μV
Average peak signal (R-max) ^[3]	~16 pT	~1.8 mV
Noise after averaging ^[3,4]	~54 fT	~1.3 μV
Typical max. S/N ^[3]	~300	~ 1700

Table 1.1: MCG and BSPM instrumentation specifications and recording parameters. Several recording parameters are hardware variable but only the standard settings have been quoted. *n* is the DSQ-400 SQUID controller DAC output range (typically *n* = 1/2 or 1).

[1] Average obtained in the 70–170 Hz bandwidth.

[2] Input shorted.

[3] Computed from data of 27 normals with an average age of 47.7 (7.6) years.

[4] Computed in the UP interval.

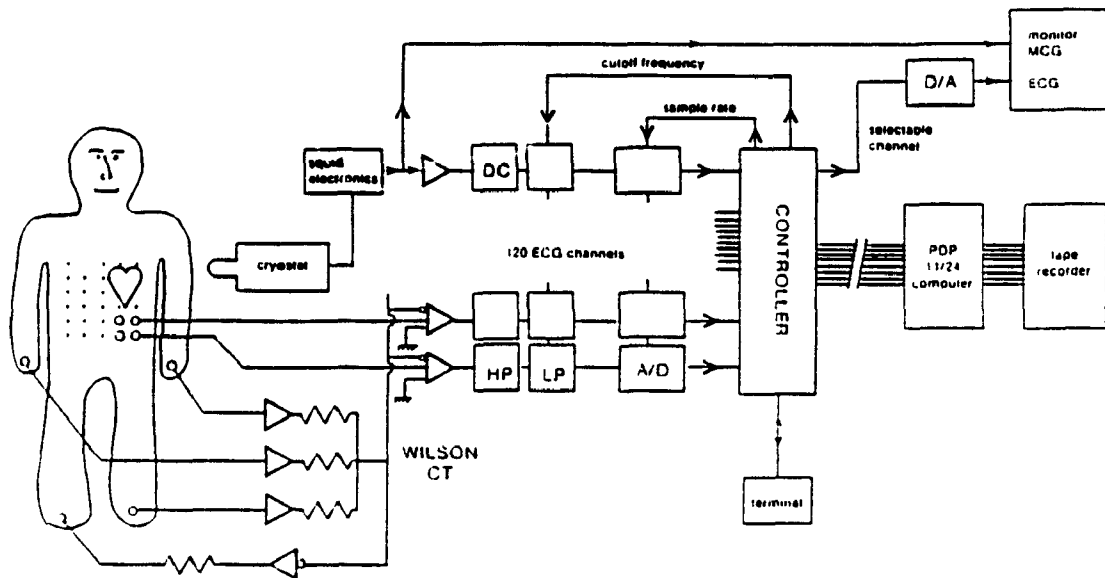


Figure 1.1: Schematic of the MCG and BSPM combined recording system.

manufactured by CTF Systems Ltd., Port Coquitlum, BC. The noise spectrum for the magnetic and body surface potential mapping systems are shown in Figures 1.2 and 1.3, respectively. These figures show that, except for 60 Hz, the patient noise limits the BSPM system performance. The MCG patient noise contributes only to frequencies below 10 Hz; above this, instrumentation noise is the limiting factor. This brief summary of the MCG and BSPM systems deserves some discussion. The issues of interest will be addressed in the following sections.

1.2 Comparison of instrumentation and protocols

1.2.1 Simultaneous versus sequential measurements

The single-channel MCG system requires that the signal at the 56 grid points be recorded sequentially. The concern in this mode of recording is twofold. The first problem to be dealt with is the alignment of (presumably) the same events recorded

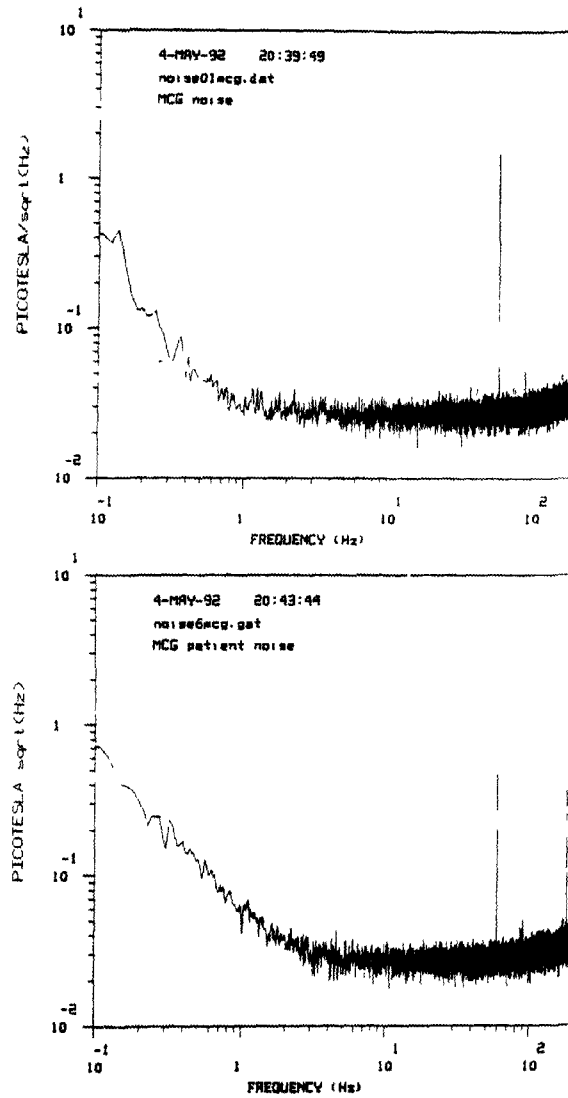


Figure 1.2: MCG noise spectra.

(Top) The instrumentation noise spectrum was obtained with the gradiometer in the shielded room, but no subject present. (Bottom) The patient noise was recorded by positioning the gradiometer at the level of a subject's knee, where no heart signal would be detected but muscle tremors and equipment vibration due to respiration and the beating heart would be detected.

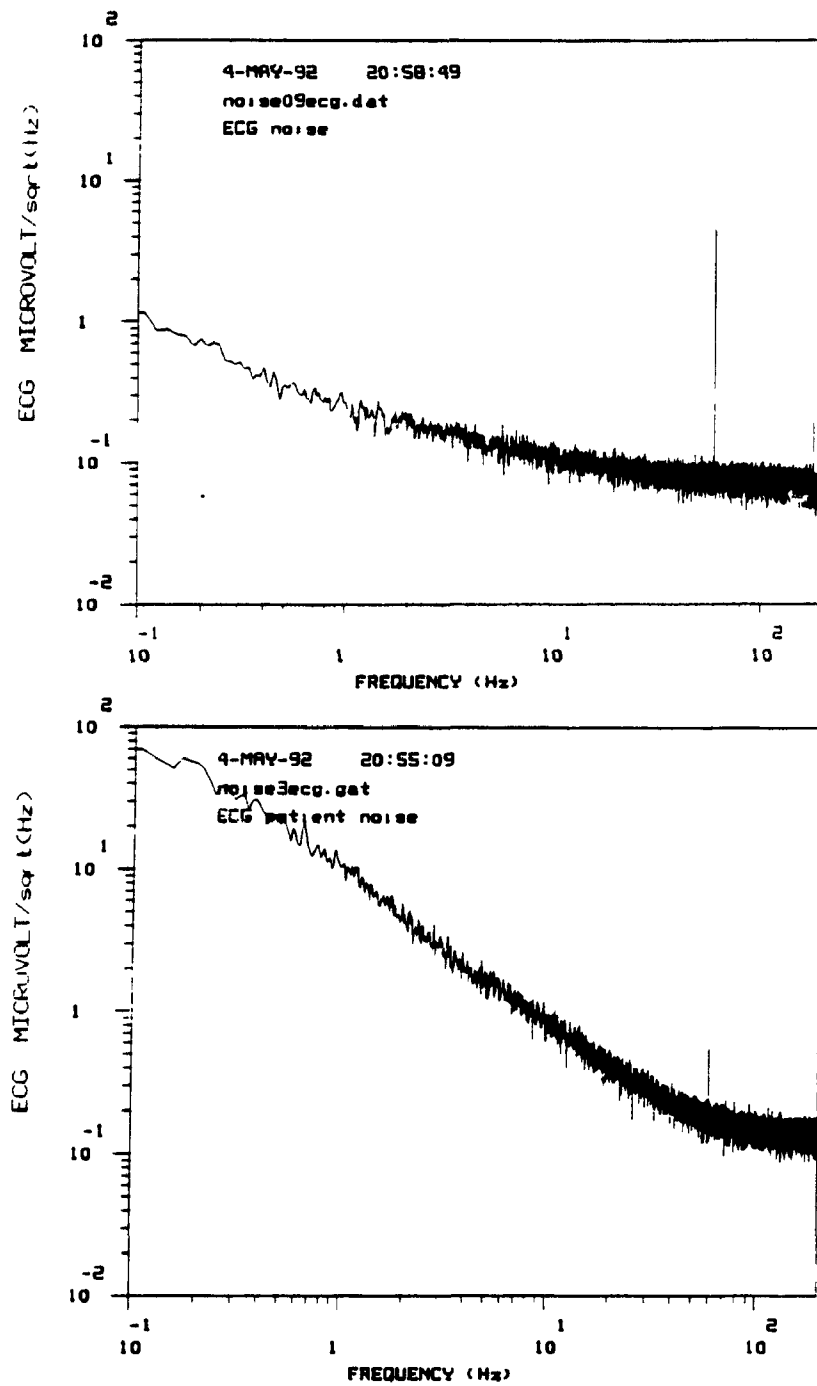


Figure 1.3: BSPM noise spectra.

(Top) The instrumentation noise spectrum was obtained with inputs to the ECG amplifiers shorted. (Bottom) The patient noise was obtained by taking the difference between 2 electrodes placed 4 cm apart on a subject's arm, thus removing the common cardiac signal but not the random muscle noise.

at the 56 different sites, and then between the MCG data and the BSPM data. The second problem arises because the heart rate may vary from the beginning to end of the BSPM and MCG recording session.

The first problem, we feel, has been dealt with satisfactorily – given the limitations of our single-channel MCG system. Simultaneously with the recording of the MCG signal, a set of 3 ECG leads are recorded. These are the 3 limb leads (right arm (RA), left arm (LA), left leg (LL) referenced to the Wilson Central Terminal (WCT)). The limb leads provide a common template for the averaging process, allowing decisions on inclusion or exclusion and alignment of heartbeats to be made with the same signal for all 56 points.

After the average of each of the 56 MCG signals is obtained, the 3 ECG leads are used to align the MCG from 56 sites relative to one another. This is accomplished using a correlation technique. From the first site, a window centered on the QRS complex of the largest ECG lead, and twice the width of the QRS, is compared to the same window for all the other 55 sites. The two windows are slid relative to one another until a maximum correlation is obtained. The temporal difference in alignment is used to adjust the detected time point of the R-wave maximum in all leads to correspond with that of the first. The 3 limb leads are also available in the BSPM data, so the same routine is used to then compare the MCG from site 1 with the BSPM data. Since the 120 BSPM leads are recorded simultaneously, they will be averaged simultaneously and have the same time lines. Generally, at most only a 1-sample-point variation (corresponding to 2 ms) is found between the different MCG points, but time-alignment differences amounting to several sampling intervals may be found between the MCG and BSPM data. The consistent MCG alignment results from the excellent R-wave maximum detection algorithm in DALECG (precision of ± 1 sample point [20]). The large difference in the MCG and BSPM alignment after averaging by DALECG is discussed in more detail in Appendix B. Briefly, it results from the fact that a different set of 3 leads is used by DALECG to determine time lines (limb leads vs. orthogonal X, Y and Z leads).

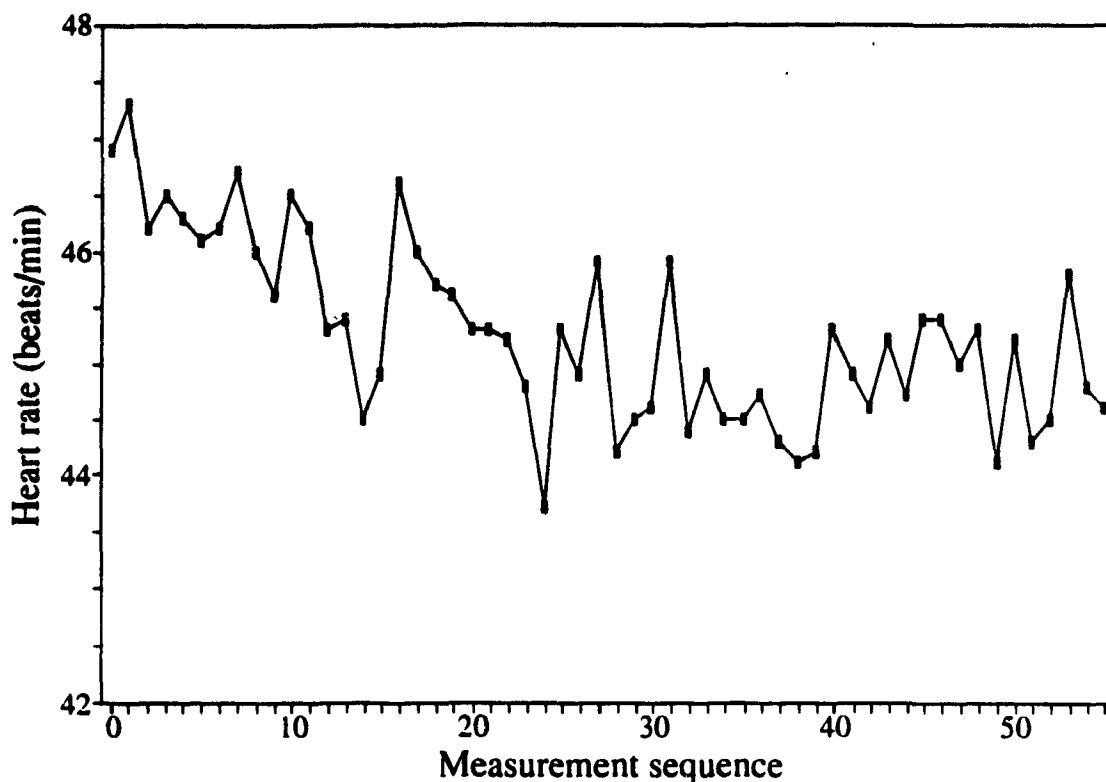


Figure 1.4: Heart-rate variability as a function of time during an MCG recording.

The second problem is more difficult to quantify and impossible to avoid with a single-channel MCG system. With 30 s per recording site and approximately another 30 s used to position the bed and adjust instrumentation, the total time elapsed between the measurement of the first and last sites is usually about 1 hour. Initially, the subject may be somewhat active, but he/she relaxes and at times falls asleep as the MCG recording progresses. In a relaxed state the heart rate (HR) is usually slower, hence as the MCG session progresses we find that the HR decreases. This is shown in Figure 1.4 where we have plotted the heart rate of a subject as a function of the recording sequence (effectively time). The trend seen, where there appears to be an initial decrease in the HR by approximately 5–10% during the first half of the session and then a relatively stable rate, is typical. Variations in HR can be accompanied by changes in the timing of events during the heart cycle of similar proportion.

These changes are of particular concern when constructing and analysing instantaneous magnetic field maps (MFM). When the HR does vary, it is possible that at a given instant the same event would not be measured in all 56 leads. Fortunately, the effects of such variations can be offset by the nature of the signal of interest. The largest instantaneous changes in the signal strength occur during the QRS, but this is the event whose length varies least when the HR changes [25]. Intervals such as the PR interval and STT segment will vary proportionally with the HR, but since the dynamical changes during this time are much slower, the effects on maps become less critical.

1.2.2 Recording bandwidths

The MCG and BSPM recording protocols both use low pass cut-off frequencies of 125 Hz, since most ECG (and MCG) power lies below 40 Hz. Significant amounts of signal energy can be measured at 100 Hz and above [26], but the choice of 125 Hz cut-off (dictated by the sampling rate of 500 Hz) for both systems is reasonable.

The lower cut-off frequencies of the two systems do differ. The recording of ECG signals requires the use of a high-pass filter since a DC-coupled input would make the preamps susceptible to saturation (at 10–20 mV) by the DC potentials arising from the electrochemical cell formed at the electrode-electrode gel-skin interface. The AC coupling also handles preamp drift. Since the bandwidth of SQUID magnetometry extends to DC no high-pass filter is used, to avoid filter-induced distortion of the waveforms. The measurements are still susceptible to some low-frequency drift, but this can be controlled by adjusting the DC level of the DAC output of the DSQ-400 to a 'rough' zero at every grid point, inducing an arbitrary DC level for each site.

The low-pass filter built into each analog BSPM (and MCG) channel is an anti-aliasing filter kept at 1/4 of the sampling frequency, so with its modest roll-off its effect on the signals is minimal. The high-pass filter may be of concern. Unless its cutoff frequency is far below the frequencies of interest, such a filter can cause distortions. These effects were pointed out by Berson and Pipberger [27] who showed

that a .05 Hz 6 dB/Oct high-pass filter can lead to distortions of the Frank leads during the T wave exceeding $50 \mu\text{V}$ in (3–6)% of 35 subjects.

Since $50 \mu\text{V}$ is only 3–4 times smaller than typical ECG P-wave maximum signals, the effects of this filter were explored in a DC BSP recording. This recording has been discussed previously [20], but we wish to present it again since it does have particular relevance to this project. A 56-lead sequential BSP recording was made from the anterior torso of a 15-year-old normal male, using a roving electrode whose potential was measured relative to the WCT. The electrode locations corresponded roughly to our standard MCG measurement grid. The roving electrode was connected to a regular AC-coupled mapping system input channel and a DC-coupled channel which were sampled at the same reduced gain to avoid saturation of the DC channel by the electrode offset potential. A second DC-coupled channel recorded the amplified difference between the input and output of an RC filter identical to that used in the AC channels. A manually adjustable offset circuit compensated for the DC electrode offset on the amplified difference channel so that the gain could be kept high on this channel. Due to the numerous adjustments required to keep the high gain difference channel from saturating, the recording took 2.5 hrs.

The first beat recorded at each of the 56 sites was extracted and written to 6 different files. These files contained the following channels: AC, DC, AC-DC, RA, LA and LL. Because this was a sequential measurement, the limb leads were recorded and used for averaging and alignment purposes as is done in MCG recordings. The AC signal recorded at all 56 sites is shown in Figure 1.5 while Figure 1.6 is the AC-DC recording. The filter distortions appear to depend on the size and shape of the ECG signal (especially QRS) and seem to peak in amplitude early during the STT segment. The maximum (peak-to-peak) distortion is, as found by Berson and Pipberger [27], about $50 \mu\text{V}$. Relative to a peak-to-peak AC ECG amplitude of 3.0 mV, this distortion, during the QRST, represents less than 1% of the signal. When we focus on the P wave, we find maximum distortions of about $2.5 \mu\text{V}$, corresponding to $\sim 2\%$ of the maximum P wave, and actually of the same value as the bit resolution.

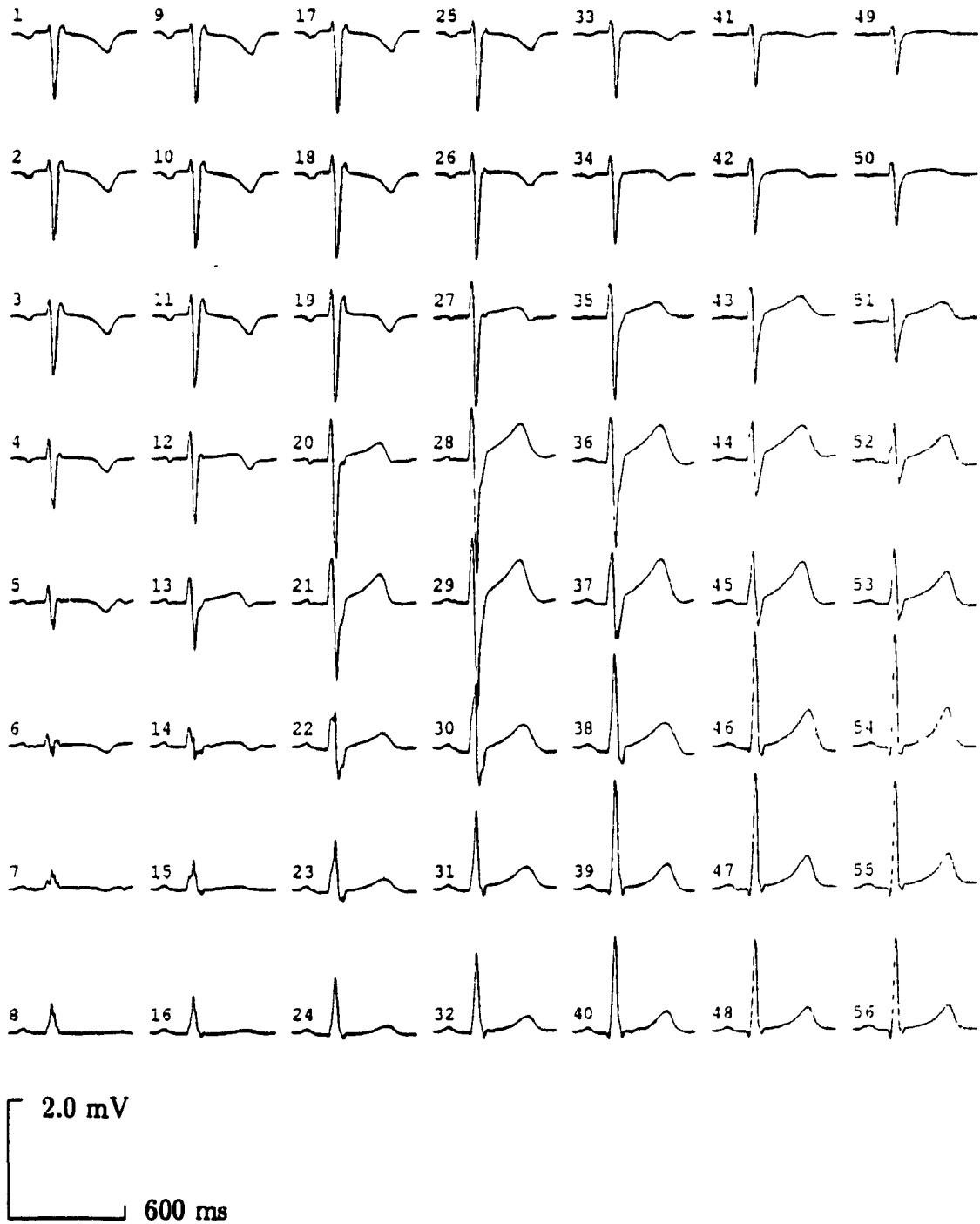


Figure 1.5: 56-lead AC BSP recording.
The interval -230/430 ms relative to R-maximum is plotted for one complex.

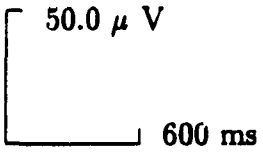
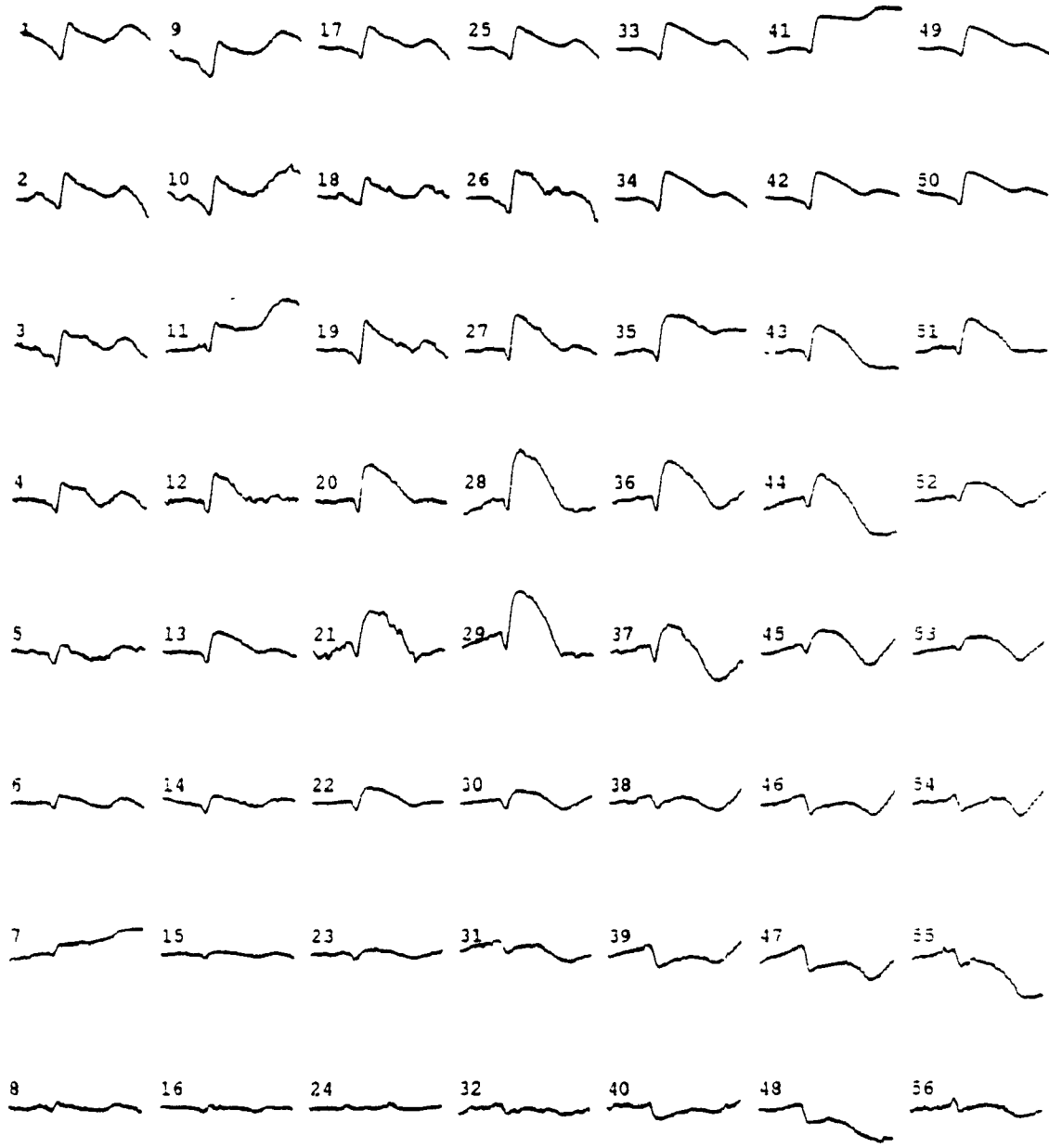


Figure 1.6: 56-lead AC-DC BSP recording.
The difference of an AC and DC recorded 56-lead BSP is plotted in the interval -230/430 ms relative to R max for a one complex.

Since our primary concern would not actually be the effects this distortion has on the P wave, but more so on the smaller atrial repolarisation, the $2.5 \mu\text{V}$ level means that our usual bit resolution will be more limiting (if at all) than will be the high pass filter distortions.

1.3 Recording protocol, averaging and data display

The details of recording, averaging and analysing the BSPM and MCG data are numerous. An attempt has been made to give the essence of the preparation and procedures required to obtain the data (see Appendix A). In addition, an overview of Dalhousie's ECG averaging program (DALECG) is in Appendix B. The more important and interesting aspects will be discussed formally in the next sections.

1.3.1 A BSPM and MCG recording

In 1986, a new isolation amplifier was designed for the BSPM system which would accept as input the DAC output from the DSQ-400 SQUID controller. Since that time, it has become routine to obtain both MCG and BSPM recordings for all participants. To date some 200 recordings have been performed in the shielded room. Approximately one-half of these have been normal subjects, recruited by various means, to be part of the normal-heart group. These recordings are used to determine normal MCG and BSPM features and to compare with patient groups. Before inclusion into the normal group, a standard 12-lead ECG and a cardiac physical exam by a cardiologist at the Victoria General (VG) Hospital were performed. Several patient groups have been studied. These include a myocardial infarction group, a ventricular tachycardia group, 1st degree A-V block patients and Wolff-Parkinson-White Syndrome (WPW) patients. All these subjects are recruited through the Cardiology Department at the VG Hospital, after appropriate diagnosis.

When a subject has been recruited, they usually arrive at the Physics Department via the VG with a cardiac research nurse. The nurse is in charge and takes care of the

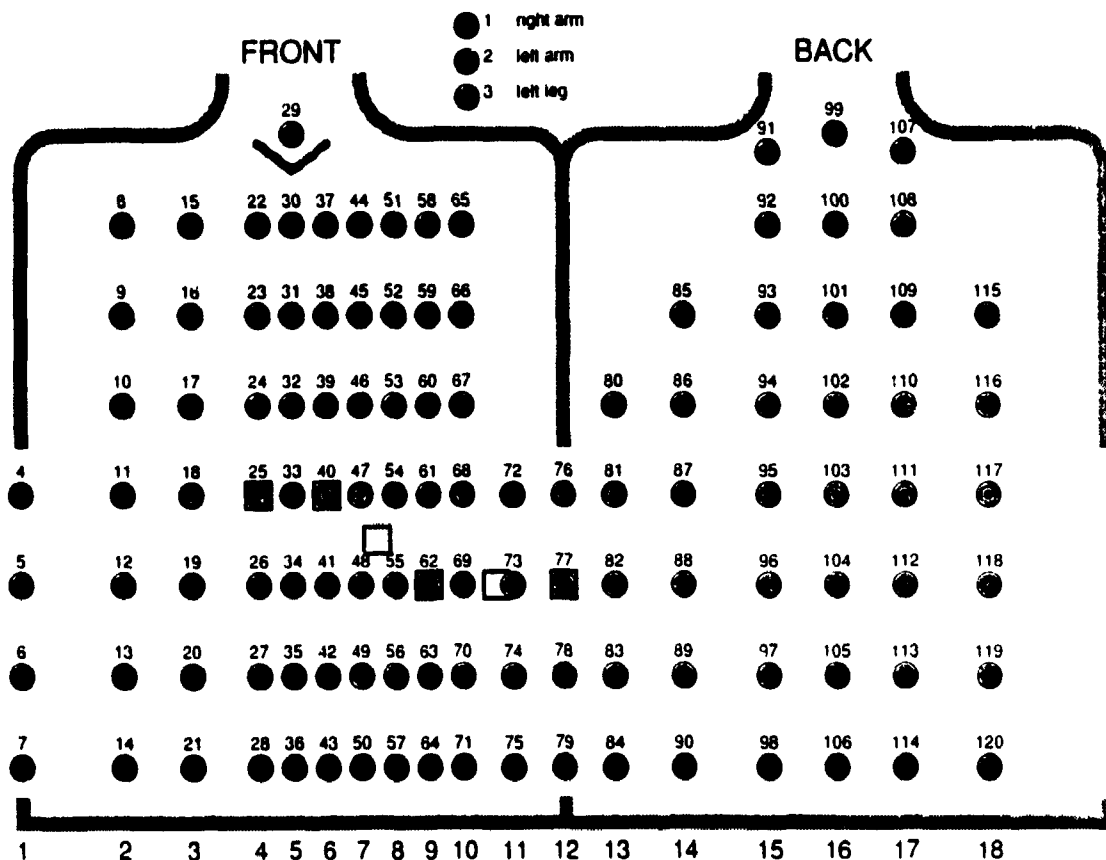


Figure 1.7: The BSPM electrode locations.

BSPM recording. A member of the Biomagnetism group will assist the nurse and be responsible for the MCG recording. Together they will review the procedure with the participant and then a consent form is signed by the subject and witnessed. Though the description which follows assumes that a nurse and technician are present, at times, both recordings have been done entirely by the technician with the assistance of another member of the research group.

Electrodes are prepared just before the subject is expected to arrive but not too far in advance since the conducting paste will begin to dry-up. Hence the BSPM recording is done first. A schematic of the relative locations of the 120 electrodes applied to the torso is shown in Figure 1.7. Electrode 33 is positioned at the intersection

of the sternum and the level of the first intercostal space¹. Other electrodes (on strips of 4–8 electrodes) are positioned relative to this reference around the torso. Many of these positions are dictated by other anatomical features. The vertical distance between electrodes is 5 cm and the minimum horizontal spacing (limited by width of the electrode strips) is 2.5 cm. Once the electrodes have been applied, approximately 20 minutes are allowed to elapse before obtaining the actual recording to allow the conducting paste to warm-up to the body temperature. After the recording is obtained all but the 4 limb leads (RA, LA, LL and right leg drive) are removed. The nurse cleans the electrodes (about 1/2 hour) while the MCG recording is done. As much as one hour has elapsed since the patient has arrived, to the time the MCG session begins.

Preparation of the subject for the MCG recording takes little time. He/she is positioned on the bed. The MCG measuring grid is shown in Figure 1.8. Grid location D3 is the common reference point and is located at the intersection of the sternum and 4th intercostal space, as is BSPM electrode 33. The dewar is positioned above the patient to within ~5 mm of the highest point of the anterior torso; the 4 limb leads are connected to the MCG limb lead harness, and the subject is made as comfortable as possible, especially to ensure that he/she is not cold. During this whole process the technician relays as much information about the whole process to the patient, thus assuring their confidence in the safety of the procedure.

Once the technician has confirmed that all preparations have been made and that everything is in working order, the recording can begin. Since there is only a single MCG channel, the measurements from the 56 points are obtained sequentially, by moving the bed relative to the probe in a set pattern (see Figure 1.8). This process normally takes 55 minutes. Since the BSPM and MCG amplifiers are battery

¹Though much caution is taken to assure that this position is accurate, because of different body shapes and sizes, it is usually difficult to localise the 4th intercostal space to more than within 1 cm. It has been suggested that the error here can be as great as one intercostal space, even by the most highly trained professionals.

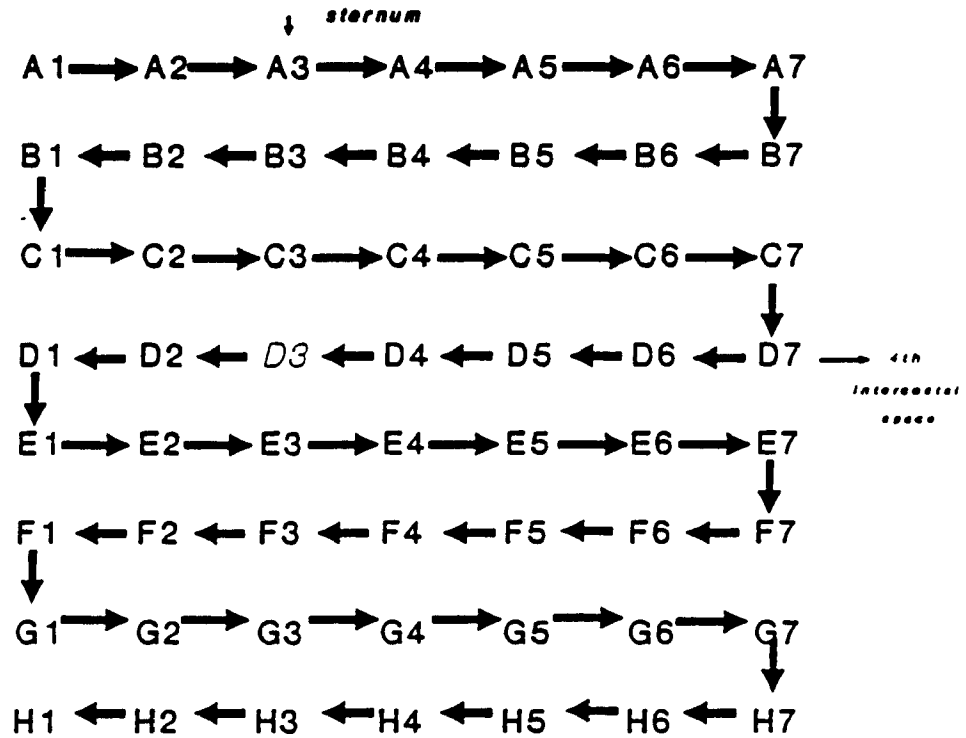


Figure 1.8: MCG measuring grid.

A fixed 7 × 8 grid of 4 cm spacing is used for all subjects. The arrows indicate the order in which the different locations are measured.

powered, care must be taken not to exceed a total of about 1.5 hrs² battery-operation time, since they may have discharged sufficiently after this period of time to be inoperable.

With the end of the MCG recording, the last 4 electrodes are removed, the patient dresses and returns with the nurse to the VG.

1.3.2 Noise reduction by averaging

The term high-resolution ECG and MCG has almost become synonymous with signal averaging. The basic premise in temporal averaging of biological signals, as first suggested by Dawson in 1951 [28], is that, ideally, when N samples of a noisy signal are aligned temporally with respect to a reference point, and then summed, the noise will be reduced by $1/\sqrt{N}$, while leaving the signal unaffected [29]. In other words, the additive combination of successive repetitions of a signal results in the reinforcement of the true coherent signal while the noise, if it is random and uncorrelated to the signal, tends to cancel itself out.

For optimal signal averaging of cardiac signals, two conditions must be met: 1) the noise contaminant must be both random and stationary, and 2) the signal of interest should be precisely synchronised to a stable reference point. Except for 60 Hz line interference, noise is satisfactorily random, that is, uncorrelated to the heart produced signal of interest [30], and its characteristics do not change significantly during a recording session.

Synchronisation of the cardiac signal to a fiducial point is not as easily achieved. Cardiac excitation and contraction can vary on a beat-to-beat basis, and additional variations in size and shape of an ECG or MCG signal are caused by the respiration cycle. The amplitude of the R wave can vary by as much as 30% between inspiration and expiration [31]. Cardiac and respiratory abnormalities may amplify this normal variability. These variations in waveform from beat-to-beat impose some degree of

²The amplifiers are actually turned-on only for about 5 minutes during the entire BSPM recording.

arbitrariness to any averaging process. Even if some fiducial point were established, such as the QRS complex, there is no assurance that other cardiac events are stable relative to that reference. The onset of His bundle potentials, for instance, may vary by several milliseconds from beat-to-beat in reference to QRS [22].

The theoretical decrease in noise level by $1/\sqrt{N}$, where N is the number of complexes averaged, was tested. In Figure 1.9 the RMS noise level vs. \sqrt{N} is plotted for MCG and ECG data. The data results from averaging, with increasing lengths of MCG recordings (e.g. 2 s, 5 s, 15 s, 25 s, ...). Results for the averaging of the 3 limb-lead ECG records are shown in Figure 1.9a, obtained during one of the MCG trials. Figure 1.9b shows the MCG results for 2 separate recordings. Logarithmic plots of the data in Fig. 1.9 confirm the $1/\sqrt{N}$ expected relationship. More interestingly, the ECG (or BSPM) noise level is found to reach a minimum at about 20 complexes, indicating that recordings longer than about 30 seconds would generally not reduce the noise significantly³. The MCG data does not appear to reach a minimum until about 100 complexes have been averaged. Unfortunately, because of time constraints (both patient comfort and battery limitations), recordings must be limited to 30 seconds. According to actual noise levels obtained from many 30-second recordings (see Table 1.1) and Figure 1.9b, the average level of ~ 60 fT is no more than about 2-3 times the minimum we might be able to achieve with longer recordings. Finally, the benefits of averaging are demonstrated in Figure 1.10. On the left is a single beat of raw data for an MCG (top) and BSPM (bottom) recording. The average of this same site/lead is presented on the right.

The program DALECG [18,32] was developed over two decades in the Dept. of Physiology and Biophysics to average ECG, BSPM and MCG data. There are various versions of DALECG in use for different tasks, but the basic structure and approach to the averaging remains the same in all. An overview of this program, as is used by this group, is presented in Appendix B.

³Since DALECG does not necessarily accept all complexes encountered for inclusion in the average beat, more than 20 seconds would be needed to guarantee this minimum.

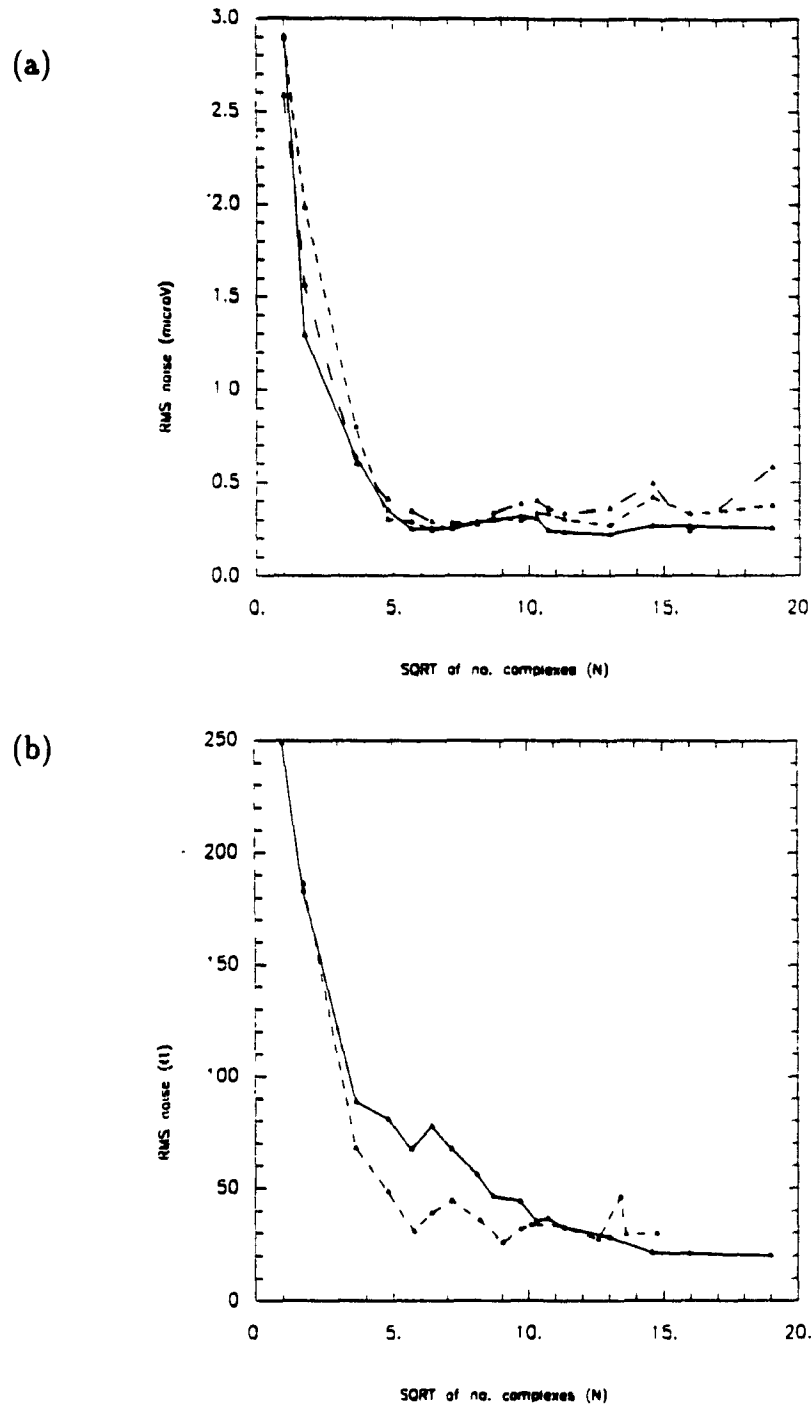


Figure 1.9: Plots of the RMS noise vs. number of complexes averaged.
 (a) ECG limb leads I, II and III. (b) 2 different MCG recordings.

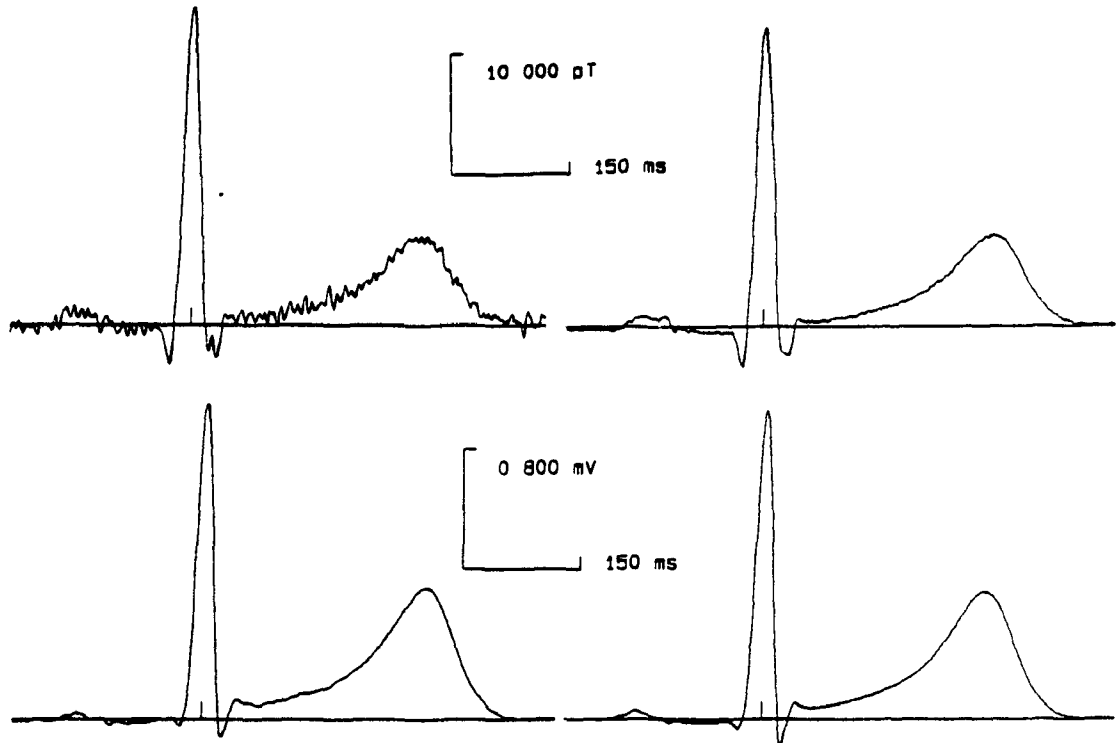


Figure 1.10: Demonstration of the noise reduction by averaging.
On the left are the raw MCG (top) and BSPM (bottom) recordings and on the right is the average for all beats recorded at MCG grid point 28 and BSPM lead 62 (MCG 28 beats, BSPM 26 beats). The scale in the center, top applies to both MCG traces and the one center, bottom applies to both BSPM traces.

Figure 1.11 depicts the steps involved in getting data from the data collection tape into files containing single beat averages of the MCG, 3 limb leads and the BSPM data. The processing of the MCG and BSPM recordings is virtually identical. Minor differences result almost entirely from the sequential versus simultaneous nature of the two data sets.

Routinely, there are bad leads in BSPM data, resulting in most cases from poor electrode-skin contact. With the large number of channels recorded, these bad leads do not represent a significant loss of information; nevertheless efforts are made to rectify these problems before the recording. A bad MCG recording is rare, but not impossible. These, when present, usually result from magnetic interference from patient's dental work or poor limb-lead contact which can affect the averaging of all 4 channels. Due to the sequential nature of the recording, other potential disturbances⁴ can be dealt with at the time of the recording on an individual basis by repeating the recording. To indicate the status of particular leads or grid points, a bad lead array (IBADLEAD) is used. This is an array containing either zeros (0) or ones (1), denoting either a bad (0) or good (1) lead. Programs read this array so that processing and analysis of the data proceeds as if the leads designated as bad never existed.

1.3.3 Standard post-average processing

Figure 1.12 outlines the final steps required in processing the MCG and BSPM averaged data files before the data is to be analysed within the framework of a particular study. In this final stage, we are concerned with correcting alignment and time-lines, and removing 60 Hz interference.

The alignment of the 56 MCG records (as described previously in Section 1.2.1) relative to one another is accomplished with a cross-correlation routine using the limb leads, adapted from an existing subroutine in the DALECG software. With optimal

⁴e.g. large drifts in the baseline due to movement of large magnetic objects in the local environment.

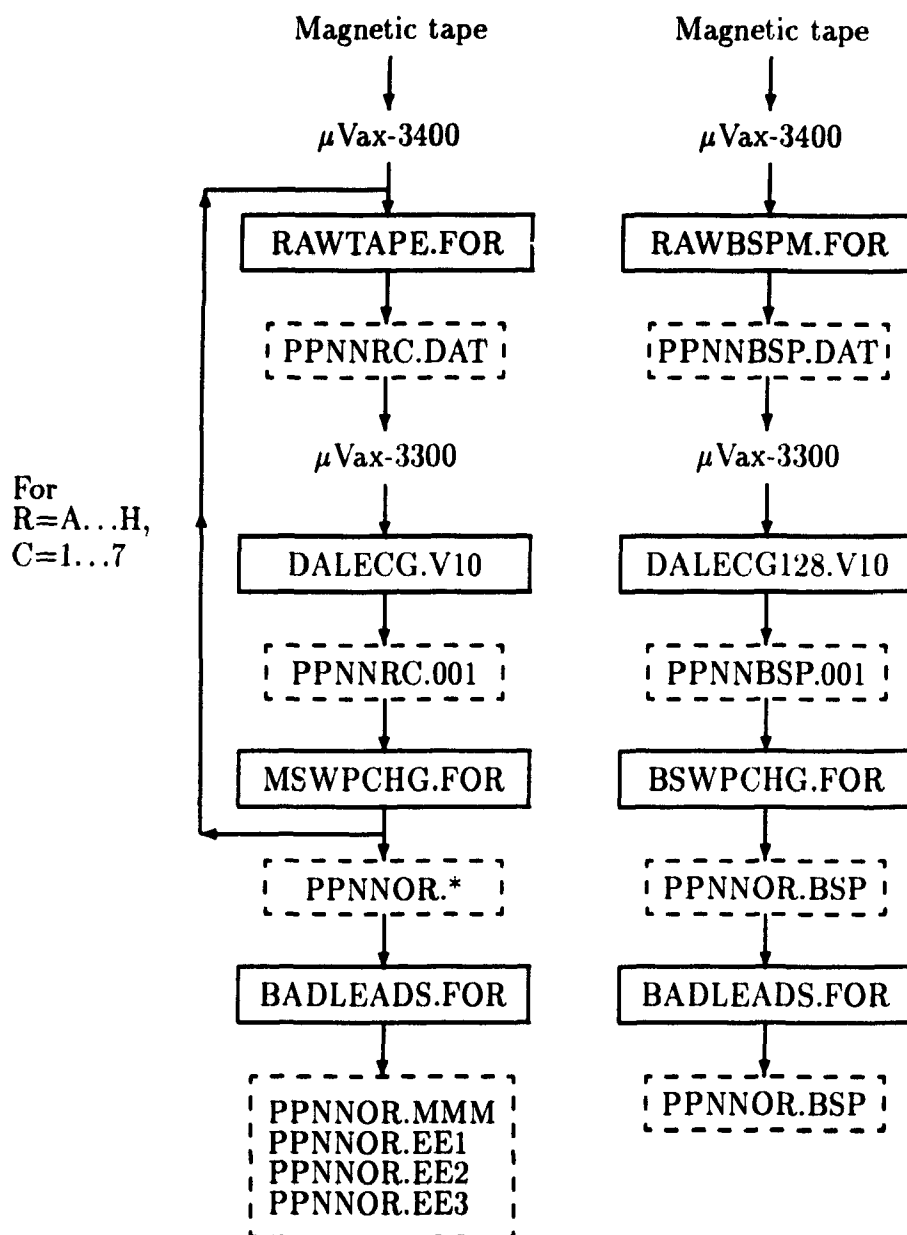


Figure 1.11: Flowchart of steps in MCG and BSPM averaging. The programs used to get from raw files to a useful averaged data format for the MCG (left) and BSPM (right) data is shown. The input and output files in each step are indicated. Solid boxes and dash boxes frame program names and data file names, respectively.

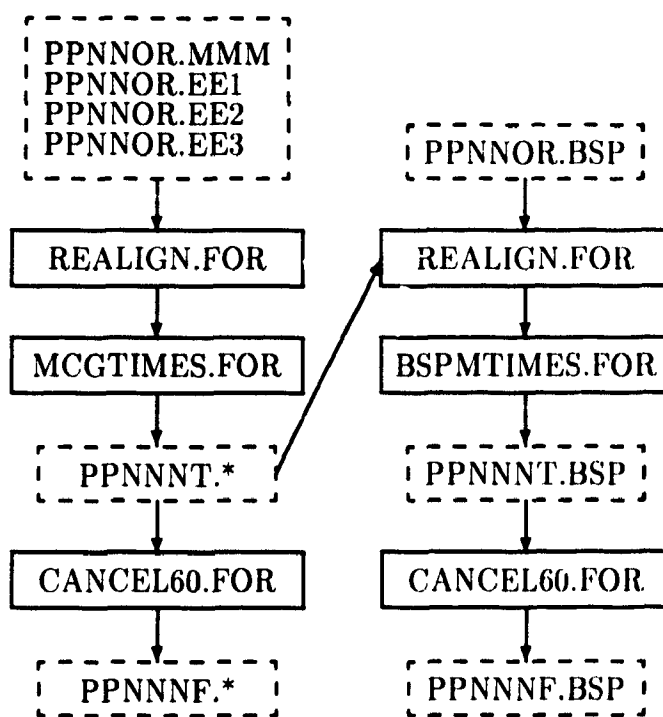


Figure 1.12: Post-average processing.
Solid boxes and dash boxes frame program names and data filenames, respectively.

alignment of the 56 MCG records achieved, new time lines are set. These time lines define the occurrence of the onset, offset and maximum of particular events in the heart⁵. Though they have been automatically determined by DALECG, the MCG in particular, will show significant variations from record to record, with the P wave landmarks being undetected or incorrectly assigned in the MCG and BSPM quite routinely. The new time points are indicated by displaying the RMS of the 56 leads and a 12 lead inset of the MCG data on a Tektronics 4010 graphics terminal and manually moving crosshairs to the new point desired. Once the MCG time lines have been set, the BSPM data will be aligned relative to the MCG, and time lines will be set using the Frank X, Y and Z orthogonal leads and their RMS.

A 60 Hz numerical adaptive filter (CANCEL60.FOR) can be applied almost any-time after averaging, but is usually used after alignment and setting new times. This filter was designed by D. Joly of the Cardiac Research Group at l'Université de Montréal. It determines the amount of 60 Hz noise present in the signal by averaging the 58, 59, 61 and 62 Hz components and comparing this average amplitude to the 60 Hz value. Any fraction of 60 Hz above the average value is attributed to noise and removed by subtracting a phase and amplitude matched sine wave.

1.3.4 General-purpose software for data analysis and display

After averaging, the signal recorded at each MCG grid point or BSPM lead location is stored in a 500- or 1000-point array, representing either a 1- or 2-second window centered on the R-wave offset. In many applications, the whole heart complex will not be analysed. A key program used in virtually all analysis of the MCG and BSPM data is called SELECT.FOR⁶. The output format of this program is used in all subsequent analysis. A brief description of this program and its output format, which we commonly refer to as FOR012.DAT, will be given next.

⁵P-on, P-max, P-off, R-on, R-max, R-off, T-max and T-off are the reference points used.

⁶This program supercedes two earlier ones called PARTBASE.FOR and RMSMAPS.FOR; SELECT.FOR was developed from these earlier two programs by this author.

This program is used to extract data for plotting or further analysis. The type of data of interest is the first question asked. The options are: temporal, spatial or RMS data. For each of these 3 options the type of data is also specified (MCG, BSPM or 56-lead BSPM). Each of these 9 options are coded in the header of the FOR012.DAT files by the integer ITYPE. In all our analysis, over 70 different ITYPE's have been defined so far, with the basic convention that numbers between 1-99 and 100-199 denote temporal and spatial organisation respectively. Once the type of data is selected, one must indicate the reference point for which the interval of interest is to be referred to and the interval in milliseconds which will be extracted. The reference point can be any of the 8 time lines set with MCGTIMES (BSPMTIMES). The output file contains a header plus the data of interest selected. The header will contain the ITYPE, start and end times (STIME and ETIME), the sampling interval (SINT), the reference zero time (ZEROTT), the patient identification code (FILE=NN), the bad lead array (IBADLEADS) and a number of other variables which are infrequently used but can be redefined for new purposes. Following the header is the data, which is either temporally or spatially organised. Temporally organised data means that the data for all t time points for each of the p leads is written to the file in a $t \times p$ array. A $p \times t$ array contains the p points forming each of the t maps selected for spatial analysis.

The plotting of the different types of data will be discussed next, using MCG and BSPM data from the same normal subject (RK156). Figure 1.13 demonstrates the plotting of MCG temporal data. The 56 points are displayed in a 7×8 grid, with an appropriate amplitude and time scale. An equivalent format is used to display the BSPM data (Figs. 1.14 and 1.15), however because of the large number of leads a two-page format is used to maintain a similar resolution as the MCG data. The 117 body surface points are arranged to correspond to their relative locations on the torso surface. The 3 limb leads are plotted as an inset.

A similar format is used to display the RMS maps. An RMS map is defined,

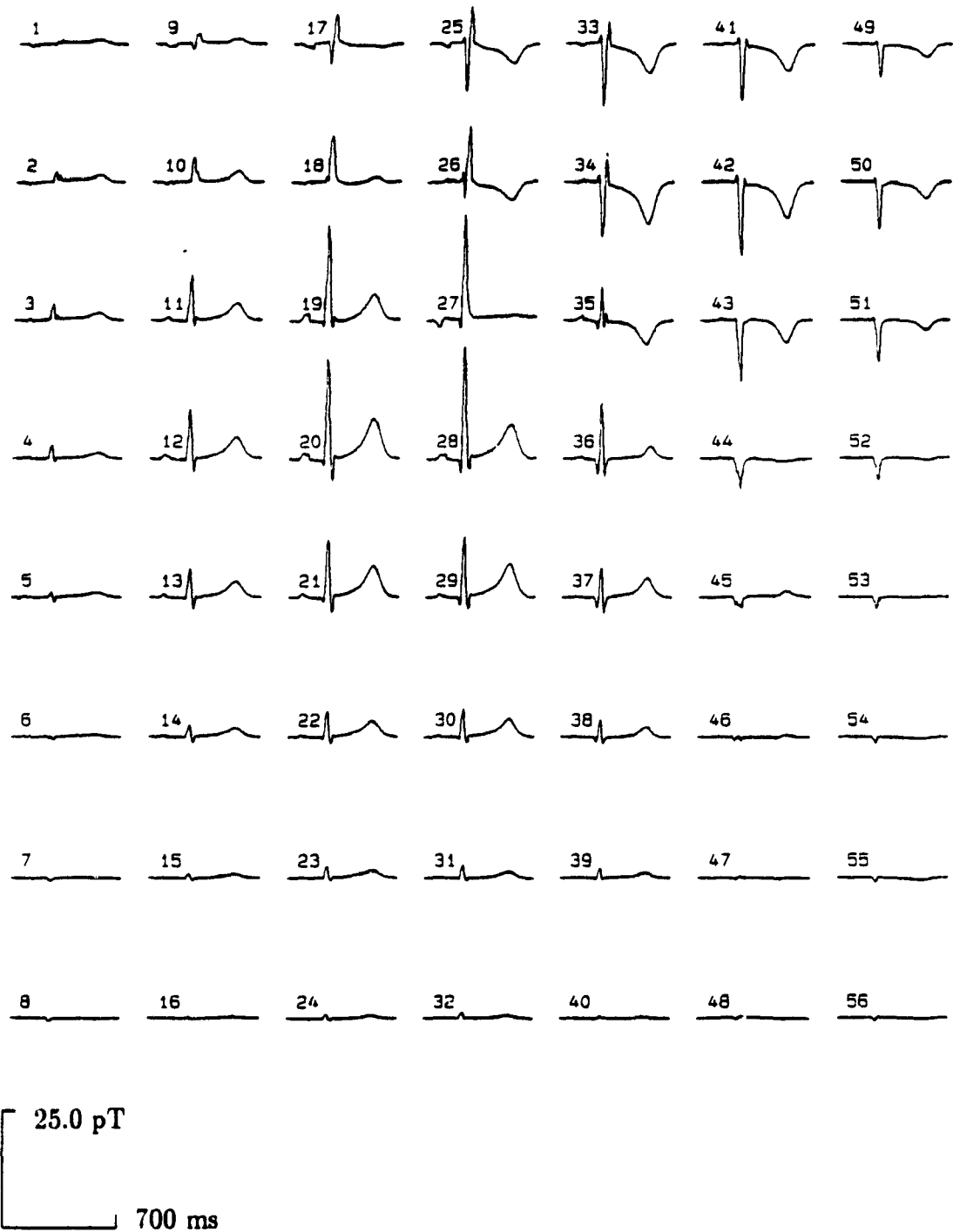


Figure 1.13: Display of MCG temporal data.



Figure 1.14: Display of BSPM temporal data leads 4-64. Leads which are flat (e.g. 15), are bad leads.

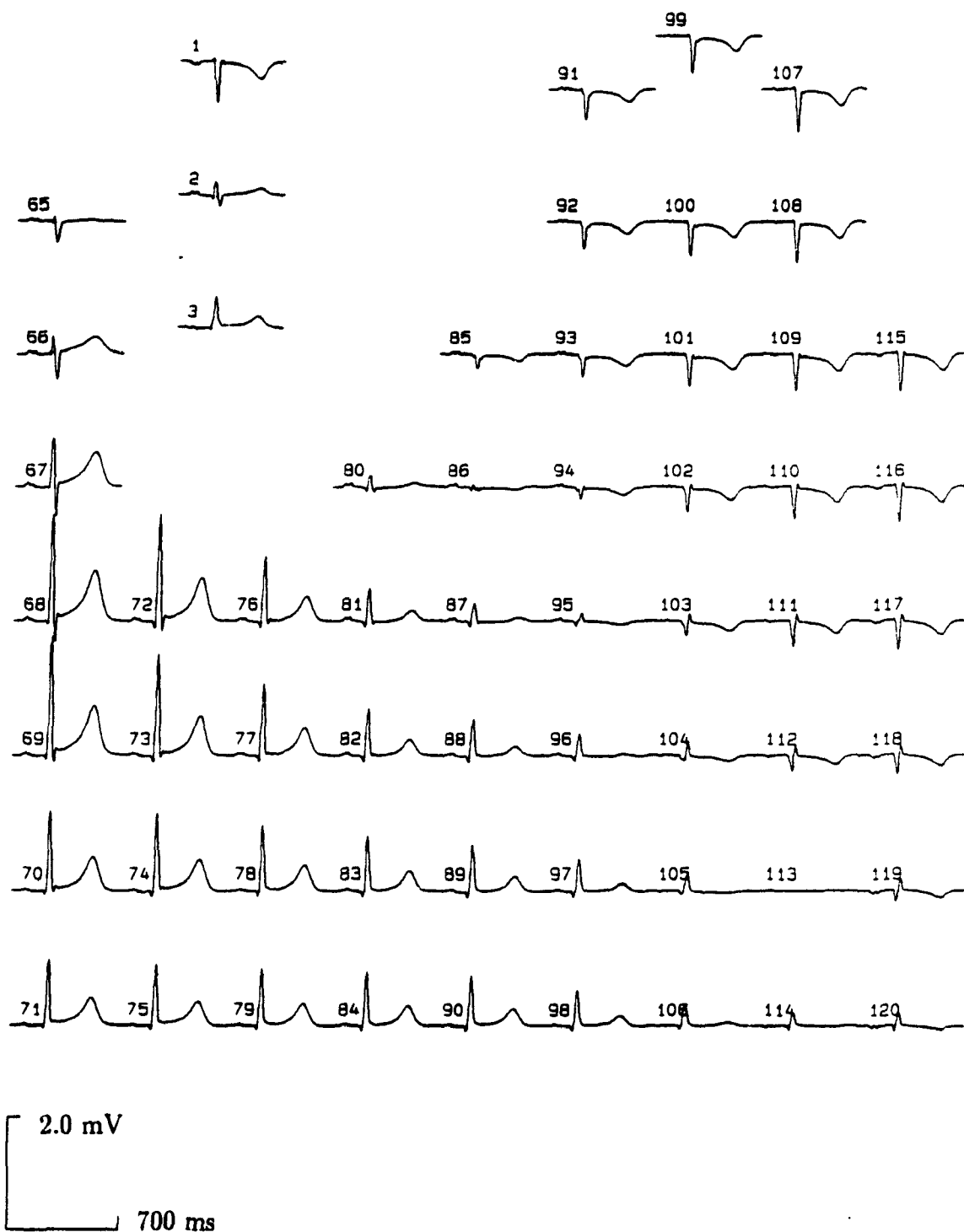


Figure 1.15: Display of BSPM temporal data leads 1-3 and 65-120.

numerically as

$$d(t)_{rms} = \left[\frac{1}{p} \sum_{i=1}^p d(i, t)^2 \right]^{1/2}. \quad (1.1)$$

An RMS value is calculated for each time point of interest. The variable 'd' can represent either MCG or BSPM data. MCG and BSPM RMS maps are shown in Figs. 1.16 and 1.17. The two traces correspond to the plotting of the data once with a fixed vertical scale (.05 pT/cm and .005 mV/cm) and then scaled to the maximum RMS value (dark trace). The RMS maps are quite valuable since they summarise a lot of data in a single plot. They can be used to get estimates of the relative timing of different events and comparisons between subjects can be made of the relative amplitudes of different events. The quality of the recording can be relayed by the height of the baseline offset and the amount of random and 60 Hz noise in the data. Numerous high-frequency peaks often suggest the presence of bad leads which have not been previously detected and marked in the IBADLEAD array.

The final commonly used display modality is spatial contour maps of iso-magnetic field or iso-potential values. Each map represents a single instant of cardiac activity. A magnetic field map (MFM) and body surface potential map (BSPM) of the R-wave maximum are shown in Figure 1.18. Both displays use spline interpolation and Laplacian smoothing. The magnetic field is interpolated from a 7×8 grid of 4 cm spacing to a 25×29 1 cm grid. The 117 BSPM leads are interpolated to cover a 37×65 grid. To achieve this, the 117 body surface potential values, measured on an irregular surface are projected onto a cylinder, then this cylinder is unwrapped onto a plane so that the edges of the plot correspond to the right mid-axillary line. The left half of the map, therefore, corresponds to the anterior torso, while the right half represents the posterior torso. The new locations of the measuring points, after projection onto a cylinder are indicated by the points (\cdot) on the plots. The interpolation and smoothing is then done on the projected potentials.

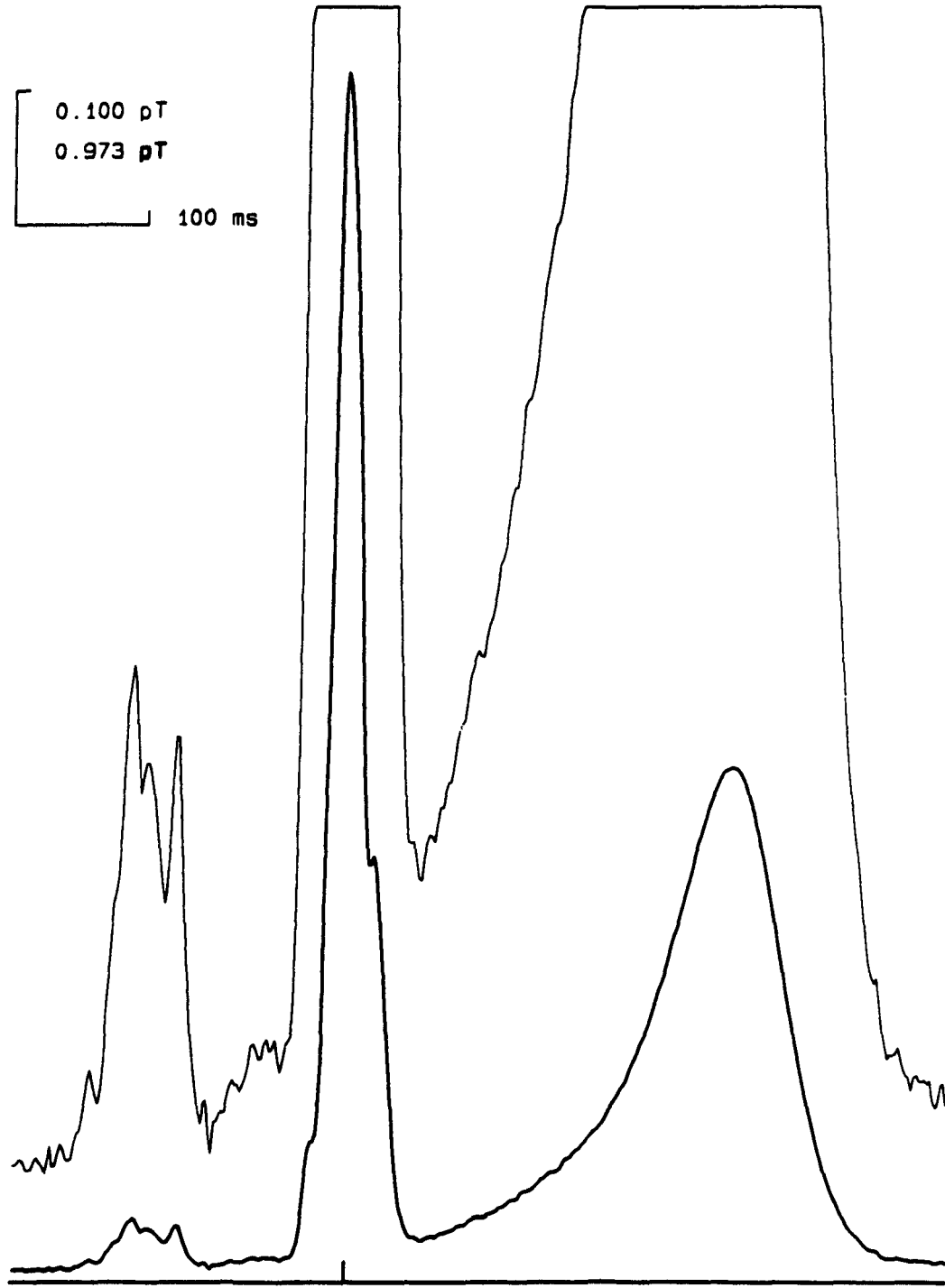


Figure 1.16: Example of an MCG RMS map.

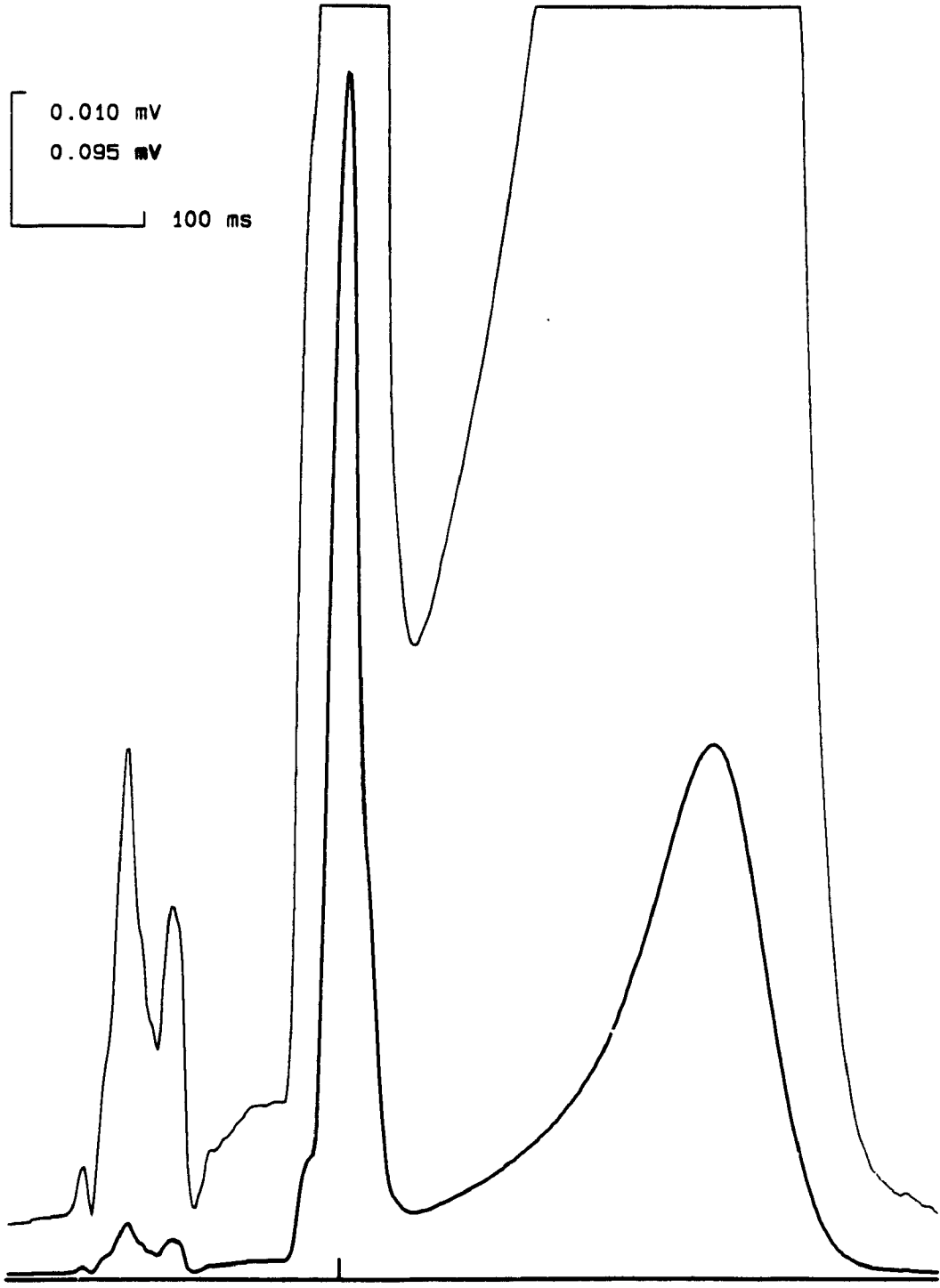


Figure 1.17: Example of a BSPM RMS map.

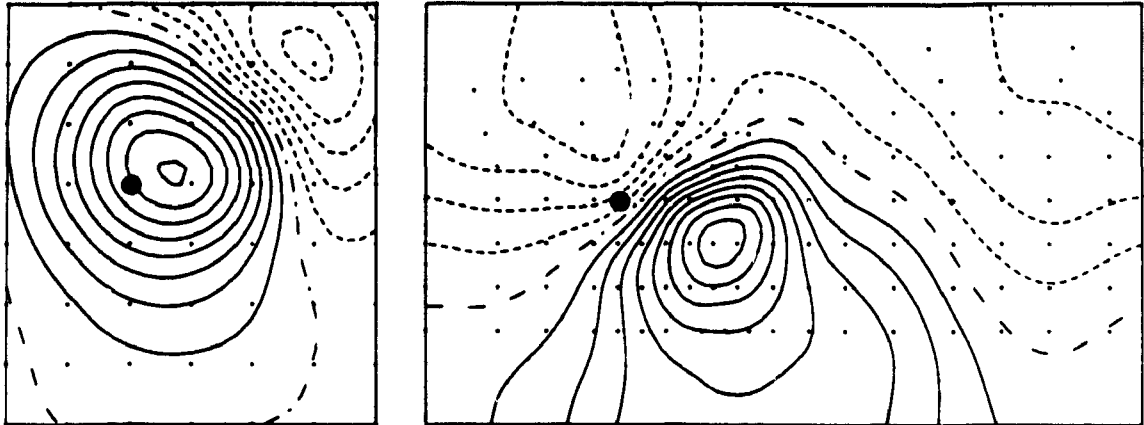


Figure 1.18: Display convention for magnetic field and body surface potential maps. The location of the measuring points are shown by points (\cdot) on the plots. The intersection of the 4th intercostal level and the sternum is indicated by a dot (\bullet) on both maps. The left/right side of the BSPM plots reflect potentials measured on the anterior/posterior torso. Unless otherwise noted the contour levels are selected automatically based on the values of the maximum and minimum fields and progress linearly. Positive field values are represented with solid lines, negative values with short dashes and zero-lines with long-dash-dot lines. Positive magnetic fields point into the body. If appropriate, the maximum and minimum field values, in pT or mV, are given below each map, along with a reference time in ms.

2 The Cardiac Sources and Volume-conductor Problem

The problem of determining the relationship between cardiac sources and body surface potentials or magnetic fields is referred to as the volume-conductor problem. Many models have been proposed to represent the cardiac sources and the volume-conductor of the human torso, but only particular choices of relevance to this work will be discussed.

2.1 The current dipole as a source model

To understand the electric and magnetic properties of the heart, a basic building block must be hypothesised. Mathematically, the current dipole can be defined as a source and a sink of current of equal strengths I , separated by a distance δl . As the separation between the source and the sink is allowed to approach zero and the current strength I approach infinity, the current-dipole moment \underline{P} tends to a finite limit:

$$\underline{P} = \lim_{\delta l \rightarrow 0, I \rightarrow \infty} I \delta l. \quad (2.1)$$

It is quite appropriate to consider the current dipole as a cardiac elemental source. Such dipoles would be distributed throughout the heart in a time-varying fashion during the cardiac cycle. The essence of the relationship between dipole sources and cellular activity was developed by Wilson et al. [33]. By considering a single cylindrical fiber, Wilson and co-workers showed that the dipole moment was related to the spatial gradient of the transmembrane action potential. This general concept was confirmed in tissue-bath experiments in one and two dimensions by Spach et al. [34,35,36]. It was later extended theoretically to three dimensions by Miller and Geselowitz [37,38], and forms an essential part of the Miller-Geselowitz ECG model.

2.2 Volume-conductor models

There is an increasing degree of complexity by which the volume-conductor model in the cardiac forward and inverse problems may be specified. Two models of particular interest in this work are discussed: the infinite homogeneous and bounded inhomogeneous volume-conductors.

2.2.1 Infinite homogeneous conductor

The volume-conductor is assumed in this case to be homogeneous and of infinite extent. The torso is assumed to be linear (obeys Ohm's law), stationary (current density is constant in time), quasi-static (no time dependence of charge density, electric, or magnetic fields, hence there are no capacitive or inductive effects), isotropic (conductivity is a scalar function of position), and non-magnetic (no ferromagnetic components and located in zero ambient magnetic field). The quasi-static assumption implies there is a duality between the problem of determining the potentials arising from current sources in such a model and the solution of electrostatic problems [39].

Along with the current-dipole source, the infinite medium conductor model has been of particular interest in the biomagnetism community. Many of the arguments favouring the power of the magnetic over the electric inverse solution, which suggest differences in information content of the two recording modalities, stem from and are most easily explained using the current-dipole model. In an infinite homogeneous volume-conductor, the potential ϕ due to a current dipole is [40]

$$\phi(\underline{r}) = \frac{1}{4\pi\sigma} \frac{\underline{P}(\underline{r}') \cdot (\underline{r} - \underline{r}')}{|\underline{r} - \underline{r}'|^3}, \quad (2.2)$$

and the magnetic field \underline{B} is given by [41]

$$\underline{B}(\underline{r}) = \frac{\mu_0}{4\pi} \frac{\underline{P}(\underline{r}') \times (\underline{r} - \underline{r}')}{|\underline{r} - \underline{r}'|^3}, \quad (2.3)$$

where \underline{r} is the field point and \underline{r}' is the source location, μ_0 is the permeability of free space, and σ is conductivity.

2.2.2 Bounded inhomogeneous volume-conductor

A more realistic and more complex volume-conductor model divides a piecewise homogeneous human torso into regions of uniform and isotropic conductivity. Surface-integral formulations for the electric potentials and magnetic fields can be found for this case [42,43,44,45]. The formulations are derived using Green's Theorem, the boundary conditions, and the fact that ϕ is a solution of Poisson's Equation.

The piecewise homogeneous volume-conductor consists of M different nonintersecting regions, each with uniform conductivity and bounded by the surface S_k . The conductivities inside and outside the surfaces S_k are σ'_k and σ''_k , respectively, and the unit normal \underline{n}_k to S_k points from the primed to double primed regions. If \underline{r} refers to a field point and \underline{r}' to a source point, then the electric potential ϕ_S for all $\underline{r} \in S_l, l = 1, \dots, M$ due to internal current sources is

$$(\sigma'_l + \sigma''_l)\phi_{S_l}(\underline{r}) = 2\sigma_S\phi_\infty(\underline{r}) - \frac{1}{2\pi} \sum_{k=1}^M (\sigma'_k - \sigma''_k) \int_{S_k} \phi_{S_k} dS_k \cdot \frac{(\underline{r} - \underline{r}')}{|\underline{r} - \underline{r}'|^3}. \quad (2.4)$$

σ_S is the conductivity at the source.

The magnetic field is given similarly as,

$$\underline{B}(\underline{r}) = \underline{B}_\infty(\underline{r}) - \frac{\mu_0}{4\pi} \sum_{k=1}^M (\sigma'_k - \sigma''_k) \int_{S_k} \phi_{S_k} dS_k \times \frac{(\underline{r} - \underline{r}')}{|\underline{r} - \underline{r}'|^3}. \quad (2.5)$$

The terms ϕ_∞ and \underline{B}_∞ are the potential and magnetic field due to a primary current source embedded in an infinite homogeneous medium. The surface integral represents the secondary current sources associated with boundary effects. If the primary source is a single current dipole then the infinite medium terms are given by Equations 2.2 and 2.3.

2.3 The forward and inverse problems

Forward and inverse problems are encountered in many areas of science, including electrocardiography and magnetocardiography. The forward problem is that of predicting the potentials or magnetic fields generated at the surface of a known volume-conductor due to a known source. This problem has a unique solution, as it is always

possible to calculate the fields to an accuracy which is limited only by the details of the particular source and volume-conductor model. Although this problem does not occur in clinical diagnostic situations, the exercise of postulating source-conductor models of varying degrees of complexity and developing numerical solutions to these is useful. Such studies can lead to fundamental understanding of the capabilities and limitations of the MCG and ECG measuring techniques, information content and data analysis.

In the more difficult inverse problem, the potentials or magnetic fields produced by dipoles embedded in a particular conducting medium are known, but the sources themselves are unknown. This is the problem which has clinical significance. From the measured surface field signals, the cardiologist will try to infer the most probable source distribution which would generate the field and decide on the clinical status of the subject's heart. The inverse problem does not have a unique solution [46,47]. The primary cardiac sources cannot be uniquely determined as long as the active region is inaccessible, since the electric and magnetic fields they generate outside any closed surface enclosing them may be duplicated by equivalent single or double layer sources on the closed surface itself. However, the solution becomes unique once a source model is chosen, which in effect applies electrophysiological constraints to that source.

Two types of inverse solutions are used in this study. The first involves the empirical approach based on the recognition of typical signals which are known to be associated with particular source configurations. This is the technique generally available in the clinical setting. An alternative method requires that one models the volume-conductor and represent the source by a simplified model such as a single dipole. This type of solution can require the use of computer models and is solved for more or less complicated conductor models. The computer implementation of the forward and inverse solutions for the two volume-conductor models presented earlier will be described in the following.

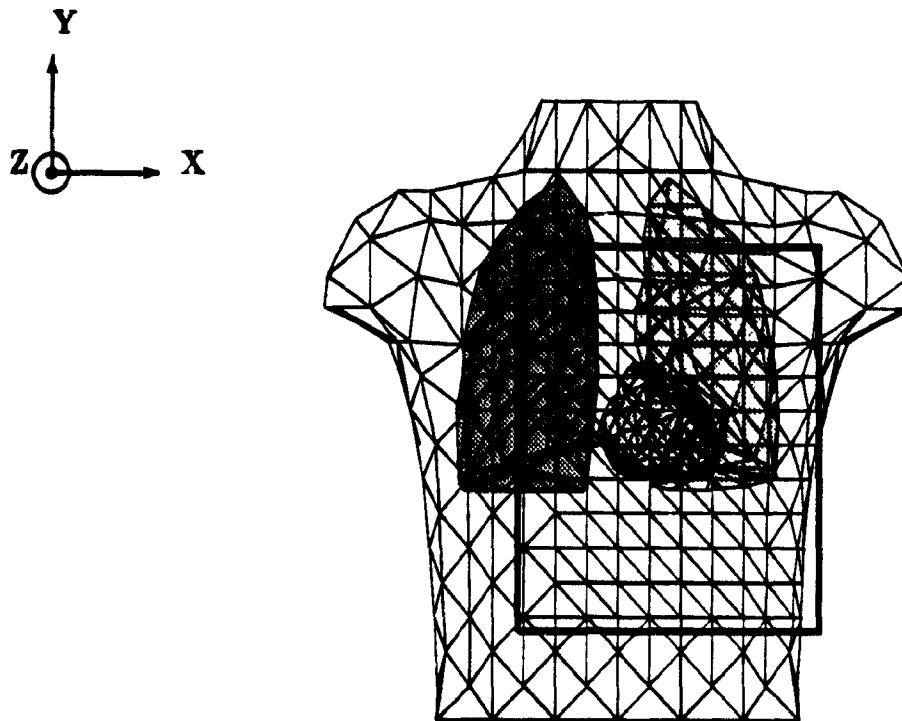


Figure 2.1: Anterior view of the human torso model with lungs and intracavitary blood masses.

The rectangular box represents the area covered by the MCG measuring grid. The right-handed coordinate system is also plotted. (See Appendix E for details of torso and epicardial relative coordinate systems).

2.3.1 The forward problem

The solutions for the electric potentials and magnetic field of a current dipole in an infinite, homogeneous volume conductor are given by Equations 2.2 and 2.3. These equations can be implemented in computer programs to solve for the fields of different sources of interest.

Equations 2.4 and 2.5 can be solved numerically by use of the boundary element method (BEM). One version of the Horáček volume conductor [48] to be used in this study is shown in Figure 2.1. The 5 boundaries of the representative male torso have been tessellated into a total of 1368 triangular area elements (700 on the outer boundary, 326 for 2 lungs, and 342 for 2 cardiac blood masses).

With the surfaces of the volume conductor described, one can then write discrete versions of Equations 2.4 and 2.5 and solve for the electric potentials and magnetic fields due to a known source. The discretised version of Equation 2.4 can be written as [49]

$$\Phi = \Phi_{\infty} + \omega\Phi \quad (2.6)$$

where Φ is an N -dimensional vector of the potentials on all the n_k area triangles, describing S_k , and Φ_{∞} is also an N -dimensional vector, containing the mean infinite medium potentials at the same elements. ω is an $N \times N$ matrix specifying the conductivity interfaces using the solid angles subtended by every surface area element at every other element. This equation can be solved iteratively, using Gauss-Siedel or Jacobi iteration, after ‘deflating’ the matrix (to obtain Ω) [50]. The deflation procedure is required because Equation 2.6 has a non-unique solution due to the fact that the potentials are arbitrary up to a constant [51].

Equivalently, Equation 2.5 is written

$$B = B_{\infty} + A\Phi. \quad (2.7)$$

If the magnetic field is measured at p locations, then B is a $p \times 1$ vector consisting of the magnetic field values at the p observation sites. B_{∞} is a p -dimensional vector of the corresponding infinite medium magnetic field values, Φ is the potential found by the solution of Equation 2.6 and A accounts for the boundary contribution in Equation 2.5 [45]. Hence, once the iterative solution for the potentials is found, the magnetic field can be calculated.

2.3.2 The inverse problem

The simplest inverse solution for the biomagnetic fields is found for the current dipole in an infinite medium homogeneous volume-conductor model. It is straightforward to show that for a dipole parallel to the measuring plane (e.g. P_x or P_y), the depth of the dipole can be specified in terms of the separation between the maximum and

minimum values of the field in the measuring plane. If δ is the separation of the extrema, then the depth d (m) of the dipole is

$$d = \delta/\sqrt{2}. \quad (2.8)$$

Because P_z is silent, this also applies to dipoles that make an angle with the measuring plane. The magnitude of the dipole moment, $|\underline{P}|$ (A·m) is

$$|\underline{P}| = \frac{2.6 \times 4\pi}{\mu_0} d^2 B_{max} \quad (2.9)$$

where B_{max} (T) is the maximum value of the magnetic field [52].

The potentials, measured in the same plane for the same tangential dipole, have an analogous inverse solution. The depth d is given by the same expression stated in Equation 2.8 and if ϕ_{max} (V) is the maximum potential measured then, similarly, the moment is

$$|\underline{P}| = 2.6 \times 4\pi\sigma d^2 \phi_{max} \quad (2.10)$$

Equations 2.8 and 2.10 become more complicated for dipoles not parallel to the measuring plane. In addition, these simple expressions for the potentials have little use in body surface potential mapping, since the potentials are not measured in a plane but follow the contours of the torso.

The inverse solution for the inhomogeneous volume conductor was, for a long time, limited by the computational requirements in solving Equations 2.6 and 2.7 in the inverse manner. Such a solution would involve repeated iterated solutions to the forward potential problem (Equation 2.6) as different possible dipole-source locations were tested. Each such iteration involved more than N^2 floating-point multiplications. This problem was circumvented when two groups [53,54,55,56], almost simultaneously, recognised that although the expression $\Phi = (I - \omega)^{-1}\Phi_\infty$, derived from Equation 2.6, could not be solved since $(I - \omega)$ has no inverse, the equivalent deflated solid angle matrix $(I - \Omega)$ could be inverted, and Φ could be solved to within a constant. In these expressions, I is the identity matrix.

The computation of the deflated inverse matrix (done by LU decomposition) would be required only once for each torso geometry. The matrix can be used for either the forward or inverse computations and, only in the case where multiple boundaries are being considered, will the potentials have to be recovered by offsetting the effects of ‘deflation’ [50]. The potentials can then be integrated numerically for use in Equation 2.7 to generate the magnetic field.

2.3.3 Implementation of the inverse solution

In the solution of the inverse problem, given either a body surface potential or magnetic field map, initial estimates for the dipole moment and location are used to calculate the forward problem. Using a Levenberg-Marquardt non-linear least-squares fitting algorithm [57], the field or potential based on this estimate is compared to the input map and a new estimate for the dipole parameters are selected until a fit to the map is obtained.

An infinite medium estimate for the dipole source can also be obtained using the same least-squares fitting algorithm. In this case, the magnetic fields measured by each gradiometer coil will be solved according to Equations 2.8 and 2.9. This direct solution is possible, since the measurements of B_z are made in a plane above the torso where B_z due to the Z -component of the moment is zero. When solving for the potentials, however, the measurement positions are defined by the torso geometry and an iterated solution to Equation 2.2 for all components of the moment is obtained.

2.3.4 Special cases of source and volume conductor

Consideration of sources such as the current dipole in simplified volume conductors has led to speculation that the magnetic and electric fields of these would reveal different information and possibly independent components [19]. Specifically, for a dipole perpendicular to the measuring plane ($\underline{P} = P_z \hat{z}$), in an infinite homogeneous volume-conductor, B_z is zero. Conversely, it is this perpendicular source which can produce the largest potential differences. These concepts are illustrated in Figure 2.2,

where the z -oriented dipoles reveal zero B_z and largest V . Since the predominant direction of the spread of excitation in the normal heart is from the endocardium to the epicardium, it was postulated that if these predictions derived from the simplified model were valid, the magnetic field measurements might be more sensitive to alterations in this normal excitation pattern, as tangential currents¹ might be affected disproportionately [58].

This suggestion was pursued from the mathematical point of view by many researchers. A forward solution of the uniform double-layer source model, as analysed by Rush [59], did not permit the existence of electrically silent sources – that is sources which generate a magnetic field but no electric potential. This removed speculation of the existence of independent information content in MCG recordings. Later, however, it was pointed out that newer data suggested that a uniform double-layer model was too simple. Corbin and Scher [60] found that the orientation of the impressed current density in a small segment of the depolarisation wavefront is not always the same as the direction of propagation of the wavefront, suggesting anisotropic conduction. Wikswo and Barach [61] then showed that if the impressed current density at any point in the wavefront is not always perpendicular to the wavefront, then configurations of cells may exist in the heart that affect the MCG more than the ECG. Such a possibility is demonstrated in Figure 2.3. Since $\nabla \times \underline{J}_i \neq 0$, $B_{anisotropy} \neq 0$ in Fig. 2.3b and the magnetic fields in these two examples are different. However, $\nabla \cdot \underline{J}_i$ due to anisotropy is zero in Fig. 2.3b, hence the 2 source distributions produce the same electric fields. Fig. 2.3 also demonstrates two current source distributions which produce the same electric fields. The inverse solutions for the potentials, arising from these current distributions, would be non-unique.

¹Tangential currents, here, refer to currents which are directed parallel to the plane of the MCG grid.



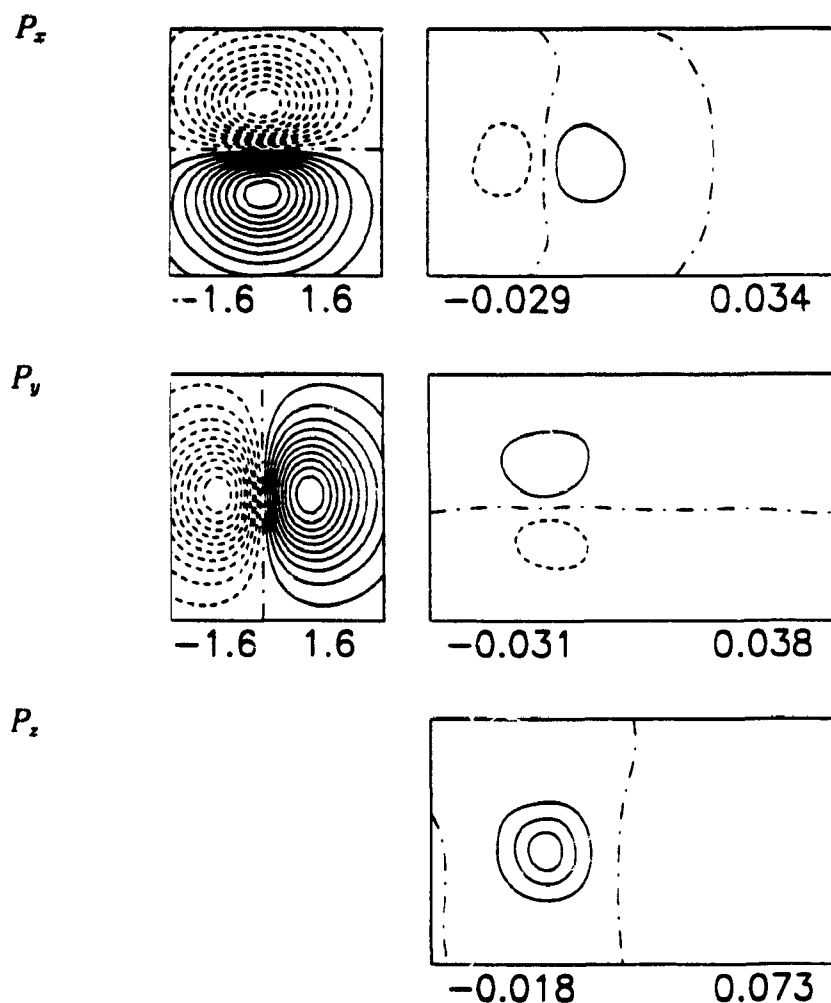


Figure 2.2: MF and BSP maps for a source in an infinite homogeneous volume-conductor.

Magnetic field (left) and body surface potential (right) maps for current dipoles of 1 A·m pointing in the 3 orthogonal directions (x, y, z) in an infinite homogeneous volume-conductor. The dipole is located at the model's ventricular onset location. A small number of contours were used in the BSPM to emphasize the difference in amplitudes of the infinite medium solution and the torso volume-conductor forward-solution maps shown in later figures.

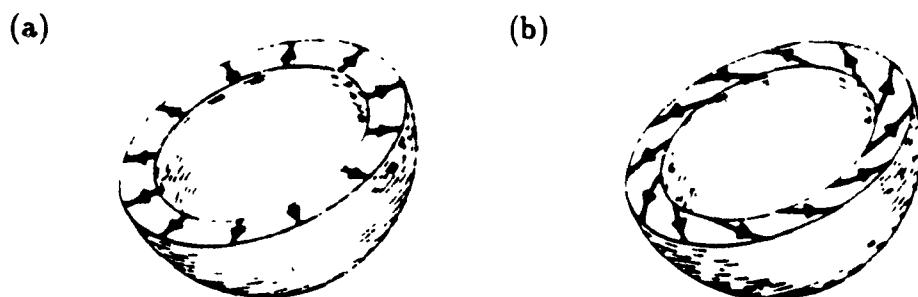


Figure 2.3: Demonstration of a situation which may give rise to electrically silent sources.

In (a) the divergence and curl of \underline{J} are both non-zero giving rise to electric and magnetic fields. In (b) $\nabla \cdot \underline{J}$ due to anisotropy is zero, hence no electric potential would be detected due to anisotropy.

2.3.5 Effects of boundaries

The proponents of infinite-medium models further suggested that volume-conductor boundaries and inhomogeneities would have little or no effect on the magnetic field component normal to the surface of the volume-conductors [62,63]. The advent of realistic torso models [64] gradually eroded this belief. These realistic models (e.g. [65,66]) have shown, via computational studies, that, on average, no clear advantage can be ascribed to either of the electric potential or normal component of magnetic field with respect to sensitivity to the boundaries and inhomogeneities. These boundary effects are illustrated in Figures 2.2, 2.4, and 2.5, where the z -component of magnetic field and the electric potentials due to a current dipole embedded in 3 different volume-conductors is calculated. The three volume-conductors are: infinite homogeneous (Fig. 2.2), a homogeneous torso (Fig. 2.4) and an inhomogeneous torso with lungs and cardiac blood masses (Fig. 2.5). The magnetic fields and potentials both show increasing amount of deviation from the simplicity and dipolarity of the infinite homogeneous model.

To illustrate the relative sensitivities of magnetic field and potential measurements to sources which are either perpendicular or tangential to the MCG measuring plane in the inhomogeneous torso model, forward solutions for 7 different dipole-source

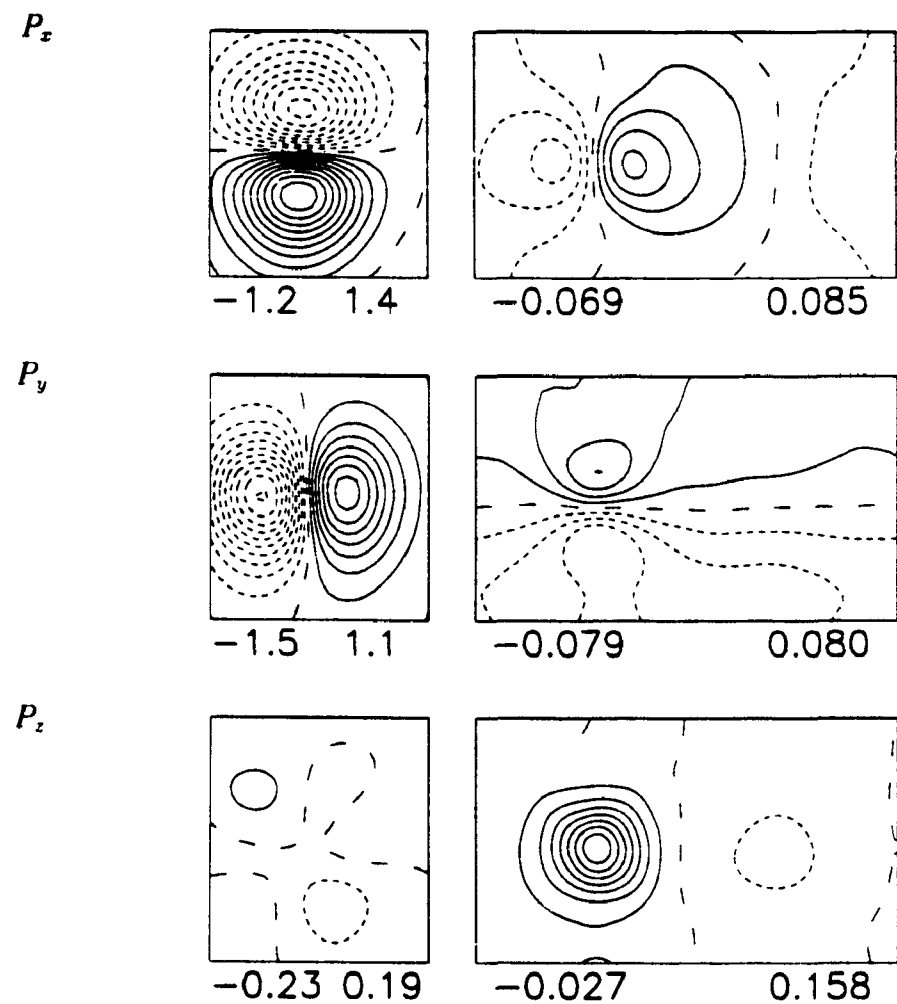


Figure 2.4: MF and BSP maps for a source in a homogeneous volume conductor. Magnetic field (left) and body surface potential (right) maps for current dipoles of 1 A·m pointing in the 3 orthogonal directions (x, y, z) in a homogeneous volume-conductor (torso boundary). The dipole is located at the model's ventricular onset location.

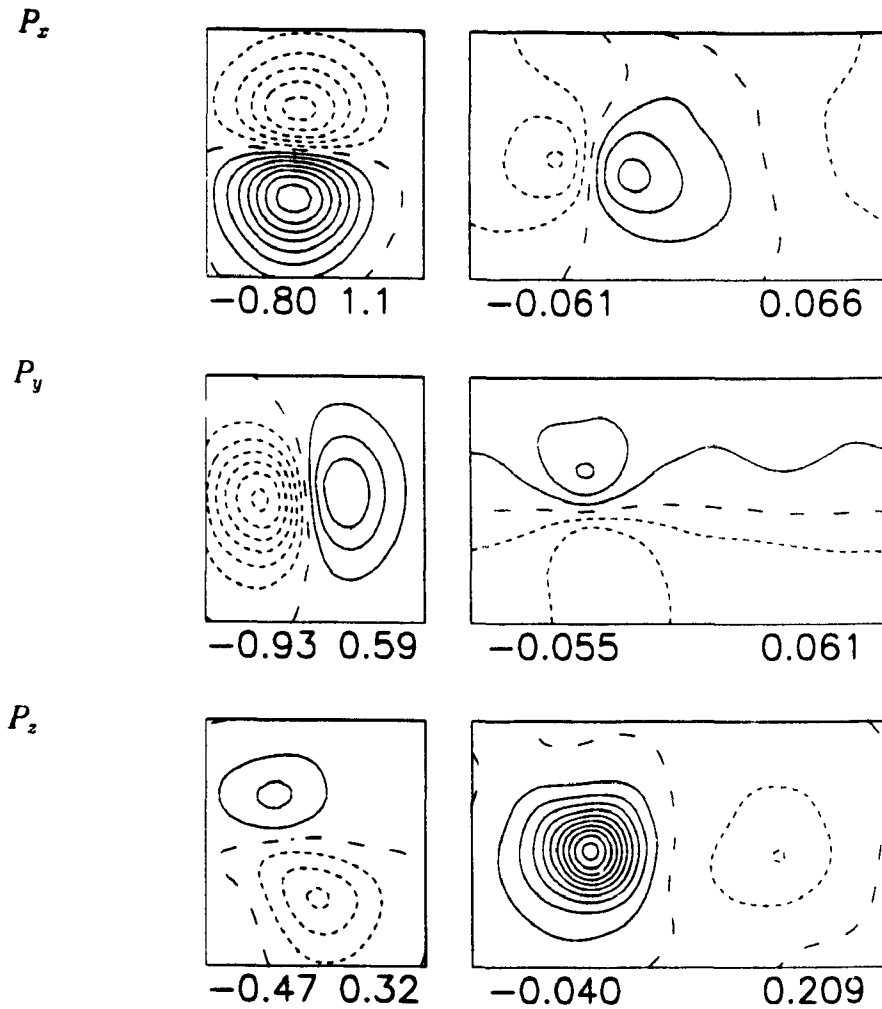


Figure 2.5: MF and BSP maps for a source in an inhomogeneous volume conductor. Magnetic field (left) and body surface potential (right) maps for current dipoles of 1 A·m pointing in the 3 orthogonal directions (x, y, z) in an inhomogeneous volume-conductor (torso with lungs and cardiac blood masses). The dipole is located at the model's ventricular onset location.

Site	MCG (pT)			BSPM (mV)		
	P_x	P_y	P_z	P_x	P_y	P_z
SA	0.97	1.90	0.47	.066	.129	.104
RA	1.20	1.30	0.39	.053	.072	.066
HS	0.78	0.82	0.45	.049	.063	.125
QN	0.95	0.76	0.40	.064	.058	.124
RV	6.10	5.65	0.56	.216	.240	.318
LV	0.26	0.24	0.28	.048	.051	.074
AP	2.70	2.55	0.90	.171	.134	.179
Ave.	1.85	1.89	0.49	.095	.107	.141
SD	2.02	1.83	0.20	.069	.068	.086

Table 2.1: Average of the extrema $(\max + |\min|)/2$ for seven test sites in the heart. Test dipoles of unit strength in the X , Y , and Z orientations were used. The average (Ave.) and standard deviation (SD) over all sites are also given. Sites adjacent to the blood masses are: Sino-atrial node (SA), right atrium (RA), His bundle (HS), Q-onset (QN), right ventricle (RV), left ventricle (LV) and apex (AP).

locations in the heart region were obtained (see reference [20] for the coordinates of the locations). The sensitivity to the sources were determined by comparing the average value of the extrema $((\max + |\min|)/2)$ for the tangential dipoles (P_x, P_y), and the perpendicular dipole (P_z). This result is presented in Table 2.1. It is found that on average the magnetic field due to a dipole perpendicular to the magnetic measuring plane is 1/4 that of the tangential sources. The potentials for the perpendicular source, however, are approximately 50% greater than the tangential dipoles. These results concur with those of Purcell et al. [66]. They also suggest that the P_z dipole could mask the P_x and P_y components in body surface potential maps. However, the relative insensitivity of the measurement of B_z to P_z dipole sources may make it ideal for detecting primarily tangential sources, such as is the situation in the normal excitation of the human atria.

2.3.6 Validity of the current-dipole source model

Introduction

In general, excitation wavefronts are not very localised, and only an approximation of the location and strength of these distributed sources can be obtained with a single current-dipole source model. However, pre-excitation via accessory AV pathways (AP) leads to an interesting and almost unique cardiac source. The initial pre-excitation, originating from a small volume of myocardium at the base of the ventricle (<1.5 mm diameter in most cases [67]), is one of the few sources which might be truly localised. The localised nature of this source suggests that it would be reliably represented by the current-dipole source model (Eq. 2.1). Localisation of the δ wave associated with pre-excitation via an AP is a clinical application of the inverse method, which also validates the source-conductor models hypothesised in these solutions. In this section, we present a theoretical validation of the current-dipole source model.

Method

A computer model of propagated excitation in a three-dimensional anisotropic human ventricular myocardium, embedded in a homogeneous volume-conductor model of the human torso, was used to simulate pre-excitation wavefronts [68,69,70]. Magnetic field and body surface potential maps of pre-excitation were generated with this model, using lead locations and a magnetic field grid consistent with the Dalhousie measurement systems.

From these maps, inverse solutions were obtained using infinite medium and homogeneous torso volume-conductor models (Fig. 2.1), while approximating the distributed source with a single current-dipole model. The initial location of excitation (a simulated ventricular insertion site) was the true dipole-source location (DSL), and the inverse solutions were compared to this site to determine the accuracy of the current-dipole approximation to the anisotropic myocardium and distributed source.

BSPM and MFM for 7 different AP locations² at 20 ms after onset of pre-excitation were tested. As well, at one site (LPP), inverse solutions were obtained for maps every 2 ms, from onset to 20 ms (10 maps).

Results

The average dipole recovery errors for the 7 different pre-excitation sites is presented in Table 2.2. In both the MFM and BSPM solutions, the infinite-medium conductor model gave a larger average error (2.55 cm and 1.72 cm, respectively), than with the use of the exact torso volume conductor, (1.04 cm and 1.42 cm, respectively). However, the improvement in the BSPM result, relative to the infinite medium solution, is much smaller at 0.3 cm than the gain made in the MFM solutions (1.5 cm).

Infinite medium inverse localisation errors				
	ΔX (cm)	ΔY (cm)	ΔZ (cm)	$ \Delta \underline{R} $ (cm)
Potential	0.85 (0.56)	0.87 (0.58)	0.96 (0.49)	1.72 (0.49)
Magnetic	1.96 (1.00)	0.70 (0.87)	1.00 (0.74)	2.55 (0.98)

Homogeneous torso inverse localisation errors				
	ΔX (cm)	ΔY (cm)	ΔZ (cm)	$ \Delta \underline{R} $ (cm)
Potential	0.52 (0.54)	0.83 (0.49)	0.76 (0.50)	1.42 (0.45)
Magnetic	0.41 (0.27)	0.32 (0.33)	0.75 (0.50)	1.04 (0.37)

Table 2.2: Inverse solution localisation errors averaged over 7 sites.

For site LPP, solutions were obtained every 2 ms from onset to 20 ms. This result is shown in Table 2.3. The deviations relative to the known dipole-source location are relative to a coordinate system in the heart (see Appendix E), where the X -axis is directed from the right heart to the left, the Y -axis posteriorly, and the Z -axis points inferiorly (base to the apex of the heart). A comparison of the BSPM and MFM solutions reveals a difference that is consistent in 6 of 7 sites (at 20 ms): the BSPM

²These locations are LPP, LPL, LAL, LAP, RAP, RAL, and RPP. These sites on the A-V ring are defined and indicated in Figure 6.1

recovered DSLs are superior (e.g. ΔZ negative) to the point of initial excitation, while the MFM solutions are below this point. Additionally, the MFM DSLs move consistently away from the initial excitation location, as reflected by an increasing ΔZ with time, while the BSPM recovered DSLs appear almost stationary.

Discussion

In patients with WPW syndrome, propagated excitation starts from the ventricular insertion site at the level of the A-V ring and the excitation wavefront spreads in the anisotropic myocardium from base to apex. Our results suggest that up to 1.4 cm error can arise with the use of the single current-dipole source model, in attempting to locate the pre-excitation source in the anisotropic heart. In our simulations, only the source models differed between the forward solutions (distributed source in anisotropic myocardium) and inverse solutions (single current dipole). The homogeneous torso, measurement sensors, lead and grid definitions were all accurately represented³. Hence, all differences found should be associated with the source model chosen.

On average, comparison of BSPM and MFM inverse solutions in the homogeneous torso reveals differences of about 2 cm between the two different approaches. This difference may reflect relative inaccuracies in modelling the source. One possible explanation is that the magnetic field and potential data reflect different spatial components of the wavefront. For example, the MFM data may account for the portions of the wavefront which are closest to the anterior chest. However, this is not likely the full explanation, since the BSPM solutions are located above the A-V ring, in the atria, and not in the ventricles. The failure for the recovered DSL to move closer toward the apex in the latter case, also suggests that additional factors have to be considered, in the source-conductor modelling.

³The forward calculations used a node-to-node BEM [23] and the inverse solutions a triangle-to-triangle method in the boundary element solutions. This difference was tested, and not found to change the results.

Potential inverse solution errors				
Time (ms)	ΔX (cm)	ΔY (cm)	ΔZ (cm)	$ \Delta \underline{R} $ (cm)
2	-0.24	0.58	-1.16	1.32
4	-0.34	0.53	-1.10	1.27
6	-0.39	0.48	-1.08	1.25
8	-0.43	0.39	-1.09	1.23
10	-0.52	0.30	-1.17	1.32
12	-0.51	0.19	-1.20	1.32
14	-0.43	0.11	-1.19	1.27
16	-0.32	0.05	-1.16	1.21
18	-0.20	0.06	-1.16	1.18
20	-0.13	0.11	-1.19	1.21
Average	-0.35	0.28	-1.15	1.26
SD	0.13	0.20	0.04	0.05

Magnetic inverse solution errors				
Time (ms)	ΔX (cm)	ΔY (cm)	ΔZ (cm)	$ \Delta \underline{R} $ (cm)
2	-0.15	-0.25	0.64	0.70
4	-0.30	-0.25	0.67	0.77
6	-0.35	-0.27	0.68	0.81
8	-0.40	-0.35	0.69	0.87
10	-0.36	-0.36	0.74	0.90
12	-0.32	-0.30	0.80	0.92
14	-0.31	-0.22	0.86	0.94
16	-0.29	-0.15	0.92	0.97
18	-0.23	-0.08	0.92	0.95
20	-0.16	-0.01	0.94	0.96
Average	-0.29	-0.22	0.79	0.88
SD	0.08	0.11	0.12	0.09

Table 2.3: Localisation errors of the inverse solution for site G6 (LPP) as a function of excitation time.

2.3.7 Validity of a standard volume-conductor model

Introduction

Previous publications dealing with MFM and BSPM inverse solutions of the δ wave in WPW syndrome (e.g. [71,72]) suggest that the use of a single standard torso model will have limited accuracy when used for widely varying subject geometry. Weismüller et al. [73] have reported successful MFM localisation of AP in 7 patients to within 2.1 cm using a semi-infinite volume-conductor model, while Tsunakawa et al. [74], with body surface potential maps, accurately located the AP in 22 of 30 patients using a standard torso model. They did not have confirmation by EPS or ablation, but relied on a pattern-matching classification of the iso-potential maps to Benson's scheme [75].

None of these studies have suggested which inverse solution – the one based on MFM or the one based on BSPM – may be more sensitive to the geometrical accuracy of the torso model. This question will be addressed explicitly in a later chapter dealing with data of patients suffering from WPW syndrome. In such a comparison, the standard model geometry will be the same for both the MFM and BSPM data, hence inaccuracies in representing individual patients' torso geometry should contribute equivalently to both inverse solutions. A factor which affects only the MFM solutions is the grid height above the chest. This height will be fixed in the inverse solutions using the standard torso. In this section we will explore the error associated with fixing the grid height, as it contributes a separate error to the MFM solutions, that will not be seen in BSPM data.

Method

The 7 WPW model maps of Nenonen et al. [70], discussed previously, were used in this simulation. Homogeneous torso inverse solutions were obtained for grid heights of -10 mm, -5 mm, 10 mm, 15 mm and 20 mm below and above the known height. Relative differences in these solutions were calculated and averaged, for each grid

height.

Results and discussion

Table 2.4 shows the average and standard deviations of the error in recovered DSL, relative to the result for the known grid height. Not surprisingly, the error is almost entirely reflected in an equivalent displacement of the Z component of the dipole-source locations in the direction and of the same magnitude as the discrepancy in grid-height. The grid height error does not change the X and Y components of the recovered DSL as much, although one location (LPL) did have a larger error in the X component than in the Z component. We will return to these results in the analysis of the data from WPW syndrome patients.

δZ (mm)	$ \Delta X $	$ \Delta Y $	$ \Delta Z $	$ \Delta R $
-10.0	2.25 (3.75)	1.24 (1.52)	8.30 (4.38)	9.54 (4.18)
-5.0	1.37 (2.75)	0.82 (1.40)	5.15 (1.88)	5.80 (2.79)
5.0	2.65 (6.19)	0.53 (0.65)	5.40 (1.86)	6.96 (5.33)
10.0	3.26 (7.00)	0.79 (0.63)	10.03 (2.82)	11.76 (5.15)
20.0	4.74 (8.28)	1.37 (0.99)	19.86 (4.97)	21.86 (5.00)

Table 2.4: Change in recovered MFM DSL as a function of grid height. Solutions are compared relative to the actual grid height (12.95 cm). Average and standard deviation, in mm, were calculated for the 7 magnetic field pre-excitation maps.

3 Signal Extraction Techniques

3.1 Introduction

As an approximation to the cardiac generators, the single current dipole source model has only limited use for most cardiac signals because these are usually the result of a distribution of sources in a relatively large diffuse region of the myocardium. A few exceptions do exist. Two sources in particular are believed to be fairly represented by a single current-dipole source model. These are the early depolarisation of the His-Purkinje conduction system and the initial excitation of the ventricles via the accessory pathways associated with Wolff-Parkinson-White (WPW) Syndrome. Both of these events have onsets during the PR interval, particularly during the period of atrial repolarisation (PR segment). Therefore, in order to localise these sources it is necessary to first remove the atrial contribution to the recorded signals.

A number of techniques have been used for the purpose of separating the spatial HPS signal from atrial repolarisation. The first of these was suggested by Horan et al. [76] in 1982. They used a correlation technique to extract the surface-recorded His bundle ECG from the background atrial signal. The concept of removing the atrial signal to enhance the HPS signals was later extended to magnetocardiographic recordings. Fenici et al. [77] and ten Voorde et al. [78] used an average map technique to characterise the atrial signal and the Dalhousie Biomagnetism group [3,79,80] explored a Karhunen-Loève orthogonal expansion technique to remove the atrial contribution to the PR segment. All these techniques revealed distributions generally described as being consistent with a single equivalent dipole representing the HPS source. The enhancement of the onset of the δ wave associated with accessory pathways in WPW syndrome has not received as much attention, but the approach taken in this case parallels the HPS problem, with both average map techniques and or-

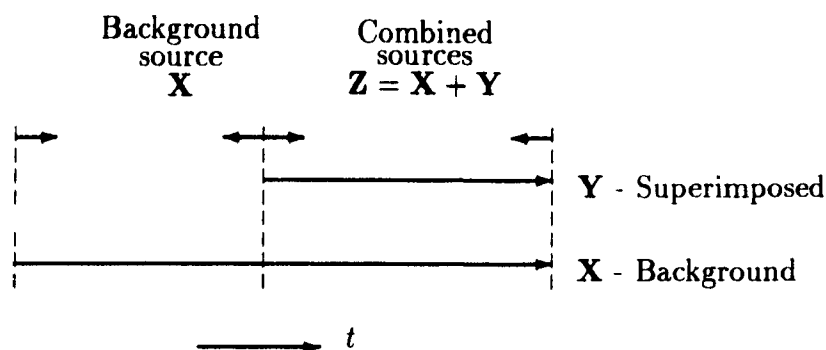


Figure 3.1: The time relationship between the background and superimposed sources. The background source is active for some period of time before the superimposed source begins.

thogonal expansion techniques having been suggested [81].

In this chapter the theory associated with these techniques will be developed. The results of simulation studies aimed at assessing the limitations of the techniques to source separation will then be presented.

To begin, definitions which apply to the theories that follow are necessary. A first definition indicates how magnetic field or body surface potential mapping data is represented symbolically in vector and matrix form. Data collected at p recording sites (electrode location or magnetic field grid point) for t successive times is represented by the real $p \times t$ matrix, $\mathbf{X}_{p \times t} = \{\mathbf{x}_1 \mathbf{x}_2 \cdots \mathbf{x}_t\}$, where $\mathbf{x}_i^* = \{x_{i1} x_{i2} \cdots x_{ip}\}$. The p entries of a given column (time) of \mathbf{X} (the vector \mathbf{x}_i) form a map.

The focus of the theory is on the separation of concurrent events in electrophysiological mapping data. In this context, the matrix \mathbf{X} will be associated with the background source of interest (such as atrial repolarisation) and the matrix \mathbf{Y} will represent a superimposed source of interest (HPS or δ wave), while $\mathbf{Z} = \mathbf{X} + \mathbf{Y}$ is a combination matrix (see Figure 3.1).

3.2 Temporal averaging technique

The temporal averaging technique (TAT) is the simplest of the techniques investigated. It relies on the assumption that the background source pattern and its ampli-

tude do not change during the time interval of interest. Having selected t consecutive maps to represent the background source, we compute the average (over time) of this sequence to obtain a single average background source vector. Symbolically,

$$\bar{\mathbf{x}} = \frac{1}{t} \sum_{i=1}^t \mathbf{x}_i \quad (3.1)$$

is the average map. The difference, $\mathbf{r}_i^{\text{TAT}}$, between this average map and a combination map becomes,

$$\mathbf{r}_i^{\text{TAT}} = \mathbf{z}_i - \bar{\mathbf{x}} \quad (3.2)$$

and a matrix of such differences is then,

$$\mathbf{R}^{\text{TAT}} = \mathbf{Z} - \bar{\mathbf{X}} \quad (3.3)$$

with the columns of $\bar{\mathbf{X}}$ all identical and equal to $\bar{\mathbf{x}}$. If assumptions are valid, then the residual matrix \mathbf{R}^{TAT} should reveal the superimposed source \mathbf{Y} .

3.3 Correlation technique

The correlation technique (CT) used by Horan et al. [76] removes the assumption that the background source amplitude is constant. After obtaining an average of the background source as in Equation 3.1, a correlation is made of this average with the combination map \mathbf{Z} to obtain a scaling factor which accounts for changes in the amplitude of the background source. This correlated fraction, defined by,

$$g_i = \frac{\bar{\mathbf{x}} \cdot \mathbf{z}_i}{\bar{\mathbf{x}} \cdot \bar{\mathbf{x}}} \quad (3.4)$$

is then subtracted from the combination map to give the residual vector (or ‘variance’ as suggested by Horan [76]) \mathbf{r}_i^{CT} ,

$$\mathbf{r}_i^{\text{CT}} = \mathbf{z}_i - g_i \bar{\mathbf{x}}, \quad (3.5)$$

or an equivalent residual matrix, \mathbf{R}^{CT} .

3.4 Orthogonal Expansions

Two types of orthogonal expansions are considered. The first is called a Karhunen-Loève Transform (KLT) while the second is Singular Value Decomposition (SVD). Orthogonal transforms of nonperiodic random processes were first introduced in electrocardiography as a means of reducing storage requirements of the ECG recordings [82,83]. The basic concept here is that typical ECGs can be represented by a superposition of fundamental features. The expansion of a number of ECGs into an orthogonal basis set allows the data to be compressed into a minimum number of independent features. The gain in storage requirement occurs because the basis functions would apply not only to the training ECG set, but also to a similar test subject group. To reconstruct the original data, one only need have stored the orthogonal feature vectors and expansion coefficients which dictate the fraction of each basis function to be used. Additional gains are achieved when the number of basis functions is limited to a minimum set. This set would comprise only those which contribute signals above the noise level, or deliver the desired representation accuracy.

In one application of orthogonal expansions to multiple, concurrent sources, the input matrix \mathbf{X} is assumed to be a result of several concurrent events (e.g. MEG recordings of multiple epileptic foci [84,85]). Douglas and Rogers [86] have suggested that the number of significant feature vectors resulting from the orthogonal expansion of \mathbf{X} corresponds to the number of original components forming the signal. We confirmed this to be true, but the actual eigenvectors resulting from this type of analysis do not correspond to independent physiological generators [87].

In an application introduced by the Biomagnetism group at Dalhousie [79], and which is of interest in this study, one uses the orthogonal expansion to first characterise a background source. This representation is then used to determine the fraction of this source which is contained in a combination map and then remove that feature to reveal the superimposed source. A description of both expansion techniques will be given next.

3.4.1 Singular Value Decomposition

The complete general theory of SVD and its computation will not be discussed (see Golub and Kahan [88], Golub and Reinsch [89] and Press et al. [90] for details). For our purposes, a short introduction to SVD in general terms is needed as a background to its application in the signal extraction problem. This presentation is somewhat original in that the expansions using either the temporal eigenvectors or spatial eigenvectors are outlined along with interpretation of this process in the context of electrophysiological mapping.

For $p \geq t$ the matrix \mathbf{X} can be written as the product of a $p \times t$ column orthogonal matrix \mathbf{U} , a $t \times t$ diagonal matrix \mathbf{W} with positive or zero elements, and the transpose of a $t \times t$ orthogonal matrix \mathbf{V} . Thus,

$$\mathbf{X}_{p \times t} = \mathbf{U}_{p \times t} \mathbf{W}_{t \times t} \mathbf{V}_{t \times t}^* \quad (3.6)$$

and

$$\mathbf{U}_{t \times p}^* \mathbf{U}_{p \times t} = \mathbf{V}_{t \times t}^* \mathbf{V}_{t \times t} = \mathbf{V}_{t \times t} \mathbf{V}_{t \times t}^* = \mathbf{I}_{t \times t}. \quad (3.7)$$

\mathbf{I} is the identity matrix and $*$ denotes transpose.

The matrix \mathbf{U} consists of the t orthonormalised eigenvectors associated with the t largest eigenvalues of $\mathbf{X}\mathbf{X}^*$, and the columns of \mathbf{V} are the orthonormalised eigenvectors of $\mathbf{X}^*\mathbf{X}$. The diagonal elements w_i of \mathbf{W} are the non-negative square roots of the common eigenvalues of $\mathbf{X}^*\mathbf{X}$ and $\mathbf{X}\mathbf{X}^*$; these are the “singular values”. The expansion given in Equation 3.6 is called the “singular value decomposition” (SVD) of \mathbf{X} [88].

The rank, r , of \mathbf{X} is, at most, equal to t . However, due to interdependencies in the data, r can be less than t . As such, only the first r eigenvectors associated with the r largest eigenvalues w_i^2 are needed to represent \mathbf{X} . This results in a form of data reduction and the decomposition in Equation 3.6 can be written

$$\mathbf{X}'_{p \times t} = \mathbf{U}_{p \times r} \mathbf{W}_{r \times r} \mathbf{V}_{r \times t}^* \quad (3.8)$$

with the normalisation condition,

$$\mathbf{U}_{r \times p}^* \mathbf{U}_{p \times r} = \mathbf{V}_{r \times t}^* \mathbf{V}_{t \times r} = \mathbf{I}_{r \times r} \quad (3.9)$$

now applying to the columns of \mathbf{U} and \mathbf{V} only.

The largest eigenvalue, w_1^2 , is associated with the feature which has maximum correlation amongst all observations in the matrix \mathbf{X} . The next largest eigenvalue, w_2^2 , accounts for the 2^{nd} most common correlated features, etc... Ordering the feature vectors $\mathbf{u}_i, \mathbf{v}_i$ to correspond with decreasing eigenvalues ($w_1 \geq w_2 \geq \dots \geq w_t \geq 0$), minimises the (least-squares) error associated with the approximation given in Equation 3.8.

In the context of signal extraction, either the \mathbf{U} or \mathbf{V} basis sets can be used to expand the matrix \mathbf{X} , which in this application, has t maps consisting of p spatial elements each. Multiplying both sides of Equation 3.6 on the left by $\mathbf{U}_{r \times p}^*$, and using the orthonormality condition of Equation 3.9, an expansion using the first r spatial eigenvectors \mathbf{u}_i gives:

$$\mathbf{U}_{r \times p}^* \mathbf{X}_{p \times t} = \mathbf{U}_{r \times p}^* \mathbf{U}_{p \times t} \mathbf{W}_{t \times t} \mathbf{V}_{t \times t}^* \quad (3.10)$$

$$= \mathbf{W}_{r \times r} \mathbf{V}_{r \times t}^* \quad (3.11)$$

$$= \mathbf{A}_{r \times t}^* \quad (3.12)$$

Equation 3.8 can now be written

$$\mathbf{X}'_{p \times t} = \mathbf{U}_{p \times r} \mathbf{A}_{r \times t}^* \quad (3.13)$$

defining \mathbf{A} as a $t \times r$ matrix of expansion coefficients associated with the r spatial eigenvectors, \mathbf{u}_i .

Similarly, multiplying both sides of Equation 3.6 on the right by $\mathbf{V}_{t \times r}$, an expansion in temporal eigenvectors, \mathbf{v}_i , becomes,

$$\mathbf{X}_{p \times t} \mathbf{V}_{t \times r} = \mathbf{U}_{p \times t} \mathbf{W}_{t \times t} \mathbf{V}_{t \times t}^* \mathbf{V}_{t \times r} \quad (3.14)$$

$$= \mathbf{U}_{p \times r} \mathbf{W}_{r \times r} \quad (3.15)$$

$$= \mathbf{B}_{p \times r} \quad (3.16)$$

Equation 3.8 can now be written

$$\mathbf{X}'_{p \times t} = \mathbf{B}_{p \times r} \mathbf{V}^*_{r \times t}, \quad (3.17)$$

defining \mathbf{B} as a $p \times r$ matrix of expansion coefficients associated with the r temporal eigenvectors, \mathbf{v}_i .

Further interpretation of the matrices \mathbf{A} and \mathbf{B} clarifies their relationship to \mathbf{X} . Each column of $\mathbf{A}_{t \times r}$ represents the spatial correlation of the i^{th} spatial eigenvector with each of the t columns (maps) of \mathbf{X} . Each column of $\mathbf{B}_{p \times r}$ represents the temporal correlation of the i^{th} temporal eigenvector with each of the p rows (temporal waveforms) of \mathbf{X} .

In the context of spatial source separation, the spatial eigenvectors \mathbf{U} resulting from the SVD of atrial repolarisation maps are applied to a combination matrix \mathbf{Z} to determine \mathbf{A} . \mathbf{A} represents the proportion of each atrial repolarisation eigenvector which is present in the combination map. The residual,

$$\mathbf{R}_{p \times t'}^{\text{SVD}} = \mathbf{Z}_{p \times t'} - \mathbf{U}_{p \times r} \mathbf{A}^*_{r \times t'} \quad (3.18)$$

is expected to reveal the superimposed source. The prime ($'$) is used to denote that the number of maps in the matrix \mathbf{Z} is not necessarily the same number which was used to determine the atrial repolarisation eigenvectors.

3.4.2 Karhunen-Loève Transform

The KLT method [91] represents a nonperiodic random process by an orthonormal basis set \mathbf{F} with uncorrelated coefficients \mathbf{C} ,

$$\mathbf{X}_{p \times t} = \mathbf{F}_{p \times p} \mathbf{C}_{p \times t}. \quad (3.19)$$

If we truncate this expansion after r terms ($r < p$),

$$\mathbf{X}'_{p \times t} = \mathbf{F}_{p \times r} \mathbf{C}_{r \times t}, \quad (3.20)$$

the mean-square error

$$\varepsilon(r) = E\{(\mathbf{X} - \mathbf{X}')^*(\mathbf{X} - \mathbf{X}')\} \quad (3.21)$$

is minimised by an appropriate choice of \mathbf{C} and \mathbf{F} . E denotes expectation value.

The optimum values of the constants \mathbf{c}_i are found to satisfy

$$E\{\mathbf{c}_i\} = 0, \quad (3.22)$$

while the optimum eigenvectors \mathbf{f}_i satisfy the eigenvalue-eigenvector problem,

$$\mathbf{K}\mathbf{f}_i = \lambda_i\mathbf{f}_i. \quad (3.23)$$

This implies that the \mathbf{f}_i are eigenvectors of the covariance matrix \mathbf{K} of \mathbf{X} and the λ_i the corresponding eigenvalues. The resulting mean-square error to the approximation

$$\varepsilon(r) = \sum_{i=r+1}^p \lambda_i \quad (3.24)$$

is minimised for all values of r if the λ_i are arranged in descending order.

The covariance matrices \mathbf{K} of the columns \mathbf{x}_i of \mathbf{X} are assumed to be equal. In practice one estimates a sample covariance matrix from all columns of \mathbf{X} . An unbiased estimate is

$$\mathbf{K} = \frac{1}{t-1} \sum_{i=1}^t (\mathbf{x}_i - \bar{\mathbf{x}})(\mathbf{x}_i - \bar{\mathbf{x}})^*, \quad (3.25)$$

with $\bar{\mathbf{x}}$ as defined in Equation 3.1. In matrix notation, this becomes

$$\mathbf{K} = \frac{1}{t-1} (\mathbf{X} - \bar{\mathbf{X}})(\mathbf{X} - \bar{\mathbf{X}})^*, \quad (3.26)$$

with the columns of $\bar{\mathbf{X}}$ all identical and equal to $\bar{\mathbf{x}}$.

As in the SVD, the KLT representation of atrial repolarisation by basis functions \mathbf{F} is applied to combination maps. The extracted superimposed source is expected to be represented by the residual matrix,

$$\mathbf{R}_{p \times t'}^{\text{KLT}} = \mathbf{Z}_{p \times t'} - \mathbf{F}_{p \times r} \mathbf{C}_{r \times t'}, \quad (3.27)$$

where $\mathbf{C}_{r \times t'} = \mathbf{F}_{r \times p}^* \mathbf{Z}_{p \times t'}$ are the KLT expansion coefficients.

Gerbrands [92] has demonstrated that under some circumstances orthogonal eigenvectors obtained via KLT and SVD can be equivalent. Using the estimated sample column covariance matrix \mathbf{K} , the eigenvectors \mathbf{F} obtained in the KLT of data matrix \mathbf{X} are found to correspond with the \mathbf{U} eigenvectors resulting from the SVD of $\{\mathbf{X} - \bar{\mathbf{X}}\}$.

3.5 Simulations of extraction techniques

One objective in the application of extraction techniques is to use the extracted maps as input to an inverse solution in an attempt to localise the sources of the distributions. Obviously, this application is reasonable only if one can have confidence in these maps. If the extraction techniques are to be used in this context, then it is necessary, through simulation studies to assess their applicability for the purposes of identifying source distributions associated with definite electrophysiological events in the heart.

To this end, the techniques described earlier (Temporal Averaging, Correlation, Singular Value Decomposition and Karhunen-Loève Transform) have been applied to simple source configurations which can be related to the problems of interest in this study. Problems and limits of the techniques can then be identified.

To accomplish this study, a current dipole in an infinite homogeneous volume conductor was used as a source-conductor model (Equations 2.2 and 2.3). The solution for the electric potential ϕ , and Z -component of the magnetic field, B_z , for this model can yield equivalent patterns, so only one of these, B_z , was used in these simulations.

B_z was calculated at the 56 locations of the Dalhousie standard MCG grid (7×8 grid of 4 cm spacing) for a number of source configurations. More complicated source models have been studied by us [93], but the results were more difficult to interpret (although, ultimately, the same observations and conclusions were reached). Knowing *a priori* all details of the input data leads immediately to conclusions about the success or failure of the extraction techniques.

We refer to Figure 3.1 to define the situation which will be simulated. As mentioned previously, the two sources of particular interest to us are the depolarisation of the His-Purkinje conduction system (HPS) and the pre-excitation of the ventricles via accessory pathways in Wolff-Parkinson-White syndrome (WPW). The HPS and pre-excitation source in WPW syndrome are the superimposed sources. Both of these events occur simultaneously with the background event of atrial repolarisation (T_a),

but generally, there is a time segment in which this background source (T_a) is active before either superimposed source begins to depolarise. Hence, this initial segment can be used to characterise the background source.

The simulations explore the potential for successfully extracting the spatial features associated with these two particular superimposed sources. This is done in two phases. First the quality of the background source representation achieved with each of the extraction techniques is evaluated. To this end, we will choose simulated sources which explicitly violate some assumptions made in characterising the background source. It seems obvious that a current generator as complex as the heart would almost always violate these assumptions, so these simulations should indicate just how sensitive each technique is to these basic assumptions.

More importantly, how would an error in representing the background source affect the superimposed source we wish to extract from a combination map? This is the question explored in the second phase of the simulations. Particularly simple choices are made to simulate the background and superimposed sources in a way that will allow us to draw conclusions applicable to many possible relative features of the two sources.

3.5.1 Results: Characterisation of background source

In characterising the background source, two assumptions are required. The first is that the amplitude of the source is constant; the second that the location remains stationary (position and orientation). The four techniques described (TAT, CT, SVD and KLT) will be used to characterise a fictitious background source and the representation achieved will be evaluated.

We wish to test independently the effects of (1) a dipole-moment amplitude changing as a function of time, and (2) a dipole-source location changing as a function of time. Only two source configurations are necessary:

- In the first case, the background source is a dipole of fixed location but with an amplitude changing over $t = 80$ ms in a triangular fashion. With the assumed sam-

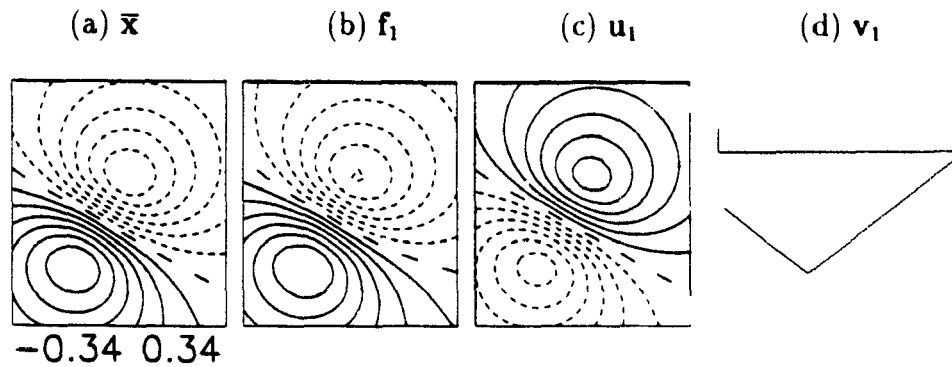


Figure 3.2: Simulation of a dipole with changing amplitude. (a) Average map used in TAT and CT; (b) KLT eigenvector \mathbf{f}_1 ; (c) SVD eigenvector \mathbf{u}_1 ; and (d) SVD eigenvector \mathbf{v}_1 . The eigenvectors (b,c and d) are normalised vectors, hence have no units and the signs of the extrema become arbitrary. The units of the average map (a) are in pT.

pling interval of 2 ms, 40 maps were produced; a maximum magnetic field of 0.58 pT was reached at $t = 30$ ms. In Figure 3.2, the representation required for each of the 4 extraction techniques is shown. The actual location and orientation relative to the grid and the change in amplitude as a function of time of the source are exactly represented by the SVD eigenvectors \mathbf{u}_1 (Fig. 3.2c) and \mathbf{v}_1 (Fig. 3.2d), respectively. \mathbf{f}_1 obtained in the KLT is shown in Fig. 3.2b. Finally, the average map obtained for the 40 maps, shown in Fig. 3.2a, is to be used in both TAT and CT.

- In the second case, the background source involves a dipole of fixed amplitude and orientation, but moving by 0.5 mm every successive time step, producing 2 cm total trajectory in the horizontal direction during the 40 time steps, each representing 2 ms. Figure 3.3 shows the first three spatial SVD (Fig. 3.3a) and KLT (Fig. 3.3b) eigenvectors for this moving source. The average map for this source is shown in Fig. 3.3c.

The effectiveness of the representation achieved for these source configurations was tested by doing a ‘self-fit’, that is, calculating the residual \mathbf{R} for each of the techniques with no superimposed source present ($\mathbf{Z} = \mathbf{X}$ in Equations 3.3, 3.5, 3.18 and 3.27). Only the 1st or 1st and 2nd eigenvectors were used in Eqs. 3.18 and 3.27.

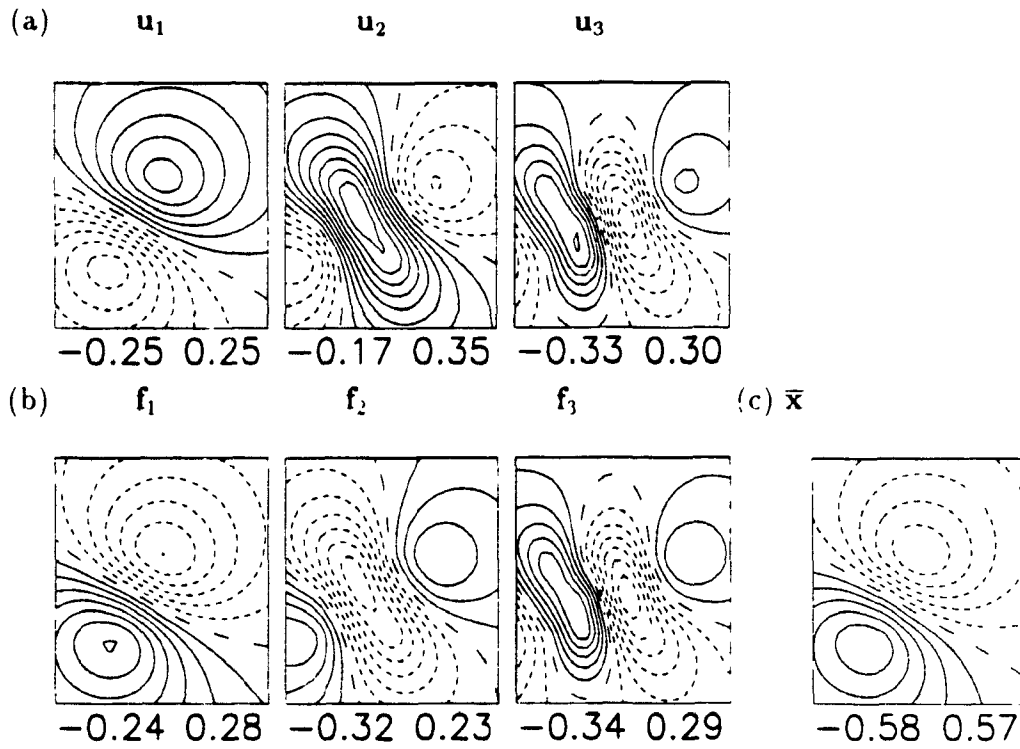


Figure 3.3: Simulation of a dipole with changing location.

(a) SVD eigenvectors u_1, u_2, u_3 ; (b) KLT eigenvectors f_1, f_2, f_3 ; (c) average map. Same display convention as in Figure 3.2 applies here.

Method	Self-fits		Cross-fits
	Background source 1	Background source 2	Combination
R^{TAT}	103.46 (248.18)	5.42 (3.11)	47.95 (89.96)
R^{CT}	0 (0)	5.41 (3.11)	113.75 (72.51)
$R^{\text{SVD}} [\mathbf{u}_1]$	0 (0)	5.41 (3.11)	113.74 (72.46)
$R^{\text{SVD}} [\mathbf{u}_1, \mathbf{u}_2]$	-	0.28 (0.17)	100.55 (12.64)
$R^{\text{KLT}} [\mathbf{f}_1]$	0 (0)	5.21 (3.00)	113.11 (69.66)
$R^{\text{KLT}} [\mathbf{f}_1, \mathbf{f}_2]$	-	0.28 (0.17)	100.55 (12.62)

Table 3.1: Percent errors of fit represented by the rms of the residuals. Errors for the self-fits and cross-fits were calculated according to Equations 3.28 and 3.29. The values given are average and standard deviation (round brackets) over all 40 maps of each sequence. The eigenvectors used in the KLT and SVD expansions are indicated in the square brackets. The self-fits correspond to fits where no superimposed source is present. Cross-fits are fits of the background representation to a combined source matrix.

The error, averaged over all 40 maps for each of these self-fits, is shown in Table 3.1. This % error in background source characterisation is defined as

$$R_{\text{prim}} = \frac{\sqrt{\mathbf{R} \cdot \mathbf{R}}}{\sqrt{\mathbf{X} \cdot \mathbf{X}}} \times 100\%. \quad (3.28)$$

Also shown in Figure 3.4 are 5 of the 40 residual maps \mathbf{R}^{TAT} for the moving source simulation.

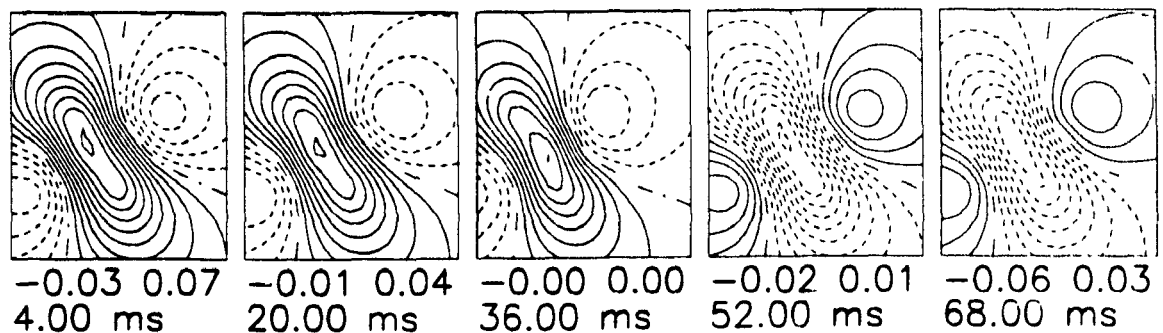


Figure 3.4: TAT residual maps, \mathbf{R} , for the moving dipole. The times and the residual magnetic field in pT are indicated below each map.

3.5.2 Results: Extraction of a superimposed source

To test the accuracy of separating a background and superimposed source, two additional data files were generated. The first represents the background source. The dipole generating this sequence of maps is the same as in the source with a moving location described above, except that the next 40 maps (Fig. 3.1) in the sequence were used (constant amplitude and orientation, but location changing by .5 mm/time step). This sequence is shown in Figure 3.5a. The superimposed source is shown in Figure 3.5b. This sequence represents a dipole fixed in location and orientation, but whose dipole moment increases from zero to twice the moment of the background source. The two files produced were added to simulate a sequence of combination maps (Fig. 3.5c).

The characterisations shown in Figure 3.3 were used to represent the background source. This simulates the data we are interested in, since an initial phase of background source is available for characterisation, and then this representation can be applied to the combination maps which follow (see Fig. 3.1). Each of the separation techniques was used to remove the background-source contribution to the combination maps. In this ‘cross-fitting’, the residual \mathbf{R} for each of the techniques is calculated for the combination matrix \mathbf{Z} where $\mathbf{Z} = \mathbf{X} + \mathbf{Y}$ in Eqs. 3.3, 3.5, 3.18 and 3.27. The resulting residual maps are presented in Figure 3.6 and the % errors of the superimposed source extraction are in Table 3.1. The error in extracting the superimposed source is calculated by,

$$R_{sec} = \frac{\sqrt{(\mathbf{Y} - \mathbf{R}) \cdot (\mathbf{Y} - \mathbf{R})}}{\sqrt{\mathbf{Y} \cdot \mathbf{Y}}} \times 100\%. \quad (3.29)$$

\mathbf{Y} is the simulated superimposed source, while \mathbf{R} represents the extracted source. This error, R_{sec} is also plotted as a function of superimposed to background signal amplitudes in Figure 3.7 for the SVD and TAT extractions.

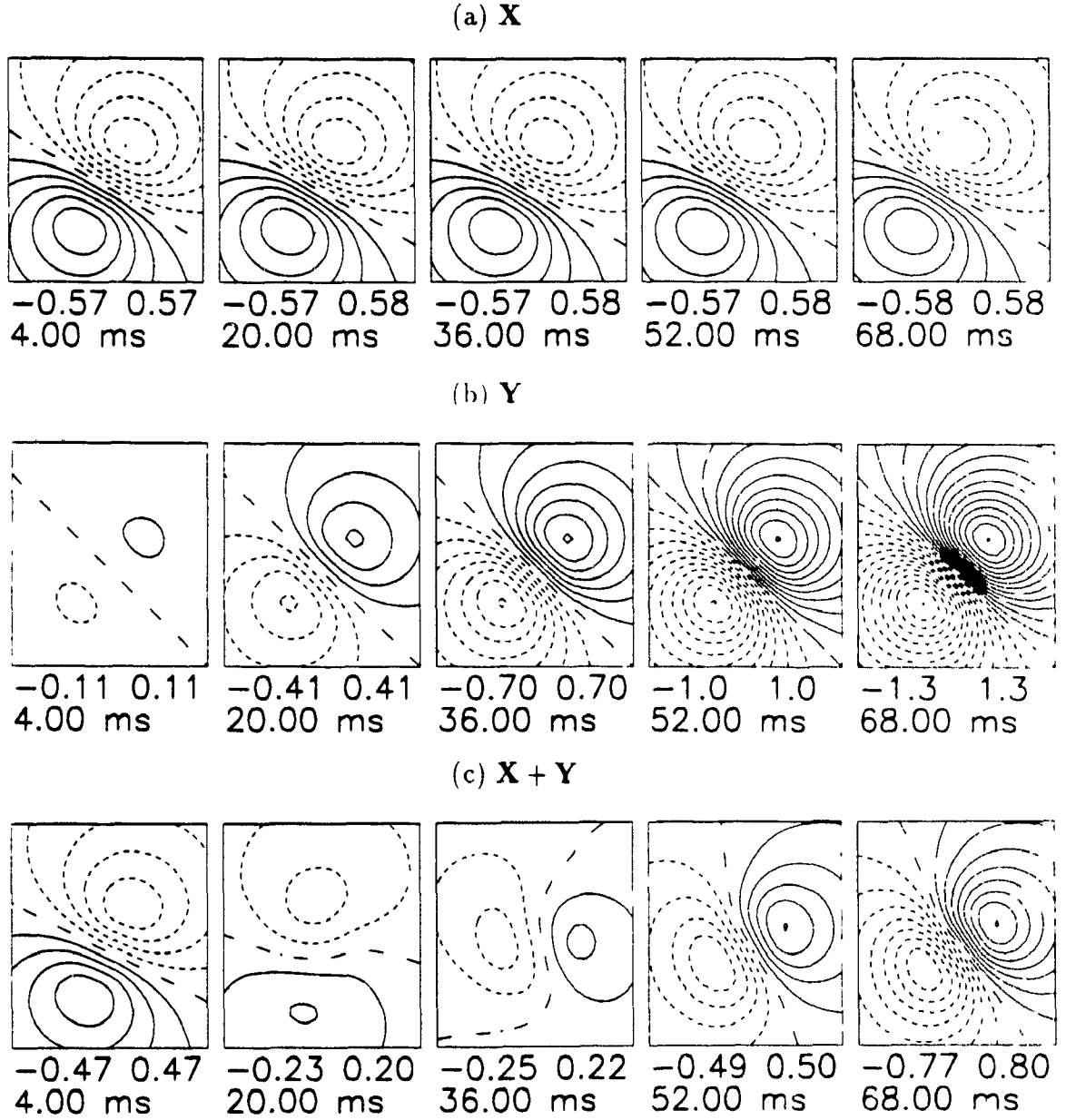


Figure 3.5: Simulated maps generated by a combined source.
 (a) Background source, (b) Superimposed source, and (c) Combined source maps at the times indicated below each map. Extrema values are given in pT.

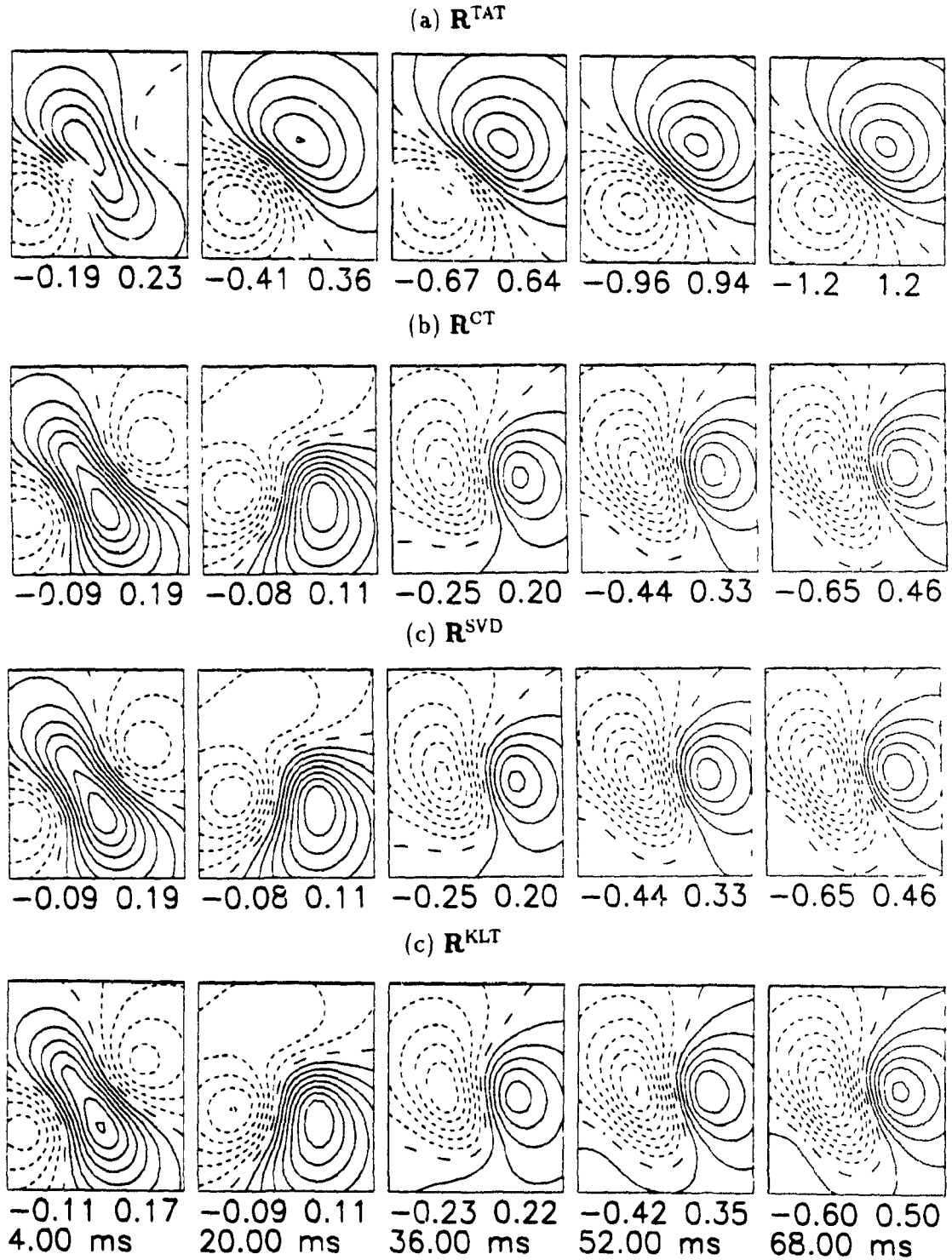


Figure 3.6: Residual maps, \mathbf{R} , for combined-source simulation. (a) TAT, (b) CT, (c) SVD and (d) KLT. In (c) and (d) only the first eigenvectors, \mathbf{u}_1 and \mathbf{f}_1 respectively, were used to represent the background source. Extrema values are given in pT.

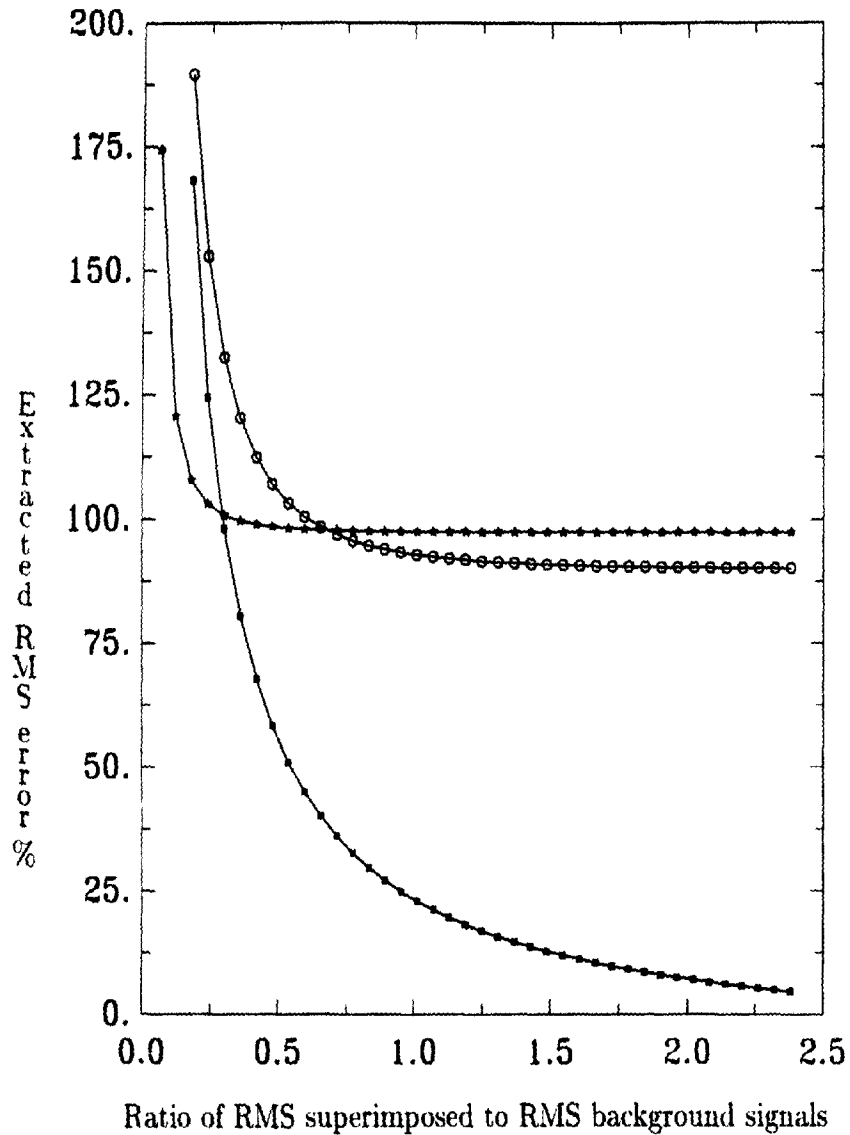


Figure 3.7: Superimposed signal extraction errors for the SVD and TAT methods. The extracted source error (Eq. 3.29) is plotted as a function of the ratio of RMS superimposed to RMS background signal amplitudes for the SVD method using the first eigenmap, u_1 (\circ), the first and second eigenmaps, u_1 and u_2 ($*$), and the TAT method (solid \square). In the SVD (u_1) and TAT cases, the first 2 maps (of the 40 simulated) were excluded from the beginning of the sequence because of their particularly large errors (e.g. $R_{sec} \simeq 500\%$ at $t=2$ ms for both techniques).

3.5.3 Discussion: Background source characterisation

The results of the background-source characterisation (Table 3.1) are not unexpected. The TAT does not work well in the case where the amplitude of the source generating the magnetic field or potential maps changes during the time segment used in the representation. The ‘average’ map will reflect the average feature found in the sequence, and larger deviations from this average will result in proportionally larger errors. The three other techniques (CT, SVD and KLT) work even if the amplitude of the source changes because all three use a correlation to determine the proportion of background source which is present.

The situation changes when the background source is non-stationary. In this case, the error of the representation will become proportional to the actual spatial variation in the field patterns caused by the motion of the source. This is demonstrated in Figure 3.4. Because the amplitude of the dipole moment was kept constant, the average map generated matched the map in the center of the sequence ($t \simeq 40$ ms). The residuals then increased as we moved further from this average, with a change in phase on either side of this minimum.

A comparison of Fig. 3.4 and eigenvectors \mathbf{u}_2 and \mathbf{f}_2 in Fig. 3.3 is interesting. It has already been stated that the first SVD eigenvalue and eigenvector are associated with the feature which has maximum correlation among all observations in matrix \mathbf{X} . The next largest eigenvalues then account for the next most common correlated features, etc... That the first eigenvectors have the same spatial features as the average map is expected. The suggested comparison, however, leads to a conclusion which is not quite as intuitive. It appears that in this particular simulation, the second spatial eigenvectors (\mathbf{u}_2 and \mathbf{f}_2 in Fig. 3.3) actually reflect the change in location of the dipole source as a function of time (Fig. 3.4). This observation explains why the residuals in the TAT, CT and SVD and KLT expansions using only one eigenvector are very similar. Although not shown, the residual maps from the orthogonal expansions using the first two eigenvectors correlate well with the third eigenvectors. The errors

in Table 3.1 (self-fits) for the orthogonal expansions thus reflect the series truncation errors (i.e. Equation 3.24), and are found to be quite small when using only a few eigenvectors to describe this simulated data.

3.5.4 Discussion: Extraction of superimposed source

In using the suggested extraction techniques on combined data, the results did not appear promising. All the correlation techniques (CT, SVD and KLT) suffered from the same problem. The expansion coefficients, \mathbf{a}_i and \mathbf{c}_i , and the correlation factors, g_i , measured the orthogonality between the background source representation (eigenvectors or average map) and the columns of the matrix being fit. These representations were not necessarily orthogonal to all other matrices (sources) of interest. For example, in the SVD case, consider the combination matrix $\mathbf{Z} = \mathbf{X} + \mathbf{Y}$, where \mathbf{X} represents the background source and \mathbf{Y} a superimposed source. Application of Equation 3.12 to \mathbf{Z} , with \mathbf{U} originating from an SVD of \mathbf{X} , would proceed as follows:

$$\mathbf{A}^* = \mathbf{U}^* \mathbf{Z} \quad (3.30)$$

$$= \mathbf{U}^* (\mathbf{X} + \mathbf{Y}) \quad (3.31)$$

$$= \mathbf{A}_x^* + \mathbf{A}_y^*. \quad (3.32)$$

The residual between the original matrix \mathbf{Z} and the fit just computed is:

$$\mathbf{R}^{\text{SVD}} = \mathbf{Z} - \mathbf{U} \mathbf{A}^* \quad (3.33)$$

$$= \mathbf{X} + \mathbf{Y} - (\mathbf{U} \mathbf{A}_x^* + \mathbf{U} \mathbf{A}_y^*). \quad (3.34)$$

To a good approximation, $\mathbf{U} \mathbf{A}_x^* = \mathbf{X}$ (see Eq. 3.13), hence

$$\mathbf{R}^{\text{SVD}} = \mathbf{Y} - \mathbf{U} \mathbf{A}_y^* \quad (3.35)$$

and the superimposed source \mathbf{Y} is recovered only if $\mathbf{A}_y^* = \mathbf{U}^* \mathbf{Y} = 0$, that is if the background and superimposed sources are orthogonal. In the simulation presented, the background and superimposed sources were not orthogonal, so that the residual

maps in Figure 3.6b to d actually represent the component of the superimposed source which is orthogonal to the background source. The minimum extraction errors R_{sec} of Fig. 3.7 for the SVD simulations reflect this non-orthogonality. A choice of background and superimposed source configurations which are more orthogonal would produce a smaller \mathbf{R}^{SVD} (\mathbf{R}^{KLT} and \mathbf{R}^{CT}). This situation translates into an over- or under-subtraction of the background-source features from the combination maps. Similar arguments apply to KLT and CT. Hence \mathbf{Y} , the superimposed source, is generally not recoverable unless it is orthogonal to the background features.

An additional comment is needed about the differences in the SVD and KLT expansions. The spatial eigenvectors found in these two expansions (Figures 3.2 and 3.3) are very similar, but recall that the SVD eigenvectors are associated with the eigenvalues of $\mathbf{X}\mathbf{X}^*$ and the KLT eigenvectors with those of the covariance matrix of \mathbf{X} . In the field patterns of the KLT eigenvectors, there is a difference in the location of the zero line and the extrema are no longer of equal value, as compared to the input data \mathbf{X} or SVD eigenvectors. Though no error is detected in the self-fits (since the expansion coefficients are defined accordingly), we see by Figures 3.6c and d that, in the combination residuals, this difference is detected.

The temporal averaging technique (TAT) does show promise. The errors presented for the combination simulation in Table 3.1 are unacceptably large. However, as can be seen in Figure 3.7, \mathbf{R}^{TAT} , is large only for the earliest combination maps. As the superimposed source grows larger, the errors due to the residual background source become less significant. In effect, R_{sec} of Fig. 3.7 for the TAT simulation, is a plot of the residual background source signal. This suggests that if, (a) the background source is relatively stable, and (b) the superimposed source is or becomes larger than the TAT *residual*, a superimposed source could be extracted from magnetic field maps using this technique. This would also be true for body surface potential mapping data since the extraction techniques are an application in pattern recognition and do not depend on the type of data considered.

4 PR-interval Mapping

4.1 Introduction

The electrocardiographic PR interval is formed by the P wave (depolarisation of the atria) and the PR segment. The PR segment, the interval between P-wave offset and the QRS complex (depolarisation of the ventricles), is caused by the delay of activation in the slow-conducting A-V node. During this time, repolarisation of the atria occurs and, as detected by intra-cavitary catheter measurements, HPS is activated; in patients with WPW syndrome, the δ wave (preceeding QRS) shortens the PR interval, and prolongs the QRS complex.

The HPS and δ wave both originate from well-localised sources, and as such have been the focus of much interest in magnetic and electric cardiac field mapping [3,77,94,79,80,95,96,97,98,78]. These sources are used to validate single-current-dipole inverse solutions [72,76,81,99,100]. The δ wave in WPW syndrome plays a role in establishing potentially lethal arhythmias (supraventricular tachycardias), and as such, WPW syndrome has a significant clinical interest. Since the atrial repolarisation (Ta) signal is also present during HPS and δ -wave activation, the latter signals of interest cannot be accurately localised unless the Ta component has been successfully removed from the combination map. Hence Ta features must be well characterised.

In order to successfully separate the Ta signal and the HPS or δ -wave signals, a good understanding of complete atrial depolarisation and repolarisation is essential. The following description is the first presentation of electric and magnetic field maps of atrial depolarisation and repolarisation, recorded from the same subjects.

4.2 Methods

Thirty subjects (10 females, 20 males) with normal P waves were studied. The average age of the group was 48.9 (SD 8.3) years, in a range of 33–66 years. Of this group, 3 subjects had prolonged PR intervals due to first degree AV block and 3 had first degree block and ventricular tachycardia. All others were clinically normal as determined by history, physical examination and standard 12-lead ECG. Voluntary informed consent was obtained from all subjects.

4.2.1 Data processing

MFM and BSPM data were obtained following the standard recording protocol (see Table 1.1). The data was averaged off-line, filtered at 60 Hz, and time-aligned on the QRS. The time-lines of the MFM and BSPM data sets were then compared. It was determined that discrepancies existed between the onset and offsets of the P waves in the 2 data sets. This resulted from the differences in S/N ratios and the use of MFM RMS signals instead of the simultaneously recorded ECG limb leads to determine the time-lines in MCG data. Because map-by-map comparisons would be necessary, the time-lines of the BSPM data were also applied to the MCG data, after confirming with the ECG limb leads recorded simultaneously with the MCG, that the same P waves were recorded in both data sets¹.

4.2.2 Baseline correction

The importance of constructing maps with an appropriate zero baseline reference was discussed in Spach et al. [101]. They determined that the UP interval would generally be the best choice, since this is the interval when cardiac currents would be non-existent, in normal, healthy myocardium. Inappropriate choices would result in false patterns, with artifacts producing regional changes simulating other patterns

¹Eight subjects originally included in the study group were rejected because of differences in the ECG limb-lead P waves recorded with the BSPM and MCG.

or events. In particular, care must be taken to avoid T-wave or U-wave overlap with the P wave.

A zero baseline in both data sets was defined in the UP interval, by removing the average signal recorded in the segment -60 to -12 ms relative to P-wave onset. In a few cases, the UP interval was shorter than 60 ms, hence a shorter interval may have been used.

4.2.3 Data analysis

Isofield contour maps

Isomagnetic field and isopotential contour maps of the PR interval were plotted for all subjects. Maps were obtained every 4 ms during the P wave and every 6 ms during the PR segment. These maps were studied for general group features, individual subject variations and differences in the information content and sensitivity of the 2 recording modalities to the PR-interval features.

Signal durations, peak amplitudes and locations

The MFM and BSPM data were compiled to determine global characteristics of the study group. Since the study does not involve any group discrimination analysis, averages of particular features are presented for summary purposes, and for comparison of the MFM and BSPM data. The features considered are defined below.

- $|P_{pos}|$ - amplitude of the peak positive P wave.
- $t_{P_{pos}}$ - time, relative to P-wave onset, corresponding to peak positive P-wave signals, normalised to P-wave duration (hence 0.0 to 1.0).
- Location (grid point or lead) of peak positive P-wave signals.
- $|P_{neg}|$ - amplitude of the peak negative P wave.

- $t_{P_{neg}}$ - time, relative to P-wave onset, corresponding to peak negative P-wave signals, normalised to P-wave duration.
- Location (grid point or lead) of peak negative P-wave signals.
- $\frac{|R-max|}{|P-max|}$ - ratio of absolute maximum R-wave and absolute maximum P-wave signals.

The peak amplitudes were found by averaging a 4 ms segment (3 points) centred on the largest positive and negative signals recorded amongst all 117 BSPM or 56 MCG signals.

4.3 Results

4.3.1 Isofield contour maps

Isofield contour maps of the PR interval were obtained for all 30 subjects in steps of 4 ms during the P wave and 6 ms during the PR segment. All these maps cannot be presented, so only a few representative cases will be shown and discussed.

Isomagnetic field and isopotential maps from one of the subjects (RF108, normal male, 59 yrs, P-wave 100 ms, PR-interval 132 ms), during the P wave (Fig. 4.1) and the PR segment (Fig. 4.2) are presented. Figure 4.1 includes, at 108 ms, a map during early atrial repolarisation. PR-interval maps are also shown for normal subject CP95 in Figure 4.3 (male, 36 yrs, P-wave 85 ms, PR-interval 135 ms). To guide the presentation and discussion of the results, sketches (Figure 4.4) were made which highlight the location of the extrema during particular phases of the PR interval. There are consistent features and particular differences to note between these two cases, which reflect variations found amongst most subjects. The understanding gained from the analysis of these maps will contribute to the analysis of data in the following chapters.

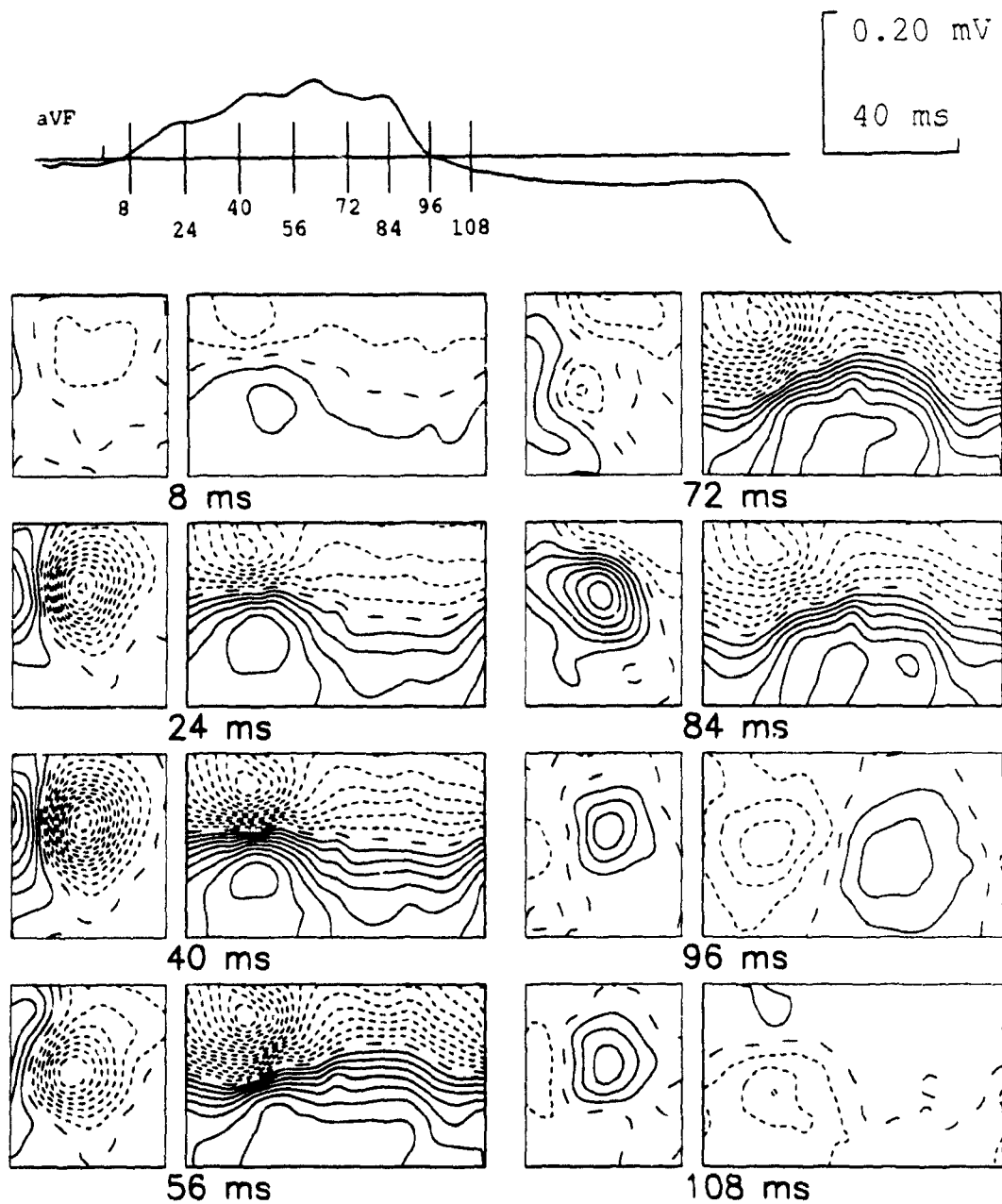


Figure 4.1: PR-interval isofield maps for subject RF108. Isomagnetic field (small frames) and isopotential (large frames) maps for the same time instants relative to P-wave onset are plotted in contour steps of 0.2 pT and 0.01 mV, respectively. ECG lead aVF of the PR interval is plotted above. The vertical lines indicate the timing of the particular maps displayed.

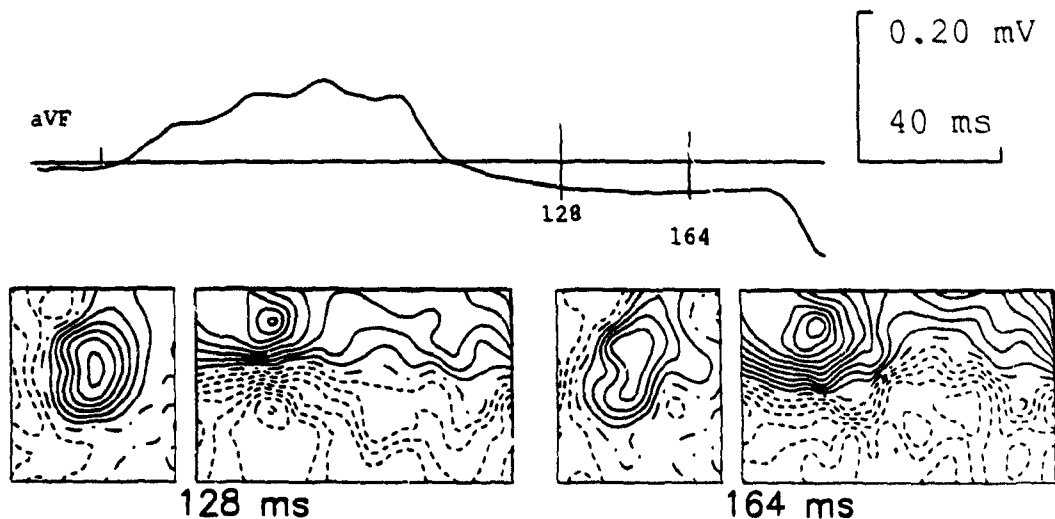


Figure 4.2: PR-segment isofield maps for subject RF108. Contour steps for the MFM and BSPM plots are 0.1 pT and 0.005 mV respectively.

Depolarisation of the right atrium in MFM and BSPM plots

The onset of atrial depolarisation (8, 24 and 40 ms of Fig. 4.1, and 12 and 30 ms of Fig. 4.3) is marked by MFM and BSPM patterns which are consistent with an equivalent current dipole (ECD) near the anterior chest wall and pointing toward the feet ($-Y$ direction), with a component pointing to the left arm ($+X$) in some individuals. This pattern is sketched in Figure 4.4a and d. This phase of the P wave reflects the depolarisation of the right atrium (RD).

Concurrent right and left atrial activation in BSPM plots

As atrial activation progresses into the left atrium, the positive potential maximum is seen to migrate left parasternally (centre of BSPM map), with the negative extremum remaining relatively stationary. This occurs at 56, 72 and 84 ms of Fig. 4.1 and 48, 66 and 84 ms of Fig. 4.3. The transition from the beginning to end of this phase is shown in Figure 4.4d and e. Only during the terminal aspect of the P wave (96 ms of Fig. 4.1), in most subjects, did this minimum move down, as the positive peak moved further to the back (right side of map). This reflects a relatively large $-Z$

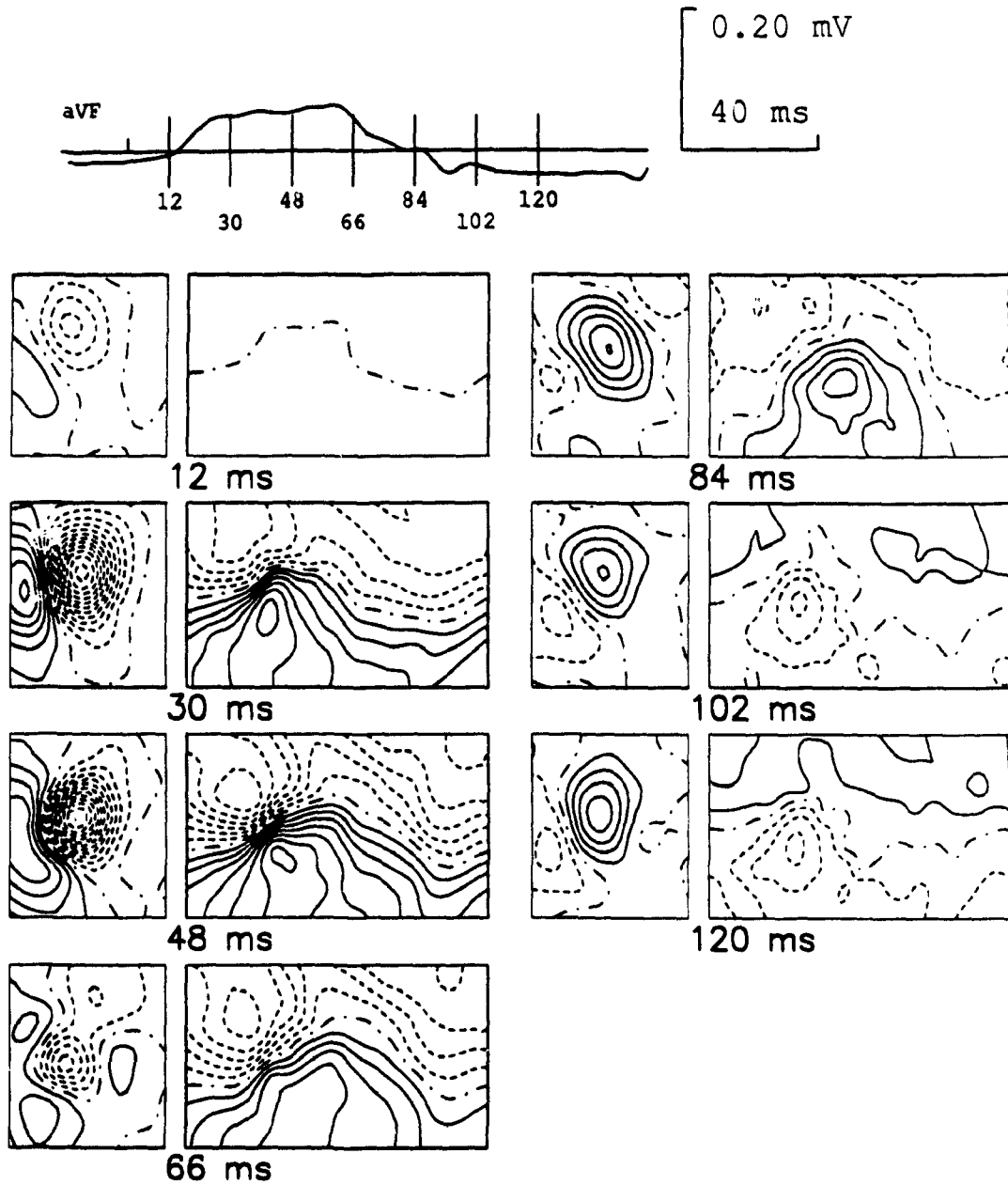
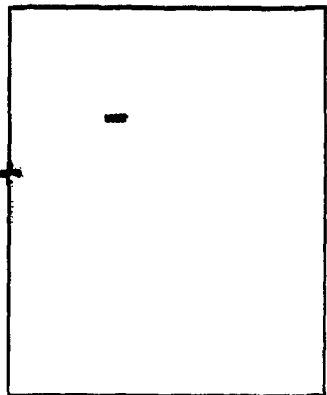
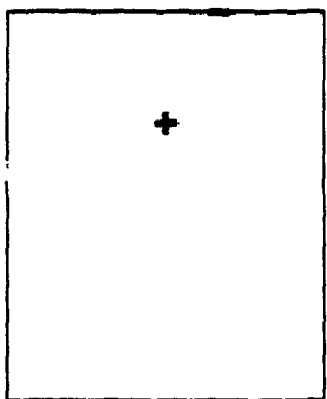


Figure 4.3: PR-interval isofield maps for subject CP95. Isomagnetic field (left) and isopotential (right) maps for the same time instants relative to P-wave onset are plotted in contour steps of 0.2 pT and 0.01 mV, respectively.

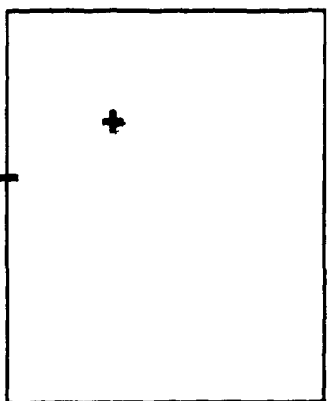
a) **Right atrial depolarisation**



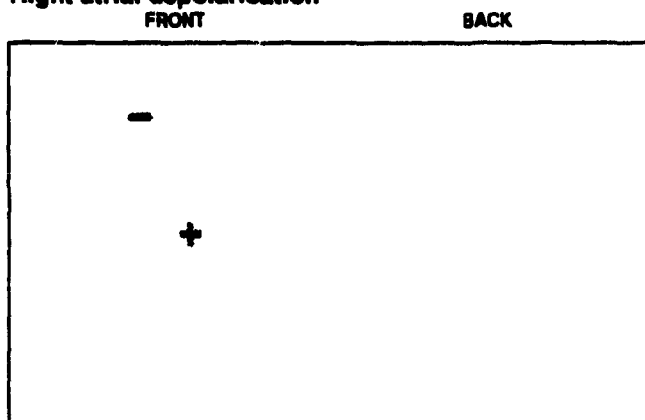
b) **Left atrial depolarisation**



c) **Right atrial repolarisation**



d) **Right atrial depolarisation**



e) **Left atrial depolarisation**

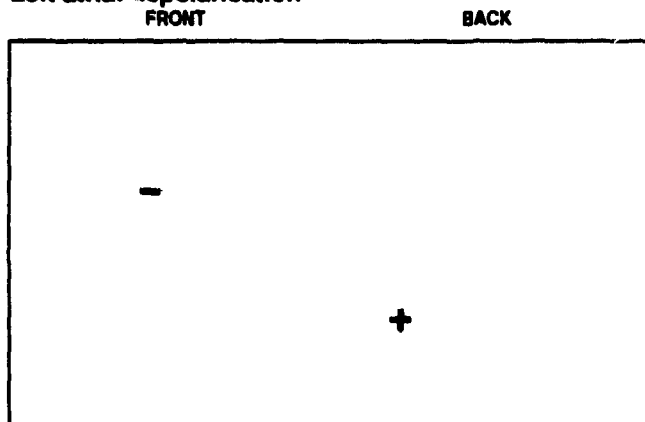


Figure 4.4: Sketches of the locations of extrema during the PR interval. These sketches reflect the approximate locations of extrema during particular phases or events during the PR interval and serve as reference to features to be highlighted in subject data.

component of atrial current flow.

Concurrent right and left atrial activation in MFM plots

As the depolarisation wave spreads into the left atrium, the magnetic field maps show an initial rotation (clockwise or counter-clockwise) of the pattern (56 ms of Fig. 4.1 and 48 ms of Fig. 4.3). In most subjects, this is followed, starting on average at about the 65 ms mark, by a sequence of multipolar maps. The 72 ms map in Fig. 4.1 and 66 ms map of Fig. 4.3 are representative of this pattern. This time also corresponds to a minimum amplitude in the measured magnetic field. In some subjects (7) where this multipolar magnetic field pattern did not emerge, the maximum P-wave amplitudes and/or S/N levels were below the average levels.

After this time, a negative field is found in two regions. First, a minimum appears at the superior border of the maps (84 ms in Fig. 4.1). Sometimes concurrently (84 ms in Fig. 4.3), but often later, a second minimum appears on the left border of the grid (96 ms in Fig. 4.1). These two minima both straddle the same larger, positive peak found near the centre of the map. These two distributions are sketched separately in Fig. 4.4b and Fig. 4.4c. This positive peak can be larger than the peak positive fields measured during the onset of the P wave.

Within the context of the ECD, the magnetic field maps at ~ 65 ms and later suggest the presence of at least two simultaneously active sources. The minimum at the top of the map, along with the positive region in the centre (as in Fig. 4.4b) are consistent with the depolarisation of the left atrium (LD). The minimum at the lower left of the maps, with the positive centre (as in Fig. 4.4c), probably represent right atrial repolarisation (RR). In the BSPM maps, it was not possible to specifically deduce the presence of these two sources.

Repolarisation in MFM and BSPM plots

When all depolarisation ends, and only repolarisation remains, the usual pattern which emerges is similar but opposite in polarity, to P-wave onset in both MFM and BSPM plots (8 ms in Fig. 4.1 and 12 ms of Fig. 4.3), suggesting that this pattern reflects primarily RR. The repolarisation pattern appears at 108 ms of Fig. 4.1, 128 ms in Fig. 4.2 and 120 ms in Fig. 4.3 and is opposite in polarity to Fig. 4.4d. It generally remains stable until Q-onset (ventricular depolarisation). In a very few cases, where the PR segment was longer and the S/N was sufficiently high, the minimum in the late PR segment of the BSPM plots migrates onto the back (right of map). This pattern is found in the 164 ms map of Fig. 4.2. It is similar in distribution, though opposite in polarity, to late P-wave activity (84 ms in Fig. 4.1 and opposite polarity of Fig. 4.4e), hence possibly reflects left atrial repolarisation (LR). A correlation with late P wave was not possible in the MFM.

Deviations from these general observations

These PR-interval distributions describe all but 5 of the 30 sets of maps examined. In Figure 4.5 are presented 2 maps during P-wave onset for subject RK156 (normal male, 40 yrs, P-wave 80 ms, PR-interval 156 ms). The onset map at 10 ms is consistent with early RD, but this pattern changes within 10 ms to a distinctly different and stable distribution in both the MFM and BSPM plots. Though the maps in all 5 of these subjects were not necessarily similar, they all had a common feature: at some time in the P wave, the positive potentials, usually found exclusively in the lower portions of the map, would extend superiorly, to the upper border. The MFM plots were suggestive of a larger ECD component in the X-direction than in other subjects. These differences are reflected in the MFM and BSPM plots at 26 ms of Fig. 4.5. The ECG tracing of lead aVF, during this interval, for these subjects was also consistently different from the main group of 25.

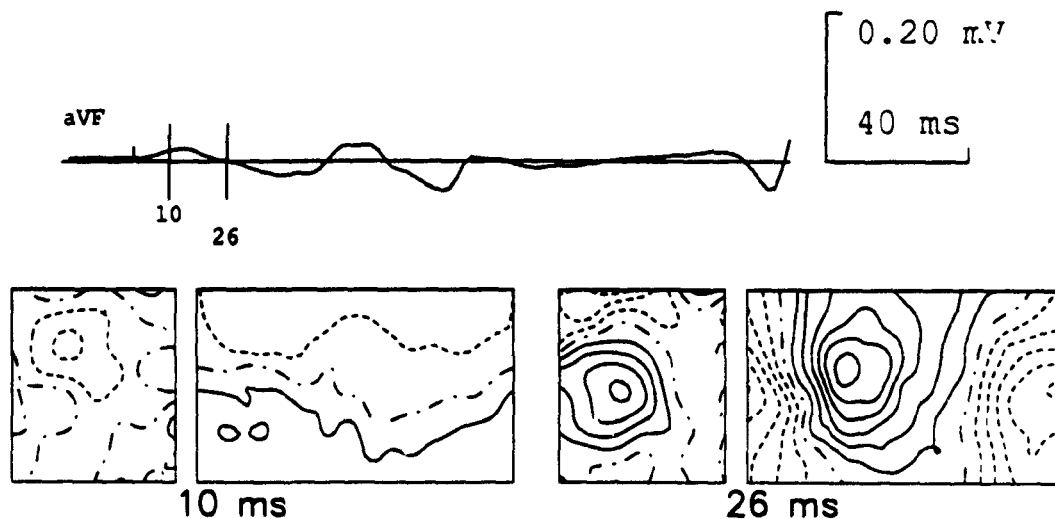


Figure 4.5: Isofield contour maps of early P wave for subject RK156. MFM and BSPM contours have been drawn every 0.1 pT and 0.005 mV, respectively.

4.3.2 Signal durations, peak amplitudes and locations

The average P-wave duration of the study group was 91.87 (SD 14.45, range 64–132) ms and PR-interval duration was 185.77 (SD 57.43, range 135–350) ms. Table 4.1 compares MFM and BSPM averages for all 30 subjects of 5 additional features. Shown in Figure 4.6 are the locations of the peak P-wave signals on the measurement grids. These results can be compared to previously published data. In Table 4.2, P-wave

	$t_{P_{pos}}$	$ P_{pos} $	$t_{P_{neg}}$	$ P_{neg} $	$\frac{ R_{-max} }{ P_{-max} }$
MFM	0.59 (0.21)	0.855 (0.429)	0.43 (0.13)	1.478 (0.746)	11.15 (4.17)
BSPM	0.49 (0.10)	77.48 (18.69)	0.54 (.09)	90.67 (26.30)	19.62 (5.63)

Table 4.1: Comparison of MCG and BSPM P-wave signal amplitudes. Entry definitions are given in the text on page 78. Averages are tabulated for all 30 subjects. Standard deviations appear in brackets (SD). Amplitudes are given in pT (MFM) and μ V (BSPM).

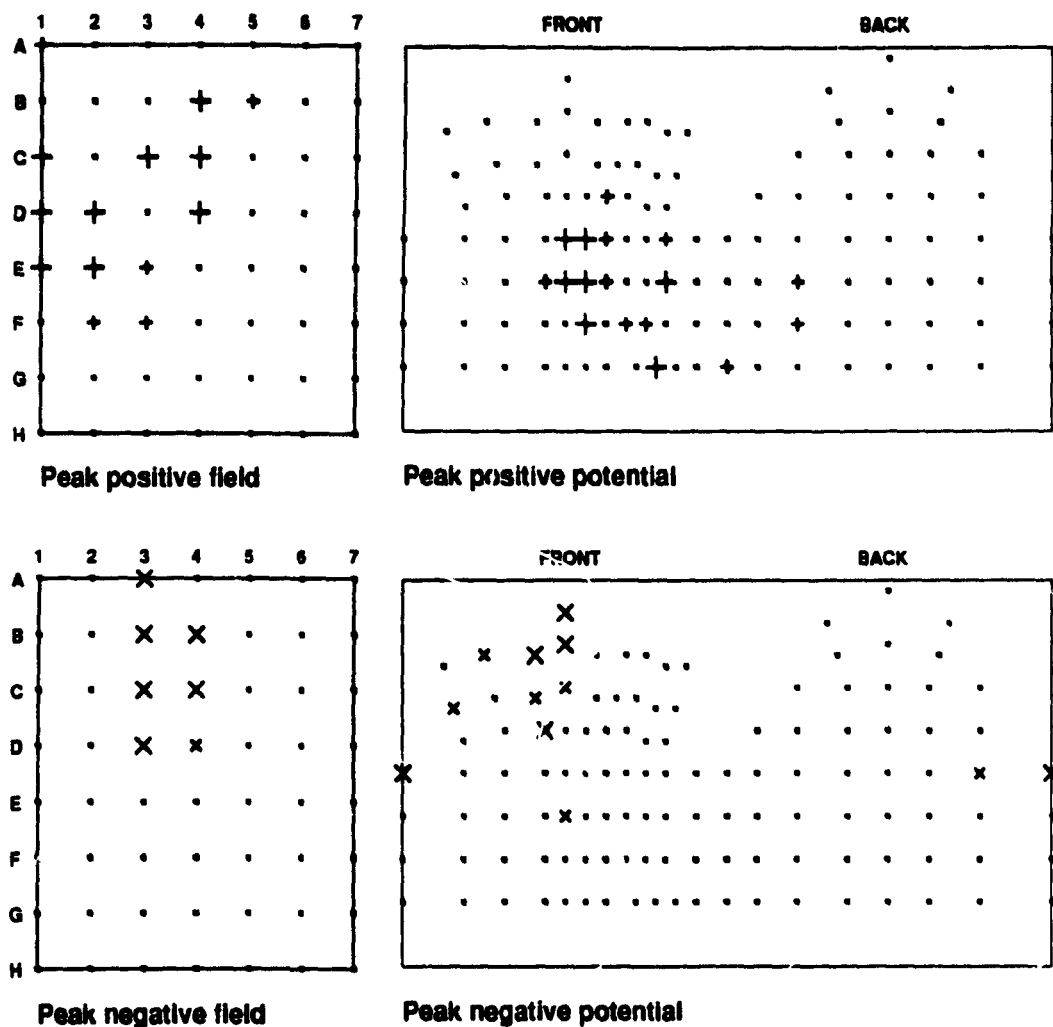


Figure 4.6: Locations of peak magnetic fields and potentials during the P wave. The magnetic field locations are shown to the left and BSPM locations to the right. Positive peak locations are plotted in the top figures with crosses (+) and negative locations in the bottom with x's. Small symbols (+ or x) correspond to a single occurrence, while 2 or more occurrences are represented by larger symbols.

Sex	P-duration (ms)	P_{pos} (V_2) (μV)	P_{neg} (V_{aVR}) (μV)	
Male	106.0 (11.2)	68 (29)	-96 (26)	Mean (SD)
	(84 - 128)	(24 - 134)	(-153 - -47)	Range
Female	104.0 (12.9)	64 (22)	-98 (23)	Mean (SD)
	(78 - 128)	(0 - 120)	(-148 - -59)	Range

Table 4.2: Normal durations and potential peak amplitudes.

Data taken from reference [15] are averages for a group (40-49) years. Peak positive amplitudes of standard leads V_2 and V_{aVR} are quoted since these have the largest positive and negative P waves of the standard 12-lead ECG. The leads are in close proximity to the regions of peak positive and negative P-wave potentials of the BSPM data used in this study.

durations and amplitudes extracted from 12-lead ECG measurements for a group of ~ 190 caucasians, aged (40-49) years, are presented [15]. P-wave magnetic field peak amplitudes of 1.24 (0.37) pT and -1.84 (0.70) pT have been reported by Takeuchi et al. [102] for a group of 60 normal (japanese) adults. These results agree reasonably well with this study, but it is noted that the MF amplitudes can vary in different studies, since the signal amplitudes will depend on magnetometer design and distance to the heart

The peak negative magnetic field (P_{neg}) is found to occur ($t_{P_{neg}}$) consistently in the early phase of the P wave, in locations A3, B3-4, C3-4, and D3-4 (Fig. 4.6). The peak positive fields (P_{pos}) are found to be more distributed both spatially and in time ($t_{P_{pos}}$). Locations at A1, C1, D1-2, E1-3 and F2-3 correspond to the early phases of the P wave during RD. Peak positive fields at locations B4-5, C3-4, and D4 occurred generally later in the P wave, during simultaneous LD and RR. Again, these locations will depend on specific gradiometer design. A longer baseline will measure maxima which are further apart, while a 2nd order gradiometer pulls the extrema closer together relative to the 1st gradient (see Appendix D for further discussion of the field pattern dependence on gradiometer design).

In their normal group, Takeuchi et al. [102] found peak negative fields in similar

locations as we have, at 56.9 (15.2) ms after P-wave onset. Their peak positive field also occurred later than the negative field, at 69.6 (23.1) ms, but was located only in the central area of the grid. Their peak positive fields correspond to the later phases of the P wave, during simultaneous LD and RR. They did not find a clumping of peak positive fields in early P wave in normal subjects, as we have, but did associate peak fields in these locations (i.e. our columns 1, 2 and 3) as a discriminator between normal and atrial overload subjects.

The distribution of peak positive (P_{pos}) and negative (P_{neg}) potentials on the torso of normals varies somewhat more in the BSPM data. The peak positive locations were found distributed primarily on the anterior torso surface (lead numbers 26, 33, 34, 40, 41, 42, 46, 47 of Fig. 1.7), either side of the sternum, at or below the level of the 4th intercostal space (Fig. 4.6). Ten additional common locations are found further left parasternally (leads 56, 63, 64, 68, 69, 79), with 2 occurring on the posterior surface (or right side of the map at locations 88 and 89). The average time of occurrence for the peak positive potentials in the latter group of 10 subjects is 0.59 (SD 0.11), suggesting that this peak is reached later in the P wave. The peak negative potentials (P_{neg}), with the exception of 4 subjects, occur on the upper right anterior chest (leads 9, 15, 22, 23, 24, 29, 30, 31) and generally appear later than the positive peaks. The 4 exceptional subjects are part of the same sub-group of 5 which includes RK156. Stilli et al. [103], in a group of 36 normal adults found a similar distribution of peak potentials, including a large dispersion in locations of the peak positive potentials onto the posterior surface during late P wave. The occurrence of the peak positive magnetic field and peak negative potentials on the outer edges of the recording areas indicates that P-wave mapping with either system would be improved if the maps were extended further into these regions.

The ratio of absolute maximum values of R wave to P wave ($\frac{|R-max|}{|P-max|}$) was found to be significantly greater (1.7x) in the BSPM data (Student's t-test, $p > .005$), suggesting a relatively larger MFM sensitivity to P waves than to R waves, as compared to BSPM measurements.

4.4 Discussion

Only a limited number of reports of body surface potential distributions of atrial activity appear in the literature [101,103,104,105,106] and even fewer magnetic field summaries exist [102,107,108,109]. The results of this study agree with these previous works, but with both MFM and BSPM data available, new insights are presented.

4.4.1 P-wave onset and the pacemaker complex

The progress of atrial excitation from the right atrium to the left is well documented [110,111], although the exact mechanism by which this occurs is still under debate [112,113,114]. Cardiac activation, in a simple presentation, begins at the S-A node. The concept of a single localised activation site however is quite simplistic. Boineau et al. [110] have defined the pacemaker site as a distributed unifocal or multifocal complex, not a single localised site. They found a predominant clustering of pacemaker complexes, under normal sinus rhythm, along the sulcus terminalis and superior vena cava-right atrial (SVC-RA) junction in the upper posterior right atrium. A smaller number of other common locations were located at extreme inferior and anterosuperior locations.

Although P-wave onset MFM and BSPM patterns are quite similar in most subjects (first maps in Figures 4.1, 4.3 and 4.5), subject-to-subject variations throughout the P wave suggest that a wide spectrum of depolarisation pathways exist. These variations support, in particular, different pacemaker locations and varying onset times of LD relative to RD. In particular the sub-group of 5 subjects, such as RK156 (Fig. 4.5), showed marked differences from other subjects in MFM and BSPM depolarisation maps during short segments or through most of the P wave. RK156 is one of two subjects during which most P-wave maps were dramatically different from the main group. The pacemaker sites in these 5 subjects are probably located at one of the extreme, but not uncommon locations indicated by Boineau et al. [110].

Given that the pacemaker complex is located almost exclusively in the right

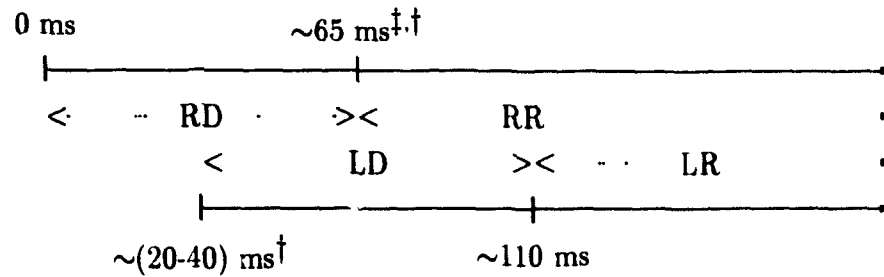


Figure 4.7: Sketch of the timing of atrial activation.

The relative times of right and left atrial activation are sketched. (RD = right depolarisation, LD = left depolarisation, RR = right repolarisation, LR = left repolarisation.) † - as suggested by Boineau et al. [110] work ‡ - as deduced from this work.

atrium, a predictable sequence of atrial activation and recovery should exist. According to Boineau et al. [110], and as is summarised in Figure 4.7, this sequence should be right depolarisation followed by right repolarisation, with left depolarisation beginning anywhere from 20 ms to 40 ms after RD onset (P-wave onset). Left repolarisation will follow LD. The degree of overlap of RD and LD will vary from person to person.

4.4.2 Spatial discrimination of LD and RR

The multipolar pattern occurring at approximately 65 ms in MFM data was a particular feature found in many subjects. With consideration of MFM patterns before and after this time, it is postulated that this event marks the end of RD and the beginning of RR. Schematically, this process is demonstrated in Figure 4.4 where the sum of frames a+b undergo a transition to form the combination of frames b+c. Regions of positive magnetic field in maps preceding ~65 ms are replaced by the negative fields associated with right repolarisation forces. The opposite change occurs in previously negative regions, with the exception of a small area on the upper edge of the grid. This persistent minimum is associated with LD. The central positive magnetic field, established after this transitional period (from ~65–110 ms), results

from the combined fields of LD and RR (Fig. 4.4b+c). In some cases, as in RF108 (84 ms of Fig. 4.1), either of the two minima can be missing, probably because of the limited size of the magnetic field measuring grid.

Epicardial potential and isochronal maps of atrial activation and recovery [106, 110] makes it possible to measure directly left atrial depolarisation and right repolarisation. The smoothing effect of the torso volume conductor on the potentials and magnetic fields measured at the body surface [66], however, reduces the ability to discriminate between the RR and LD sources.

Despite these smoothing effects, because of the relative proximity of the right atrium and the large distance of the left atrium to the planar measuring grid RR can be detected particularly well with the gradiometer in MFM data. Electrodes placed on the torso surface are at a similar distance to both atria. The right and left atrial depolarisation currents are then sensed equivalently and right repolarisation currents are usually masked by the larger LD signal.

Also, there is a relatively lower sensitivity of the magnetic field measurements to p_z (atrial currents flowing toward the gradiometer), hence mainly currents flowing parallel (p_x and p_y) to the magnetic probe are recorded. Since the right and left atria are separated by a few centimeters, this can result in two spatially separated parallel currents originating from each of the two atria. The opposing currents flowing during RR and LD result in clearly separated negative magnetic field components from each atria.

4.4.3 Sensitivity of MFM to atrial activation

It is interesting that the resolution of RR and LD also means that the pattern with a central negative magnetic field measured before the transition from RD to RR (before ~ 65 ms) can be interpreted as the sum of the minimum associated with RD and the positive maximum resulting from the superiorly and posteriorly located LD source (e.g. Fig. 4.4a and b). The onset of LD (after $t > 20$ ms) results in a decrease in the peak negative magnetic field while the peak positive potentials may continue to

grow. Despite this effective decrease in the maximum measured magnetic field, the relative size of the P-wave magnetic field is larger than in BSPM measurements, as compared to the size of the ventricular QRS complex (see Table 4.1).

This result further supports the suggestion made by Spach and co-workers [115] that there are significant tangential atrial currents – to which the BSPM measurements are less sensitive [116]. However, the relative insensitivity of MFM measurements to the left atrial currents suggests that MFM recordings should not be used exclusively for studying the PR interval. The apparently equivalent sensitivity to the LD and RR sources here could cause confusion. In most subjects, it was virtually impossible to obtain a clear P-wave offset time using MFM data, particularly because of the coincidence of the positive fields of LD and RR. This problem is further enhanced if either of the two negative extrema go undetected, because of the size and position of the measurement grid relative to the atria

4.4.4 Atrial repolarisation

P-wave offset is generally followed by a distribution consistent with repolarisation. This pattern correlates well with the early P-wave maps, hence right depolarisation, but is opposite in polarity. This finding is not unexpected since experimental epicardial measurements have demonstrated that the atrial regions which depolarise first will be the first to repolarise [111]. Descriptions of the repolarisation process in body surface measurements [103,105] suggest that the repolarisation phase is characterised by a stable pattern, in which the negative extremum is sometimes seen to migrate slightly to the left of the body. A similar leftward migration of the positive extrema during the P wave, resulting from a growth in LD currents and decrease in RD, leads to the conclusion that the BSPM map at 164 ms of Figure 4.2 may represent left atrial repolarisation. This pattern was found only in a few subjects with longer PR intervals. The MFM distributions at these same times, do not correlate with LD. They continue to resemble either RR, some intermediate pattern between LR and RR, or, at times, lose any dipolar features as S/N levels decrease significantly. The

explanation for this observation may be that since the LR sources are relatively far from the magnetic sensor and small in amplitude, only residual RR signals will be detected.

4.4.5 Final comments

The simultaneous analysis of MFM and BSPM PR-interval distributions has allowed further insight into the complementary nature of the body surface magnetic fields and electric potentials of the atria, and suggests potential for future research. Results of this study could be pursued to further the effort toward understanding the cardiac atrial activation process.

The use of MFM measurements may be particularly useful to determine complete right atrial depolarisation times non-invasively (estimated to be ~ 65 ms from these measurements). This would be facilitated with an expanded measurement grid to the right and superior aspect of the torso, since in some subjects the limited size of the grid, in relation perhaps to larger torsos, does not allow one to record the minimum fields associated with RR. It is interesting to note that the Dalhousie MCG grid, because of its larger size and fixed dimensions, in most subjects covers a greater area of the anterior torso surface than the Finnish standard grid [107], which is used by all other biomagnetism groups.

The greater spatial resolution of magnetic field measurements to right and left atrial depolarisation suggests that MFM studies may be more sensitive to changes in maps due to right and left atrial overload. This topic has already been pursued by Takeuchi et al. in a number of related papers [102,108,109]. However, we note that comparison of their results with the present study suggests that their results, originating from analysis of the locations of peak field values, should be reconsidered. We have a number of normal subjects with peak negative fields in locations which they associate with atrial overload. These sites were probably found because of the fixed grid size used in our study. How much their results would have differed with the use of a larger grid area will not be suggested. The analysis may, after

reconsideration, be appropriate since the increased depolarisation signal occurring from atrial hypertrophy could translate not only in an increase in signal amplitudes, but also from a shift of the peak fields, because of a different balance in the combined right and left sources.

Despite similarities in the MFM and BSPM data of most subjects, the 5 exceptions to the main group indicate that body surface magnetic or potential measurements reflect variations in the location of the natural pacemaker complex. MFM and BSPM measurements could possibly be used to determine the location of the natural pacemaker complex. Because of the localised aspect of the depolarisation currents at the pacemaker site and during initial right atrial activation, it would be reasonable to model these sources as single current dipoles. The impediments to this kind of study are numerous, but not impossible to overcome. A decrease in the noise level, particularly in the MFM measurement, is necessary. An expansion of the measurement grid and lead system in the upper right torso regions would ensure that both extrema are recorded during right depolarisation. The repeated occurrence of peak negative potentials and positive magnetic fields at extreme edges of the grids (Fig. 4.6) suggests that the true extrema may be missed by the present BSPM electrode placement and MFM grids. And most importantly, realistic torso geometries would be needed for optimal results.

Finally, it is proposed to model atrial activation and recovery with two current dipoles. As such it may be a useful exercise to apply multiple current dipole inverse solutions to the PR interval. A combined magnetic and electric inverse solution may fare quite well in solving this problem given the complementary nature of the distributions found.

5 Extraction Techniques Applied to PR-segment Events: I. His-Purkinje System

5.1 Introduction

Conduction of activation currents from atria to ventricles of the heart (which are otherwise electrically isolated) is made possible by the atrio-ventricular (A-V) node and the His-Purkinje conduction system (HPS). Excitation of the heart is initiated at the sino-atrial (S-A) node, located on the posterior surface of the right atrium (RA) (see Figure E.1). The currents propagate through the right and left atria and will eventually reach the A-V node found in the posterior right atrium. The slowly conducting (5 cm/s) cells forming the A-V node will typically delay the passage of currents to the HPS for approximately 110 ms. The slow conduction through the A-V node ensures efficient pumping action of the heart, by preventing simultaneous atrial and ventricular contractions. Ventricular excitation will occur only after the currents at the A-V node are allowed to pass to the ventricles via the structures forming the His-Purkinje system: the common bundle or His bundle (HB), left and right bundle branches, and Purkinje fibre network. Conduction velocity through the fine filament of tissue forming the His bundle accelerates to ~ 1 m/s. The branches of the common bundle arborise to the right and left ventricles via a network of Purkinje fibres, which almost completely cover the walls of the ventricular chambers. The speed of conduction through the HPS establishes fast and efficient depolarisation of the entire ventricular mass in less than 110 ms in the normal myocardium.

The time of electrical conduction from the His bundle to the onset of ventricular depolarisation, in the absence of cardiac disease, is effectively constant in normal human subjects (43 ± 12 ms [117]). In the case of disease (that affects the HPS),

the ability to record the onset of His activity helps to determine the nature and origin of conduction disturbances. Unfortunately, the small size of the HB does not allow one to record this signal in a standard ECG (see Figure E.1). In fact, classically the interval from end of P wave to R-wave onset is considered isoelectric. The signal originating from the His bundle remained effectively undetectable until 1969, when Scherlag and co-workers [118] described a method for consistently recording the electrical activity of the HB in man. This routine procedure, used still today in hospitals during cardiac electrophysiological studies (EPS), involves inserting a recording catheter percutaneously into the right femoral vein and advancing it with the aid of fluoroscopic images into the right atrium.

The first attempts to record HPS activity at the body surface were made shortly afterwards by Berbari et al. [119] and Flowers et al. [120] in 1973 and 1974. Their techniques relied on high-gain amplification, selective bandpass filtering, and signal averaging applied to a selected number of optimal surface leads. The success in recording the His bundle signal at the body surface marked the beginning of high resolution electrocardiography (HRECG). These advances in HRECG occurred at the same time that magnetic field recordings of the heart were made feasible by advances in SQUID technology [8]. The first magnetocardiographic (MCG) studies of the HPS by Farrell et al. [95] appeared in 1978.

By the early 1980's, the HRECG and MCG recordings of HPS became generally accepted. The information extracted from these recordings was twofold. In Berbari et al. [119] and Flowers et al. [120] much of the emphasis was on high-frequency spikes found in the PR segment, revealed after high-pass filtering averaged data, with a filter setting varying from 10 Hz to 80 Hz. These waveforms, only of a few microvolts in amplitude, are associated with the conduction of current through the His bundle and allowed one to determine a His-to-ventricular (H-V) conduction time non-invasively. Further work by Berbari et al. [121] and by researchers in the bio-magnetism community [95,96,122] focussed interest on the low-frequency ramps, and 'bumps' superimposed on these ramps, measured during the PR segment. The ramps,

and associated features, were associated with the depolarisation of the conduction system, with the bumps arising perhaps from sudden changes in the direction of the conduction wavefront. This last belief was supported by measurements on subjects with bundle branch block [119], where more marked departure from smooth ramps, relative to normal conduction, was detected.

When high resolution body surface mapping became available, efforts in HPS recordings turned toward the detection of spatial features of the His-Purkinje system [76,77,78,79]. One particular interest in mapping the HPS stems from a belief that the small, localised structure of the His bundle could be reasonably modelled with a single-current-dipole source. Measurements of the spatial features of the HPS could then be used to test and validate current dipole inverse solutions.

The results of these studies were not immediately accepted. The particular issue which arose early, and is still debated, is the degree to which atrial repolarisation (Ta) also contributes to the signals and ramps recorded during the PR segment. In magnetocardiographic measurements, another reason to attempt to map the signal recorded during the PR segment, stemmed from the belief that, although Ta and HPS ramps could perhaps not be separated, their spatial features might be sufficiently different to achieve this goal. These spatial differences may be enhanced by the increased spatial sensitivity of the magnetic recording systems.

At one end of the spectrum, there is published work which supports the claim that the ramp pattern could be associated entirely with atrial repolarisation [123]. However, more recent work by Leiniö et al. [124] provides convincing evidence that the HPS is detectable at the body surface. These studies involved MCG and/or ECG recordings on subjects with A-V block. In the first case [123], the authors were able to successfully match the PR-segment ramp patterns of normals to the early PR segment (only Ta) of subjects with 1st degree A-V block. The conclusion drawn from this match was that the PR segment in normals contained no HPS signal. With exceptionally low noise levels ($4.5 \text{ fT}/\sqrt{Hz}$ and $< 1 \mu V_{p-p}$) the Finnish group [124] recorded a ramping signal just before Q-onset, in a subject with total

A-V block. Since atrial and ventricular events are disassociated in these subjects, an average of QRS complexes without overlapping atrial activity on the HP signal could be created. The ramp, associated with bundle branch and Purkinje fiber activity, reached a maximum of 0.2 pT and 5 μ V before Q-onset. The dipolar contour maps (BSPM and MFM) of this signal are consistent with what is expected from the depolarisation of the conduction system.

An earlier, similar study on individual MCG waveforms by Mäkijärvi et al. [125] suggests that the Ta to HPS signal ratio is ≤ 5 . Although Leiniö et al. [124] successfully mapped the bundle branch pattern, the signal was weak and its detection required the most sensitive instrumentation available. Only in a few locations was it possible to detect the magnetic HPS activity in real time; averaging had to be used to improve the signal to noise ratio.

Given the level of confusion and uncertainty, it is still questionable under normal circumstances (i.e. in normal subjects and in a noisy environment) that the ramps measured in the PR segment can be successfully identified and separated into Ta and HPS components in body surface potential and magnetic field maps.

Numerous authors recognise that the Ta signal contributes to the PR segment. Thus working on the premise that the HPS and Ta signals are both recorded, various techniques for separating the two sources [76,78,79,99,126,127] have been developed.

Despite many publications dealing with the non-invasive detection of HPS, magnetically and electrically, the degree of contribution of the Ta and HPS signals to the PR-segment signal has not been established unambiguously. It follows then that the separability of these two sources is still debatable.

In Chapter 3 the various signal-extraction techniques used by different authors [3,76,77,78,79,94,99] to separate the atrial repolarisation (Ta) and HPS signals are presented. The 4 techniques (Temporal Averaging (TAT), Correlation (CT) and two orthogonal expansions: Karhunen-Loève (KLT) and Singular Value Decomposition (SVD)) were explored through simulations to determine limitations and understand how the techniques may be related. Inquiry into the nature of atrial activation and

recovery in BSPM and MFM data was presented in Chap. 4. The question of spatial separation of the HPS and Ta sources will be re-examined in the present chapter by applying the different signal-extraction techniques to BSPM and MFM data and comparing the results. These results will be evaluated and discussed with particular attention given to the electrophysiology of the sources in question and mathematics behind the various extraction techniques. With this approach, we hope to obtain conclusive evidence as to the recordability and, in particular, the spatial separability of the Ta and HPS sources in the PR segment.

5.2 Method

The BSPM and MFM data as described in Chapter 4 (PR-interval mapping) were used in this study. Amongst the 30 subjects available for study were 6 subjects with A-V block. These patients were considered necessary to confirm our results, since in this group the atrial repolarisation may be considered completed before HPS onset.

In addition to BSPM data recorded with the 125 Hz low-pass filter already studied for this group, 0.05–250 Hz filtered data was examined for some subjects. This data was used to answer a number of questions which arose when comparing our results to other studies [76,119,121] performed using a wider bandwidth than our standard protocol.

Following the theory outlined in Chapter 3, the four signal-extraction techniques were applied to the 30 subjects. Measurements with better spatial S/N were examined and studied more closely. The background signal considered is atrial repolarisation which is expected to be the only source active until (43 ± 12) ms [117] prior to Q-onset when activity due to the superimposed source (HPS) begins (see Figure 3.1). Amongst the subjects used for this study, the PR-segment duration ranged from 45 ms to 290 ms. This range provided data with a spectrum of overlap of the HPS and Ta sources.

5.3 Results

As an example we present HPS extraction results for one subject (RF108 with PR-segment duration of 80 ms) in Figures 5.1 and 5.2. For these results, the segment -70 to -50 ms relative to R-wave onset was used to characterise atrial repolarisation. This segment is before expected HB-signal onset, thus no HPS signal should be present. The T_a representation was calculated according to Equation 3.1 for the CT and TAT techniques, using Eq. 3.6 for SVD and Eq. 3.19 for KLT. As suggested in Chapter 3 and published previously by us [128], the KLT and SVD expansions produce similar results. This was confirmed in this data, hence the KLT result is not shown. These representations were then applied to the entire PR segment and the residuals were plotted. Shown in Figure 5.1a, b and c are the BSPM residuals to each of these fits, using Equations 3.18 (u_1), 3.5 and 3.3, respectively. Maps at -74 ms, -44 ms and -14 ms relative to R-wave onset are plotted. The equivalent MFM residuals are shown in Figure 5.2.

The BSPM results of Horan et al. [76] were obtained using the correlation technique (CT) and with the T_a representation derived from an approximately 20 ms interval in late PR segment, during concurrent HPS and T_a . The reasons for the different approach will be discussed later. To simulate their result, the interval from -30 to -10 ms relative to R-onset was used to characterise T_a . This representation was then subtracted from the PR segment in an appropriate manner using all four techniques. The result for subject RF108 is presented in Figures 5.3 and 5.4.

In these two results (an early and late PR segment representation of T_a), we have found that all four techniques (SVD, KLT, CT, TAT) reveal very similar, and at times identical, residual patterns for each T_a segment. The MF residual maps at -14 ms of Figure 5.2 (when both T_a and HPS are active) reveal dipole patterns, which are similar to those previously published [3,77,78,79,99], and found to be consistent with a single current dipole representing the HPS source. The sequence of residual BSP maps of Fig. 5.3 are similar to results published by Horan et al. [76] and the BSP

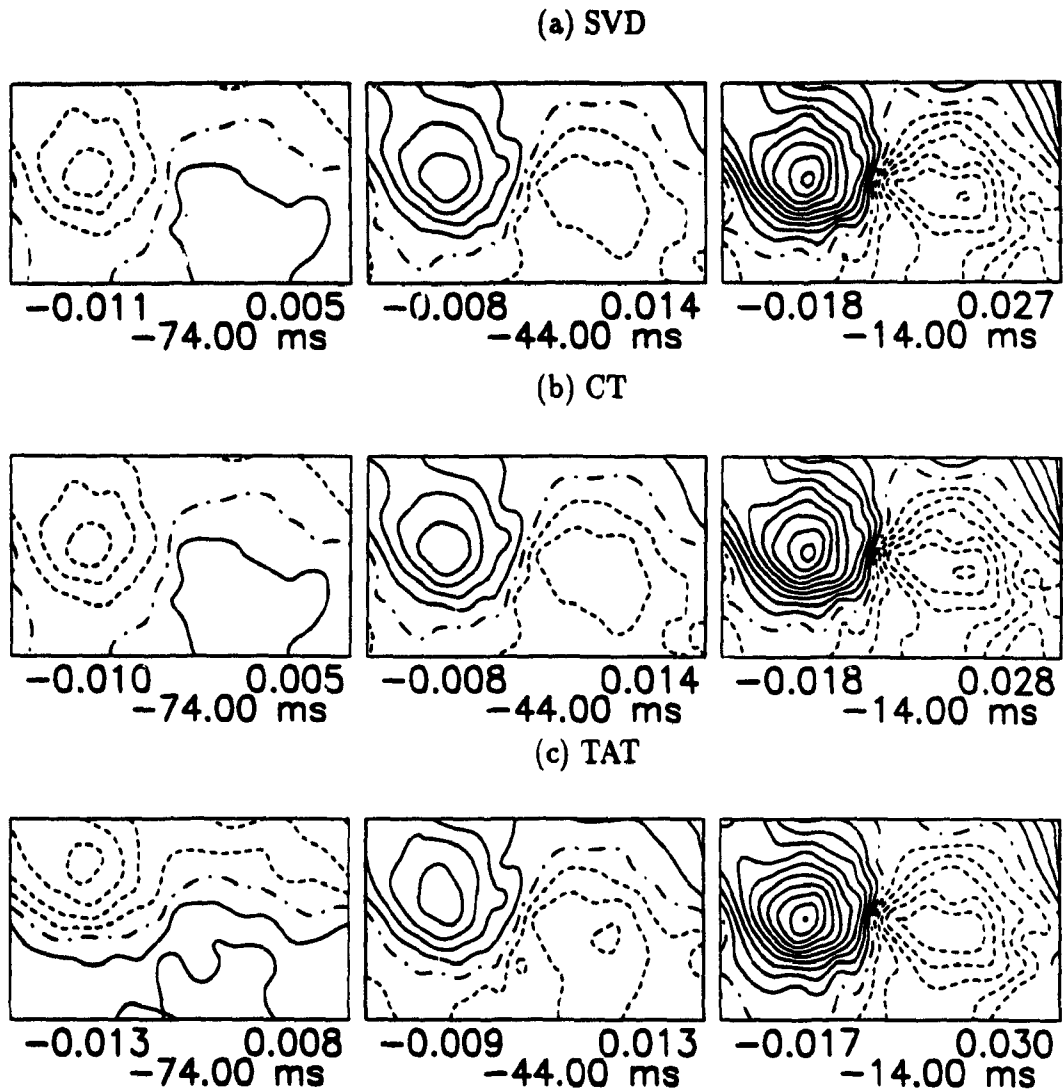


Figure 5.1: BSPM residuals for subject RF108. The SVD (a), CT (b) and TAT (c) residuals resulting from a fit of a Ta representation derived from -70 to -50 ms relative to R-onset are shown at -74 , -44 , and -14 ms before R-onset. Contour steps are $3.0 \mu V$.

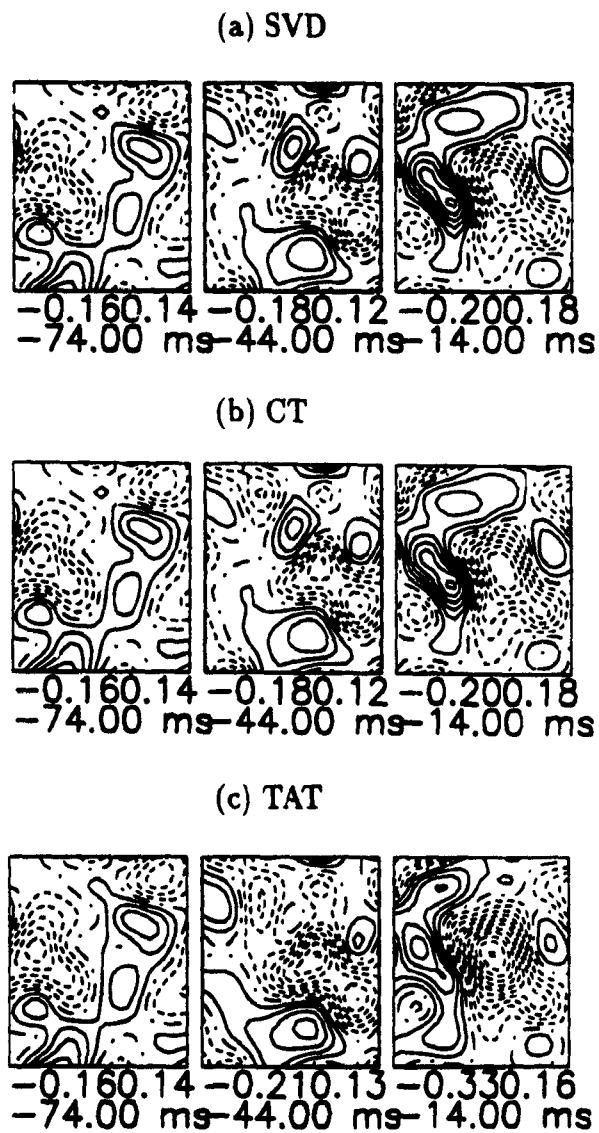


Figure 5.2: MFM residuals for subject RF108. The SVD (a), CT (b) and TAT (c) residuals resulting from a fit of a Ta representation derived from -70 to -50 ms relative to R-onset are shown at -74 , -44 , and -14 ms before R-onset. Contour steps are 30.0 fT.

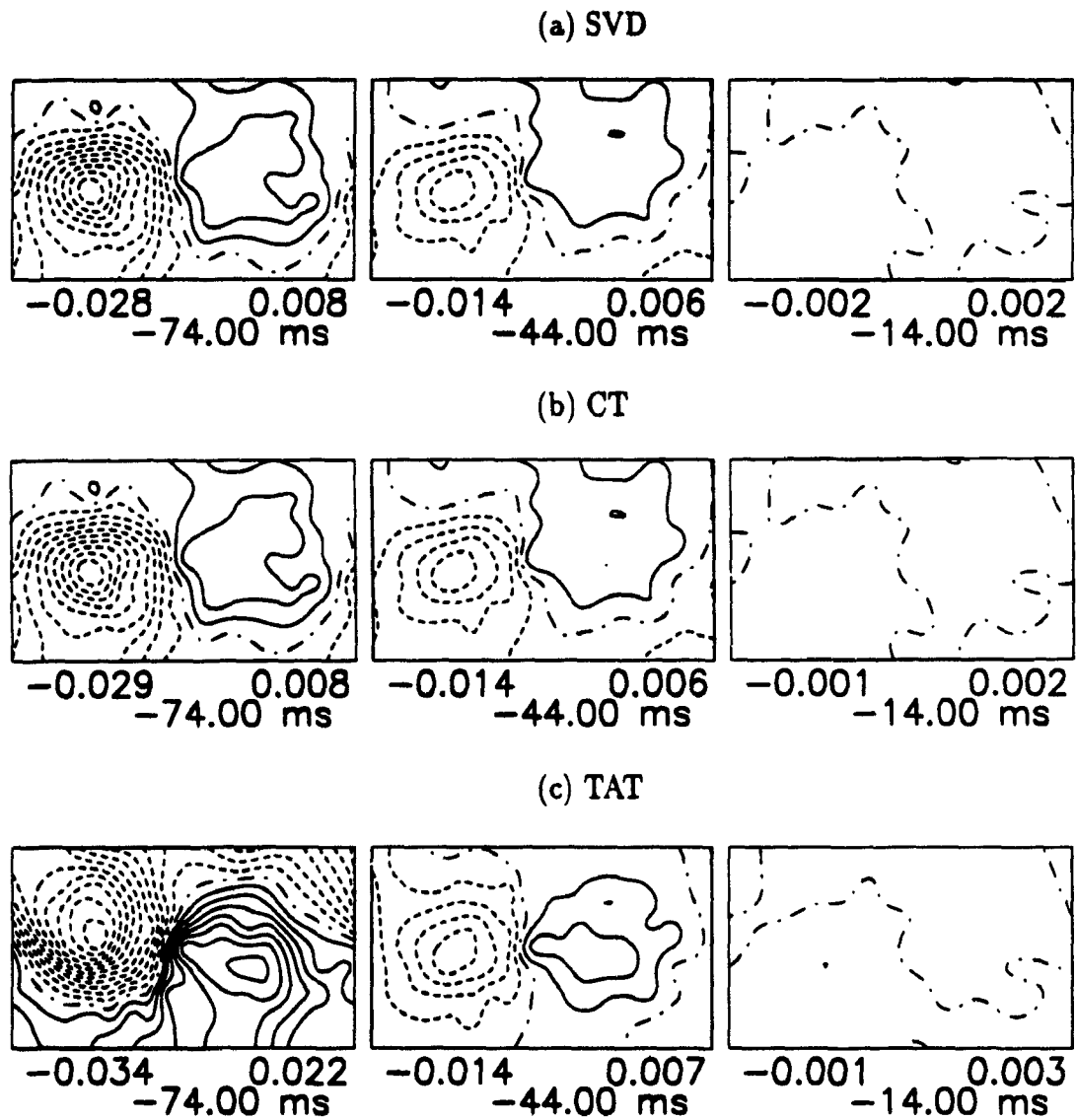


Figure 5.3: BSPM residuals for subject RF108, using a late T_a representation. The SVD (a), CT (b) and TAT (c) residuals resulting from a fit of a T_a representation derived from -30 to -10 ms relative to R-onset are shown at -74 , -44 , and -14 ms before R-onset. Contour steps are $3.0 \mu V$.

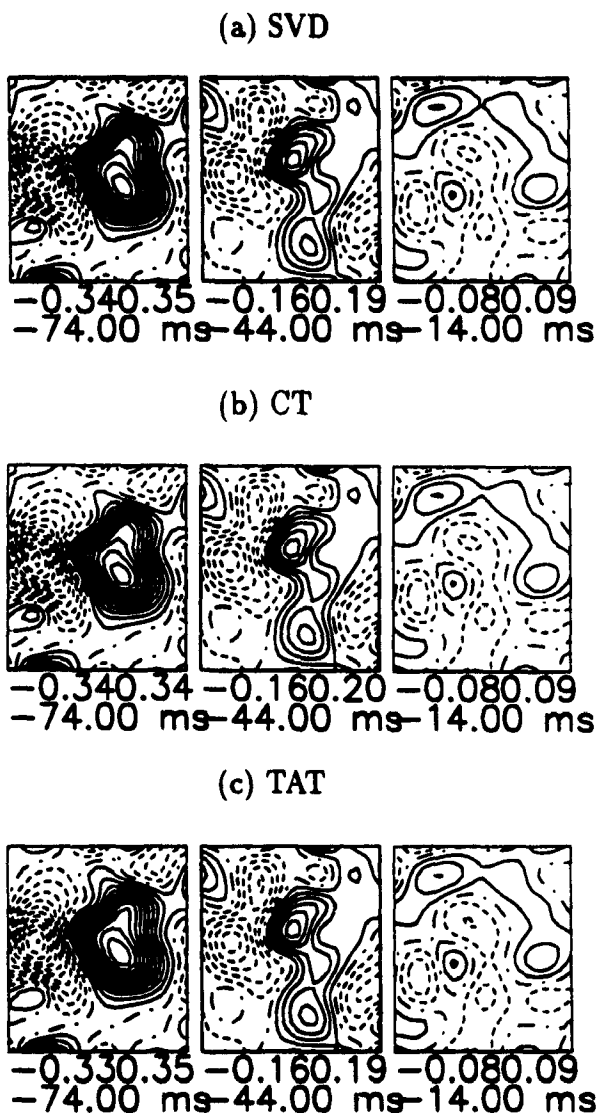


Figure 5.4: MFM residuals for subject RF108, using a late T_a representation. The SVD (a), CT (b) and TAT (c) residuals resulting from a fit of a T_a representation derived from -30 to -10 ms relative to R-onset are shown at -74 , -44 , and -14 ms before R-onset. Contour steps are 30.0 fT.

maps of Fig. 5.1 consistent with Jie and Schoffa [129]. The fact that their results are similar to ours demonstrates that the different techniques used are well understood. However, an alternative interpretation of these results will be presented.

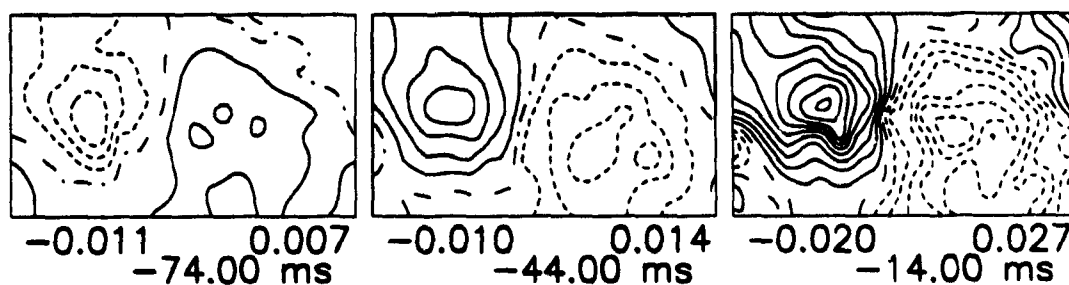
The high frequency cut-off in the previous BSPM results was 125 Hz. To demonstrate differences which might result from the use of a wider bandwidth, BSPM recordings using a 0.05–250 Hz bandwidth (1000 Hz sample rate for 15 s) were also examined in a few cases. One such result (again subject RF108) is presented in Figure 5.5. This recording was obtained minutes before the 500 Hz data. The data is aligned to within 1 ms of the 500 Hz recording, and the same interval was used for characterising early atrial repolarisation (–70 to –50 ms relative to R-wave onset). In this figure only the SVD and TAT results are shown. Comparison of Figures 5.1 and 5.5 show that the two recording bandwidths give very similar residual distributions. The results also show that the measurements and analysis are reproducible.

The results presented for subject RF108 are typical of most subjects studied in this group. A few deviations from this result can be attributed to signal-to-noise levels. In these cases, poor PR-segment maps led to noisy residual distributions.

In a few instances, the residual distributions were different from this example. These were found amongst subjects who had noticeably different P-wave maps, as in the group of 5 subjects discussed in Chapter 4. One such example is presented in Figure 5.6. This is the same subject (RK156) whose PR-interval maps are shown in Fig. 4.5. It is believed that differences in the PR-interval maps in this subject occur as a result of a non-typical natural pacemaker site.

For purposes of the discussion, SVD PR-segment eigenmaps (\mathbf{U}) for 4 subjects are presented. In Figure 5.7, the first two eigenmaps, representing \mathbf{u}_1 and \mathbf{u}_2 , are shown for 3 different PR-segment intervals for subject RF108 (PR-segment 80 ms). In Figure 5.8, the \mathbf{u}_1 and \mathbf{u}_2 for 3 additional subjects (TH175 - PR-segment 245 ms; HS25 - PR-segment 52 ms; RK156 - PR-segment 70 ms) are presented. These subjects were chosen because of the wide range of PR-segment durations represented. The MFM and BSPM \mathbf{u}_1 eigenmaps in all these cases (Figs. 5.7 and 5.8), look like the

(a) SVD



(b) TAT

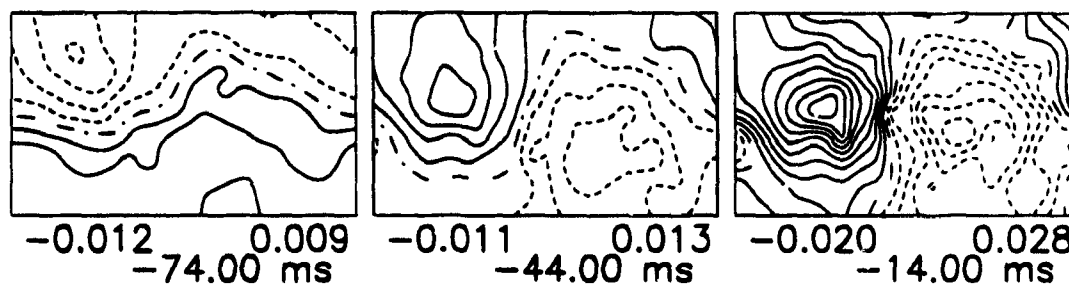


Figure 5.5: BSPM (1000 Hz sampling frequency) residuals for subject RF108. The SVD (a) and TAT (b) residuals resulting from a fit of a Ta representation derived from -70 to -50 ms relative to R-onset are shown at -74, -44, and -14 ms before R-onset. Contour steps are $3.0 \mu V$.

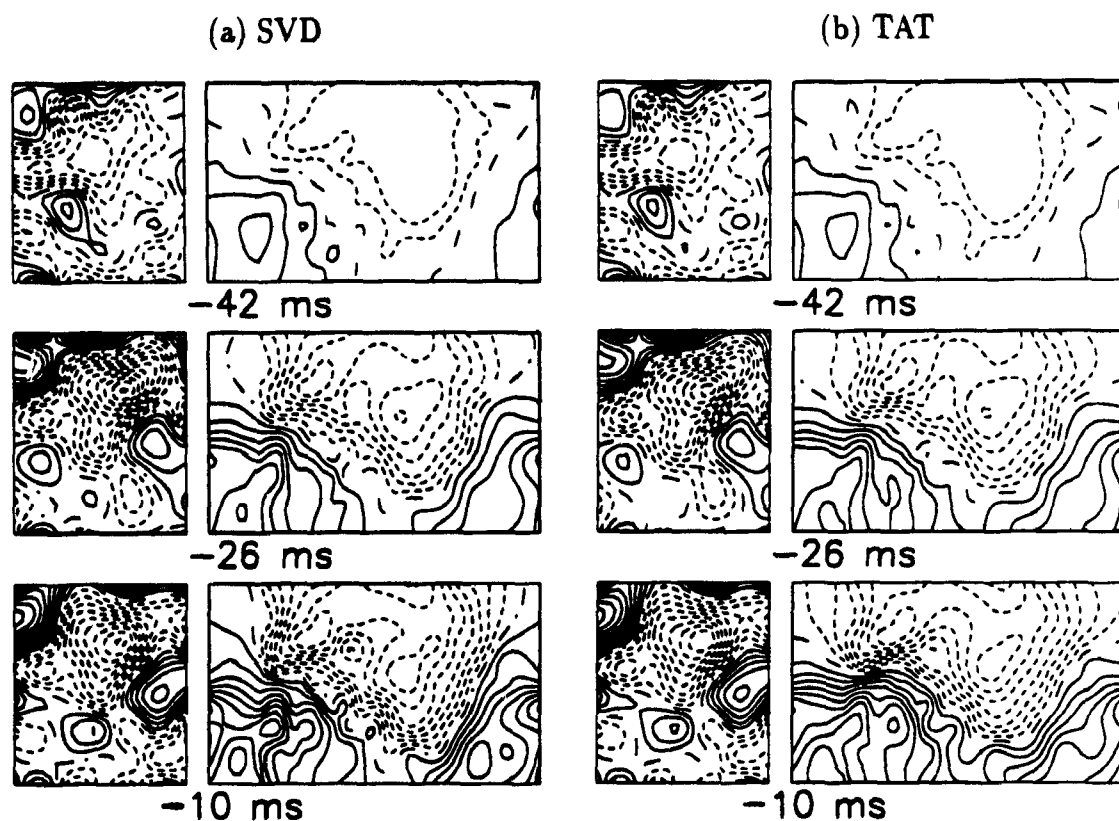
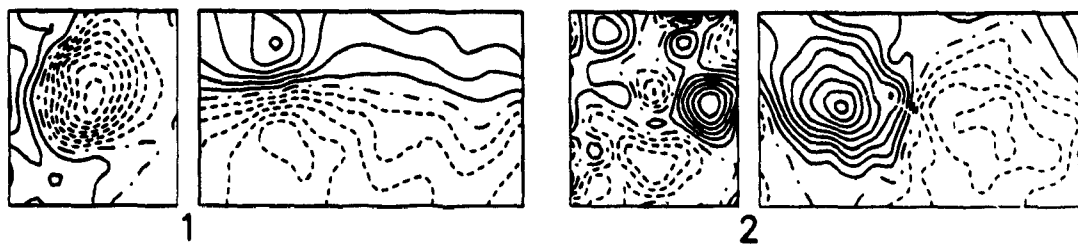
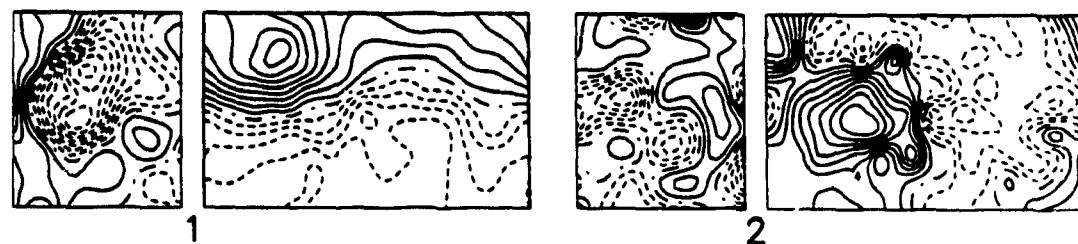


Figure 5.6: BSPM and MFM residuals for subject RK156. The SVD (a) and TAT (b) residuals resulting from a fit of a T_a representation derived from -60 to -50 ms relative to R-onset are shown at -42 ms, -26 ms and -10 ms before R-onset. Contour steps are 30.0 fT and 2 μV .

(a) 10 to 30 ms



(b) 50 to 70 ms



(c) 10 to 70 ms

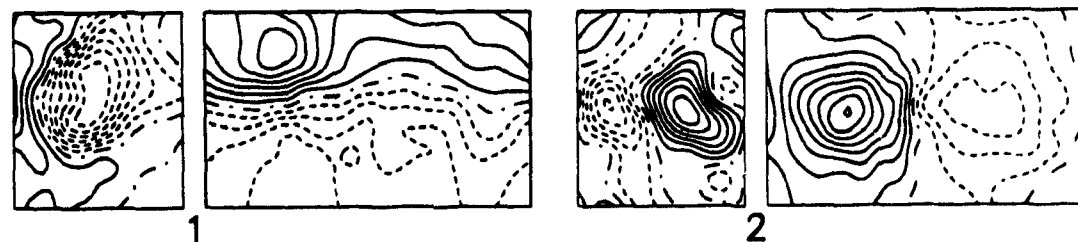
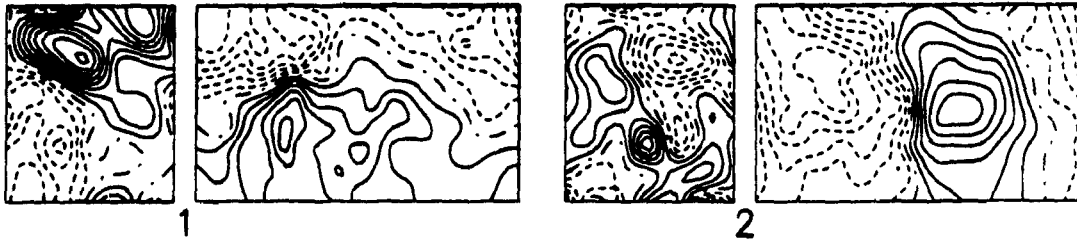


Figure 5.7: BSPM and MFM SVD eigenmaps u_1 and u_2 for RF108. Intervals, relative to P-wave offset, used in the computation of U are displayed above the maps.

(a) HS25 10 to 50 ms



(b) TH175 20 to 100 ms



(c) RK156 10 to 60 ms

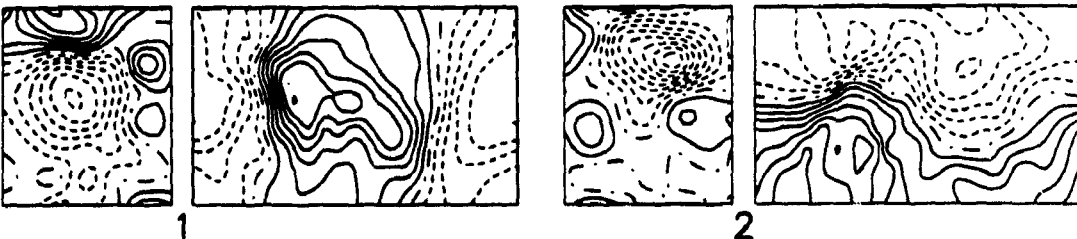


Figure 5.8: BSPM and MFM SVD eigenmaps u_1 and u_2 for HS25, TH175 and RK156. Intervals, relative to P-wave offset, used in the computation of U are displayed above the maps.

dominant PR-segment pattern for each subject. Differences seen in \mathbf{u}_1 's for RF108 between the first two intervals (Fig. 5.7a and b) reflect the changes seen in the PR segment from P-offset to R-onset (see Fig. 4.2). Fig. 5.7c, representing \mathbf{u}_1 for the entire PR segment, is a composite of the entire PR-segment pattern.

The BSPM \mathbf{u}_2 eigenmaps in most cases (i.e. Figs. 5.7 and 5.8a and b) are quite similar. They all reveal a basic separation of the front and back aspects of the torso into regions of opposite polarity. The MFM \mathbf{u}_2 eigenmaps are also dipolar in nature, generally. However, as is seen in the MFM \mathbf{u}_2 eigenmaps of Fig. 5.7, this feature can be obscured by the presence of noise. Noise effects in the BSPM data are reflected by the difference in quality of the BSPM \mathbf{u}_2 eigenmaps resulting from the two short intervals relative to the long interval, consisting of the entire PR segment (Fig. 5.7a and b, versus c). The consistent pattern found in the PR-segment \mathbf{u}_2 eigenmaps in most subjects suggests that the mechanism generating these patterns is common to most people, and *independent of PR-segment duration*. Consequently, these patterns must be associated with a feature persistent over this range for all subjects, which can only be atrial repolarisation.

5.3.1 Interpretation of results

5.3.2 HPS signal amplitude at body surface

Only a small mass of cardiac tissue is contributing to the genesis of the His bundle (HB) signal and there are diverse geometries of the bundle branches (BB) and Purkinje fibre network [130]. These features make it difficult to realistically model the HPS, or hypothesize on the amplitude of signals expected at the body surface. In order to get an appreciation of the amplitude of the potentials which might be measured at the body surface, two approximations of the expected body surface potentials and magnetic fields due to the His bundle were obtained

Body surface His bundle signal size estimates from HB electrograms

The first approximation requires the use of potential values obtained in endocardial HB electrograms (HBE) measurements. This information is not easily found in the literature. Only timing information is of clinical interest in HBE measurements, therefore few amplitude scales are presented with such results. These measurements are most often obtained using bipolar electrodes, placed in proximity to the HB. Without accurate information of recording details, the use of such measurements to estimate surface unipolar signals can only reveal approximate results. We made an attempt at such a calculation, assuming a homogeneous, isotropic volume conductor and ignoring any possible signal variations in the HBE potentials due to measurement conditions.

Defining x_H as the potential measured by the HBE, in close proximity to the HB, the potential for the same source measured at a further distance x_b , can be given as a function of x_H , x_b and V_H , where V_H is the measured His bundle potential. Using Eq. 2.2, we can write

$$V_b = V_H \frac{x_H^2}{x_b^2}. \quad (5.1)$$

Amplitudes of HBE were shown in figures presented by Flowers et al. [120] to be $\sim 300 \mu\text{V}$ peak-to-peak (p-p), while Leiniö et al. [124] show measurements suggesting an amplitude of $25 \mu\text{V}$ (p-p). The distance from the HB to the endocardial recording electrode and the torso surface would be on the order of 1 cm (or less) and 10 cm respectively. Using Equation 5.1 and these estimates, one finds measured potentials at the body surface V_b of the order of $.25\text{--}3 \mu\text{V}$ (p-p).

Body surface His bundle signal size estimates from single strand extracellular potential measurements

A second estimate of the amplitude of the surface His bundle signal can be obtained from extracellular potential measurements at the membrane surface of isolated dog Purkinje strands [34]. In this paper the authors (i) obtained extracellular potential

measurements at the surface of the strand membrane, and (ii) derived a model for determining the extracellular potentials from measured intracellular potentials.

The model assumes an idealised cylindrical geometry for the Purkinje strand, with a radius R_P and an excitation wave propagating along the axis of the cylinder. They showed that the extracellular potentials derived from intracellular potential measurements accurately reproduced recorded extracellular waveforms.

For our purposes, we have made further assumptions based on this simple cylindrical model to obtain estimates of potentials measured at the body surface for the His bundle. We first assume a uniform intracellular current density (\underline{J}_i). We further assume a similar packing of individual fibres so that this same \underline{J}_i can be found in both the Purkinje fibre and the larger His bundle and that similar conductivities and conduction velocities exist in the two types of fibres. Hence, in analogy to the electrostatic problem of a uniformly distributed charge density within an infinitely long cylinder, the potential within the cylinder is assumed to be linearly proportional to the distance r from the center of the cylinder and falls off as $1/r^2$ outside the cylindrical radius.

Hence, if the extracellular potential measured at a radius of R_a is known to be V_e , then the extracellular potential measured in a cylinder of radius R_b with the same uniform current density can be expressed as

$$V_e(R_b) = V_e(R_a) \frac{R_b}{R_a}. \quad (5.2)$$

$V_e(R_b)$ is now the extracellular potential that would be measured at the surface of the cylinder of radius R_b . Similarly, the potential, V at any point r outside the cylinder, is given by

$$V(r) = V_e(R_b) \frac{R_b^2}{r^2}. \quad (5.3)$$

Combining Equations 5.2 and 5.3, we obtain an expression for the potential anywhere outside a larger cylinder representing the His bundle, as a function of the extracellular potentials measured in the smaller Purkinje strand. The equation de-

rived is

$$V(r) = \frac{V_e(R_b) R_a^3}{R_b r^2}. \quad (5.4)$$

The width of the His bundle is estimated to be 0.5–3 mm [130,131]. Spach et al. [34] measured extracellular potentials at the surface of a Purkinje fibre strand of 150 μm diameter to be 1 mV (p-p). Hence, with $R_a=0.25\text{--}1.5$ mm, $R_b=75$ μV and $V_e(R_b)=1$ mV (p-p), we calculate that at a distance of $r=10$ cm from the His bundle, the measured potentials in a infinite homogeneous volume conductor would be 0.02–4.5 μV (p-p).

Estimate of the magnetic field due to the His bundle

Combining Equations 2.9 and 2.10, one obtains $B(r) = \mu_0\sigma V(r)$ as an estimate of the magnetic field from the potential. The previous estimated potential produces a magnetic field of the order of .005–1 pT. When applied to recorded subject data, this procedure always results in an over-estimate (by a factor > 10) of the amplitude of the measured magnetic fields. Hence, a more realistic estimate for the magnetic field is .5–100 fT.

Interpretation of these estimates

Our recording systems have bit resolutions of 2.5 μV (BSPM) and 75 fT (MCG) and noise levels, after averaging, of ~ 1.3 μV and 54 fT, respectively. These numbers suggest that under the present recording protocols, the HB signal-to-noise ratio is at best 2 ($S/N \leq 2$), and possibly much worse.

It is well known [65,66] that surface boundary contributions tend to decrease the amplitude of measured potentials (and magnetic fields) at the body surface, suggesting that these estimates are upper-limits to the probable size of the HB signal on the body surface. The variety of geometries and cancellation effects of converging wavefronts in the proximal BB and Purkinje fibre network makes it difficult to estimate the body surface potentials and magnetic fields. Given the larger size of the BB

structures, though, we suggest that their amplitude should be as large or larger than the HB, and possibly, growing as activation spreads. However, as noted by Massing and James [130], there is diverse inter-individual geometry of the BB and Purkinje network. These variations would produce a large variation in total cell volume contributing to body surface BB signals. Therefore, there is no guarantee that the BB signal amplitude increases with time.

The numbers given above are confirmed in a model of the HPS by Kafer [132]. She calculated penetrating HB potential activity at the body surface to be $0.6 \mu\text{V}$, and BB potentials reaching a maximum of $\sim 10 \mu\text{V}$ after 40 ms. The magnetic field maxima for HB and the BB calculations were 7 fT and ~ 300 fT, respectively. With a magnetic noise level of 75 fT after averaging 30 complexes, these numbers suggest HB and BB S/N levels of $< .1$ and 5, respectively.

Kafer notes that the HB activity calculated was 'somewhat smaller than reported by others', suggesting a similar qualification might be applied to the BB values. On the other hand, the potentials due to atrial repolarisation, reported in this same work, are on the order of $5\times$ greater than found in the present study (see Chap. 4). However, the amplitudes of the simulated HPS signal do agree with the extrema of the residual maps of Figures 5.1 and 5.2 at -14 ms, as well as those measured by Leiniö et al. [124] in the subject with complete A-V block.

Hence, although the upper limits of magnetic field and body surface potential estimates for the His bundle and estimates and measurements of the BB signals are above the noise level, it is questionable whether or not these signals can be consistently measured at the body surface. The diverse individual geometries and the extremely small size of the lowest estimates of the signals makes it impossible to confirm, based on these size estimates, whether the extracted maps reflect the depolarisation of the HPS.

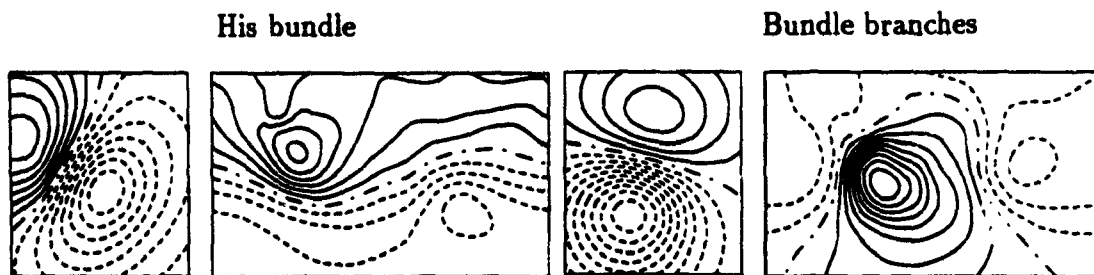


Figure 5.9: BSPM and MFM HPS model maps.

These maps of the His bundle (left) and proximal bundle branches (right) were generated using the Kafer HPS computer model [133]. Contour levels are 1 fT/0.1 μ V (HB) and 25 fT/1 μ V (BB).

5.3.3 Expected spatial distribution of HPS maps

To evaluate the techniques for the spatial separation of HPS and Ta a discussion about the expected body surface distributions of the HPS source is in order. As previously stated, the MFM studies have yielded distributions which were believed to be consistent with a single current dipole representing the HPS source.

The BSPM patterns found in this study are not consistent with the HPS source. With successful results, the distribution extracted in Fig. 5.1 at -14 ms before Q-onset would be consistent with bundle branch activity. In fact, the extracted BSPM pattern corresponds to one that would be generated by a Z-oriented current source. Such a current direction does not appear to be consistent with the anatomical orientation of the heart and conduction system within the human torso.

The model of Kafer [132,133] provides isofield magnetic and potential maps for the HB and BB. The Kafer model consists of a 3-D network of rhombododecahedra fixed in an inhomogeneous torso model. His bundle and proximal bundle branch patterns generated from this model are shown in Figure 5.9. Neither the MFM or BSPM extracted HPS maps in this study agree with these model maps.

5.3.4 Atrial repolarisation and PR-segment eigenmaps

In applying the 4 extraction techniques (SVD, KLT, CT and TAT), one assumes that atrial repolarisation is stationary, i.e. that the amplitude and position of the source do not change with time. However, only the position must be constant for all techniques. The requirement of a constant amplitude can be removed in the SVD, KLT and CT methods, since all these use some form of weighting of amplitude, which is built into their definitions. An assumption of constant amplitude cannot be removed in the TAT method.

It was shown in Chapter 3 that small changes in the location of the background source were reflected in the higher-order eigenmaps (Fig. 3.3). With smaller grids, these maps could look dipolar and be mistaken for a superimposed source. Certain features of PR-segment eigenmaps suggest that the location of the atrial repolarisation source is changing as a function of time. Physiologically, this is to be expected as wavefronts propagate from the right to the left atrium.

The eigenmaps shown in Figures 5.7 and 5.8 suggest that, given a reasonable S/N, the u_2 SVD eigenmaps have a pattern consistent with a non-stationary background (Ta) source. The simulation results in Chapter 3, for a moving background source, support this conclusion. When the amplitude of the background signal changed, only the first eigenmap (u_1) was significant (Fig. 3.2). Higher order eigenvalues, and associated eigenmaps, were zero. When the dipole position changed as a function of time, the higher order eigenvalues, and associated eigenmaps, were no longer negligible (Fig. 3.3).

Additionally, in the SVD of the PR segment, we have found a recurrent u_2 eigenmap pattern, *independent of PR-segment duration* (see Fig. 5.7 and 5.8a and b). An HPS contribution in normal subjects would result in different u_2 's than that of subjects with 1st degree A-V block. The fact that u_2 is similar in both groups, proves that the u_2 pattern cannot be associated with HPS in those with short PR segments.

The amplitudes of the residual maps reach minimum values during times corre-

sponding to the segment used to represent Ta and grow at times moving away from this segment, with opposite polarities on either side of the segment. This same feature was observed in the residual maps of the extraction simulations with a moving source (Fig. 3.4). At -74 ms of Fig. 5.1 the residuals are primarily opposite in polarity to the -14 ms maps, and the residuals at -44 ms are opposite in polarity to the residuals displayed at this same time in Fig. 5.3. We note that the BSPM u_2 eigenmaps for subject RF108 (Fig. 5.7) have a similar back-to-front orientation of an equivalent dipole as the corresponding residual distributions found at -14 ms (Fig. 5.1 and 5.3). These observations are not found in the MFM residuals because of noise limitations. It is also noted that the MFM residual maps at -14 ms in Figure 5.2 and at -74 ms in Fig. 5.4 are similar to the SVD eigenmap u_2 from the -70 ms to -10 ms segment in Fig. 5.7c, supporting the belief that the MFM results are limited by noise.

These observations suggest two conclusions. First, because the residuals have the same features as u_2 eigenmaps, there cannot be any significant HPS contribution to the residual pattern or the ramps measured in the PR segment. Secondly, u_2 actually reflects the continual changes in atrial repolarisation patterns as a function of time. The reversal in polarity of the residual pattern along with a minimum signal during the Ta representation segment is consistent with a non-stationary Ta source. A map earlier/later in time has a source location before/after the location of sources generating the segment used to represent the Ta source. The greater the time difference between these points, the larger the relative locations and associated residual patterns. These results also support the conclusion made in Chapter 4, associating pattern changes as a function of time during the PR segment with the gradual propagation of the atrial repolarisation currents over the atria.

5.3.5 Orthogonality of Ta and HPS

The question of orthogonality between the Ta and HPS sources must be considered, since three of the extraction techniques (SVD, KLT, CT) will demand that, to get perfect HPS extraction, the maps of the Ta and HPS sources must be orthogonal. It

was confirmed mathematically (see Equation 3.34) that the only circumstances under which a superimposed source can be extracted perfectly, is when it is orthogonal to the background source. It is apparent that the probability that two independent sources create maps that are always perfectly orthogonal is minimal. Hence it is unlikely that these techniques could successfully extract a superimposed source pattern.

The problem of orthogonality also puts limits on the number of eigenmaps that can be used in the SVD and KLT representations. Including too many terms in this kind of expansion just increases the probability that more superimposed source (HPS) is removed, further distorting any recorded HPS signal.

5.3.6 Recording bandwidths

The BSPM data recorded with a high-frequency cut-off of 125 Hz and 250 Hz showed very little differences in residual patterns, and although not presented, the ramps observed in the PR segments were also similar. This observation supports the conclusion that the ramps seen in this data are of the same origin as that reported by authors using wider bandwidths. This conclusion does not exclude the possibility that the wider bandwidth recordings, along with high-pass filtering and lower noise levels, can reveal high-frequency notches and bumps superimposed upon the ramps, which are associated with the His-Purkinje system. In particular, a number of investigators have used such bumps to determine the onset of His activity at the body surface [119,120,126,134,135,136,137,138]. The noise level excluded the possibility of detecting notches and bumps associated with His-onset in the BSPM and MFM recordings used in this study, nor was this of specific interest to us.

5.3.7 Comparison of extraction techniques

The four extraction techniques gave very similar results in late PR segment, independent of recording bandwidth. With this and the previous observations under consideration we propose that the residual patterns shown in Figures 5.1, 5.2, 5.3 and 5.4 *reflect the gradual changes found in the atrial repolarisation pattern as a*

function of time. These changes are of the same nature and develop similarly in time as in atrial depolarisation; little HPS (particularly bundle branch) signal contributes to the pattern.

The observation of similar results using all of the extraction techniques can be used to support this conclusion mathematically. Let \mathbf{Z}_1 and \mathbf{Z}_2 represent segments in the early and late phases of the PR segment, such that $\mathbf{Z}_1 = \mathbf{X}_1$ contains only a background source, and $\mathbf{Z}_2 = \mathbf{X}_2 + \mathbf{Y}$ contains a background and superimposed source. Further, assume that $\Delta\mathbf{X} = \mathbf{X}_2 - \mathbf{X}_1$ is small, such that following an SVD expansion of \mathbf{X}_1 , the following holds,

$$\mathbf{U}_1^* \mathbf{X}_1 \simeq \mathbf{U}_1^* \mathbf{X}_2 = \mathbf{A}_{\mathbf{X}}^{1*}, \quad (5.5)$$

and that \mathbf{X}_1 is approximately constant so that, $\mathbf{X}_2 - \bar{\mathbf{X}}_1 \simeq \Delta\mathbf{X}$. The \mathbf{A} 's define spatial expansion coefficients (see Eq. 3.12), with the superscript (1) referring to expansions made using the eigenvectors (\mathbf{U}_1) arising from the SVD expansion of \mathbf{Z}_1 .

According to Eq. 3.3, subtracting the temporal average map of \mathbf{Z}_1 from \mathbf{Z}_2 gives

$$\mathbf{R}_{\text{TAT}} = \mathbf{Z}_2 - \bar{\mathbf{Z}}_1 \quad (5.6)$$

$$= \mathbf{X}_2 + \mathbf{Y} - \bar{\mathbf{X}}_1 \quad (5.7)$$

$$= \mathbf{Y} + \Delta\mathbf{X}. \quad (5.8)$$

The residual \mathbf{R}_{TAT} contains the superimposed source plus some contamination due to small changes in background source.

Similarly, we can solve Eq. 3.18 for an SVD expansion of \mathbf{Z}_1 applied to \mathbf{Z}_2 to form the residual,

$$\mathbf{R}_{\text{SVD}} = \mathbf{Z}_2 - \mathbf{U}_1 \mathbf{A}_{\mathbf{Z}_2}^{1*} \quad (5.9)$$

$$= \mathbf{Z}_2 - \mathbf{U}_1 \{ \mathbf{U}_1^* \mathbf{Z}_2 \} \quad (5.10)$$

$$= \mathbf{X}_2 + \mathbf{Y} - \mathbf{U}_1 \{ \mathbf{U}_1^* (\mathbf{X}_2 + \mathbf{Y}) \} \quad (5.11)$$

$$= \mathbf{X}_2 + \mathbf{Y} - \mathbf{U}_1 \{ \mathbf{A}_{\mathbf{X}_2}^{1*} + \mathbf{A}_{\mathbf{Y}}^{1*} \} \quad (5.12)$$

$$= \mathbf{Y} - \mathbf{U}_1 \mathbf{A}_{\mathbf{Y}}^{1*} + \mathbf{R}_{\Delta\mathbf{X},\epsilon}. \quad (5.13)$$

In the last step, we have made use of the following equality, which arises from the SVD definition and Equation 5.5 above:

$$\mathbf{X}_2 = \mathbf{U}_1 \mathbf{A}_{\mathbf{X}_2}^{\dagger \epsilon}. \quad (5.14)$$

ϵ is defined as the SVD series truncation error resulting from the use of a minimum (say only 1) number of spatial eigenvectors in the previous equality, so that the residual $\mathbf{R}_{\Delta\mathbf{X},\epsilon}$ defines a function of \mathbf{X}_1 , \mathbf{X}_2 , and their differences, $\Delta\mathbf{X}$, only.

It has already been noted that the TAT and SVD extraction techniques give the same residuals when applied to the problem of extracting HPS from the PR segment (e.g. Fig. 5.1). Hence, a comparison of Equations 5.8 and 5.13 can be made. The common term \mathbf{Y} is associated with the superimposed source assumed to be present in \mathbf{Z}_2 . The remaining terms, given the observed equality, require that

$$\Delta\mathbf{X} = \mathbf{U}_1 \mathbf{A}_{\mathbf{Y}}^{\dagger} + \mathbf{R}_{\Delta\mathbf{X},\epsilon}. \quad (5.15)$$

The expansion coefficient in the first term is

$$\mathbf{A}_{\mathbf{Y}}^{\dagger} = \mathbf{U}_1^* \mathbf{Y}. \quad (5.16)$$

This term will not be zero generally, since it would require that the HPS and Ta sources (or \mathbf{X}_1 and \mathbf{Y}), be orthogonal at all times. The second term on the right is known, as defined previously, to be a function of the background source only and its changes as a function of time ($\Delta\mathbf{X}$). Since the term on the l.h.s. of the equation is also a function of the background source only, Eq. 5.15 can hold only if $\mathbf{Y} = 0$, *that is if no superimposed source is present in the maps.*

5.3.8 Summary

Our objective had been to separate the spatial features of concurrent HPS and atrial repolarisation activity during the PR segment. By viewing the results obtained from a number of different perspectives, we have come to the conclusion that this objective has not been accomplished. There is no significant HPS contribution to the

residual patterns or the ramps measured in the PR segment. The strongest evidence to support this conclusion follows from the comparison of the extracted 'HPS' maps (residual maps) with the SVD and KLT eigenmaps. In particular, because these residuals have predominantly the same features as the u_2 atrial repolarisation eigenmaps (compare Figures. 5.1 and 5.2 with Figure 5.7), there could not be any significant HPS contribution to the residual pattern. This conclusion was further supported by a comparison of the extraction techniques, and expectations of their associated residuals in the presence of multiple sources. The underlying statement that now follows, of course, is that no significant HPS signal was actually recorded.

Finally, we have concluded that the extracted patterns actually reflect the continual changes in atrial repolarisation current sources as a function of time, as reflected at the body surface. These temporal variations are of the same nature as those seen in atrial depolarisation.

5.4 Discussion

Various techniques are used in body surface detection of HPS activity. These can be grouped into two sometimes overlapping topics: detection of His bundle onset to determine non-invasively His-to-ventricular onset times, and the isolation of HPS spatial features for validation of inverse solutions. A comparison of this study with some previously published work generates many questions about the significance of those previous results.

In particular, the results presented here suggest that inappropriate interpretation of data may have occurred previously. This will be demonstrated by reviewing a number of previously published papers, and offering alternative interpretations, based on our contention that the PR-segment map features are dominated by the atrial repolarisation source and, in particular, its temporal variations in location.

5.4.1 Variance maps of Horan et al.

The first attempt to remove the atrial repolarisation spatial features from the PR segment was made by Horan et al. [76] in 1982. The technique used to extract the His-bundle signal is referred to as the Correlation Technique (CT) in Chapter 3. Three assumptions, upon which later data processing was based, form the basis for the difference in their approach, as compared to the MFM papers which appeared later. We quote these assumptions.

“(1) Surface maps during early P-R segment probably were the result of both late atrial activation and early atrial repolarization; (2) maps at the time of maximum rapid change probably were caused by the combined effect of common bundle firing and continued atrial repolarization; and (3) maps late in the P-R segment probably were the result of both the large steady pattern of atrial repolarization and the small, rapidly changing pattern of activation of distal bundle branch and Purkinje network [76]”.

We agree with the first assumption. This description is particularly supported by the MFMs of the PR interval shown in Chap. 4. The second item assumes that the His bundle signal is large enough to be recorded and detected at the body surface. Previous calculations and discussion (Section 5.3.2) suggest that the signal originating in the His bundle is less than a few microvolts in amplitude on the body surface. Peak amplitudes during the PR segment are commonly $40 \mu V$. With a $S_{HPS}/S_{T_a} \leq .1$, it is unlikely that the His bundle deflection could be distinguished from T_a and its own variations as a function of time.

Horan et al. elaborate further on the third assumption, saying that “the highly variable effect of activation of the distal branch and Purkinje network would be cancelled and the essential pattern of atrial repolarisation would be preserved in the mean T_a map” [76]. This statement is not supported by Leiniö’s data. The bundle branch signal is ramp-like, hence would not average out to zero over any segment.

The authors proceed to extract a HB signal using the correlation technique on 5 subjects (PR-segment durations ranging from 54 to 75 ms). One set of residual maps are presented in their figure 2. A comparison of the latter figure with the results in this chapter supports our belief that they also have extracted the variations of Ta with time, and not HB. The particular features found that support this view are: (1) their “HB” map occurs during the still rapidly varying signal initially after P-wave offset, undoubtedly resulting in a large residual in Equation 3.5; (2) amplitude of residual maps get smaller as maps progress into the segment used to form the average atrial repolarisation map. Both these features can result from the changes occurring in atrial repolarisation, with larger differences present in maps further from the average Ta segment.

There are numerous observations and statements made by Horan et al. to substantiate their belief that they have extracted spatial features of the His bundle and proximal bundle branches. For brevity, we will not elaborate on detailed counter arguments to this belief. Instead we choose to quote a concluding paragraph in the paper, which affirms their viewpoint and argues against alternative interpretation. From [76], we cite

“Whereas we are convinced that rational extraction of conflicting signal (i.e., removal of the simultaneous atrial repolarisation signal) permitted detection of the His bundle signals, it might be argued that arbitrary manipulation of the body surface potential pattern permitted an interesting but also arbitrary result which only coincidentally resembled that expected from His bundle activation with a limited number of samples. This consideration must be addressed, but the consistent and repeated pathway we have illustrated from our subjects, as well as the serial map pattern consistent with the rational division of one source into two, strongly suggest that we have identified the electrical trail down the common bundle and its branches. With responses to the intervention as just mentioned, this objection should disappear.”

The first sentence firmly expresses our viewpoint that these results are totally coincidental. The next statements can be explained by our alternative interpretation of the results of these “arbitrary manipulations”. Atrial activation and recovery processes are effectively the same in all subjects. Any manipulations on the signals recorded at the body surface due to atrial depolarisation and repolarisation will also be consistent in these subjects. In fact, we have found cases (RK156 in Fig. 5.6c) where PR-interval maps in subjects differing from the typical pattern, demonstrate residual patterns also different from the usual pattern, but still correlating well with u_2 eigenmaps characterising atrial repolarisation. This consistent correlation of u_2 eigenmaps and residual patterns suggests that u_2 and the residuals reflect relative changes in the temporal evolution of the atrial repolarisation source.

Finally, validation of Horan and co-workers’ inverse solution results was not done using true cardiac images of the subjects. The inverse solution results were projected onto a stylised representation of the HPS anatomy. In other words, the location of the HPS and its anatomy was not based on imaging techniques such as Magnetic Resonance Imaging (MRI) or X-ray. They assumed that the earliest maps corresponded to His bundle depolarisation. The associated inverse solutions were then used as an absolute reference by fixing these points to the His bundle aspect of this assumed anatomy. Later solutions follow the reference point along a short segment extending less than 1 cm in each of the 3 orthogonal planes. This result only demonstrates a consistent relative location of their extracted maps, but does not prove that this location actually corresponds to the HPS.

5.4.2 Isolation of His-Purkinje system signal from magnetic field maps

A number of papers were published in the Biomagnetism community which claim to have extracted features in the PR segment, consistent with a single equivalent current dipole representing the HPS source [77,78,79,80,127,139]. TAT and KLT are the background techniques which have been used. In most cases, HPS extraction

followed the successful recording of ramps, notches and bumps in the PR segment of MCG recordings. Earlier papers associate some or all of the ramp features (ramps, spikes, bumps) to HPS [97,122,140,141,142,143,144,145]. However with the work of Lorenzana et al. [123], showing ramp features in patients with 1st degree A-V block similar to those found in normals, the interpretation of the measured signals changed. The emphasis shifted toward associating sudden changes in the slope of the ramp in the PR segment to the onset of HPS [77,146]. At this time the first attempts [77,79,139] to separate spatial features of the HPS and Ta were made.

Qualitatively, the extracted 'HPS' maps compare to the MFM residual maps of Figure 5.2. The extracted maps show minimum magnetic field amplitudes during times coinciding with the segment used to characterise atrial repolarisation and reach a maximum just before Q-onset, as would be expected from HPS features. However, as was discussed in Section 5.3.4, this feature is also consistent with continual changes in atrial repolarisation patterns, due to the shift in location of the atrial source as a function of time. The results of these earlier studies were validated by single equivalent current dipole inverse solutions in a semi-infinite homogeneous conducting medium. Solutions generally located the source in a region consistent with the HPS anatomy. Again, the accuracy of these results were not confirmed using actual images of the subject's anatomy. It was accomplished by comparing the expected relative locations of the atria, conduction system and ventricles.

Erné et al. [139] found a location and pathway consistent with HPS in some subjects, but in a number of maps the ECD pathways could not be associated with the anatomical structures of HPS. We propose that this discrepancy could, in some cases, be a result of the naturally varying site of the cardiac pacemaker, found to occur in as much as 15% of our study group (see Chap. 4 and Fig. 5.6). The variations in pacemaker locations will change the atrial activation and recovery pathways equivalently, thus also changing the temporal variations of atrial repolarisation, relative to the typical subject. These variations will be reflected in the residual patterns found after extracting the representative, dominant atrial repolarisation distribution. Again, we

feel that such patterns are not related to HPS.

5.4.3 Peper's time-shift method

Peper et al. [4,126,134] attempted to remove P waves in HRECGs in an effort to enhance the PR segment, in subjects with PR segments shorter than the normal H-V time. In these subjects, particularly children, the P wave overlaps the His bundle signal, thus preventing surface detection of His-onset. The method makes use of spontaneous fluctuations of the PR interval. In the technique, ECGs having a relatively short PR interval and those having a longer PR interval are averaged separately. In the two averages, the atrial signal components are shifted relative to the QRS, while signal components having a fixed time relation to the QRS complex, like the His signal, are the same in the two data sets. If the two average beats are subtracted, the P wave or PR interval can be reconstructed using a transfer function derived from a backshift operator [147] (see Appendix C). This reconstructed P wave is then subtracted from an original beat to reveal only events correlated to ventricular activation.

This paper is discussed because, although the technique is applied only to a single ECG lead, in practice, if atrial events are truly removed from the PR segment, the technique should apply equally well to spatial extraction by removing the PR interval in all body surface leads. In light of what has been found in our study, and some apparent misinterpretation of their results by other authors [13], further discussion can be made as to the usefulness and intent of the Peper technique. As stated initially, Peper et al.'s [4,126,134] intent was to develop a method to isolate the His bundle signal from the larger overlapping P waves in subjects with short PR intervals. A step-like signal they record and associate with His-onset is generally obvious in most subjects, particularly adults, and does not require enhancement.

In the results presented by Peper et al. [4,126,134], it is difficult for us to accept that the technique can be applied universally to isolate the His bundle from atrial signals, particularly because of the lack of validation of successful examples presented.

There is no published systematic validation of the technique on a large sample using HBE confirmation. Even the few results presented in papers were not validated with HBE measurements. In particular, the lack of HBE confirmation does not validate the association of the step-like signal with the His bundle. The authors indicate that optimal surface leads were chosen based on HPS modelling results, for which to detect the His signal. However, there are concerns which will have particular relevance when applying the technique to any arbitrary lead.

There is an apparent oversight or misunderstanding by the authors of the nature of atrial activation and recovery. They state that in the PR segment “the P wave has vanished and the repolarisation of the atrium has not yet started [134]”, indicating that the authors have not even considered the possible association of this step or the ramp of the PR segment with atrial repolarisation.

Another point of concern, which the authors mention themselves, is that the shape of the P wave in a patient, even at rest, often shows pronounced changes. The changes found in the P wave should be reflected equivalently in atrial repolarisation, but at a slower rate. Superimposing plots of the two beats with different PR-interval times aligned relative to R-onset show ramps in the PR segment that coincide extremely well. This suggests to Peper et al. that the ramps are not atrial in origin, but are due to activation of the HPS. The problem with this conclusion is that, due to the small amplitude of the atrial repolarisation currents, any differences in the two averages result in extremely small signals. These may not be detectable when plotted at scales which are optimised to plot P waves. The problem in the way the authors apply the technique is that in some cases the reconstruction stops immediately after the P wave or does not include the entire PR segment and the step-like ‘His’ signal. As a result, this does not allow the step or ramp to be removed in the reconstruction process, if, as we suggest, these are atrial in origin.

Also to note is that the ramp in the PR segment is small in amplitude, as are the differences resulting from slightly differing P waves. The removal of the atrial contribution to this ramp could be hampered by the presence of noise, particularly

baseline offsets and drifts. This can pose problems because the reconstruction algorithm is an integrating function (see Appendix C). The baselines in the two averaged beats can differ and will not cancel each other during subtraction, so that during the reconstruction process an integration of the differences of the two baselines is obtained, which will be larger than the original baseline. The effect will be that a simple baseline offset is reconstructed into a ramp of constant slope and any existing drifts will be transformed into higher-order functions. This effect is demonstrated by simulation in Appendix C.

5.5 Conclusions

The initial goal in this work had been to isolate *spatial features* of HPS in the PR segment from the concurrent atrial repolarisation source in both BSPM and MFM data. This topic had been pursued with MFM data in previous work [3,80] by the author, following the work by others suggesting this was possible not only in MFM, but also BSPM data [76,77,78,79,99,129]. At the time, the MFM results were found to be consistent with ‘a single current dipole representing the HPS source’, but the extension of the technique to BSPM data did not always reveal patterns which were consistent with HPS [94]. Thus began an effort to understand the origin of discrepancies between the two different results. The focus ultimately turned toward understanding the mathematics of the extraction techniques, the real (electrophysiological) nature of the sources involved and the interaction of the two.

We have concluded that no significant HPS signal was recorded in the PR segment and that the ramps in the PR segment reflect atrial repolarisation. By considering the interactions of the mathematics (especially assumptions) with the sources under consideration, the results of this study suggest that, under the recording protocols used, the variations in atrial repolarisation patterns as a function of time are significant. As a result, the extraction techniques considered could not remove all Ta contributions from the PR segment. It might be argued that including more eigenmaps in the

SVD and KLT techniques would remove these additional Ta components. However, as demonstrated in Chapter 3, including more terms only increases the probability of removing any HPS component that may have been present. With this conclusion, further discussion of previously published work suggesting alternative interpretation and explanation of these results has been presented.

The recent paper by Leiniö et al. [124] is convincing evidence that a bundle branch signal can be recorded both magnetically and electrically at the body surface. A limiting factor that emerges from this paper is that in the case of normal subjects, the amplitude of the PR segment is significantly larger than the His bundle, indicating it is unlikely that the His signal will be detectable.

It should be emphasized that this work does not address whether the spike, bump or step-like signals reported by others¹ are due to HPS. In most cases, these features are extracted only after filtering and other signal processing which are difficult to verify. Our objective was to enhance the spatial distribution of the HPS signals in MFM and BSPM, with the underlying intent of applying inverse localisation programs.

¹Recent review articles [13,148,149] of this topic can be found.

6 Extraction Techniques Applied to PR-segment Events: II. Wolff-Parkinson-White Syndrome

6.1 Introduction

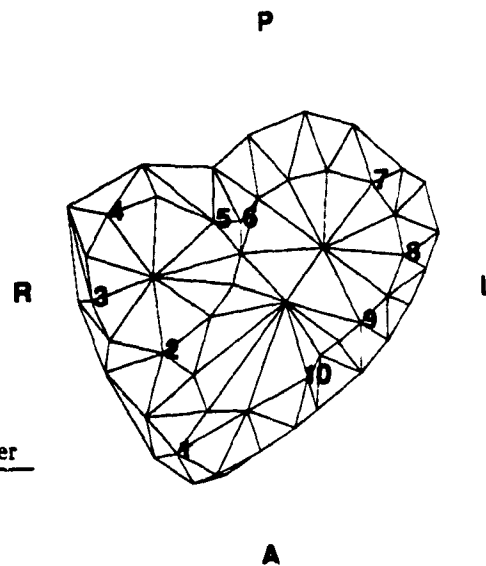
Wolff, Parkinson and White described, in 1930, an electrocardiographic syndrome consisting of functional bundle branch block, and a short PR interval occurring in otherwise healthy young people with paroxysms of tachycardia. The ECG abnormality associated with Wolff-Parkinson-White (WPW) syndrome is found in 1-3 per 1000 people [150].

The ECG description of WPW syndrome is a manifestation of ventricular pre-excitation. Pre-excitation denotes a premature activation of the ventricular myocardium by an impulse originating in the atrium, occurring earlier than would be expected if the impulse reached the ventricles via the normal (HPS) conduction system. The pre-excitation is facilitated by the existence of an accessory pathway (AP) of specialised conducting or extra myocardial tissue between the atria and ventricles. Some common locations of AP sites are shown in Figure 6.1.

In the ECG of WPW patients, the existence of the AP is usually marked by a shortened PR interval, the presence of a δ wave during the PR segment, and a prolonged QRS duration. The δ wave is the electrocardiographic manifestation of the premature ventricular excitation. Contrary to the normal QRS complex which has a sharp onset, the δ wave is slurred and small at onset, but generally grows as currents propagate through the ventricles. At some point, which varies as a function of accessory pathway location, and the atrial/A-V nodal conduction properties [150], the normal excitation of the ventricles via the HPS begins, and fusion of the δ wave and QRS complex occurs.

Site	δ -wave polarity in the first 40 ms											
	I	II	III	aVr	aVI	aVf	V ₁	V ₂	V ₃	V ₄	V ₅	V ₆
G1	+	+	+/ \pm	-	\pm /+	+	\pm	\pm	+/ \pm	+	+	+
G2	-	+	-/ \pm	-	+/ \pm	\pm /-	\pm	+/ \pm	+/ \pm	+	+	+
G3	+	\pm /-	-	-	+	-/ \pm	\pm	\pm	\pm	+	+	+
G4	+	-	-	-	+	-	\pm /+	\pm	+	+	+	+
G5	+	-	-	-/+	+	-	\pm	+	+	+	+	+
G6	+	-	-	-	+	-	+	+	+	+	+	+
G7	+	-	-	\pm /+	+	-	+	+	+	+	+	-/ \pm
G8	-/ \pm	\pm	\pm	\pm /+	-/ \pm	\pm	+	+	+	+	-/ \pm	-/ \pm
G9	-/ \pm	+	+	-	-/ \pm	+	+	+	+	+	+	+
G10	+	+	+/ \pm	-	\pm	+	\pm /+	+	+	+	+	+

/ = One or the other of 2 entries is found
 - = Initial 40 ms of δ wave is negative
 + = Initial 40 ms of δ wave is positive
 \pm = Initial 40 ms of δ wave is isoelectric



Abbrev.	Anatomical	Gallagher
RAP	Right anterior paraseptal	G1
RA	Right anterior	G2
RAL	Right antero-lateral	G2.5
RL	Right lateral	G3
RPL	Right postero-lateral	G3.5
RP	Right posterior	G4
RPP	Right posterior paraseptal	G5
LPP	Left posterior paraseptal	G6
LP	Left posterior	G7
LPL	Left postero-lateral	G7.5
LL	Left lateral	G8
LAL	Left antero-lateral	G8.5
LA	Left anterior	G9
LAP	Left anterior paraseptal	G10

Figure 6.1: Accessory pathway locations and Gallagher 12-lead localisation scheme. The Gallagher localisation scheme (From Gallagher [150]), view of the heart at the level of the A-V ring, with the 10 common accessory pathway locations suggested by Gallagher and table of nomenclature used in identifying AP sites are displayed.

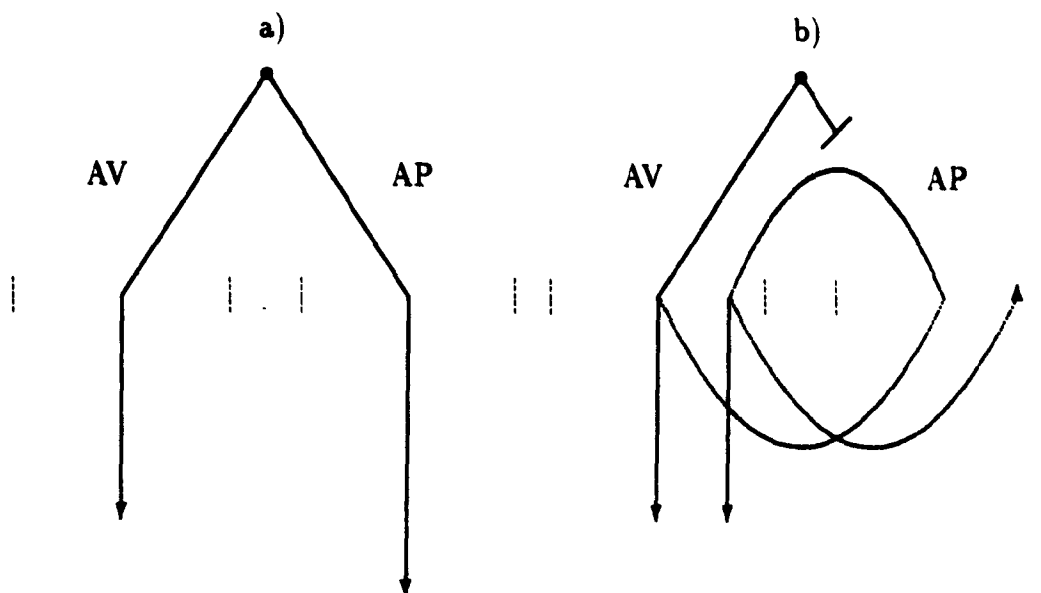


Figure 6.2: Conduction mechanism in WPW syndrome. AV denotes the normal conduction pathway from the A-V node to HPS. AP indicates an accessory pathway. a) illustrates the conduction mechanism that inscribes the typical WPW pattern. The atrial impulse is conducted through both pathways concurrently but at a faster rate through the anomalous pathway. b) illustrates conduction during paroxysmal tachycardia: anterograde through the normal pathway followed by retrograde conduction through the AP.

The significance of these accessory pathways (AP) lies primarily with their ability to participate in establishing supraventricular tachyarrhythmias. Such arrhythmias occur when the AP or normal HPS system are capable of retrograde conduction (see Figure 6.2).

Intervention in the treatment of WPW patients at risk of sudden cardiac death varies. In asymptomatic patients, treatment may not be necessary at all. Actual treatment can consist of drug therapies aimed particularly at addressing mechanisms responsible for maintaining the dysrhythmias (i.e. conduction properties of the atria,

ventricles, HPS and AP), or implanted pacemakers to interrupt arrhythmias. However, the long-term side-effects of drug treatments, particularly in younger patients, is not always desirable. These can now be avoided. First surgical ablation [151,152], then more recently radiofrequency (RF) ablation [153,154,155] of such pathways has become available. When presented with a patient with symptoms or factors suggesting a need for therapeutic intervention, a more accurate assessment of the AP properties becomes necessary. The choice is made after extensive invasive electrophysiological studies (EPS) aimed at assessing the conduction properties of the myocardium affected by single or multiple accessory pathways and determining their location.

Today, the success rate of RF-electrical ablation procedures [155], is shifting the preference of therapy toward permanent ablation of the pathway, removing the risks associated with long-term drug use or the more invasive open-heart surgical ablation procedures. In contemplating electrical (or surgical) ablation of the AP, it is desirable to actually localise the site of the pathway non-invasively. The choice to ablate the pathway will still require invasive EPS procedures, primarily to confirm the non-invasive findings. However, in the case of electrical ablation, previous localisation will enable the cardiologist to confirm the location and perform the ablation in a single session. This course of events will minimise the time required to perform the invasive assessment and therapeutic intervention, reducing the risks (e.g. X-ray) and discomfort to the patient.

6.1.1 Non-invasive localisation of AP

A number of non-invasive techniques have been developed to determine the site of accessory AV conduction pathways. These include: 12-lead ECG, vectorcardiography, body surface potential mapping (BSPM), 2D echocardiography, and BSPM and magnetic field map (MFM) inverse solution localisations. EPS mapping and epicardial mapping, both invasive techniques, are also used to identify the site of pre-excitation pathways.

A review of most of these techniques (excluding inverse solutions) was prepared

by Yuan et al. [156]. They conclude that the 12-lead ECG classifications were the simplest and most convenient methods for initial evaluation of the AP site. BSPM criteria can be quite successful, and more sensitive than 12-lead ECG [75,157] classifications. However, the large number of electrodes and more extensive processing required for BSPM data renders it less practical than standard ECG.

The 12-lead ECG and BSPM localisation techniques use pattern matching criteria based on the polarity of the δ wave, QRS configuration or QRS axis in particular leads. However, the most common and successful ECG criteria use the polarity of the δ wave [150,158] to determine the most probable AP location. Figure 6.1 shows one such scheme.

It has been determined that in δ -wave body surface maps, the potential maximum is always located on the left anterior chest, while the minimum rotates around this maximum, in accordance with the relative location of the AP on the A-V ring [75,159]. Variations when applying this observation by different authors primarily affects the time point during the δ wave which is classified. The different comparison points have included the distributions at 40 ms after δ -wave onset [75,157,160], the distribution when the negative potentials reach $-150 \mu V$ [161] which is usually earlier than 40 ms, but not at the same time for all patients, and the 40 ms STT maps [75,160].

Recent work by Dubuc et al. [162] suggests adopting a BSPM pattern matching technique during the actual ablation procedure. BSP maps recorded during pacing in the area of the ventricular insertion site are compared to maps recorded in sinus rhythm. The correlation between these maps reflects the accuracy of the position of the pacing catheter in relation to the ventricular insertion site of the accessory connection. Ablation of the paced site which produced maps which correlate best with the δ -wave maps obtained during sinus rhythm maps had a 93% success rate while reducing the investigation time. Such a procedure could also be considered with a multi-channel MCG unit in the hospital environment.

Localisation of AP sites using electrocardiographic and magnetocardiographic inverse solutions is gaining interest. In fact no other technique but inverse so-

lutions has been researched for the magnetic field measurements (see for example [72,73,81,163,164,165]) and magnetic inverse localisation of AP far outnumbers similar BSPM attempts [71,74,166].

6.1.2 Limitations of non-invasive AP localisation criteria

In subjects exhibiting minimal pre-excitation, the size of the δ wave is small in amplitude or short in duration and is not easily classified using non-invasive techniques. There can be extremely early fusion of normal ventricular activation in this subgroup of WPW patients. Both the small size of the δ wave and the fusion with normal ventricular activation result in unknown distortion factors to the δ wave when applying the 12-lead ECG and BSPM classification criteria. As a result, classifications based on existing 12-lead ECG and BSPM criteria often exclude patients with small or short δ waves. Since the degree of pre-excitation does not correlate with the potential risks for sudden death, this group does require the same investigative protocol in arriving at an appropriate therapy¹.

Aside from the limitations in resolution of standard electrocardiographic equipment, onset of the δ wave is not easily identified because of the interference of other cardiac signals. In particular, the contribution of atrial repolarisation signals can be large during onset of the δ wave. Even during normal cardiac activation, the atrial repolarisation Ta wave overlaps with the QRS complex. In cases of pre-excitation, the Ta-wave overlap can distort the δ -wave onset. Additionally, Duchosal et al. [167] have shown that in subjects with extremely premature ventricular excitation, particularly in right-sided pathways, ventricular pre-excitation can begin during the P wave. In a group of 51 WPW patients, they found the atrial and δ wave overlap to begin as early as 45 ms before P-wave offset. But, they also found δ -wave onset occurred as late as 23 ms beyond P-wave offset. They have particularly emphasized the effect this overlap with atrial activity has on distorting the apparent δ -wave onset.

¹As do WPW patients with accessory pathways capable only of retrograde conduction. These subjects show no electrocardiographic manifestations of AP, but do experience arrhythmias which can lead to sudden death. The lack of ECG changes excludes this group from this study.

6.1.3 Enhancement of early δ -wave signal

This WPW study was multi-faceted. Primarily, it comprised the first comparison of body surface potential and magnetic field maps in a group of WPW patients. Two underlying motivating factors guided this comparison.

Firstly, the localisation of the accessory pathway using inverse solutions that utilise a single current dipole as an equivalent source will have its accuracy limited by the distance travelled by the propagating wavefront since δ -wave onset. With a ventricular myocardial conduction velocity of approximately 0.6 m/s along the myocardial fibres, after 40 ms, the wavefront could have travelled as much as 2.4 cm. This error can be minimised by obtaining inverse solutions to the earliest maps in the δ wave. So our aim will be to obtain such maps. Secondly, we wish to determine if these early δ -wave maps can be used to successfully locate the AP site in all subjects, including those with minimal pre-excitation.

To address both these objectives, it is necessary to use the onset of the δ wave to determine the location of the accessory pathway. The extraction techniques discussed in Chapter 3 were explored for application to WPW patient data to remove the atrial repolarisation signal from the PR segment during the early δ wave. The results of Chapter 5 suggest that there is no HPS contribution to BSP and MF maps during the PR segment, so this signal does not have to be considered. We did not previously determine how successful the techniques examined could be at removing a background source, but we confirmed that after removing Ta signals only small residual signals occur. These residuals are small enough not to severely distort the δ -wave onset. In cases where δ -wave onset coincides with the P wave, errors associated with subtracting the larger P-wave signal could be much larger.

6.2 Recording protocol and WPW study group

The study group included 16 subjects with clinically diagnosed WPW syndrome. Fifteen subjects had AP locations determined by invasive EPS. Later, 9 subjects

underwent electrical ablation of the AP, including one subject with two right-sided pathways. Age, sex, PR interval and QRS durations for this group are presented in Table 6.1. Five patients had either small or short-duration δ waves.

Measurements consisted of a 56 point sequential MFM using a 7×8 grid and a 117-lead simultaneous BSPM recording. The measurements were obtained at a sampling rate of 500 Hz, in an aluminium shielded room. The 56 points where magnetic field was measured were sampled for 30 seconds, while the BSPM data were sampled for 120 seconds – all during the same session. All data were averaged off-line, filtered for 60 Hz, and aligned (MFM relative to BSPM) on R-wave maximum. A zero isoelectric or isofield baseline was defined in the UP interval.

For one subject (CM186), an intermittent AP prevented us from obtaining a MFM recording. For another subject (WG200) instrumentation failure permitted only a 35 point magnetic field recording. In the case of the subject with 2 accessory pathways (DI189), we determined that for most beats during the MFM and BSPM recordings both AP were active concurrently. This subject's data were therefore excluded from the group. However, in the longer BSPM recording, strings of excitation via only one of these pathways were found. These data were included in the study. Further discussion of this particular patient's data is found in Appendix F.

6.3 Development of the enhancement protocol

The enhancement techniques and protocols were primarily developed with the BSPM data of the patient showing an intermittent WPW condition. During the recording, the atrial to ventricular conduction switched between a normal AV path and an accessory pathway in this patient. For the first 90 seconds a normal heartbeat was recorded. During the last 30 seconds, strings of WPW beats were intermingled with the normal beats. The sequentially recorded MFM data were not useable because of the intermittent condition. The waveform was unpredictable and dominated by a normal heartbeat. The presence of both normal and pre-excitation beats enabled us

Patient	Sex	Age (Yrs)	PR-int (ms)	QRS (ms)	Ta	Ta	δ -wave onset	
					ms relative to R-max		BSPM	MFM
KG162 ^s	M	42	132	121	-80/ - 64	-74/ - 64	-62	*
HB177	F	50	75	160	none	-98/ - 88	-84	-80
BS184 ^s	M	19	104	113	-84/ - 60	-70/ - 60	-58	*
SL185	M	24	104	128	-86/ - 80	-86/ - 76	-74	-60
CM186 ^m	F	16	112	135	-98/ - 86	-96/ - 86	-84	-
MR187	M	57	128	128	none	-82/ - 72	-70	-70
JS188	M	31	108	134	-94/ - 88	-94/ - 84	-82	-80
DI189 ^m	F	27	70	151	none	-116/ - 106	-102	-
VP190	F	37	75	130	none	-100/ - 90	-90	-90
EA191 ^s	F	50	135	113	-100/ -74	-84/ -74	-72	-72
MS193	F	38	126	156	-126/ -102	-112/ -102	-98	-88
DK195 ^s	M	44	96	120	-76/ -60	-70/ -60	-60	-48
LC196	M	26	115	132	-102/ -84	-94/ -84	-82	-78
CN197	F	30	120	139	-124/ -102	-112/ -102	-100	-90
LA199 ^s	M	21	128	108	-80/ -60	-70/ -60	-56	-52
WG200 ^m	M	22	80	144	none	-110/ -100	-100	-90
Averages:		33	107	132				
SD:		12	22	15				

Table 6.1: WPW patient group summary.

PR interval is defined from P-wave onset to δ -wave onset and QRS is the interval from δ -wave onset to S-wave offset. Ta indicates the interval during which atrial repolarisation patterns were found. Where 'none' is listed, the δ wave begins during atrial depolarisation. \overline{Ta} indicates the segment used to represent atrial activity. The interval times ('/' means 'to') for Ta, \overline{Ta} , and onset times are quoted relative to R-wave maximum. Superscripts s=small size or short duration δ wave, and m=missing or partial MFM recording.

* δ -wave MFM onsets are not given because of an unclear onset.

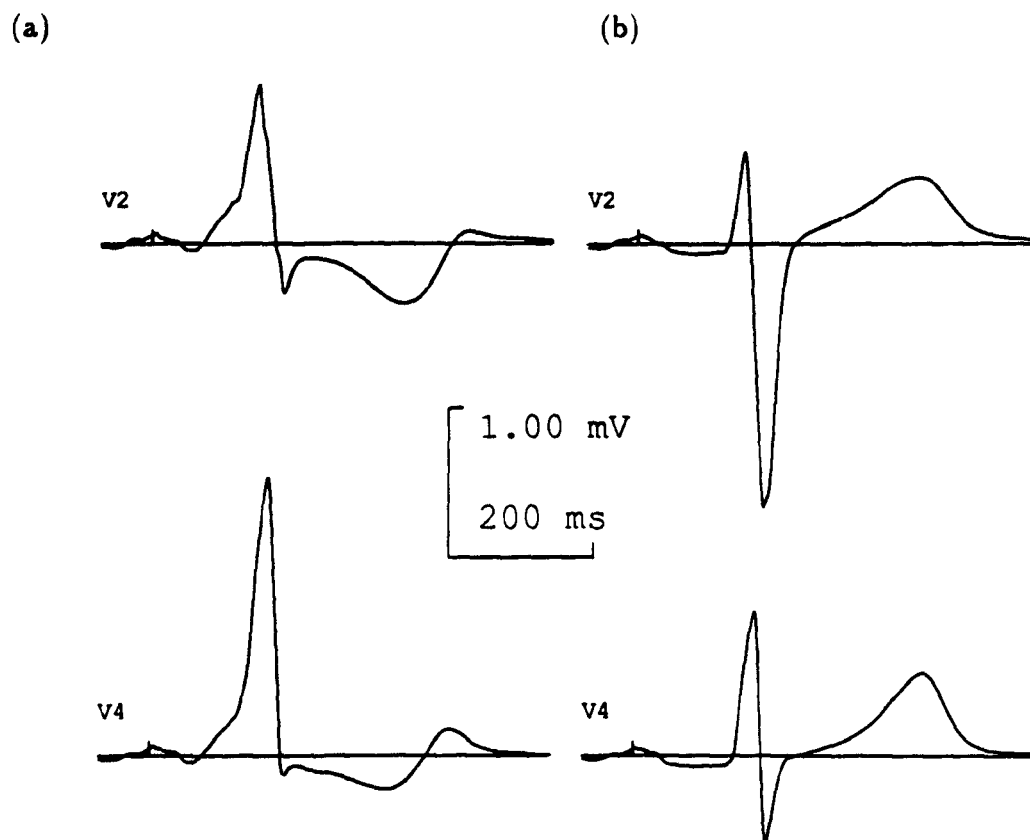


Figure 6.3: Normal and accessory pathway ECG leads for subject CM186. ECG leads V_2 and V_4 for (a) the average of 11 WPW beats and (b) average of 108 normal complexes.

to remove the complete T_a signal, and determine the contribution that incomplete or incorrect removal of atrial repolarisation from the average will make to the enhanced δ -wave maps.

6.3.1 Method

From the 120 second BSPM data, two averaged complexes were formed. The first complex was an average of 11 consecutive WPW beats (WPW file). The other was formed from the 108 beats present during the initial 90 seconds of the recording (normal file). Two BSPM leads for each of these averages are presented in Figure 6.3.

From the 12-lead ECG, RMS distributions and contour maps of the PR interval it was determined that the atrial activity in the averaged files was the same. There was no evidence of a wandering pacemaker site which would result in distinctly different atrial conduction mechanisms and prevent direct comparison of the files. The maximum of the P wave was chosen as a common reference point to align data files, as the changes in the ventricular activation wavefronts during normal and WPW fusion modes did not allow alignment to be made on the QRS complex.

A common Ta segment in the files occurred from 48 to 60 ms after P-wave maximum. After 60 ms, the PR-segment maps in the WPW file diverged from the 2 normal files, presumably due to δ -wave onset. A 10 ms interval in the PR segment of each file – representing the same atrial repolarisation events – was chosen to characterise Ta. Three enhancement techniques were applied to these maps to enhance the δ -wave signals as early as possible after onset.

These techniques were:

- 1) SVD enhancement consisting of representation of Ta maps from the WPW file by orthogonal expansion (SVD), and subtraction of the fitted Ta eigenmaps from the δ wave;
- 2) TAT enhancement by means of subtraction of the average Ta map (from the WPW file) from the δ wave;
- 3) Enhancement consisting of subtraction of the normal file from the WPW file on a map-by-map basis (with alignment of the two files based on P-wave maximum).

By subtracting on a map-by-map basis, theoretically, we would be removing any atrial repolarisation component resulting from temporal variation in amplitude and position of the Ta source. This term is small but not negligible as was demonstrated in Chap. 5.

In the last method (3), the baselines of the normal and WPW files should match accurately. To accomplish this, the map-by-map subtraction was performed on normal and WPW beats with isoelectric intervals defined during their own PR segments. The 'isoelectric' segment chosen was the same as the segment used to characterise Ta

(50 to 60 ms after P-max).

6.3.2 Results

The signal-enhanced δ -wave maps obtained using the three enhancement methods are presented in Figure 6.4 along with the original unenhanced maps. Most strikingly similar are the average Ta map (Fig. 6.4c) method and the theoretical, map-by-map difference, method (Fig. 6.4d). The unenhanced δ -wave maps (Fig. 6.4a) have contributions due to the concurrent atrial repolarisation signal. This is reflected particularly by an apparently poor S/N in the earliest δ -wave maps as compared to the map-by-map difference technique. The Singular Value Decomposition (SVD) method (Fig. 6.4b) also shows poor S/N spatial features, but the particular causative agent in this case is the non-orthogonality of the δ -wave and Ta-wave maps, resulting in a distortion of the δ -wave pattern.

Of particular interest in this work will be the application of single-moving-current dipole (SMD) inverse solutions to the δ -wave maps in order to locate accessory pathways. To determine the success of the enhancement techniques on the δ -wave maps, single current dipole inverse solutions using a standard torso conductor model, were obtained for all cases, and compared to the ‘theoretically’ correct map-by-map difference version (method 3). The inverse solutions were performed during the interval from (66–122) ms relative to P-max (4 ms to 60 ms relative to δ -wave onset). At 124 ms, Q-onset begins in the file of the normal beat, hence comparisons would not be useful beyond this time instant.

The inverse solution results of the different methods are compared in Table 6.2. The recovered dipole source locations of the theoretically correct map-by-map result and each of the other 3 inverse solutions are compared. The distances between solutions ($|\Delta\vec{R}|$) every 8 ms during the δ wave was calculated, as well as the average and standard deviation.

The largest differences relative to the theoretical result are found earliest in the δ wave, when atrial and residual atrial signals may affect the solutions. The average

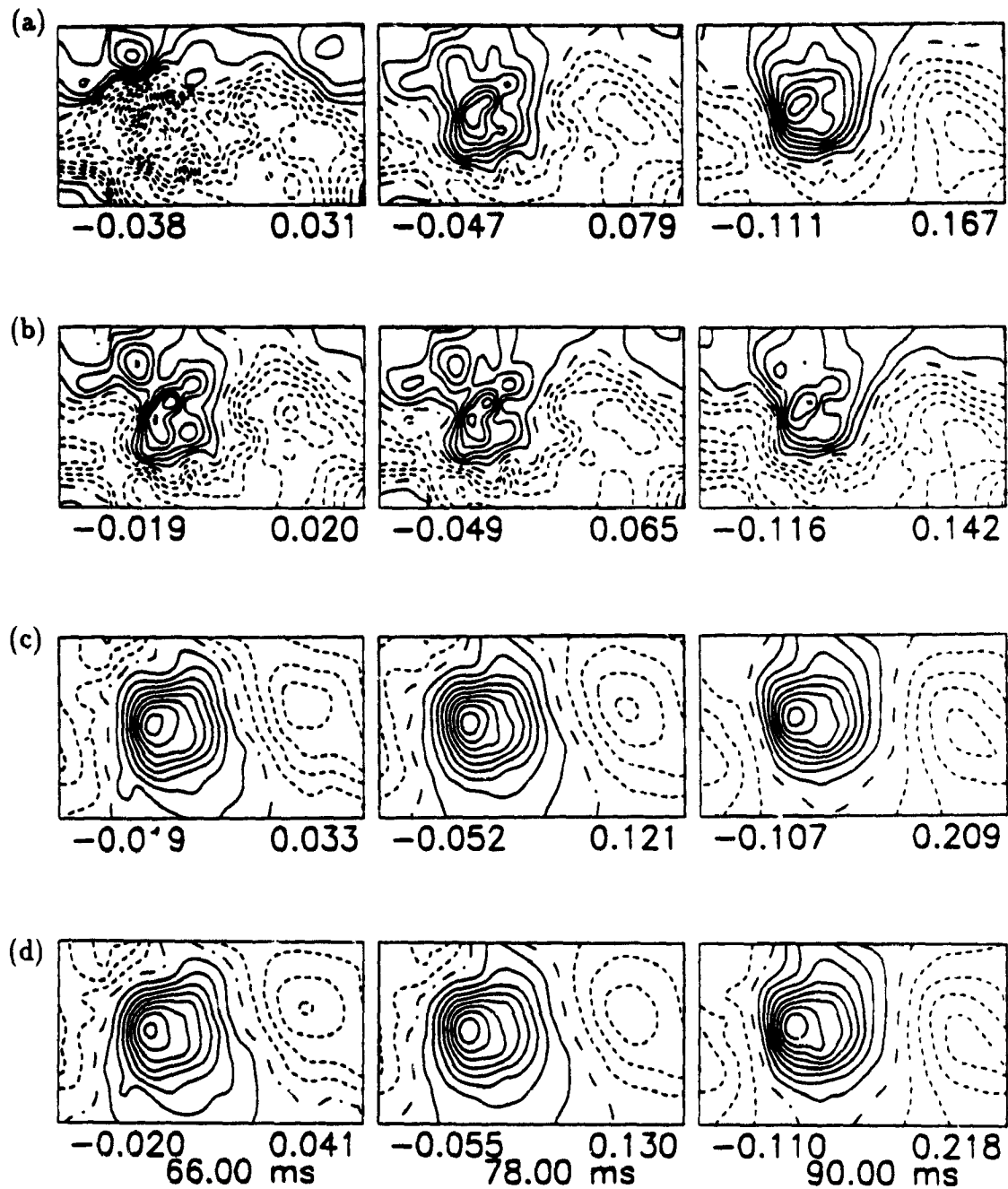


Figure 6.4: Enhanced δ -wave maps for the different methods studied. (a) unenhanced, (b) SVD method used to characterise T_a , (c) T_a characterised by an average segment, and (d) map-by-map subtraction of the 108 normal beat PR-segment signal from the WPW beat.

Time (ms)	SVD		TAT
	Unenhanced	Enhanced	Enhanced
4	9.00	4.06	0.90
12	2.96	3.03	0.46
20	2.19	3.20	0.29
28	1.27	2.26	0.22
36	0.97	2.10	0.17
44	0.76	1.73	0.18
52	0.54	1.25	0.12
60	0.27	1.10	0.11
Average	2.24	2.34	0.31
St. Dev.	2.87	1.02	0.27

Table 6.2: Inverse solutions compared to theoretical solution. Recovered DSL for each enhancement technique is compared to the map-by-map solutions, with the 3-dimensional difference in locations given in cm. Times are relative to δ -wave onset.

differences for the unenhanced and SVD-enhanced solutions are always larger than the TAT-enhanced solution, which on average is only 3.1 mm away from the theoretical solution.

6.3.3 Discussion

The similarity of the early enhanced maps by methods 2 and 3 to the later δ -wave features confirm that the enhanced maps reflect the pre-excitation source. The AP associated with these early δ -wave maps should be as successfully located as the later maps.

The inverse solution results help demonstrate the benefits of using some form of signal enhancement to remove the atrial repolarisation (Ta). The RMS display of the WPW beat does suggest the δ -wave onset as early as 70 ms after P-max; however, at this time the size of the signal is still of similar amplitude as the atrial repolarisation signal. As a result, no attempt can be made to localise the accessory pathway with an SMD solution until ~ 90 ms. The removal of the Ta signal, however,

would result in an earlier localisation of the pathway. As conduction proceeds through the ventricles, via the accessory pathway, the centre of the equivalent current dipole will be moving further from the origin of the pathway. Thus the earlier a localisation result is obtained, the closer the result will be to the actual pathway.

The relatively large contributions of a Ta signal to the unenhanced maps and the SVD-enhanced maps (method 1) accounts for the large errors of fit in the first maps. As can be seen in Figure 6.4a and b, there is a very low effective signal to noise ratio in these first maps. It is interesting to note that Nenonen et al. [72,81] used an orthogonal expansion method to remove the Ta signal in magnetocardiographic WPW maps, but did not report any unusual results.

The final two methods give reasonable results. By not removing the temporal variations in the Ta source, but just the average representation, it appears that a difference of the order of 1 cm or less is found during initial δ -wave onset (before 20 ms, Table 6.2). By 20 ms after δ -wave onset, the improvements fall below 2.9 mm.

It is suggested then that a map-by-map difference of atrial repolarisation ideally provides the best possible localisation results. However, the \overline{Ta} enhancement would only yield approximately 5–10 mm error during the early δ wave, as compared to more than 2 cm error with unenhanced data. The localisation error falls to less than 3 mm within 20 ms of δ -wave onset, probably because of the increased size of the δ -wave signal compared to temporal variations of the Ta-wave.

6.4 Method of WPW-signal enhancement

Having established that the average map technique is the best and simplest method to enhance the early δ -wave maps, a protocol was developed to be used for all subjects. The signal-enhancement protocol followed for both the MFM and BSPM data was:

- Maps of the PR interval and early QRS, from -170 ms to 0 ms relative to R-wave maximum, were plotted every 6 ms. Although R-max is an arbitrary point from subject-to-subject, particularly in pre-excitation subjects, it always

occurs well after δ -wave onset.

- The segment corresponding to atrial repolarisation was identified. This was sometimes done by plotting maps every 2 ms, particularly in cases with very short PR segments, and early pre-excitation. The Ta segment identified for each subject is listed in Table 6.1. In 12 subjects, atrial depolarisation was complete before any evidence of pre-excitation appeared in the maps. Hence a definite, but sometimes short, repolarisation segment could be identified. In 4 other subjects the δ wave begins during the P wave.
- A 10 ms segment was chosen to represent atrial repolarisation. The offset of this segment corresponded to δ -wave onset, except in cases where the duration of the Ta segment was less than 10 ms. For these subjects, the end of the Ta segment was allowed to overlap with δ -wave onset. When the P wave and δ wave overlapped, the representative segment was chosen to start at the time with the first evidence of pre-excitation in the maps. Of course, this means that we had to include up to 10 ms of the δ -wave onset in the Ta representative segment. The Ta representative segment chosen for each subject is listed in Table 6.1 as \overline{Ta} .
- This segment was averaged and subtracted from the PR-segment and QRS onset maps. The signal-enhanced δ -wave maps were plotted every 4 ms, and δ -wave onset was determined from both the MFM and BSPM isocontour plots.

Visual inspection of the resulting enhanced δ -wave maps is one method to evaluate the success of the enhancement procedure. Further confirmation was achieved by means of less subjective – although not necessarily more accurate – techniques. To determine that the pattern emerging in the early enhanced δ -wave maps indeed reflected pre-excitation via the accessory pathway, a computerised Gallagher AP classification was performed [150].

The Gallagher scheme, presented in Figure 6.1, is a 12-lead electrocardiographic classification scheme for pre-excitation. In this scheme, specific AP locations have an expected δ -wave polarity in each of the 12 standard ECG leads. The scheme was proposed after an analysis of the mean equivalent sources during the initial 40 ms of ventricular depolarisation in documented cases of single accessory pathways, with maximal pre-excitation (large δ waves). In our application, classification was made of the initial 10, 20, 30 and 40 ms of the δ wave before and after enhancement. The AP location was chosen to be the site which had the largest number of correctly matched polarities (of 12 leads). If more than 3 leads did not match, no AP site was identified. This computerised search was compared to the 'usual' 12-lead classification of a 12-lead ECG derived from the BSPM data and location of AP determined during ablation or EPS.

A number of examples showing general results and benefits of the enhancement of the early δ wave will be presented initially. Following this, the non-invasive 12-lead ECG classification scheme results will be discussed. We will then compare the BSPM and MFM patterns as a function of site around the A-V ring. Finally, we will describe the localisation of the ventricular insertion sites of the AP by means of inverse solutions that calculate a single moving current dipole from the measured BSP and MF maps.

6.5 Examples

Examples showing the effects of removing the Ta contribution from the early δ wave are presented for 3 particular subjects. The early δ -wave enhancement results for all other subjects will be discussed with reference to these examples.

6.5.1 Left-sided pathways

The first set of maps, presented in Figures 6.5 and 6.6, are typical results for left-sided pathways leading to significant ventricular pre-excitation. The subject (CN197) had a definite 22 ms (long) atrial repolarisation (Ta) segment between P-wave offset and

δ -wave onset. In the unenhanced maps presented in Fig. 6.5, typical Ta patterns are seen in BSPM and MFM at -10 ms (relative to δ -wave onset). By 10 ms, a growing negative potential on the posterior torso and an increased magnetic field are associated with the δ wave. As time progresses, both positive and negative potentials due to atrial repolarisation are masked by the growing δ -wave potentials. In the MFM, the presence of the δ wave is evidenced by the growth of the negative field maximum from the left to the right side of the maps. A stable pattern is present in both sets of maps from 30 ms to 40 ms.

The earliest δ -wave maps were enhanced by removing the dominant Ta signal. The maps from -12 ms to -2 ms were averaged and then subtracted from the PR-segment and QRS-complex maps. These enhanced maps are presented in Figure 6.6. There is little evidence of either the Ta or δ -wave signals at -10 ms. Starting at 0 ms, a stable BSPM pattern consistent with a left lateral (LL) pathway [75] emerges and grows in amplitude. The magnetic field map has a low S/N ratio at 0 ms, particularly due to the larger noise level, but the pattern is stable and grows as a function of time.

6.5.2 Right-sided pathways

An example of BSPM and MFM δ -wave patterns for a right postero-lateral (RPL) pathway are presented in the next two figures. The unenhanced maps for subject VP190 are presented in Figure 6.7. In this subject, as in all four right-sided pathways in this study, no pure atrial repolarisation phase occurred. The maps at -10 ms are consistent with very early atrial repolarisation, but this pattern changed immediately due to very premature ventricular excitation via the accessory pathway. δ -wave onset in the isopotential maps was signaled by the sudden, strong emergence of a potential maximum on the right anterior torso (0 ms of Fig. 6.7), coinciding with much smaller minimum potentials posteriorly. The MFM are almost entirely negative at onset.

The enhanced maps for this subject are shown in Figure 6.8. The segment from -10 to 0 ms used to remove the contribution of atrial repolarisation undoubtedly contains a significant δ -wave signal. The residual maps at -10 ms result from the

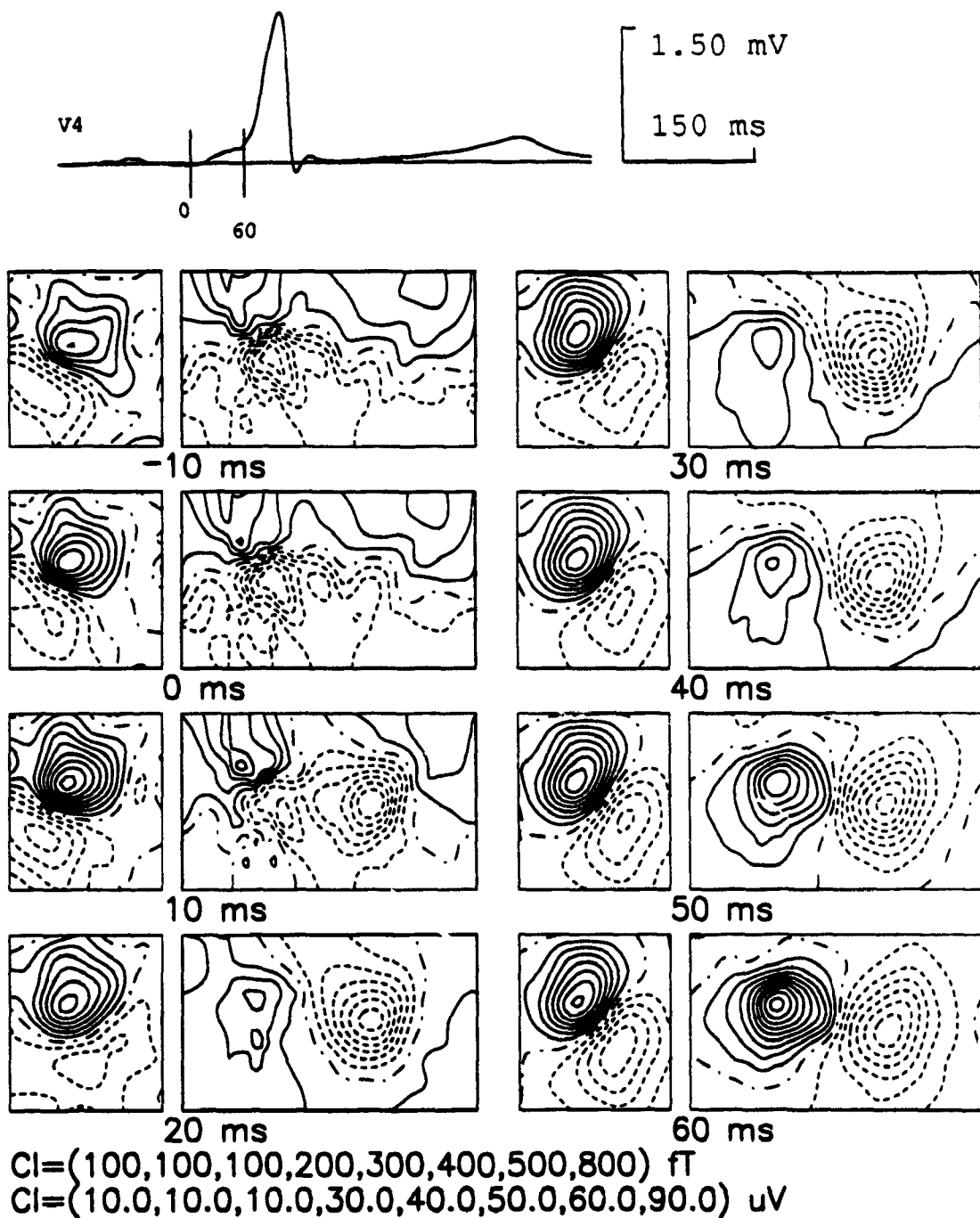


Figure 6.5: Unenhanced PR-segment and early QRS-complex maps for subject CN197.

Selected contour intervals of the MF and BSP maps are displayed below the maps.

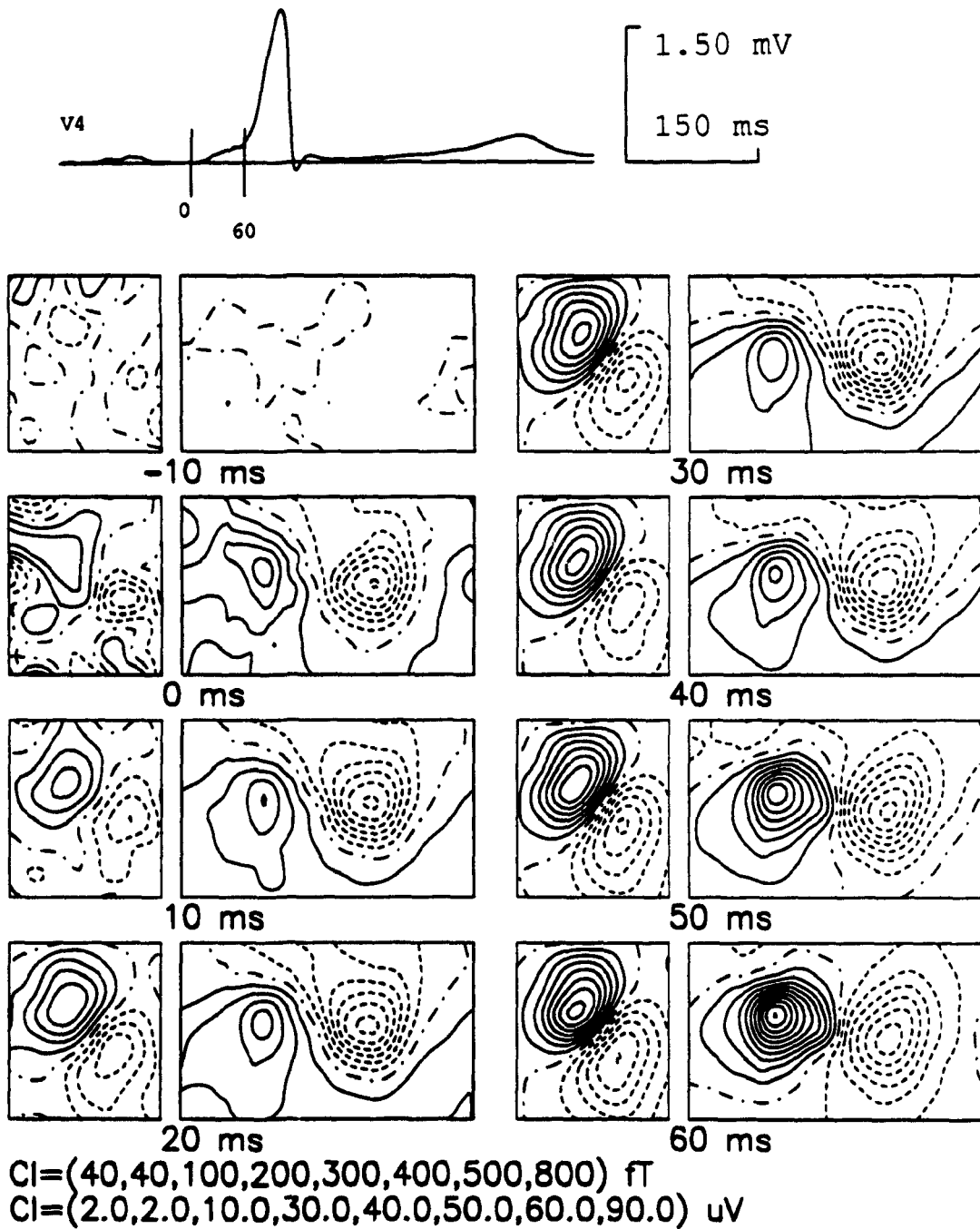
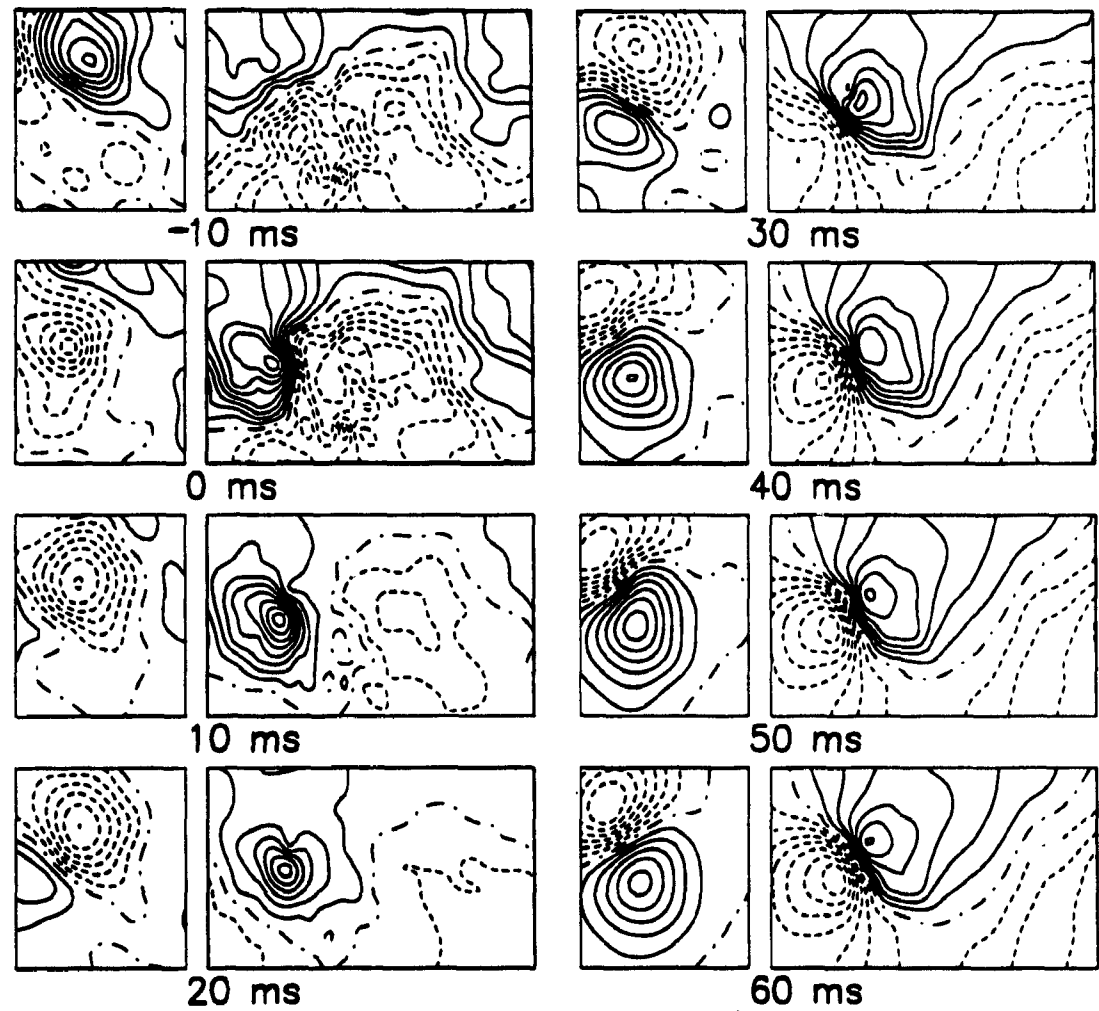
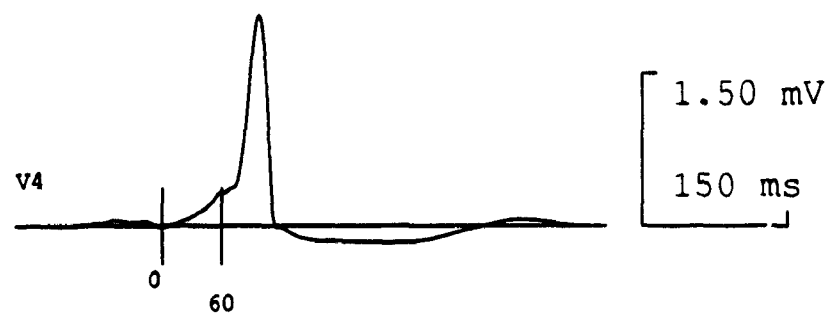


Figure 6.6: Enhanced PR-segment and early QRS-complex maps for subject CN197. The segment from -12 to -2 ms relative to δ -wave onset was averaged and subtracted from the QRS complex.



CI=(100,100,150,200,200,450,650,1250) fT
CI=(5.0,5.0,10.0,20.0,20.0,30.0,60.0,100.0) uV

Figure 6.7: Unenhanced PR-segment and early QRS-complex maps for subject VP190.

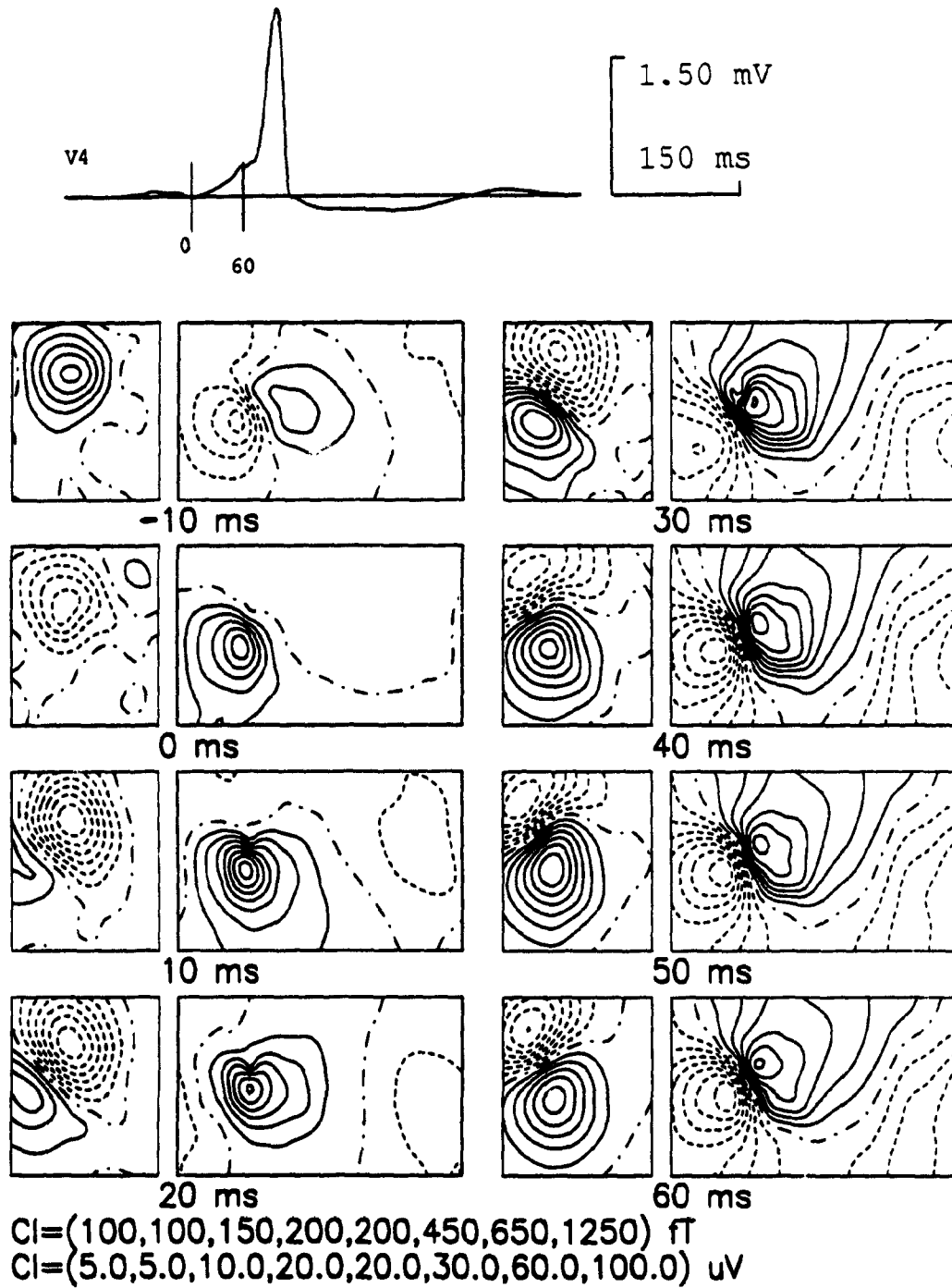


Figure 6.8: Enhanced PR-segment and early QRS-complex maps for subject VP190. The segment from -10 to 0 ms relative to δ -wave onset was averaged and subtracted from the QRS complex.

changes in the non-stabilised atrial source, plus a contribution from the strong δ -wave onset. The early sequence of maps in this right postero-lateral pathway varies greatly for 30 to 40 ms, but stable BSPM and MFM patterns emerge after this time.

In the early maps, the minimum potentials are much smaller than the maximum values, suggestive of a strong current source directed toward and located close to the anterior torso. Later, these areas of positive potentials become negative, now suggesting a current flow moving away from the same region. Benson et al. [75] have pointed out that this pattern can easily be confused with a left lateral pathway. This feature, found in 3 right-sided pathways, suggests this may be a common characteristic of these locations. It has not received much attention in past publications - to the extent that the BSPM pattern which has been suggested as typical for these sites actually does not appear until 30 ms after δ -wave onset in this group. These changes are further discussed later.

6.5.3 Small or short δ waves

Unenhanced PR-segment and early QRS maps for a third subject (BS184) with a LAL pathway and associated small δ wave, are shown in Figure 6.9. This patient had a PR-segment duration of 24 ms. The maps at -2 ms show typical Ta BSPM and MFM patterns. At 4 ms, a negative potential extremum emerging on the posterior torso (right side of map) marks the onset of the δ wave in the BSP maps. In the MFM, there is no clear indication of the emergence of a second source in the early maps, until the map at 22 ms. Here the positive magnetic field has moved superiorly, while the minimum has moved to the right in the map.

The enhanced δ -wave maps are shown in Figure 6.10. The early body surface potential maps are similar to those in Figure 6.6, supporting the belief that the 2 subjects in question had similar AP locations. However, because of the small size of the δ wave, and the higher noise level, it was not possible to isolate a stable, dipolar pattern consistent with pre-excitation in this subject's magnetic field maps. The MF maps in this subject do not reveal a clear pre-excitation signal, nor was there a

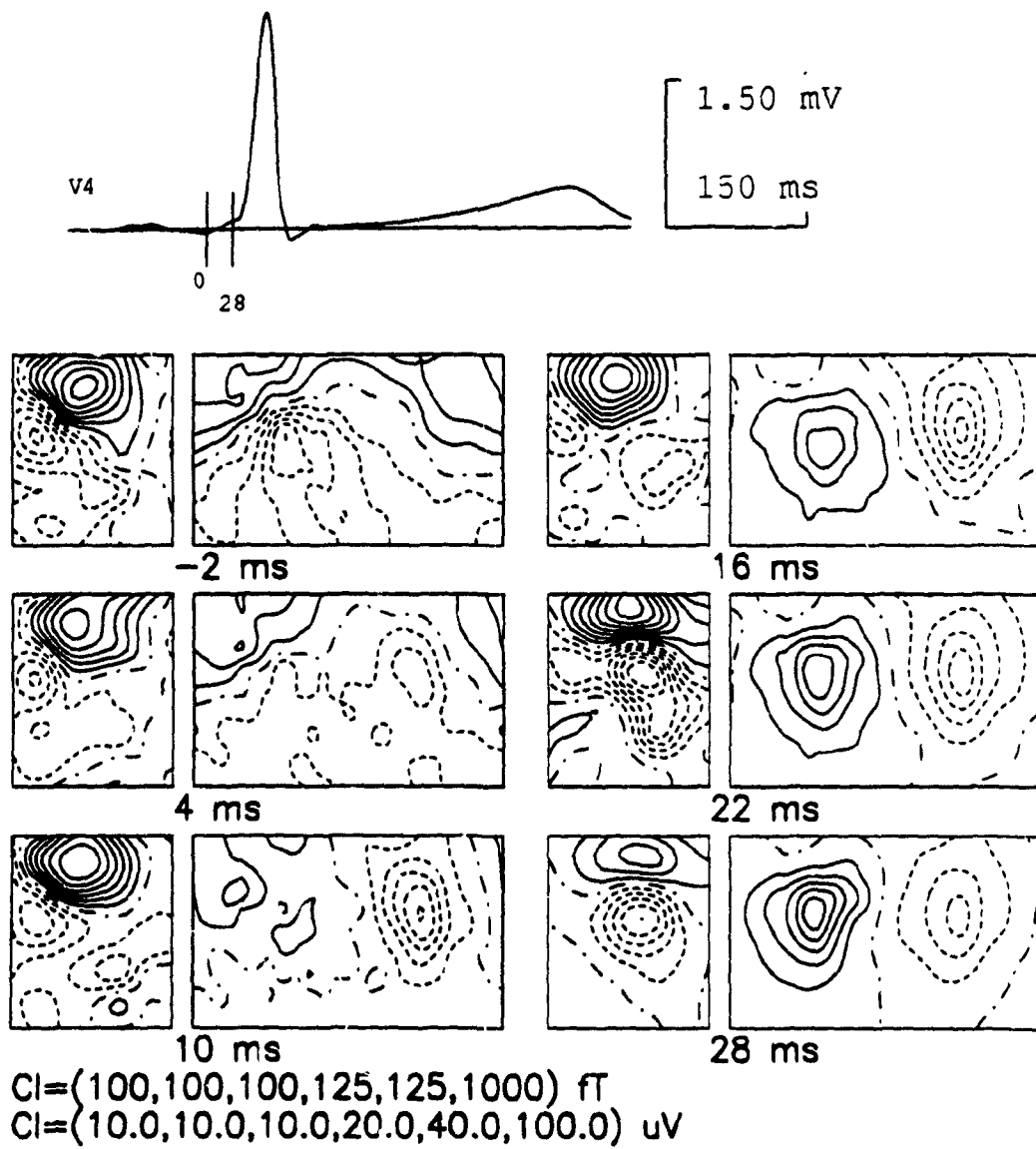


Figure 6.9: Unenhanced PR-segment and early QRS-complex maps for subject BS184.

significant δ wave in the magnetic field temporal waveforms. By 28 ms, the MFM is consistent with early, normal QRS activity.

All 12 subjects with left-sided pathways had early BSPM δ -wave maps which could be successfully enhanced. In 3 subjects, the δ waves were significant in amplitude, but short in duration, resulting in a QRS duration less than 120 ms. In these 3 cases, as in 6 other subjects with significant δ waves, it was possible to extract the atrial repolarisation signal from the early MFM δ -wave signal. Two subjects, BS184 (Fig. 6.10) and KG162, did not have large δ waves. The Ta and δ -wave features in their MFM could not be clearly separated. There was no MFM measured for the twelfth subject (CM186).

6.6 12-lead ECG localisation of AP

Results for Gallagher's classification of pre-excitation are presented for each subject in Table 6.3, and summarised in Table 6.4. Twelve of sixteen AP could be successfully localised within 1.5 Gallagher sites² using the 12-lead ECGs derived from enhanced BSPM data obtained during the first 20 ms of δ wave.

The most important observation that can be derived from these results is that the enhancement protocol successfully separated the early δ wave from the contaminating background signal generated by atrial repolarisation. Had there been significant residual atrial signal, the 10 ms and 20 ms classifications would not have been successful. The enhanced 12-lead ECGs, derived from the enhanced BSPM data, generally yielded more successful classifications earlier in the δ wave.

Better classification results, using the automated computerised technique (unenhanced and enhanced) could have been achieved for cases with right-sided pathways, if δ -wave onset in this group had been chosen later, to coincide with the beginning of the stable pattern emerging only 30–40 ms after our onset. Three of the four cases which could not be classified to within ± 0.5 in the first 20 ms had right-sided AP

²Gallagher localisation is quoted to within ± 0.5 sites. This occurs because the actual pathway was located between adjacent sites or fit either of two adjacent sites equally well.

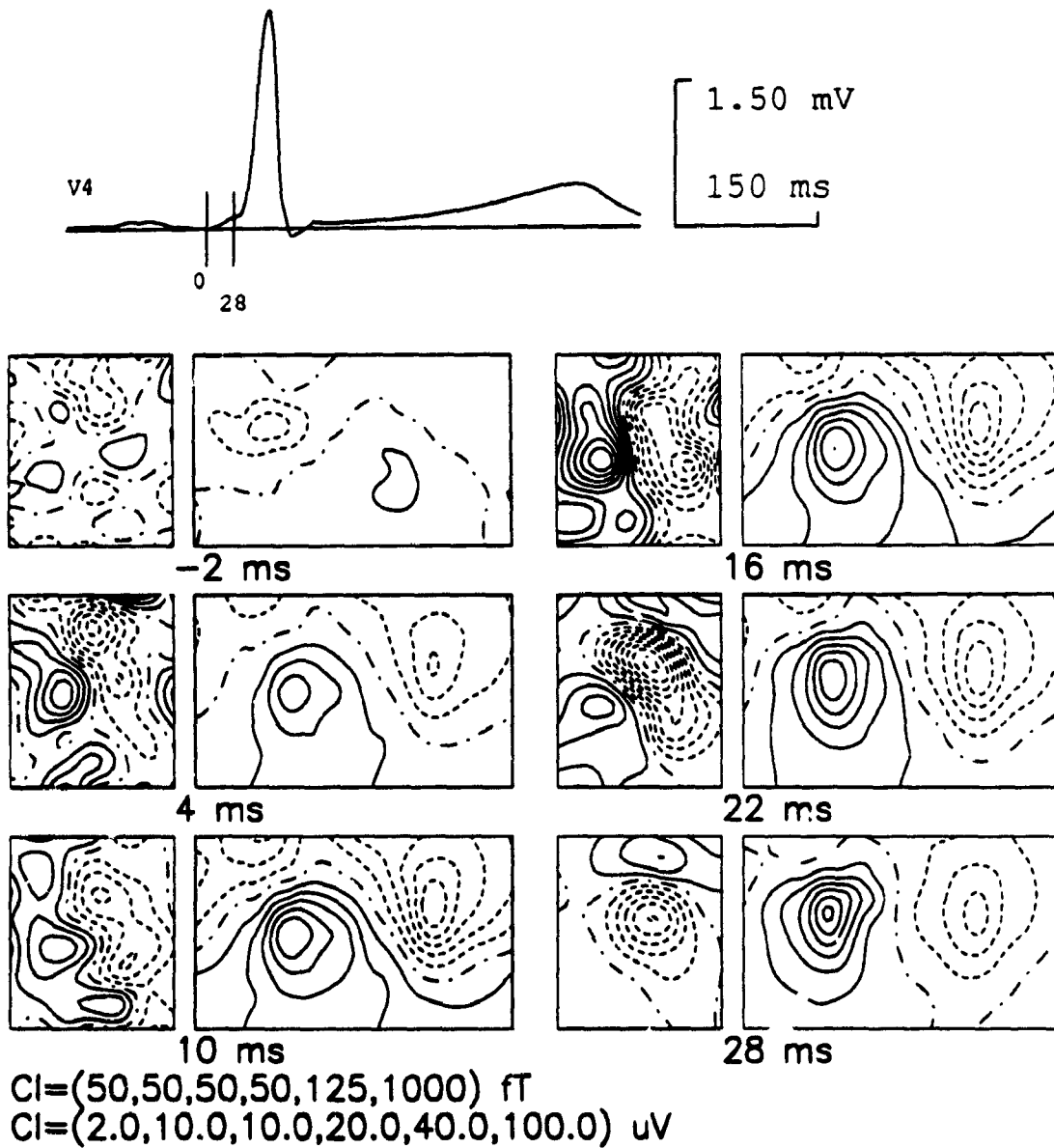


Figure 6.10: Enhanced PR-segment and early QRS-complex maps for subject BS184. The segment from -12 to -2 ms relative to δ -wave onset was averaged and subtracted from the QRS complex.

Patient	EPS/Ablated	Clinical	10 ms	20 ms	30 ms	40 ms	
SL185	G6 ^e	G6	G7 G6	G5.5 G6	G5.5 G6	G6 G6	UE E
KG162	G7 ^e	G3	- G6	G5 G6	G6.5 G6.5	G2/6 G2/6	UE E
CM186	G7	G5	G5 -	G6 G6	G6 G6	G6 G6.5	UE E
LC196	G7.5	G3	- G7.5	G6 G6	G6.5 G6.5	G6 G6	UE E
JS188	G8 ^e	G2	G2.5 G2	G2 G2	G2 G2	G2 G2	UE E
MS193	G8	G8	- 8	- G8.5	G9 G9	G9 G9	UE E
CN197	G8 ^e	G8	- G7.5	G8 G8	G8 G8	G8 G8	UE E
LA199	G8.5	G8	G9 G9	G8.5 G9	G9 G9	G9 G9	UE E
BS184	G9	G8	G5 G6	G8 G8	G9 G9	G9.5 G9.5	UE E
EA191	G9	G9	- G9	G9 G9	G9 G9	G9 G9	UE E
MR187	G9 ^e	G9	G2 G2	G2 G2/6/10	G0.5 G10	G0.5 G10	UE E
DK195	G10*	G10	- -	G1 G1	G0.5 G0.5	G0.5 G0.5	UE E
WG200	G1.5 ^e	G1	G7 -	G7 G7	G6 G5	G2 G2	UE E
DI189 ²	G2	G2	- -	- -	G7.5 -	G9 G8	UE E
VP190	G3.5	G4	G7.5 G7.5	G7 G6	G6.5 G5.5	G6.5 G6	UE E
HB177	G5	G3	G2/5.5 G2/5	G2/6 G2/6	G2/6 G2/6	G2/6 G2/6	UE E

Table 6.3: Locations of WPW accessory pathway.

The ablated AP location, when available, is used to confirm the predicted location. In relevant cases, EPS confirmations are indicated by the superscript *e*. The unenhanced (UE) and enhanced (E) Gallagher scheme classifications were determined by computing the average potential after 10, 20, 30 and 40 ms. When a site is given as 'G6.5', this means that the actual pathway was located between the adjacent sites G6 and G7 or fit either of two adjacent sites equally well. When more than one distinct, but equally possible match was found, the '2/6' nomenclature was used. A match with any of these sites was later accepted as a correct classification. * This subject did not have EPS or ablation therapy confirmation; the site suggested is the 12-lead clinical determination.

Number of subjects where:		Interval ending (ms)				N
		10	20	30	40	
Accuracy within $\pm G0.5$	Unenhanced	2	3	3	1	9
	Enhanced	7	0	3	2	12
	Clinical					10
Accuracy within $\pm G1.5$	Unenhanced	3	6	3	1	13
	Enhanced	8	4	0	1	13
	Clinical					11

Table 6.4: Comparison of results obtained by 12-lead Gallagher classification. The number of subjects where the AP was located within ± 0.5 or 1.5 Gallagher sites after a given time relative to δ -wave onset is tabulated for 12-lead ECGs derived from unenhanced and enhanced BSPM data. The clinical results are also summarised.

The sites which were generally incorrectly classified by a clinician were sites G7 and G8 (4 cases).

The 12-lead ECG localisation criteria of Gallagher et al. [150] presented in Figure 6.1 were derived from the polarity of the 12-lead ECG obtained during rapid atrial pacing, resulting in maximal pre-excitation. The AP locations were determined by epicardial mapping during operation in patients with single accessory pathways and no associated anomalies. They suggest that their results should be applied to patients in whom the QRS duration is more than 140 ms. Lemery et al. [168] tested the merits of various electrocardiographic AP classification schemes, including that proposed by Gallagher et al., on resting 12-lead ECGs. In their study, they concluded that this technique could only successfully classify 15 out of 47 AP locations (32%).

The success of Gallagher's criteria used on our resting 12-lead ECGs (derived from the enhanced BSPM measurements) suggests a contrary conclusion. All but one of 12 subjects with left-sided pathways could be classified successfully using the Gallagher criteria to within 1.5 (Gallagher) sites. The right-sided AP classifications were not as successful, primarily because of the choice of δ -wave onset in these cases.

A few observations from the 12-lead ECG classification data prompted an evaluation of the classification scheme itself. In our data, the best fit site was chosen

Site	G1	G2	G3	G4	G5	G6	G7	G8	G9	G10	Average	SD
G1	0	1	3	3	4	5	7	8	3	1	3.5	2.6
G2	1	0	1	1	1	2	4	6	4	1	2.1	1.9
G3	3	1	0	1	2	3	5	9	8	6	3.8	3.1
G4	3	1	1	0	1	1	3	9	6	5	3.0	2.9
G5	4	1	2	1	0	1	2	8	6	4	2.9	2.6
G6	5	2	3	1	1	0	2	8	5	4	3.1	2.4
G7	7	4	5	3	2	2	0	6	7	6	4.2	2.4
G8	8	6	9	9	8	8	6	0	6	6	6.6	2.6
G9	3	4	8	6	6	5	7	6	0	1	4.6	2.6
G10	1	1	6	5	4	4	6	6	1	0	3.4	2.4

Table 6.5: Self-fit test of the Gallagher 12-lead scheme.

The Gallagher scheme [150] for the 10 site accessory pathway determination was tested against itself to determine its sensitivity. Entries represent the number of leads (out of 12) which did not fit the criteria.

as the one which had the maximum number of polarity matches, without exceeding 3 incorrect polarities. In many cases there was a broad distribution of sites which had less than 3 incorrect polarities, and rarely was there an exact match with all 12 polarities for that best site. Furthermore, we observed that some sites (especially G2) were recurrently chosen incorrectly as the best-fitting site.

To determine the accuracy of the Gallagher classification scheme, the scheme was tested against itself. For example, the polarities of the 12 leads for G1 were compared to all 10 sites as if that data set were taken from a patient. The number of unmatched polarities were counted for all sites compared to one another. This result is presented in Table 6.5. For site G2, 7 of 10 sites have only 2 or less polarities wrong, resulting potentially in many incorrect classifications. On the other hand, criteria for site G8 would be highly selective, resulting in few wrong G8 classifications. The better selectivity for sites G7–G9 (higher average number of wrong match counts) may reflect the fact that AP are more common in these sites, resulting in better statistics when the original scheme was developed by Gallagher.

The ambiguity and large changes in the onset of right-sided pathways may in itself account for the low success in correctly classifying these AP and propensity to incorrectly choose these sites. The similarity of the δ -wave onset in the patterns of left-lateral sites, and smaller number of right-sided pathways may have resulted in poor statistics when determining the criteria for these sites.

This being said, we suggest that increased success may be achieved with a modified Gallagher scheme, which first determines whether the pathway is right- or left-sided (e.g. Rosenbaum type A or B [169]), then restricts the classification to either the right or left criteria. An additional criteria for right- or left-sided pathways might include P-wave to δ -wave onset duration. The averaged 'PR interval' for right-sided pathways was 75 (4) ms for this sub-group, as compared to a whole group average of 107 (22) ms (see Table 6.1). It might even be appropriate today to take advantage of the ability to obtain larger sample sizes, to design a newer set of criteria. The widespread use of catheter ablation could provide the essential confirmation of the AP location. Previously, confirmation was obtained during the much less frequent surgical ablation procedures. This limitation reduced the number of subjects available in developing the criteria.

6.7 BSPM and MFM as a function of AP site

BSPM δ wave patterns have been described extensively [75,157,159,161,170,171]. In summary, the isopotential maxima are located near the center or left side of the anterior chest wall. Discrimination between the sites is possible, because the potential minima rotate around the maxima in a set pattern, according to the AP location around the A-V ring. The minimum is located on the back for left-sided AP and on the right anterior chest for right-sided sites. The negative potentials extend along the inferior borders of the map (diaphragm) for posterior sites and along the superior edge (neck) for anterior locations.

All but 2 of the 16 single accessory pathways resulted in BSPM patterns which

could be successfully classified within 1.5 sites by comparison to the 40 ms representative maps suggested by Benson et al. [75] and simulated maps of Nenonen et al. [70]. The maps of Benson were obtained under maximal pre-excitation during pacing, thus are not considered representative of pre-excitation during sinus rhythm. However, with the assumption that maximal pre-excitation minimises interference from other sources, the earlier enhanced maps could mimic this situation, since interfering atrial signals and ventricular fusion are eliminated. This assumption is supported by a study of Giorgi et al. [170] which demonstrates that modifying the degree of pre-excitation does not essentially change the distribution of potentials. These observations permitted successful classification of the early δ -wave maps in most cases, including subjects with small δ waves. The classification of right-sided pathways was done with the maps measured 40 ms after δ -wave onset. This successful classification served primarily to confirm that our enhanced BSPM patterns agreed with previously published maps.

With this confirmation, a retrospective arrangement of the body surface potential and magnetic field maps as a function of site around the A-V ring was produced. Subjects with pre-excitation site confirmed by catheter ablation were arranged initially; the remaining subjects were positioned afterward. Since the results obtained by EPS localisation are not as accurate as those yielded by the ablation procedure, some liberty was taken to place these subjects. The order of patients in Table 6.3 reflects this relative positioning.

The BSP- and MF-enhanced ventricular maps as a function of site at 20 ms and 40 ms for 10 subjects are shown in Figures 6.11 and 6.12, respectively. Before any discussion of these maps, we emphasize that some of these maps do not represent pure pre-excitation, since fusion with normal ventricular activation can be significant in subjects with small δ waves.

The BSPM patterns at 20 ms and 40 ms are quite similar in most right-posterior and left-sided AP maps. However, amongst this group are 3 subjects with small δ waves (LA199, BS184, EA191). Two of these have a clear change in the location of

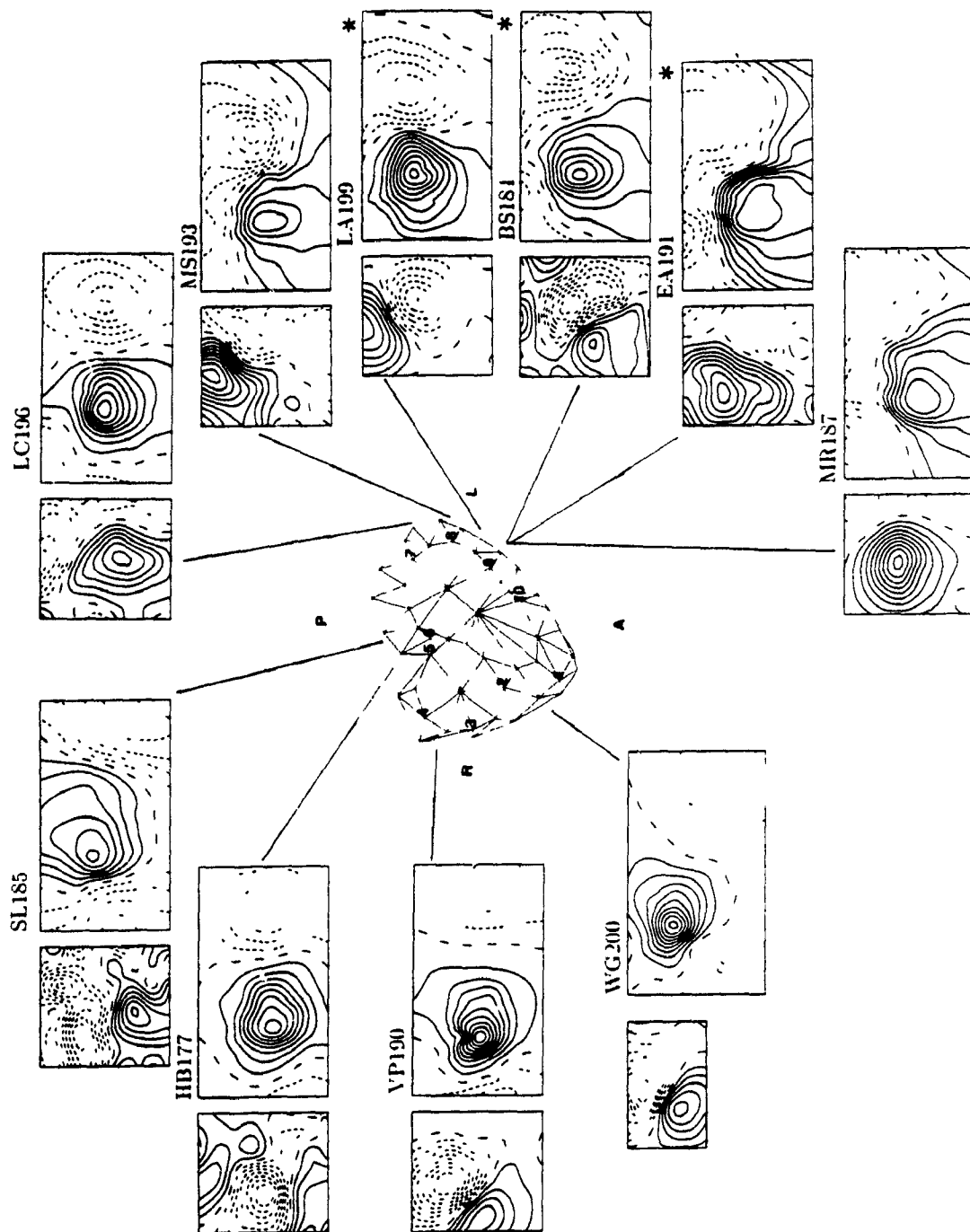


Figure 6.11: MF and BSP ventricular excitation maps at 20 ms into the δ wave as a function of AP location.

Subjects with small δ waves are marked by *.

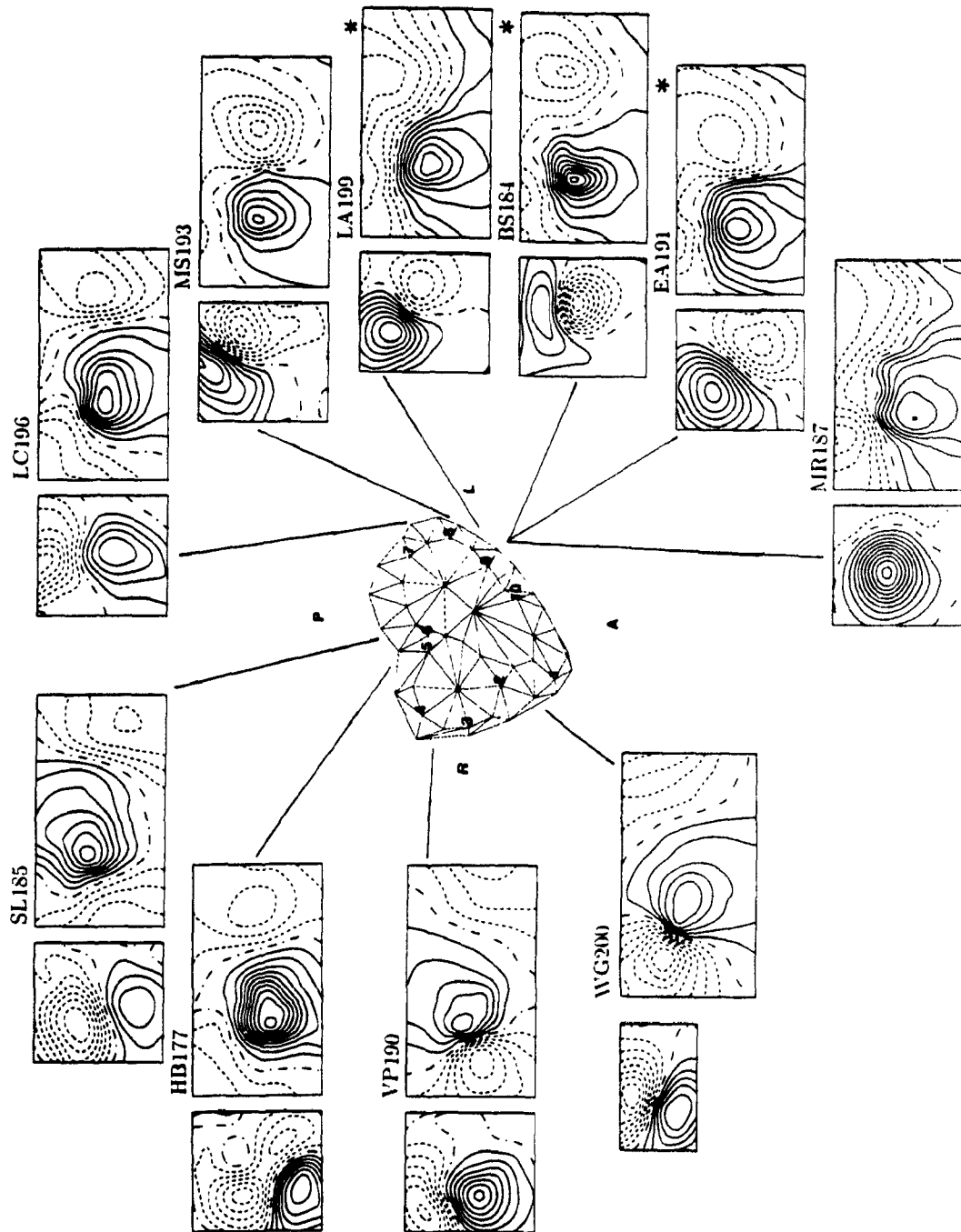


Figure 6.12: MF and BSP ventricular excitation maps at 40 ms into the δ wave as a function of AP location.

Subjects with small δ waves are marked by *.

the maximum negative potentials from 20 ms to 40 ms. Two subjects (WG200 and VP190) with right-sided AP show the greatest variability between the 20 ms and 40 ms maps.

Variations in the magnetic field maps obtained in the frontal plane as a function of site around the A-V ring, are consistent with the orientation of the A-V ring in the torso as in the case of the BSP maps (see Fig. E.5). Pre-excitation maps originating from right-sided, right- and left-posterior pathways (roughly from G1 to G7) are similar, with negative magnetic fields in the superior portions of the maps and positive fields covering inferior portions. However, close examination reveals variations consistent with the relative locations of the AP around the A-V ring. Extrema associated with anterior sites are generally more superior than their posterior counterparts (i.e. WG200 versus SL185 in Fig. 6.11). Also, the positive and negative extrema of right-sided pathways are closer to each other than for left-sided AP, consistent with their closer proximity to the anterior torso (VP190 versus LC196 in Fig. 6.12). At 40 ms, the relative orientation of the MFM extrema at these sites is consistent with the X and Y components of the equivalent current dipole (ECD) moment (P) of the BSP maps. For example, in Figure 6.12 in WG200's MF maps, the current flow, reflected by the vector perpendicular to the line joining the two extrema, points in a similar direction as the vector joining the maxima in the BSP maps. Both vectors point from the right shoulder to the left hip. For some locations, when making this association, one has to disregard the contribution of P_z to the BSP maps.

The MFM for subject HB177 at 20 ms deserves special explanation. While at 40 ms a clear dipolar pattern of pre-excitation has emerged, at 20 ms there are two maxima in the distribution. However, closer investigation of this subject revealed that pre-excitation originated from a right posterior paraseptal site; thus the superior maximum should be associated with residual atrial repolarisation, or possibly late left atrial depolarisation, while the inferior maximum is due to ventricular pre-excitation. This analysis is supported by the short PR-interval duration (see Table 6.1) typical of all right-sided AP, resulting in characterisation of atrial events during the end of

the P wave. In this case it was not possible to remove the atrial contribution because it is still varying significantly during δ -wave onset. Fenici et al. [99] recorded similar MF maps in a subject with a right posterior paraseptal AP.

MF maps of δ waves associated with AP located at left lateral to left anterior sites (G8 to G9) are distinct from other sites, with two particular patterns found. Subject MR187 has a left anterior AP (G9), confirmed by EPS. The MF maps at 20 and 40 ms show an almost monopolar pattern, with only a small negative field detected in the left upper area of the torso. A similar pattern was recorded, in the 20 ms δ -wave MF maps, for two subjects (DK195, not shown, and EA191) with δ waves of short duration. In these two cases, the area of negative magnetic field is slightly larger (see Figure 6.11, subject EA191) encompassing two minima on the left side of the torso. These two minima are suggestive of two different sources, creating a single large positive maximum. The lower of these two minima evolves and dominates at 40 ms (Fig. 6.12, EA191). The MF maps of MR187 (AP site G9) are actually consistent with the previous description of sites G1 to G7. The ECD direction correlates with P_x and P_y suggested by his BSP maps. The nearly monopolar MF maps is a consequence of the extremely anterior and deep LA location of AP, resulting in a negative field maximum outside of the measured grid area.

The MFM patterns of other patients with AP originating near G8 and G9 had the distributions found for subjects MS193 and LA199 in Figure 6.11 and 6.12 and subject CN197 (Fig. 6.6). These patterns are characterised by the separation of the MFM into positive and negative areas suggestive of current flow pointing along an oblique line roughly running from the left shoulder area to the right waist. The general description of MF maps for other sites does not apply to these maps.

Very few magnetocardiographic studies of WPW syndrome have discussed the general features of maps for varying AP locations. A number of papers produced by a Finnish group [72,81,172] have described a dipolar pattern for right and posteroseptal pathways, in agreement with our findings. However, they have described posterior and left-sided AP as generating monopolar field patterns. Good agreement is found

with maps published by Fenici et al. [173], including the left-free-wall pathways.

6.8 SMD localisation of AP from BSP and MF maps

6.8.1 Method

Standard torso model

We performed single-moving-current dipole inverse solutions on magnetic field and body surface potential maps of the enhanced δ -wave maps. Two volume-conductor models were used: (a) infinite medium, and (b) standard homogeneous torso model (Fig. E.4). Inverse solutions were obtained for seven maps selected from an interval 0 ms to 40 ms after δ -wave onset. To improve signal-to-noise before performing the inverse solutions, maps at $t - 2$ ms, t , and $t + 2$ ms were averaged to get the solution at t . A starting location for all maps was chosen near the center of the heart, at the level of the A-V ring.

In all cases, the recovered dipole source locations were compared to the known Gallagher sites in the standard torso. The A-V ring projection of Figure 6.1 and known AP locations on this epicardial surface were used in the comparison.

Individualised torso models

For two subjects (BS184 and MS193), torso models were created from MR images of their geometries. The procedure used to obtain the tessellated torsos is described in detail elsewhere [174]. Briefly, points on the boundaries of interest are first digitised and then a spherical harmonic expansion of the digitised data is obtained, resulting in the specification of the thoracic geometry at all points on its surface. From this complete description of the torso surface, any set of node points can be defined. This last feature is particularly important for the BSPM inverse solutions, where electrode locations must be specified on the torso surface with fixed distances of 5 cm along the surface in the Y direction. Inverse solutions were obtained for the infinite medium

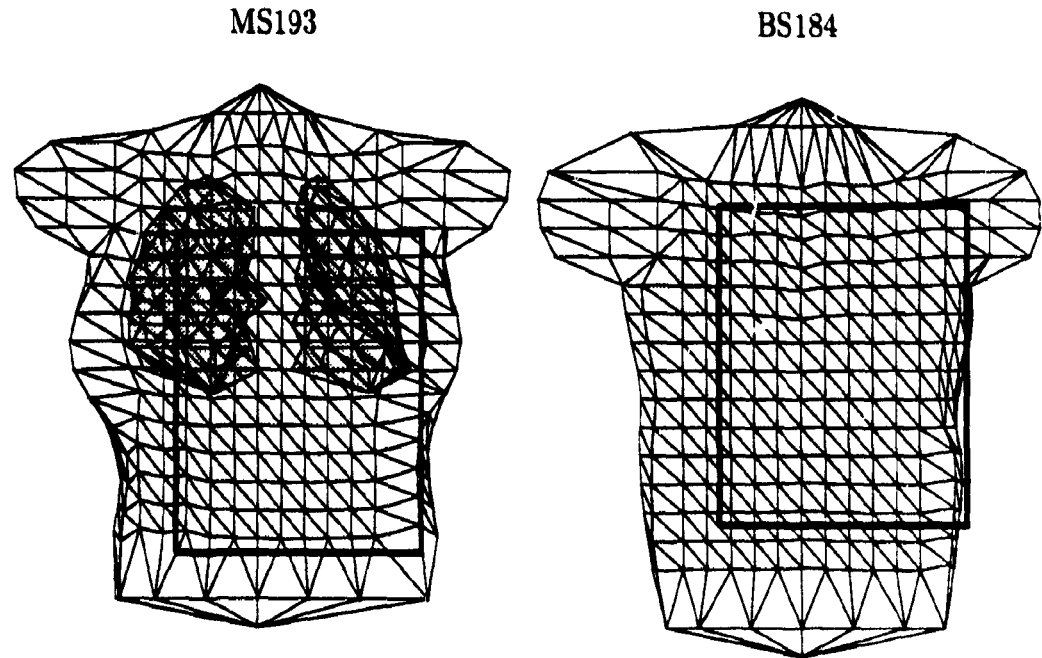


Figure 6.13: Torso models for two WPW patients. The torso surfaces have 383 node points and 762 triangles. The lungs for MS193 have 190 node points and 372 triangles.

and homogeneous torso volume-conductor models – at the same time points as the standard torso solutions. In addition, an inhomogeneous torso with right and left lungs were also used in the solutions for MS193.

The torso models for MS193 and BS184 are shown in Figure 6.13. The position of the 4th intercostal level and sternum, used as reference for the MFM grid and BSPM lead positions, were determined from markers during the MRI sessions and measurements made during the recording sessions.

To evaluate the success of the enhancement of the early δ wave, inverse solutions were also obtained from the unenhanced mapping data using the infinite medium and homogeneous volume-conductor models for both subjects. These results were compared to the equivalent enhanced data solutions.

$ \Delta R $ (cm)		8 ms	20 ms	32 ms
MFM	Infinite medium	7.64 (2.86)	6.97 (2.29)	6.06 (2.15)
	Homogeneous torso	7.33 (2.87)	6.56 (2.29)	6.63 (2.14)
BSPM	Infinite medium	4.06 (1.38)	3.86 (1.23)	4.07 (1.41)
	Homogeneous torso	3.81 (1.25)	3.81 (1.02)	3.91 (1.35)

Table 6.6: Average distance and standard deviation of the recovered DSL to the correct AP location in a standard torso model.

6.8.2 Results and discussion

Standard torso model

Standard torso inverse solution results are presented in both tabulated and graphical form. In Figure 6.14, the recovered dipole source locations, 20 ms after δ -wave onset, using the homogeneous torso model, are plotted on two views of the epicardial surface. In both views, the MFM results are extremely scattered in space, while the BSPM results are found to be located in close proximity to the A-V ring.

These results are further summarised in Table 6.6. In this table, the 3-dimensional distance ($|\Delta R|$) from the known AP location to the recovered DSL for all subjects was calculated and averaged. Inverse solutions for BSPM in infinite medium and homogeneous torso models are, on average, closest to the true AP site (~ 4 cm). DSLs recovered by inverse solutions for the MFM using infinite medium and homogeneous torso models are located ~ 6.5 cm to 7.5 cm away. In both the MFM and BSPM solutions, the infinite medium and homogeneous torso solutions are similar.

Table 6.7 list the averages of the absolute values of the components of the distance to the AP location at 20 ms after δ -wave onset. The discrepancies in the MFM X and Y directions are, on average, 2 cm larger than the BSPM discrepancies, while at 1.3 cm, the difference in the Z component is slightly smaller.

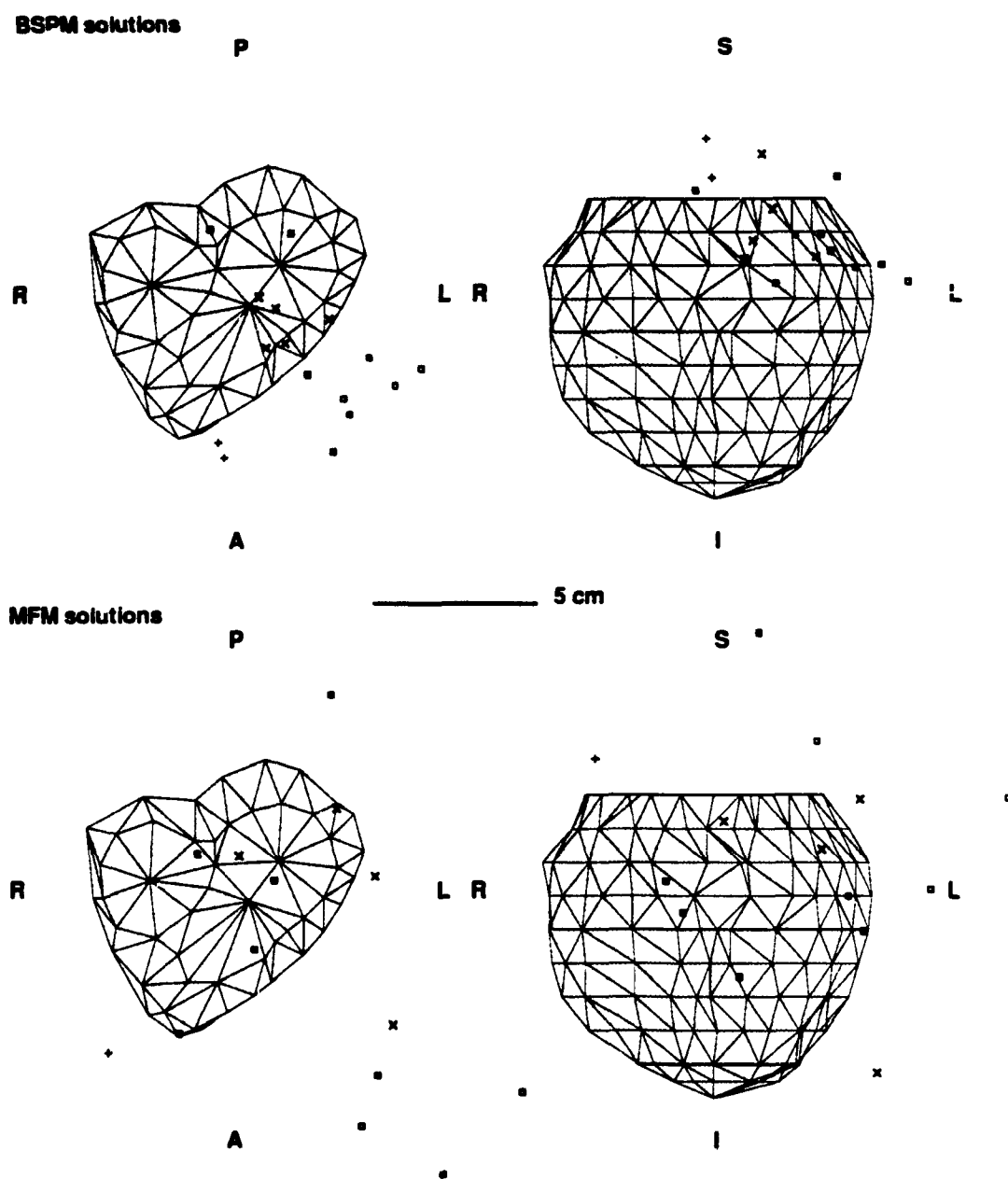


Figure 6.14: DSLs recovered at 20 ms in the standard torso. Solutions are plotted on a basal view of the epicardium at the level of the A-V ring (left) and an anterior view (right). Four different symbols were used to plot locations, depending on the known AP sites: (\times) Left posterior (G6-G7), (open \square) Left lateral/anterior (G8-G10), (+) Right posterior (G3-G5), and (solid \square) Right anterior (G1-G2).

Distances (cm)		$ \Delta X $	$ \Delta Y $	$ \Delta Z $	$ \Delta R $
MFM	Average	3.72	3.37	2.73	6.50
	S.D.	(2.68)	(2.31)	(1.75)	(2.29)
BSPM	Average	1.72	2.43	1.40	3.81
	S.D.	(1.14)	(1.60)	(1.07)	(1.02)

Table 6.7: Average distance of the recovered DSL to the correct AP location in a homogeneous, standard torso model at $t=20$ ms.

Gulrajani et al. [71] had already shown, in BSPM recordings of a group of 28 WPW patients, that the same torso conductor model used for all subjects was only able to resolve AP locations to 3 general regions of the heart: right-side, posterior and left-side. Figure 6.14a suggests a similar clustering of BSPM solutions into particular areas of the A-V ring. However, these areas do not correspond to the same areas found by Gulrajani et al. In particular, none of their solutions were laying outside the heart, where most of our left-lateral and left-anterior sites were located. These differences could result from different standard torso geometries, and in particular, variations in location and orientation of the epicardial surfaces of the heart within the torso. A clustering into regions is not found in the MFM solutions.

The MFM inverse solutions are generally further from the immediate area of the A-V ring than the BSPM. It is difficult to account for such a large difference. One possibility relates to the MCG grid position relative to the standard torso, as compared to the actual subject. The origin of the BSPM and MFM grids are at the same X and Y locations of the torso during the recordings, where MCG grid point D3 located at the intersection of the 4th intercostal space and sternum, corresponds to BSPM lead position 33. Any alignment error of these points relative to the torso model for an individual patient will be equivalent in both BSPM and MFM inverse solutions. On the other hand, the location of the MCG grid above the subject's chest can vary, and as shown in Table 2.4, will be reflected primarily in an equivalent difference in the Z coordinate of the recovered DSL. By using a constant distance to

the standard torso, a difference in the definition of the origin of the Z axis between the BSPM and MFM data, is introduced during the measurements and the modelling. However, if this were a significant factor, there would likely be a larger difference in the discrepancies of the MFM Z location than either X or Y . In fact (see Table 6.7), the Z component difference is on average smaller than that of either X or Y .

Generally, the use of the same standard (male) torso for all subjects gave somewhat better results for BSPM solutions than for MFM data. However, it should be noted that the cross-sectional area of the A-V ring is in itself only $\sim 6.5 \text{ cm} \times 7.5 \text{ cm}$. Hence, although the BSPM solutions are closer than the MFM results, relative to the actual size of the A-V ring, both results are of limited clinical value.

The objective in removing atrial repolarisation signals from the early δ wave was to minimise the AP localisation error due to movement of the wavefront from the ventricular insertion site. However, this objective can as well be abandoned in the use of a standard torso model, since the modelling errors themselves will introduce greater discrepancy than can be accounted for by the effect of distance travelled by the wavefront from the insertion site of AP. This in part explains the focus of the results just presented on the maps obtained 20 ms after δ -wave onset. In addition to the modelling errors, the MFM noise level is larger than the BSPM data, so that it is not always possible to obtain a magnetic field inverse solution much earlier than at 20 ms. The magnetic noise level affects the onset maps in subjects with small δ waves in particular, but not exclusively. In this group, fusion of ventricular pre-excitation with excitation via the HPS occurs sooner than in most other subjects – thus preventing comparisons later in the δ wave.

Individualised torso models

Inverse solutions for subject MS193 were obtained for three volume-conductor models: infinite medium, homogeneous torso and torso with lungs. The solutions for the torso with lungs, projected onto the subject's MR images, are shown in Figure 6.15. The solutions at 14 ms during the δ wave for both the MFM and BSPM results are shown.

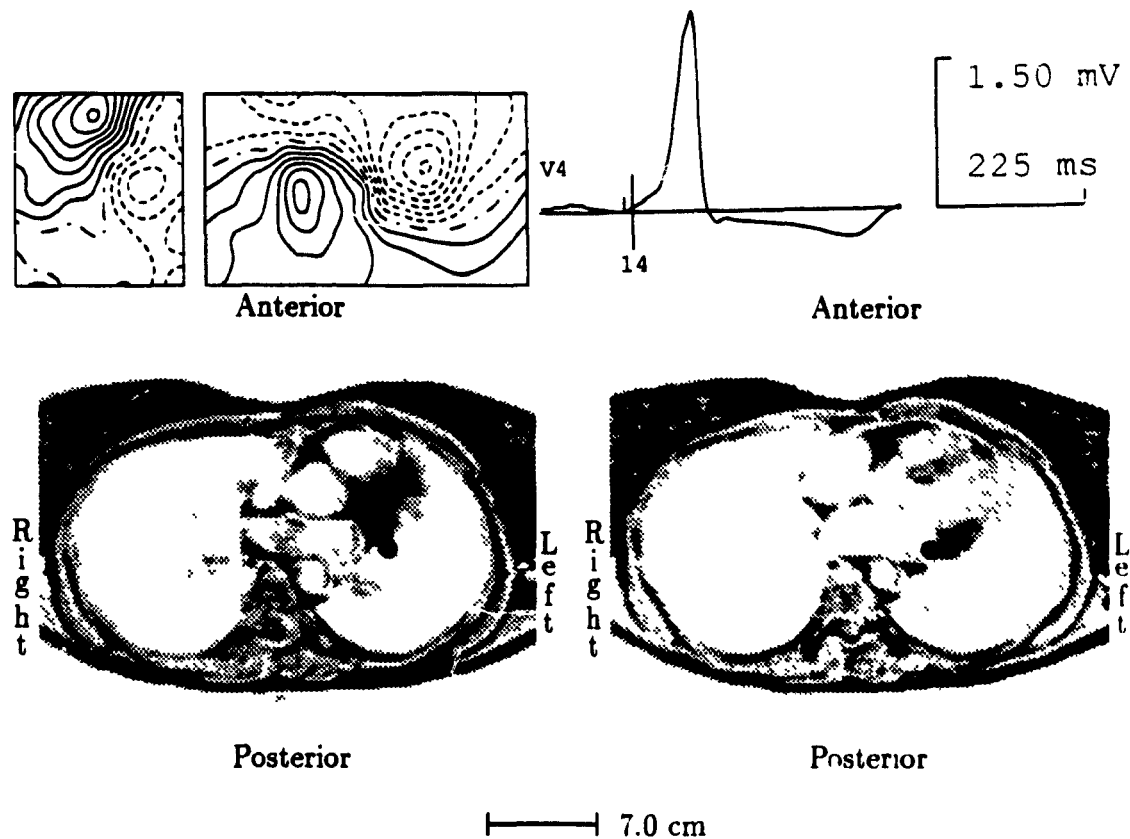


Figure 6.15: Recovered DSL projected onto MR transverse images of subject MS193. The solutions at 14 ms during the δ wave, using an inhomogeneous volume-conductor, are plotted for the MFM data (left) and BSPM data (right) with a \bullet . Above the images are displayed the maps at 14 ms and ECG lead V4.

The BSPM solutions (right) recovered a correct left lateral AP slightly above the level of the A-V ring, while the MFM solutions (left) suggest a more anterior location on the left ventricular wall.

The relative displacements of DSLs recovered from the BSPM and MFM are depicted in Figure 6.16. The two solutions are shown on frontal and sagittal views of the digitized torso (top) and expanded scales of these same views (bottom), for the first 40 ms of the δ wave. The BSPM and MFM solutions both move anteriorly, while the two solutions diverge in other directions. The MFM solutions move superiorly and

the BSPM locations move inferiorly. Included on these projections are the recovered vectors of dipole moment and relative magnitudes at each location.

BSPM solutions for subject BS184 suggest a left-anterior AP in the first 14 ms. The equivalent MFM solutions during this time were not confined to any particular region of the heart. The MFM and BSPM inverse solutions obtained using the standard male torso model placed the recovered dipole sources at 5.23 cm and 3.59 cm from the known LAL site. The same solutions placed recovered AP of subject MS193 at 20 ms after the δ -wave onset, respectively, at 10.34 cm (MFM) and 4.49 cm (BSPM) from the LL location. The result for subject MS193 was the furthest of all from the known AP in the MFM data and only 0.6 cm away from the worst BSPM result.

A comparison of the solutions obtained using the 3 different models of volume-conductors models for MS193 is presented in Table 6.8. This table contains, on the diagonal elements, the difference between the MFM and BSPM results obtained with the 3 conductor models. In the upper off-diagonal elements the MFM solutions using the 3 conductor models are compared to each other, while the bottom off-diagonal elements contain the BSPM comparisons. The average three-dimensional distance, as well as standard deviations, were computed for the 7 maps.

Ave. & S.D. (cm)	Infinite medium	Torso	Torso & lungs
Infinite medium	2.48 (0.30) ^{MB}	2.64 (0.61) ^M	2.32 (0.67) ^M
Torso	0.96 (0.09) ^B	4.42 (0.55) ^{MB}	1.47 (0.52) ^M
Torso & lungs	0.88 (0.08) ^B	1.08 (0.02) ^B	2.99 (0.46) ^{MB}

Table 6.8: Relative differences in recovered DSL for subject MS193. Infinite medium, homogeneous torso and inhomogeneous torso (torso and lungs) are compared. Superscripts *M*, *B* and *MB* denote comparisons made between 2 MFM, 2 BSPM and MFM vs. BSPM solutions, respectively.

In general, the BSPM solutions for MS193 only change by 1 cm with different volume-conductor models. The small standard deviation on all 3 BSPM comparisons reflect the stability in the solutions during the entire δ wave. The total change in

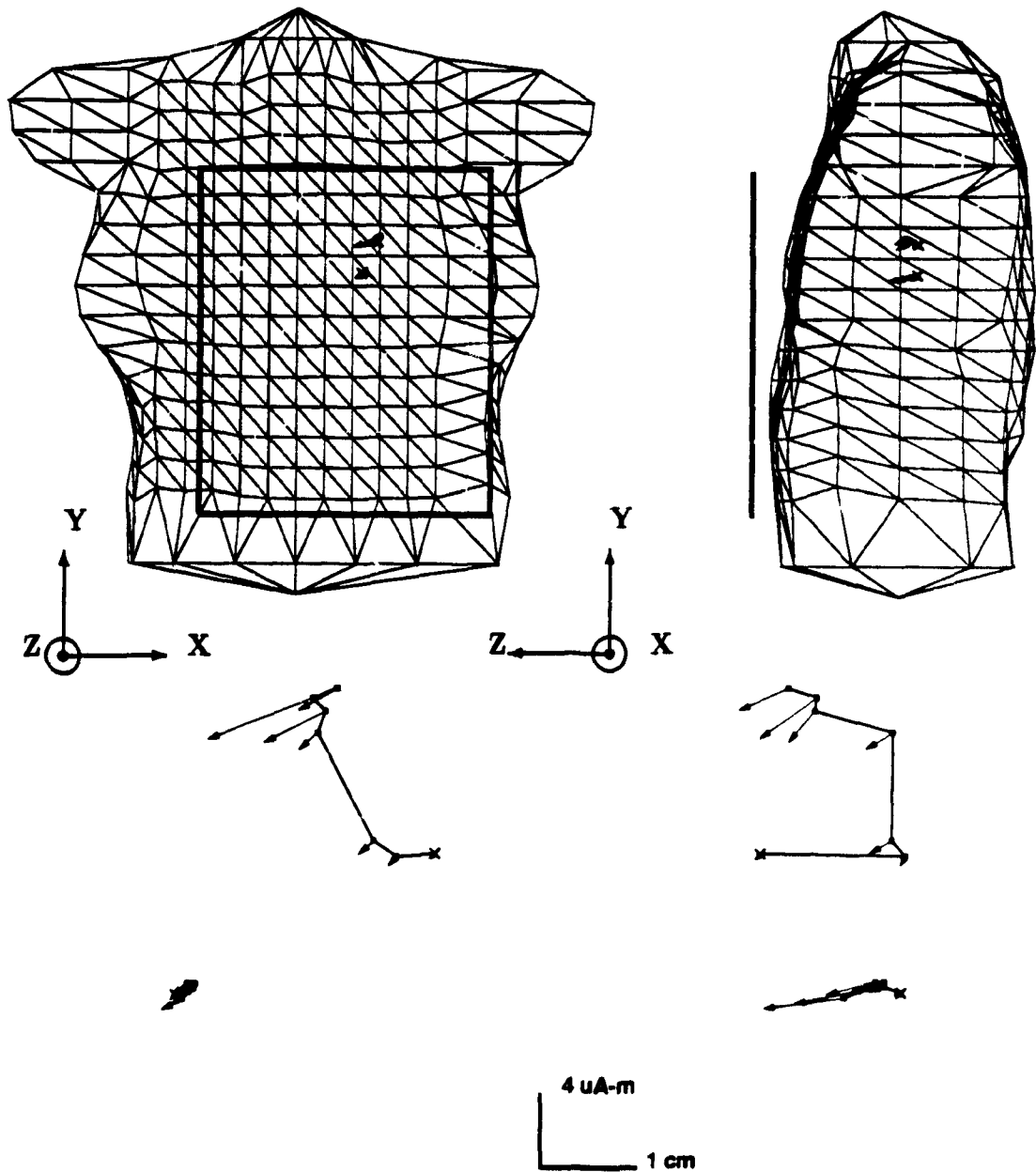


Figure 6.16: The recovered DSL projected onto the torso model of subject MS193. The solutions from 0 ms to 40 ms during the δ wave, using an inhomogeneous volume-conductor, are plotted for the BSPM and MFM data in frontal and sagittal views. The MFM solutions are above the BSPM results in both views. In the bottom, the same results and views are plotted at an enhanced scale.

Average for all subjects:	
- Standard homogeneous torso	6.11 (2.24) cm
For MS193:	
- Standard homogeneous torso	6.78 (1.67) cm
- Tailored homogeneous torso	4.42 (0.55) cm
- Tailored torso with lungs	2.99 (0.46) cm

Table 6.9: Average difference (S.D.) between MFM and BSPM recovered DSL in various volume conductor models.

location from 0 ms to 40 ms (inhomogeneous solution) was 0.6 cm.

The larger variability of DSL among conductor models suggests that the MFM inverse solutions are more sensitive to modelling parameters, but the decision as to which volume-conductor model is most appropriate cannot be made with only two MFM and BSPM data sets. The larger differences in the MFM solutions reflect the greater variability in recovered DSL during the δ wave, using various conductor models, which may in turn follow in part from the higher signal-to-noise level relative to the BSPM data (by factor of ~ 6 , Table 1.1). The total change in location during the δ wave in the MFM data was 2 cm, with the greatest displacement found in the Y direction (toward the head).

The relative differences between the MFM and BSPM solutions are not easily interpreted. These differences are repeated in table 6.9, along with standard torso results. If one assumes, that ideally both inverse solutions can recover the correct DSL, then the most accurate volume-conductor model should yield no difference in the two solutions. This rule cannot be applied universally, since the effects of any volume-conductor approximation might be more or less equivalent in both inverse solutions. However, it is known that infinite medium MFM inverse solutions are not as accurate as homogeneous torso solutions [72,81]. The small differences in the BSPM and MFM solutions for subject MS193 (2.5 cm) for the infinite medium model then

probably reflect a similarity in modelling approximation errors. The other results (comparison of a standard homogeneous, tailored homogeneous and tailored inhomogeneous torsos) more likely reflect the relative accuracy of each solution, suggesting that the MFM and BSPM inhomogeneous solution with tailored torso geometries (difference of 3 cm) most accurately reflects the true accessory pathway location.

Because of the poor S/N of the δ wave, subject BS184 had differences between MFM and BSPM solutions that were >7 cm, but the comparison of BSPM solutions for the infinite medium and homogeneous conductor models yields only a 0.36 (0.09) cm difference. The MFM solutions for these two conductor models differed by 0.99 (0.98) cm.

Unenhanced versus enhanced δ -wave solutions

In Table 6.10, the difference between the enhanced and unenhanced δ -wave BSPM and MFM inverse solutions for a homogeneous volume-conductor are presented for both subjects. The larger differences occur for maps obtained less than 20 ms after the onset of δ wave; in both the MFM and BSPM solutions this can be accounted for by the contamination from the atrial signals. The discrepancy is smaller after the 20 ms mark since for subject MS193 the δ wave dominates the measured maps and in subject BS184 the small difference confirms that similar solutions were found. However, the source that has been located in these latter solutions, in particular by the MFM solution, corresponds to normal ventricular activation (see Figs. 6.9 and 6.10). Also, the differences in the latter case are smaller than in subject MS193 because the signals due to normal ventricular activity are larger (S/N is higher).

For subject MS193, there is a particularly small difference in the BSPM solutions after 20 ms, and a very short distance is travelled by the recovered DSL in the enhanced data (0.6 cm); this supports the conclusion that even the very earliest enhanced maps reflect the pre-excitation signal. Whatever residual atrial signal might be present, it minimally affects the localisation results of these maps.

In the case of MFM solutions for subject MS193, the larger differences that occur

MS193	2	8	14	20	26	32	38 (ms)
BSPM	5.22	2.56	1.14	0.63	0.37	0.22	0.15
MFM	8.64	12.14	13.64	14.36	1.48	1.28	1.33

BS184	2	8	14	20	26	32	38 (ms)
BSPM	9.32	2.93	1.13	0.74	0.16	0.06	0.04
MFM	6.35	8.78	9.67	7.40	0.73	0.28	0.12

Table 6.10: Difference (cm) between recovered DSL in unenhanced and enhanced data.

These results are for homogenous volume-conductor inverse solutions.

after 20 ms into the δ wave might be explained by a number of factors. The lower S/N of the MFM may result in poorer localisation results, even during times of significant pre-excitation. The volume-current contributions due to inhomogeneities may be more important in the MFM solutions [174]. However, another explanation may be that the atrial signals were not satisfactorily removed. The greater sensitivity of the magnetic measurement system to right atrial repolarisation sources (see Chap. 4), particularly due to the closer proximity of the right atrium to the front-end coil, may result in larger residual atrial signals. These residual signals would distort the δ -wave maps, which due to the deep location of the left lateral pathway, could be relatively smaller than the BSPM signals.

The contributions of atrial repolarisation are reflected in the results for subject BS184, who has a small δ wave. Stability of the DSL recovered from the BSPM data during the first 20 ms of the δ wave by the inverse solution suggests that the atrial signal was successfully removed from the early maps, and that the enhanced δ -wave maps faithfully reflect the ventricular pre-excitation signal. The solutions for the MFM data might have been better with a higher S/N level. But the greater sensitivity of the gradiometer to the proximal right atrial sources may always adversely affect cases in which small δ waves are encountered, particularly because the associated AP are found almost exclusively in the deep, left ventricular wall.

6.9 Discussion

6.9.1 Success of δ wave enhancement

The primary objective in enhancing the δ wave onset was to (i) include subjects with minimal pre-excitation, whose δ waves are small, and (ii) minimise errors of localisation by inverse solution due to travel of the pre-excitation wavefront. In the case of the BSPM data, the stability of the enhanced patterns and recovered dipole source locations confirm that the enhancement technique will allow both objectives to be met. However, the DSLs recovered by BSPM inverse solutions spanned only 5 mm during the entire 40 ms of δ wave for the subject with a large δ wave (MS193). This suggests that the enhancement is not critical for all subjects.

In the case of the subject with a small δ wave (BS184), the early BSPM location of the AP to the left antero-lateral area confirms the success of the enhancement. Soon afterward, fusion of pre-excitation and normal ventricular depolarisation interfere with successful localisation of the maps. This result suggests that the enhancement of the early δ wave would be beneficial in localising AP in this sub-group of WPW patients. A universal application of such a protocol in the pattern-recognition techniques would allow most patients with ECG manifestations of pre-excitation to be included in non-invasive protocols for localisation of AP site.

Right-sided pathways, because of their tendency to cause extremely early pre-excitation, overlapping with the P wave, may need special consideration in an enhancement protocol. In actual fact, right-sided pathways (with a normal right-sided pacemaker site) are unlikely to produce a small δ wave, and may not need any enhancement.

Two factors may have contributed to some of the problems in the early δ wave MFM enhanced patterns. Inherent to the magnetic field measurement system is its higher sensitivity to atrial signals and right-atrial activation in particular (Chap.4). This feature may have, in some cases (HB177 is an extreme example) prevented the removal of most of the atrial signals. These residual atrial signals will distort maps at

the onset of δ wave, and in the particular case of some small δ waves, the atrial signal has severely distorted the δ wave of short duration.

The noise in the MFM recording system could have also prevented successful enhancement of the small δ waves. This noise level also affected the early MFM in other subjects, but in these cases, the effect primarily resulted in a later δ wave onset time (see Table 6.1).

6.9.2 Map features

Early δ wave for cases with right-sided pathways

The BSPM and MFM of subject VP190 and other subjects with right-sided pathways (Fig. 6.8) are a clear example of the preferential detection of radial³ currents in BSPM recordings and of tangential currents in MFM recordings. At least two publications [75,159] have associated the onset pattern in right-sided pathways with an initial endocardial-to-epicardial movement of the depolarisation wavefront. This is consistent with the finding that a majority of right-sided pathways have a subendocardial course [67].

In these right-sided pathways, the subendocardial ventricular connection produces an initial endo-to-epicardial wavefront propagation as observed by DeAmbroggi et al. [159] and Benson et al. [75]. This wavefront, initially spreading within the thickness of the right-ventricular wall, will produce a strong radial component, preferentially detected in the potential measurements, and consistently reflected as a strong posterior-to-anterior current direction. This effect would be most significant in pathways located closest to the anterior chest (e.g. right lateral sites), as opposed to the deeper right anterior and posterior pathway sites. Concurrently, the axial propagation in the myocardial wall produces a current component parallel to the anterior chest. The relative insensitivity of the magnetic field measurements to radial sources results in a preferential detection of this axial current flow.

³Terms radial and tangential refer to the directions with respect to cavities of the heart chambers (atria and ventricles)

The initial large positive potentials on the anterior torso and very small negative potentials in posterior regions reflect the posterior to anterior current direction, due to a source located relatively close to the anterior chest wall. This significant radial current will exist only temporarily. The change in δ wave BSP maps 30 to 40 ms after onset reflects the transition to a dominant axial current flow. At this time, areas in the BSP maps which were previously positive are now negative because the source is now moving away from the site of initial pre-excitation, at the base of the heart.

An endocardial-to-epicardial current flow may also be present in left-sided pathways. However, the relative depth of the left heart in particular, as well as the absence of a large change in orientation of the left heart wall, obscure the detection of this change.

Effects of fusion

It has been suggested that by 20 ms, the MFM of subject BS184 primarily reflected normal ventricular activation. The association of later MFM patterns with normal QRS features was obvious in subject BS184. However, the similarity of this pattern with the δ wave MFM data of other left-lateral AP (G8/G9), creates doubt as to the origins of the typical left-lateral MFM recorded in this study group. In some cases, these maps are clearly taking place during pure pre-excitation, but the similarities may, in other cases, lead to false classification to a left-sided pathway.

This situation arises because the sensitivity of the gradiometer to proximal sources during the magnetic field measurement results in a higher sensitivity of this measurement to the normal ventricular activation processes. Early QRS depolarisation originates from the septal and apical areas [175]. The left-lateral ventricular wall, involved in the actual pre-excitation, is deeper, hence when fusion occurs, there could be significant contribution from normal excitation, possibly greater than in the BSP maps, even in subjects exhibiting relatively large pre-excitation. The MF maps described previously for these sites, in some cases, may in fact be a combination of normal ventricular excitation (e.g. 40 ms for BS184 - Fig. 6.12) and a pre-excitation

pattern similar to that recorded for MR187 (Fig. 6.11).

AP site determination with MFM patterns

With the exception of deep LL and LAL pathways (G8 and G9), we have established a description of δ wave MF maps consistent with the relative locations of the AP sites around the A-V ring (Section 6.7). Although MF maps of sites G8 and G9 may be affected by normal ventricular onset, this pattern is nonetheless typical for these sites. The current direction at these locations, as suggested by the orientation of the zero-lines, is generally pointing from the left shoulder to the right waist. This pattern would be highly selective for the G8 and G9 sites. For sites G1–G7, the source current depth and orientation is reflected by the relative location and orientation of the maximum and minimum fields. The zero-lines suggest current flow from right to left, while pointing toward the shoulder for posterior locations and to the waist for anterior locations. The criteria found for discriminating AP sites from the MF maps of this group of WPW patients can now be used as a training set, and applied to locate AP sites in test groups of WPW patients.

6.9.3 Single-current-dipole inverse solutions

Accuracy of localisation

A number of parameters may limit the accuracy of AP-localisation results independent of the choice of volume-conductor model. Some of these have been explored in different parts of this study (Sec. 2.3.6 and 6.3.2) and will now be summarised.

- Because of the small size of the accessory connections (<1.5 mm diameter by 1 cm to 2 cm in length [67]), the insertion in the ventricle should create a fairly localised source at onset. However, inverse solutions of the WPW maps from the Horáček anisotropic heart model [70] (Sec. 2.3.6) suggest that ~ 1.4 cm error should be associated with the approximation of the pre-excitation wavefront by a single current dipole.

- The residual contributions of atrial activity, in the case of the BSPM data, are small (Section 6.3.2). Very early in the δ wave 0.5–1.0 cm error may be attributable to these residual signals, but within 14 ms the error drops to less than 3 mm. These estimates result from comparison of solutions obtained for the TAT-enhanced data of subject CM186, versus an accurate (theoretical) removal of the atrial contribution. In the case of the MFM, these numbers were not determined, but the increased sensitivity to atrial activity suggest this contribution to the error could be larger.
- Independent of any source and volume-conductor model, the δ wave is the signature of ventricular pre-excitation. Localising this signal, using any of the techniques studied, yields a result correlated to the site of ventricular insertion of the accessory connection. This point is 1–2 cm beyond the insertion point in the atria [67]. Further, the course travelled along the A-V ring, from the atria to the ventricles, is unpredictable. Since the atrial insertion side of the connection is often ablated, this discrepancy in sites cannot be removed.

In summary, these effects contribute on the order of 3.0–4.5 cm uncertainty in the localisation results.

Volume-conductor effects

No previous study has addressed the relative inaccuracies of BSPM and MFM inverse solutions applied to measured patient data. In previous separate studies (some of the more extensive ones are [71,72,73,74,81,165]) a variety of source and volume-conductor models have been used, making direct comparisons of results somewhat difficult. Our choice of a single current dipole source and standard volume-conductor model, provided a comparison and direct information on the relative difference of the two solutions. Our approach did not require any individualised patient geometry, and in a clinical setting, could have been the most efficient method to localise the AP with either MFM or BSPM data and inverse solutions.

The results obtained for the infinite medium and standard torso model are not promising, particularly for MFM data. In the case of the BSPM data, the average discrepancy of 4 cm is within the expected uncertainty of 3.0–4.5 cm. The additional discrepancy in the MFM data has not been accounted for with any certainty, but may confirm the results of modelling studies in our laboratory which have suggested that magnetic inverse solutions are more sensitive to the accuracy of the conductor model [174,176]. In both cases, a large contribution to the differences should be associated with variations in position and orientation of the heart between individuals, which will not only affect the localisation results relative to a standard epicardium, but in extreme situations may also change the measured distributions, influencing pattern recognition localisations.

The present study confirms previous reports [71,70,177,176,174] which conclude with a need for individualised torso geometries to increase the accuracy of SMD inverse solutions. Although only two subjects were studied, there is convincing evidence that the BSPM inverse solutions have an accuracy well within the expected uncertainty and are less sensitive to the volume-conductor models and hence, volume-current contributions. In fact, since the change in recovered DSL with different conductor models (infinite medium, homogeneous and inhomogeneous torsos) was much smaller (1 cm) than the 3.0–4.5 cm uncertainty from other factors, the simplicity and speed of an infinite medium solution make it very attractive and practical. In this model, the potentials must however be calculated on a surface representative of the subject's geometry. The MFM results, relative to the BSPM solutions, suggest that a realistic inhomogeneous volume-conductor (torso with lungs) is necessary in order to obtain an equivalent level of accuracy. Finally, the difference of the recovered MFM and BSPM DSL for subject MS193 using the inhomogeneous torso solution is only 3 cm on average. This difference, within the expected accuracy, and source locations on the left lateral aspect of epicardium close to the A-V ring, suggests that both MFM and BSPM solutions can reflect the AP location equally well.

To absolutely determine the accuracy of MF and BSP map single-current-dipole

inverse solutions the following information would be required:

- individualised torso geometries, with lungs.
- accurate correlation of reference points on body to MR images and, as suggested by Hren [174] from simulation results, knowledge of the absolute location of the electrodes on the torso surface and the positions of the MFM grid points above the anterior chest.
- X-ray image of RF ablating catheter in place.

Merits of pattern recognition versus numerical inverse solutions

The pattern recognition techniques (12-lead and BSPM) applied to the enhanced data in this study were quite successful. The simplicity of these inverse techniques for WPW accessory pathway localisation compared to the numerical inverse solutions merits further effort toward automating and increasing the accuracy of the pattern matching techniques. Much effort is presently directed toward improving MFM and BSPM inverse solution accuracy. The present cost of time and resources necessary to obtain the accurate numerical inverse solution estimates of AP locations may not be justifiable in the clinical setting.

6.10 Conclusions

Two primary conclusions can be derived from results yielded by this study. First of all, the enhancement of the early δ wave in WPW data by removing the interfering atrial repolarisation signals is beneficial when localising the AP from BSPM data in patients exhibiting minimal pre-excitation. A consistent protocol, which includes enhancing the early δ wave, applied to all suspected cases of left-sided accessory connections would allow the non-invasive localisation of such pathways. Performed before invasive EPS and ablation, this procedure would minimise the time involved in such procedures and decrease risk to the patient. Enhancement of δ waves due to right-sided pathways may be of limited use, since these subjects rarely exhibit

minimal pre-excitation. As well, the overlap of atrial depolarisation because of very premature pre-excitation may contribute a large residual atrial signal.

Secondly, many factors suggest that the ideal objective of accurately localising accessory pathways in WPW patients, and perhaps other cardiac sources non-invasively, may be futile. The maximum accuracy of 3.0–4.5 cm, estimated from results of this study and from the anatomical nature of these pathways, has been achieved long ago. For example, the 12-lead ECG schemes such as Gallagher's [150], extensively in use already, subdivide the A-V ring into 10 locations or segments. With an approximate cross-sectional area of 6.5 cm × 7.5 cm, the total perimeter of the A-V ring is only ~22 cm. The Gallagher scheme, hence has already subdivided the A-V ring into ten 2 cm representative segments of sources of pre-excitation as accurately as can be expected. All that may be necessary are additional locations representative of the rarer septal locations. This does not suggest specifically that Gallagher's scheme should be universally applied. As suggested by Yuan et al. [156], other ECG schemes have better predictive value, but they are all similar in nature, ultimately yielding accuracies within the limits we have determined. We have also proposed that catheter ablation of sites could facilitate the design of a new, possibly more accurate non-invasive classification schemes based on 12-lead ECG or MFM. Such schemes should consider the PR-interval duration as a primary discriminator between left- and right-sided pathways.

Conclusions

PR-interval mapping

A comparative analysis of BSPM and MFM patterns in a group of 30 subjects was presented and the following conclusions were made:

- Magnetic field signals generated by the atria are relatively larger than corresponding electrical potentials, due to an increased sensitivity of gradiometers to the right atrial current sources.
- This increased sensitivity permits the identification of the transition period from right-atrial depolarisation to right-atrial repolarisation in MF maps. This time occurred at ~ 65 ms after P-wave onset.
- Because of an effectively decreased sensitivity to left-atrial sources in MF maps, BSP maps are advantageous when studying left-atrial activity. In particular, the end of left atrial depolarisation and onset of pure atrial repolarisation was easier to identify in BSP maps.
- The occurrence of peak fields on the edge of both BSP and MF mapping areas suggests that future atrial mapping studies would be enhanced by extending the measurement grid.
- Atrial repolarisation is measured during the PR segment of BSP and MF maps.

His-Purkinje-system mapping

In a group of 30 subjects, various signal-extraction techniques were used in an attempt to isolate the spatial features of the His-Purkinje system from the atrial repolarisation pattern in the PR segment. In summary, the following conclusions were made:

- In a normal subject, the spatial features of HPS cannot be measured and separated from the atrial repolarisation pattern.
- The PR-segment ramps reflect atrial repolarisation currents. No significant HPS signal contributes to these ramps.
- The dipolar patterns found by means of the four extraction techniques (SVD, KLT, CT, TAT) reflected, at the body surface, the continuous changes in the atrial repolarisation current sources as a function of time. Such changes violate the assumptions made in the extraction techniques, leading to erroneous conclusions about the origin of these dipolar patterns.

δ -wave mapping and AP localisation in WPW syndrome

The signal-extraction techniques were applied to a group of 16 WPW patients, exhibiting varying degrees of pre-excitation. Analysis of these enhanced maps led to the following conclusions:

- An average atrial repolarisation map can be successfully removed to enhance the early δ wave, particularly in left-sided pathways.
- During pre-excitation onset via some right-sided APs, the axial wavefront propagation (relative to heart) is detected mainly by the gradiometer, while the radial current flow is reflected predominantly in the BSP maps.
- Amongst all 4 subjects with right-sided AP, δ -wave onset occurs sooner relative to P-wave onset ($75 \text{ ms} \pm 4 \text{ ms}$) than in other subjects belonging to the study group. This observation, if found to be consistent in right-sided AP, could be an additional criteria in AP localisation pattern recognition schemes.
- MFM and BSPM δ -wave patterns both reflect the relative location of the sites of accessory pathways on the A-V ring. MF maps obtained in this study, and their description, could be used as a training set in the determination of AP from MFM δ -wave patterns.

- Catheter ablation of AP will assist in developing these improved non-invasive AP localisation schemes, which include determination of PR-interval time and signal enhancement of the early δ wave in sinus rhythm.
- We found that MFM and BSPM single-moving-dipole inverse solutions of the δ waves have a limited accuracy of 3.0–4.5 cm. This results purely from limitations in the SMD source and volume-conductor models, and the actual length of the accessory connections. Increased inverse solution accuracy will be achieved with individualised torso volume-conductor models, taken from MR images, and source models which reflect the distributed nature of the propagation wavefront. However, such numerical inverse solution techniques are extremely labour intensive. Consequently, effort should be directed toward developing improved pattern-recognition schemes to obtain preliminary estimates of the anatomical location of the AP. At this time, the pattern-recognition schemes are easier and more practical to use than numerical inverse solutions in the clinical setting, while leading to similar accuracy. Following these preliminary estimates, invasive methods which match the pattern of a pacing catheter with the δ -wave pattern can be used to accurately locate the AP. Having located the AP, ablation follows.

Final comments

The measurement and parallel analysis of cardiac magnetic field and body surface potential maps has provided new insights into electrophysiological mapping and signal extraction.

- Manipulation of electrophysiological mapping data should proceed with caution. Before associating any physiological significance to numerically manipulated data, as in the signal-extraction techniques explored in this study, a firm understanding of the nature of the mathematical descriptions and all physiological parameters associated with the problem in question is necessary. Applied

appropriately, a technique which might fail in one problem (e.g. HPS) could be successful in another (e.g. WPW).

- A number of examples have been identified where the information contained in BSP and MF maps provides complementary information about the electrical processes of the heart. In particular, MFM is more sensitive to sources closest to the gradiometer and anterior chest, and might reveal specific information about the electrical function of the right heart. On the other hand, this increased sensitivity to the proximal sources in the heart can interfere with the detection of events in the deeper left heart. As a result, BSPM more accurately reflects the electrical processes of deeper sources.
- Although the MFM results in this study were at times limited by a higher noise level than the BSPM data, it is clear that measurement of both the magnetic and electric fields would provide the most complete, non-invasive facility for the study of electrical processes in the heart. Most often equivalent information can be deduced from both systems, but as suggested, because of the sensitivity of the MFM to the right heart, there can be exceptions. Particularly in the research environment, this complete data set would be beneficial to understanding heart function and developing the most accurate diagnostic tools.

A MCG and BSPM Recording Procedures

A.1 Before participant arrives

- get 3, 2400' recording tapes from Biophysics
- charge razor and batteries
- make sure dewar is topped with He
- put dewar in shielded room
- tune SQUID
- prepare electrodes - apply collars, apply paste, remove excess, remove collar peel backs
- clean tape drive
- load mapping program from boot tape

A.2 Have the following available in the shielded room

- electric razor
- 4 disposable limb electrodes
- alcohol swabs
- alcohol bottle
- gauze wipes
- measuring tape and chest calipers
- surgical tape
- ECG limb electrode and MCG cables
- towel
- pen
- MCG recording information sheet
- clothing for participant

A.3 Participant arrives

- sign consent form if not already done
- allow participant to change in shielded room
- remove all jewellery, watches, dentures etc.
- get participant info - height, weight, DOB, measurements
- apply limb electrodes - shave, alcohol rub, dry

A.3.1 BSPM

- prepare skin - shave, alcohol rub, towel rub down
- mark 4th intercostal space around torso
- applying electrodes
 - back first, with participant sitting
 - electrode tails around left side
 - tape down back, participant lies back
 - apply and tape down front electrodes
- connect limb electrodes
- pass BSPM cables through hole and connect
- enter participant/recording information
- turn on batteries
- view all BSPM electrode signals - attempt correction of noisy ones
- remember - electrode number = dial number + 1
- turn off batteries and wait at least 20 minutes from time of electrode placement to ensure proper conductivity
- do Quality check at terminal
- lights off in shielded room
- record BSPM
 - normally 30 seconds at 5mV, 500 Hz
 - WPW: 2 minutes at 5mV, 500 Hz
- turn off batteries (and anytime there is a delay)
- unplug BSPM cables and pass back through hole
- begin removing electrodes from participant's front, then back
- wipe clean with gauze and wet facecloth
- do not remove limb electrodes, but change to MCG cable
- re-mark 4th intercostal space on front
- give participant top if female or if cold

- dismount BSPM tape, mount MCG tape

A.3.2 MCG

- connect MCG limb electrode cable
- make sure participant is lying straight on bed
- level chest and shoulders
- lower gradiometer to within ~ 0.5 cm of highest point on chest
- position D3 at mark
- adjust sliding X and Y markers to read D3
- check range of bed
- measure SQUID to chest distance at all reference points
- pass MCG cable through hole and connect
- turn on power to MCG channel
- check that signal is being picked up by SQUID
- position participant at A1 - cover if cold to avoid shivering
- enter participant/recording information
- turn on batteries, do Quality check
- check that all channels are present - 114,115,116,127
- begin recording, observing signal on scope
- be sure to note any repeats on MCG recording sheet

A.4 End of session

- remove remaining limb electrodes, clean, participant dresses, call cab
- charge batteries
- clean electrodes - remove paste from electrodes, clean cups with alcohol and swabs, wipe entirely with alcohol, wipe tails, apply new collars

B Averaging and DALECG

B.1 The averaging process

The term averaging implies the accumulation of N observations and then the division by N of this sum to obtain a single representative value. In practice, when obtaining this average of (semi-)periodic waveforms, such as an ECG complex, for the purpose of improving S/N levels, other functions are involved besides the actual summation and averaging. Usually it is one particular step in the full process that makes each program novel and is thus emphasized by the names of many techniques and programs [119,138,178,32].

Specific steps required in any averaging of ECG or MCG complexes are beat detection, inclusion/rejection testing and alignment of successive waveforms. The most common techniques required and used to perform these tasks are:

- 1) **Level Triggerring** - The time reference point is detected when the signal's value exceeds some preset threshold.
- 2) **Contour Limiting** - A contour (or template) is constructed as a reference waveform and the detection occurs as the successive waveforms are fitted in the contour.
- 3) **Correlation** - A correlation function is evaluated between a template and the successive waveforms to obtain the optimal alignment. Alperin and Sadeh [179] have shown that the correlation techniques have higher success rates for correct alignment.

The averaging process used in this work exemplifies how some form of all these functions can be required in a complete averaging package. The averaging program has been developed over many years by members of the Department of Physiology and Biophysics at Dalhousie University [22,32]. The Dalhousie ECG Analysis Program (DALECG) is a highly flexible program, written as a collection of modules which can be combined and adapted to accommodate a wide variety of data (e.g. 12 lead

ECGs, Frank lead ECGs, body surface potential maps (BSPM), magnetocardiograms (MCG), etc...). The versatility is achieved mostly through the large number of parameters defining such essentials as the number of multiplexed leads, sampling rate, sampling time, etc... The program has 2 main functions. Firstly, as in this application, it is used for straight (off-line) ECG/MCG averaging. It also provides a separate set of routines used for ECG classification and diagnostics (Novacode ECG Classification Program [32]).

The following short description of DALECG applies to both the BSPM and MCG data averaged in this work. The whole process can be grouped into three main steps: beat detection, family assignment and beat alignment, and averaging. A more detailed description of each of these steps follows.

B.1.1 Beat detection

Up to 3 independent leads are used for beat detection. The three leads used for beat train selection in the BSPM and MCG recordings are the Frank X, Y and Z orthogonal leads and limb leads I, II and III, respectively. Each of the 3 leads are scanned using 8 slope and 11 amplitude detection algorithms. From these 3 to 19 'beat trains' are identified. A beat train consists of a sequence of time points where an event, as defined by each of the 19 criteria, is detected. At the end of the scan, one beat train from each lead is selected as appropriate for that lead. From these three trains, up to 7 combinations are formed, to maximise the number of beats detected. These new trains are then checked for number of beats, minimum and maximum variation of the R-R intervals, and number of R-T-R patterns to choose the single beat train to be used in all further processing which best represents the recording.

A check was made for differences in averages using the two different lead groups in BSPM and MCG recordings by setting up a BSPM version which used the limb leads for the detection rather than the Frank leads. It was found that although the detected R-wave maximum location may vary by several milliseconds, the actual average waveform is identical. The equivalent check was not made for the MCG data

since the torso electrodes required to obtain the Frank leads would interfere with the magnetic recordings.

B.1.2 Family assignment and beat alignment

Each beat detected becomes the template of a new family or is assigned to an existing family. The first beat automatically becomes the template for family 1. The next beat will either be assigned to the first family or will become the template for family 2. Several tests are performed to assign beats to a family.

- A correlation algorithm is used to time-align the candidate beat with the template, using one of the family's large amplitude leads. The co-variance is calculated over a window centered on the QRS complex, using a width twice that of the QRS. A notch filter centered at 60 Hz is applied to the data to prevent aligning on cycles which are in phase.
- Similarity tests are performed on a number of pre-defined leads (pre-cordial in BSPM case or limb leads in MCG's). The top 10 consistently directed rises and falls are located in the template. The search is done through the complete one or two second window. The inner 50% of each of these segments are located and then compared to the same points in the candidate beat. If these tests are passed then the reverse comparison is performed. The top 10 rises and falls of the candidate beat are now identified and the family template is examined for similar rises and falls. We have now tentatively assigned each beat to a family.

B.1.3 Averaging

Non-linear interpolation is now used to re-sample the candidate beat (to .5 ms accuracy) to match the sampling of the template beat. All beats in all leads assigned to a family have their baselines adjusted to match the baseline of its family template beat. This process is demonstrated in Figure B.1. The candidate and template beats are subtracted (after alignment and re-sampling) to obtain their relative drift. A third order polynomial is then fit to the difference to obtain the desired correction. This fit

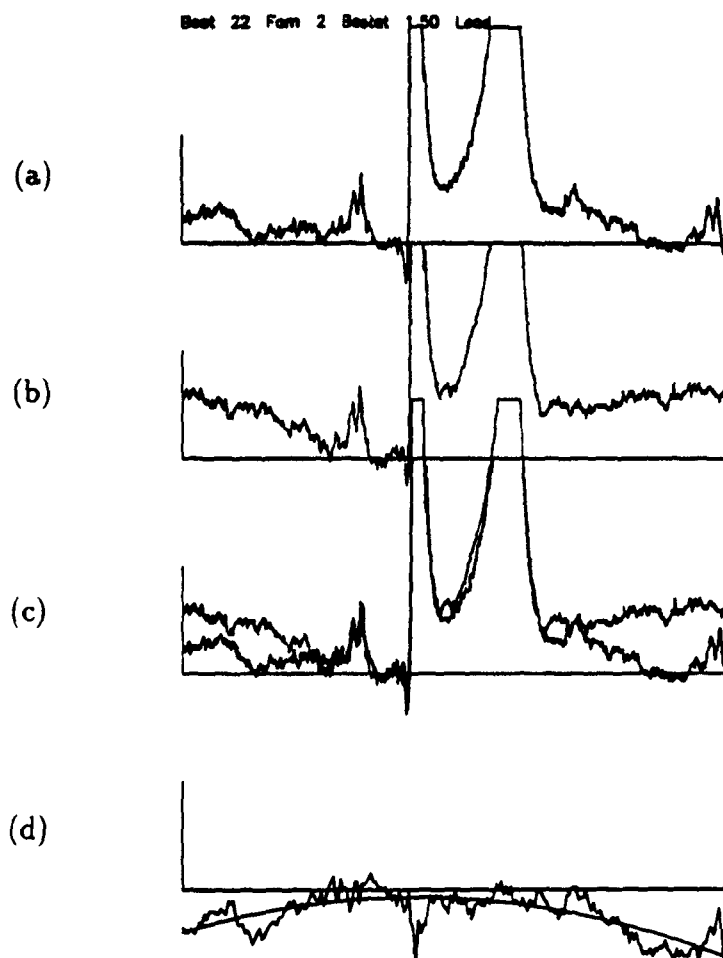


Figure B.1: Baseline adjustment of candidate beat.
(a) Template Beat; (b) Candidate beat; (c) Superposition of (a) and (b); and (d) Difference (a) - (b) and 3rd order polynomial fit.

is then added to the candidate beat to obtain a new baseline which better matches the baseline of the template. However, if a satisfactory fit cannot be achieved the candidate beat is not included in this family, independent of decisions made for other leads.

During the process of matching the candidate baseline with that of its family template, a test is made to identify which beat in a family actually has the flattest baseline. This is done by comparing the average level in a 50 ms segment -100 to -50 ms before R-onset (during the PR interval) of the candidate beat to the same level in the preceding and following beats. As each comparison is made, and a new flattest beat is identified, the baseline correction used to match the baseline of this new flattest beat to that of the template is saved in an accumulator. This information will be used after the final average has been obtained to adjust the baseline to correspond to that of the flattest member beat of that family.

In most cases more than one family is obtained. Usually the family with the most members is chosen as the representative family. Other or all families can be selected (i.e. ectopic beats) if desired. The members of the representative family are now summed, calibrated and averaged and the correction for flattest beat is applied.

A final baseline adjustment to the average is necessary. Although the average obtained so far is as flat as the flattest beat, there is no guarantee that this flattest is satisfactorily flat. To correct for this a final baseline correction procedure is used. In this instance, a third order polynomial fit to irregularly sampled data is obtained. The data fit in this case contains only a subset of points which exclude the P wave and the QRST complex. Finally, a single, refined set of onsets and offsets are determined for P, QRS and T wave events. These onset and offset times can be manually corrected if not satisfactory (see Chapter 1.3.3).

B.1.4 Specific programs, their functions and output data format

This description of programs used to get data off magtape, averaged and stored follows from Figure 1.11. The magnetic tapes with the MCG and BSPM raw data are brought to the Dept. of Physiology and Biophysics where a magnetic tape drive is available to download the data to a μ VAX-3400, where it is then transferred for processing to the μ VAX-3300 located in the Dept. of Physics. The program which brings the data to the VAX-3400 is called RAWTAPE (RAWBSPM)¹. At this stage the data is unpacked from 12 bit to 16 bit words, appropriate calibration is applied and, in the case of MCG data, ECG leads RA, LA and LL are combined to form the Burger leads I=LA-RA, II=LL-RA and III=LL-LA. A convention for file names is used. The initials of the surname and family names form the first 2 digits (PP). A recording session number forms the next 2-3 digits (NN). In raw data files, the 2 letter code (RC) indicates the MCG grid location (R=A to H, C=1 to 7) as indicated in Figure 1.8. This code is replaced by the letters BSP to designate BSPM data.

Each MCG file is independently averaged with DALECG and each of the 4 channels recorded are stored in a data base file using the program NSWPCHG while all 120 BSPM leads are averaged simultaneously then arranged into a permanent file using BSWPCHG. The new files have names which begin with the 4 (or 5) digit patient code and two additional letters to indicate the file is an original averaged data file (PPNNOR). The 4 different channels processed (MCG, and limb leads I, II, and III) are distinguished by the extensions .MMM, .EE1, .EE2 and .EE3 respectively while the averaged BSPM data file will be PPNNOR.BSP. The PPNNOR.* files are direct access files, so that the 56 grid points or 120 BSPM leads are written to 56 or 120 different records containing first a header, then either 500 or 1000 data points. The number of data points will vary depending on whether a 1 or 2 second window around each beat was averaged. A final record (57 or 121) is used as a bad lead array indicator.

¹Program names in brackets are the equivalent BSPM versions.

C Peper's time shift method

C.1 The shift operator

The basis for Peper's method originates with an application of the shift operator in Z-transform theory [180]. Applied to sequences, the shift operator is defined by the relations, $u_{r+1} = Eu_r$, and $u_{r+2} = Eu_{r+1} = E^2u_r$, such that, in general,

$$E^n u_r = u_{r+n}. \quad (\text{C.1})$$

If $u(t)$ is a function of the continuous variable t and if τ is a given constant, we define the shift operator E here by the formula

$$E^{n\tau} u(t) = u(t + n\tau). \quad (\text{C.2})$$

In applications to difference equations, the shift operator plays the same role as the differentiation operator D in differential equations [180].

C.2 Application to cardiac traces

Let $f(t)$ and $s(t)$ be two independent time functions, of which $s(t)$ follows $f(t)$ with a time-difference T_{fs} . Let $f(t - \tau)$ and $s(t)$ be the same functions, but with a time difference now of $T_{fs} - \tau$. The two functions, shown in Figure C.1a and b, can be described with the equations $g_a(t) = f(t) + s(t)$ and $g_b(t) = f(t - \tau) + s(t)$. The two sequences are aligned relative to the second signal $s(t)$. Subtracting trace (a) from (b) in Fig. C.1, we get

$$h(t) = f(t) - f(t - \tau). \quad (\text{C.3})$$

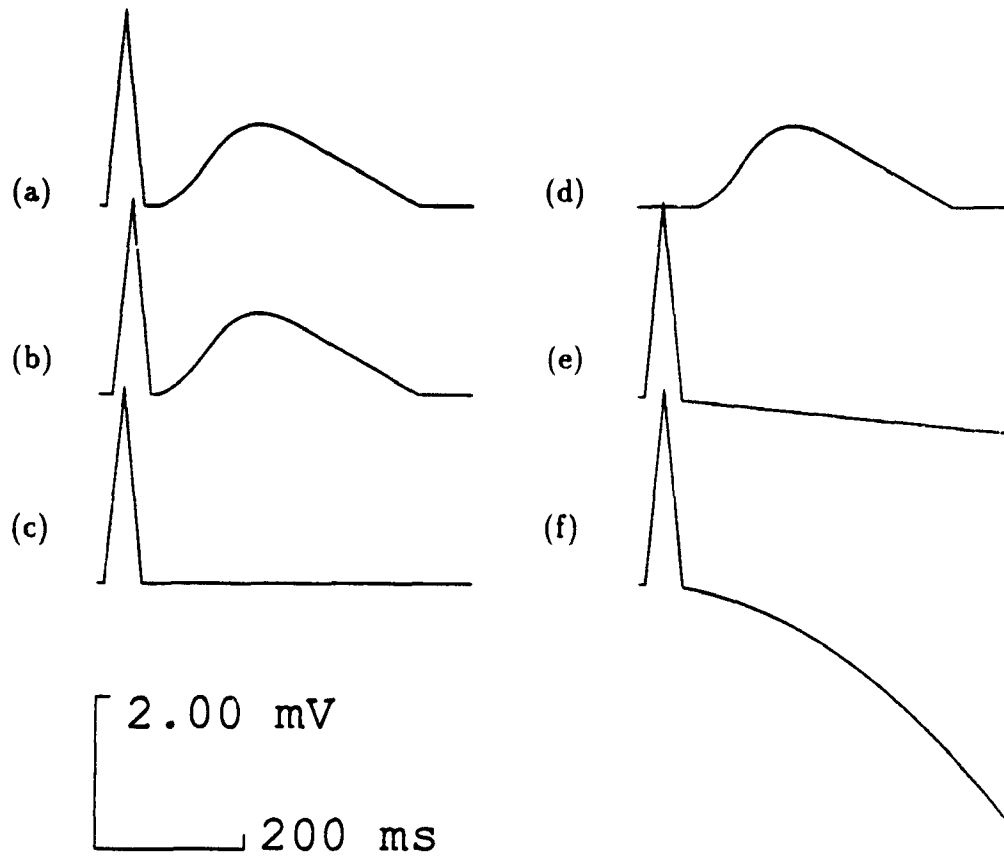


Figure C.1: Simulation of Peper's signal separation technique.
 (a) $g_a(t) = f(t) + s(t)$, (b) $g_b(t) = f(t - \tau) + s(t)$, where $\tau = 10$ ms, (c) reconstructed $f_r(t)$ using Eq. C.11, (d) isolated $s(t) = g_a(t) - f_r(t)$, (e) inclusion of a constant noise term of $1 \mu\text{V}$ is integrated into a sloping noise source, and (f) a slope of $.25 \text{ mV/s}$ becomes parabolic in the reconstruction process. Scales apply to all traces.

If we make use of the shift operator [147] as in Equation C.2, we can represent $f(t - \tau)$ as a function of $f(t)$,

$$z^{-\tau} f(t) = f(t - \tau). \quad (\text{C.4})$$

Substituting Equation C.4 into C.3, we then have a difference equation in $f(t)$,

$$h(t) = f(t) - z^{-\tau} f(t) \quad (\text{C.5})$$

$$= (1 - z^{-\tau}) f(t). \quad (\text{C.6})$$

Or, solving for $f(t)$,

$$f(t) = \frac{h(t)}{1 - z^{-\tau}}. \quad (\text{C.7})$$

Now, the binomial expansion applied to $1/(1 - z^{-\tau})$ allows C.7 to be written,

$$f_r(t) = \sum_{i=0}^K z^{-i\tau} h(t) \quad (\text{C.8})$$

$$= \sum_{i=0}^K h(t - i\tau) \quad (\text{C.9})$$

$$(\text{C.10})$$

where K is the integer value of t/τ and $h(t) = 0$ for $t < 0$.

The discrete version is simply

$$f_r(n) = \sum_{i=0}^K h(n - im) \quad (\text{C.11})$$

where in the discrete case $t \Rightarrow n$ and $\tau \Rightarrow m$, such that $K = \text{int}(n/m)$ and $h(n) = 0$ for $n < 0$.

In Peper et al. [126,134,4], Equation C.11 is used to reconstruct the signal $f(t)$ (or $f(t - \tau)$ as required). In the reconstructed signal $f_r(t)$, $s(t)$ is absent (see Fig. C.1c). If we now subtract $f_r(t)$ from the original signal $g_a(t)$, we obtain $s(t)$ isolated from $f(t)$ (Fig. C.1d). Although the traces shown in Figure C.1 are not similar to the true signals of interest, in the isolation of the His bundle (or HPS) signal, $f(t)$ would represent the P wave, and $s(t)$ is the HPS signal. In an actual ECG, in trace d, we

would have isolated events correlated in time with the QRS complex, including the His bundle signal.

Though this technique is promising, there are limitations and problems which are discussed in Chapter 5. For these reasons, this technique was not pursued in much detail. One problem, which we'll demonstrate, could result from baseline wander.

Suppose in g_b there is an additional noise term not present in g_a , such that $g_b = f(t - \tau) + s(t) + p(t)$, and the difference as given in Equation C.3 now becomes,

$$h(t) = f(t) - [f(t - \tau) + p(t)]. \quad (\text{C.12})$$

With the use of the Z-transform shift operator, $f(t)$ can again be isolated, but the new equation becomes,

$$f_r'(t) = \sum_{i=0}^K [h(t - i\tau) + p(t - i\tau)]. \quad (\text{C.13})$$

In accordance with Jury's remarks [180], this equation now represents an integration equation. Hence, the additional term $p(t)$ is integrated in the reconstruction process. This effect is demonstrated in Figure C.1e-f. In trace (e), $g_b(t)$ included a noise term, equivalent to an offset of $10 \mu\text{V}$. In the reconstruction, this constant offset is integrated to a baseline of constant slope. Trace (f) results from the reconstruction of a term which includes a noise source of constant slope, equivalent to $.25 \text{ mV/s}$.

D Gradiometer Design

The magnetic field measurements in this study were all obtained with a 2nd order asymmetric gradiometer with a 4 cm baseline. It is well understood that the sensitivity of the system decreases as a function of gradient of the measuring system [181,182]. However, the actual field patterns measured have not been analysed as thoroughly. In pattern recognition types of inverse solutions, any dependence the measured maps may have on gradiometer design will have to be addressed.

D.1 The measured fields

From Equation 2.3, in an infinite homogeneous medium the Z -component of the magnetic field, B_z^0 , due to a current dipole source, $\underline{P} = P\hat{y}$, located at the origin is given by,

$$B_z^0 = \frac{\mu_0}{4\pi} \frac{Px}{(x^2 + y^2 + z^2)^{3/2}} \quad (\text{D.1})$$

where x, y and z are coordinates in the measurement plane. This equation assumes a magnetometer design with a point-size front-end coil diameter.

A similar point-size 1st order gradiometer, for the same source configuration, measures

$$B_z^1 = B_z^0(x, y, z) - B_z^0(x, y, z + b), \quad (\text{D.2})$$

and the field sensed by a 2nd order gradiometer is

$$B_z^2 = B_z^0(x, y, z) - 2B_z^0(x, y, z + b) + B_z^0(x, y, z + 2b), \quad (\text{D.3})$$

where b is the baseline of the gradiometer (distance between adjacent coils).

One of the most prominent features of measured maps is the location of the extrema. From this location one can infer the source depth. To explore the effect of gradiometer design on the field patterns a numerical simulation was performed.

Forward solutions for the equations of a magnetometer, and 1st and 2nd order gradiometers of varying baselines were obtained. The locations of the field extrema were determined for the different gradiometer designs. For the previous choice of a dipole moment, $\underline{P} = P\hat{y}$, the location of the extrema will be found on the x -axis at $y = 0$, perpendicular to the direction of the dipole moment. Hence the actual simulations are restricted to the $y = 0$ line.

D.2 Simulations

Figure D.1 is a plot of the location of the maximum measured field as a function of source depth (z). The 5 curves result from calculations of the locations determined for a magnetometer, and 1st and 2nd order gradiometers at 2 baselengths each (4 cm and 8 cm).

The location of the field extrema, x_{max} , for the source configuration and magnetometer described by Eq. D.1 is $x_{max} = z/\sqrt{2}$. The first curve (in Figure D.1a) is a plot of the solution of this equation. For deep sources (generally deeper than the baseline) the other 4 curves reflect two trends: (i) as the baseline of the gradiometer gets shorter, the extrema get closer together, and (ii) as the gradiometer order increases, the extrema again get closer. Both these features result in a perception of a shallower source depth, as compared to the magnetometer design.

Further examination of the curves reveals a few additional trends. In all 4 gradiometer types examined (curves b to e), at large source depths there is a linear or near-linear dependence of the location of the maxima as a function of source depths. At very small source to sensing-coil distances, the slopes follow the magnetometer solution more closely. There is a transition to a different slope at approximately $z = b$ for the 1st and 2nd order gradiometers.

Because of these differences it would be necessary to normalise measured field patterns to a standard gradiometer design. This would be necessary if pattern matching techniques of MF maps were applied to data originating from different systems, mea-

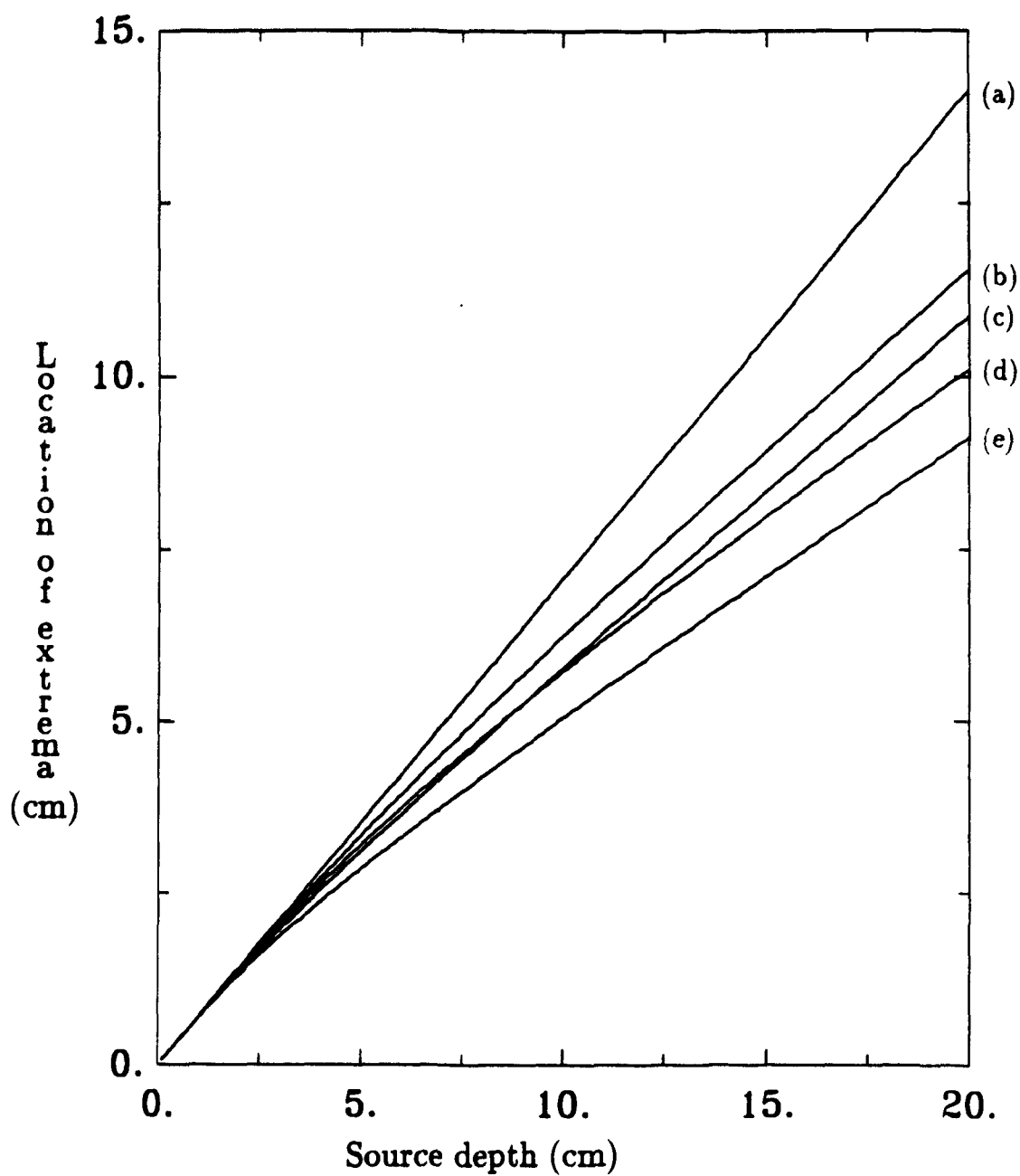


Figure D.1: Location of extrema for various gradiometer designs. The 5 curves plotted correspond to (a) a magnetometer, (b) a 1st order gradiometer of 8 cm baseline, (c) a 1st order gradiometer of 4 cm baseline, (d) a 2nd order gradiometer of 8 cm baseline, and (e) a 2nd order gradiometer of 4 cm baseline.

suring sources at distances exceeding the baseline. In future clinical applications, it will be imperative to designate a world standard gradiometer design in order to have universally applicable MFM diagnostic criteria. This standardisation would be equivalent to the present standardisations (i.e. Wilson Central Terminal reference) applied to clinical ECG equipment.

E Heart and torso anatomy

E.1 Anatomy of the heart and ECG trace nomenclature

In Figure E.1, a sketch of the human heart shows some of the gross anatomical parts of the heart. The heart is composed of four chambers. The right/left heart is on the left/right side of the sketch. The right and left atria are superior to the right and left ventricles. The conduction system is composed of the sino-atrial (S-A) node, the atrio-ventricular (A-V) node, the common or His bundle, bundle branches and Purkinje fibre network. These last 3 structures, as a composite, are commonly called the His-Purkinje system (HPS). The A-V ring is a non-conducting structure which electrically isolates the atria and ventricles.

Also shown in Figure E.1 are representative ECG recordings from each region. The P wave is associated with atrial depolarisation. The QRS complex is the signature of ventricular depolarisation and the T wave, ventricular repolarisation. Further nomenclature is summarised in Figure E.2. This terminology is also used for the MCG signals.

As will be discussed in Chapter 6, in the condition known as Wolff-Parkinson-White (WPW) syndrome extra or anomalous myocardial connections can exist at this level which permit alternative conduction pathways from the atria to the ventricles. An example of such a connection is shown in Figure E.3.

E.2 Heart and torso coordinate systems

Anatomical references will be made to both the heart and torso. Terminology used in reference to the two structures is the same, however the relative orientation of the heart in the body results in potential confusion. The plots of Figures E.4 and E.5

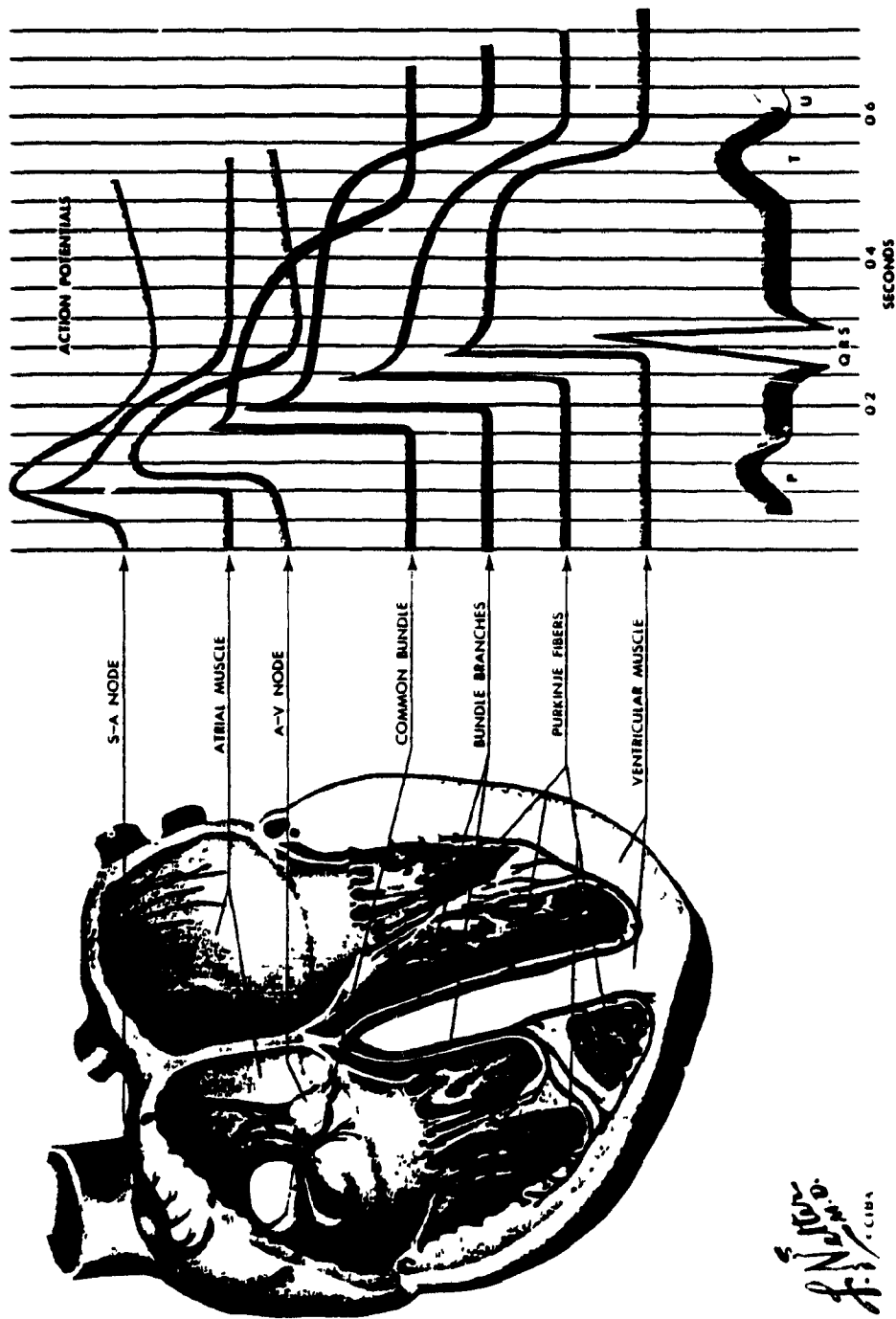


Figure E.1: Anatomy of the heart.

On the right are representative ECG recordings from each region. They are positioned with respect to their depolarisation in the cardiac cycle and the composite ECG recording in the lowest trace. (From reference [175]).

F. N. S. S. S.
L. C. I. B. A.

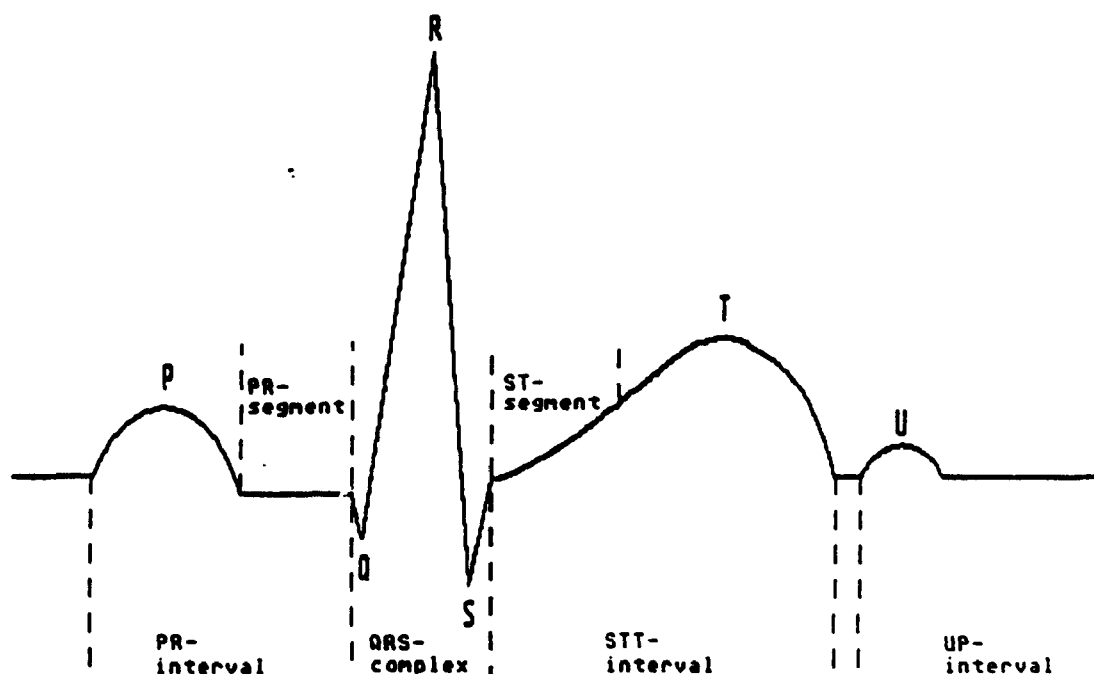


Figure E.2: Electrocardiographic nomenclature of the heart cycle.

(top) show the location of the heart in the torso with references to a coordinate system where the X axis points from the right to left, the Y axis from the feet to the head (inferior to superior) and the Z axis from back to front (posterior to anterior).

Shown in Figure E.6 are similar views of the ventricular epicardium, also with anatomical references. Included on the view of the A-V ring are ten common sites for accessory connections (1-10). The anatomical references of the heart are not the same as in the torso. This perspective is demonstrated by Figure E.5 (bottom). This view of the epicardial surface shows that the anterior sites (i.e. 1 and 10) on the A-V ring are closer to the head than the posterior sites (5 and 6). The right side of the heart (sites 2,3,4) is closest to the anterior chest and gradiometer.

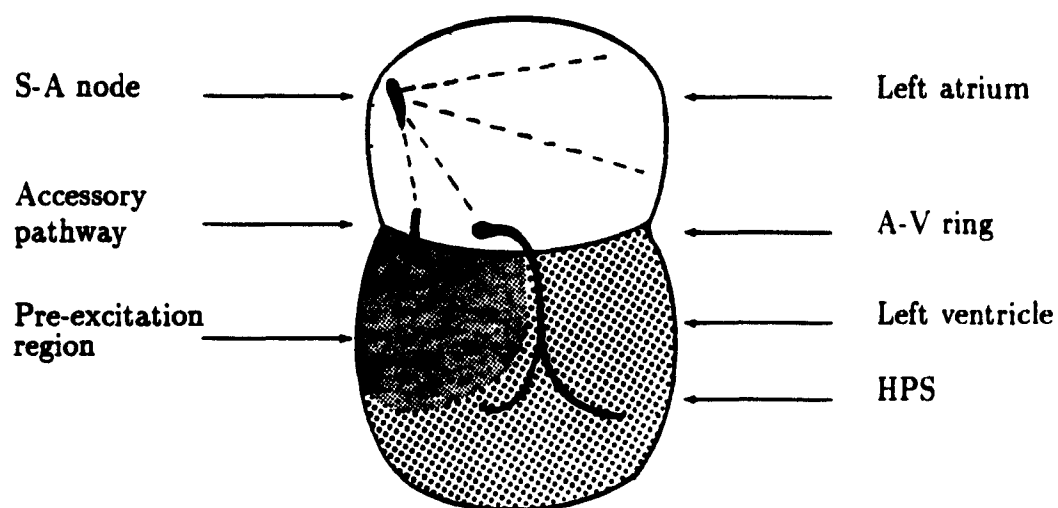


Figure E.3: Sketch of heart with accessory connection at A-V ring. The area of ventricular insertion of the accessory connection initiates ventricular depolarisation (pre-excitation) before excitation via the usual conduction system (HPS).

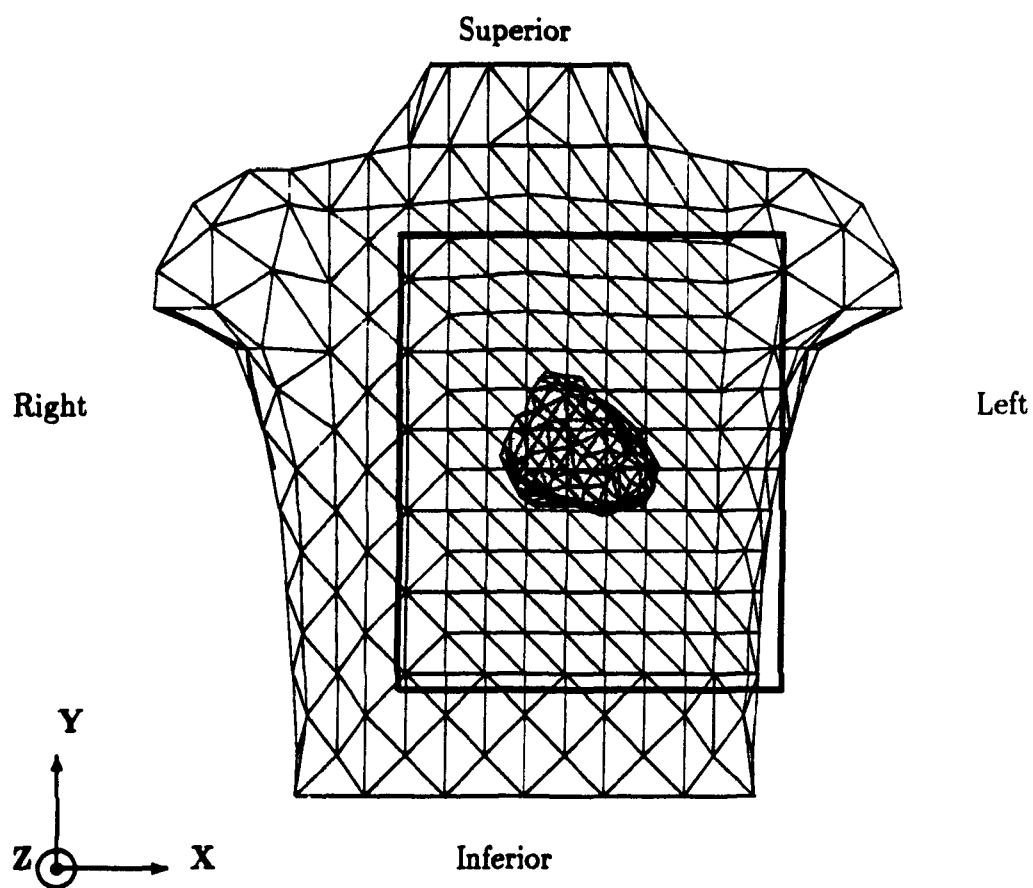


Figure E.4: Anterior view of torso model and ventricular epicardial surface. The torso coordinate system is plotted.

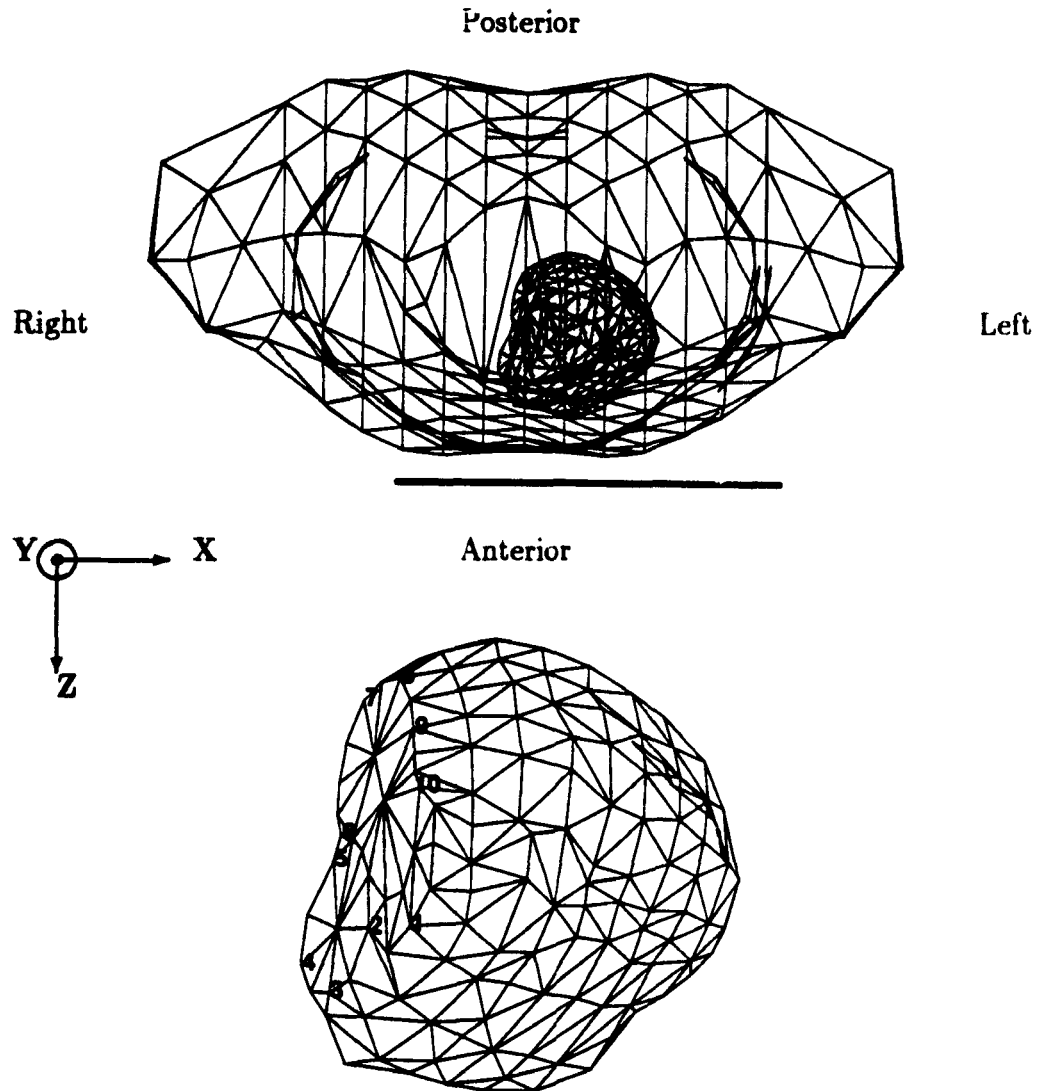


Figure E.5: Transverse view of torso model and ventricular epicardial surface. The torso coordinate system is plotted. Below the torso is an enlarged plot of the same view of the epicardial surface. The numbers correspond to the 10 Gallagher sites for accessory pathways in WPW syndrome.

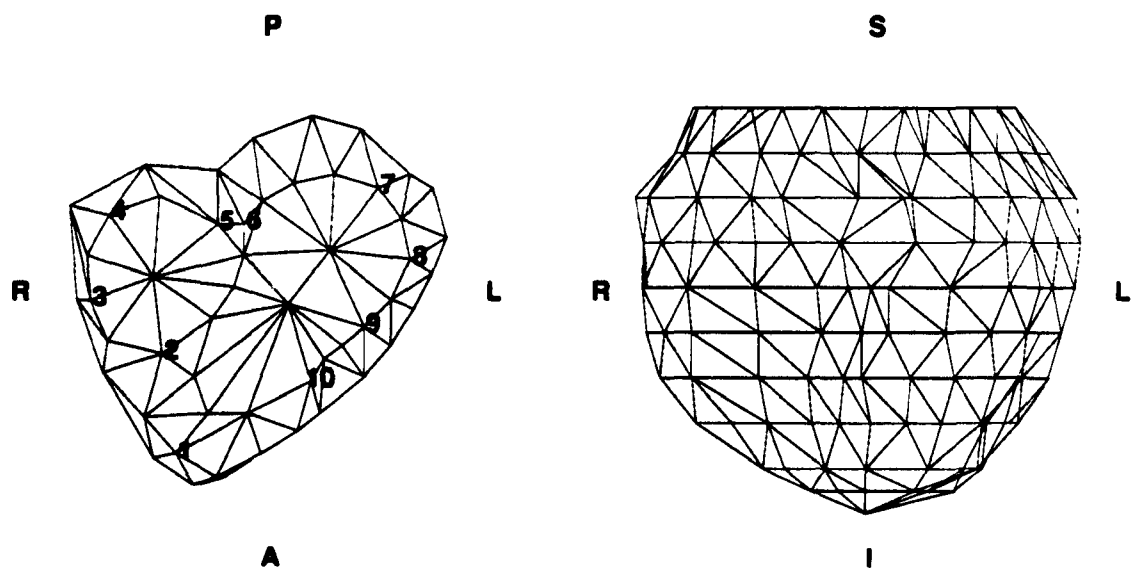


Figure E.6: Plots of the epicardial surface.
The labels refer to the epicardial anatomy: R=right, L=left, P=posterior, A=anterior, S=superior and I=inferior.

F Case study: WPW syndrome patient with two accessory pathways and atrial pacemakers

F.1 Introduction

In this study, we present the case of a 27 year old female WPW patient with two (2) right sided accessory connections, with the additional pathology of two (2) distinct atrial pacemaker sites. The presence of multiple accessory atrio-ventricular pathways (AP) in Wolff-Parkinson-White (WPW) syndrome patients is not an unusual occurrence. In many such cases, the different AP can simultaneously contribute to pre-excitation of the ventricles. This concurrent activation usually results in an inability to successfully determine the locations of the AP non-invasively. In this patient, more than one ventricular complex was recorded. Due to the presence of the 2 atrial pacemaker sites, we were able to determine the nature of the different ventricular complexes present.

F.2 Method

During a course of routine clinical evaluation for suspected (then confirmed) Wolff-Parkinson-White syndrome, the patient in question underwent invasive electrophysiological (EPS) investigations. As part of an ongoing research project, the patient also agreed to body surface potential mapping and cardiac magnetic field mapping. During this time, a 117-lead body surface potential map (BSPM) and a 56 point magnetic field map (MFM) were obtained in an AI shielded room. After EPS evaluation, the patient was referred to another hospital where she underwent RF-ablation therapy.

F.2.1 BSPM and MFM recording systems

The 117 BSPM unipolar leads referenced to WCT were recorded simultaneously for 120 seconds at a sample rate of 500 Hz. The magnetic field sensor (1 channel only) consisted of a 2nd order asymmetric gradiometer arrangement, with a 4 cm baseline and 2.5 cm front end coil diameter. Since only one detector was available, the 7 × 8 MFM grid of 4 cm spacing was sampled sequentially, with ECG leads I, II, III recorded simultaneously with each of the 56 points to serve as reference for alignment later in the processing. Each point was recorded for 30 seconds, again at a sample rate of 500 Hz. Data was averaged off-line and filtered for 60 Hz line interference. An isoelectric interval was defined during the UP interval.

F.3 Results

When the BSPM and MFM recordings were originally obtained, it was not known that 2 AP existed. Only after examining the BSPM data did it become evident that more than one cardiac complex was present. In fact, as is displayed in Figure F.1, the different beats, labelled A, B, C, and D, have similarities, but no two are identical. The 4 ventricular waveforms, under careful examination are found to be all different, but with A and C, then B and D, resembling each other. These differences are seen primarily as amplitude variations, but also slight waveform differences are observed, which are not attributable to normal cardiac fluctuations.

Groups of beats from each of these 4 complex types were averaged. Only beat types A, B and C were found in the first 20 ms of the recording. Five (5) to 10 beats were averaged in each case. The rest of the BSPM recording, as well as the magnetic field map, contained beat types B and D, with type D most prevalent.

F.3.1 BSPM data

Body surface potential maps during the P wave and ventricular complex were plotted for each beat type. A selection of these maps, arranged in columns, along with

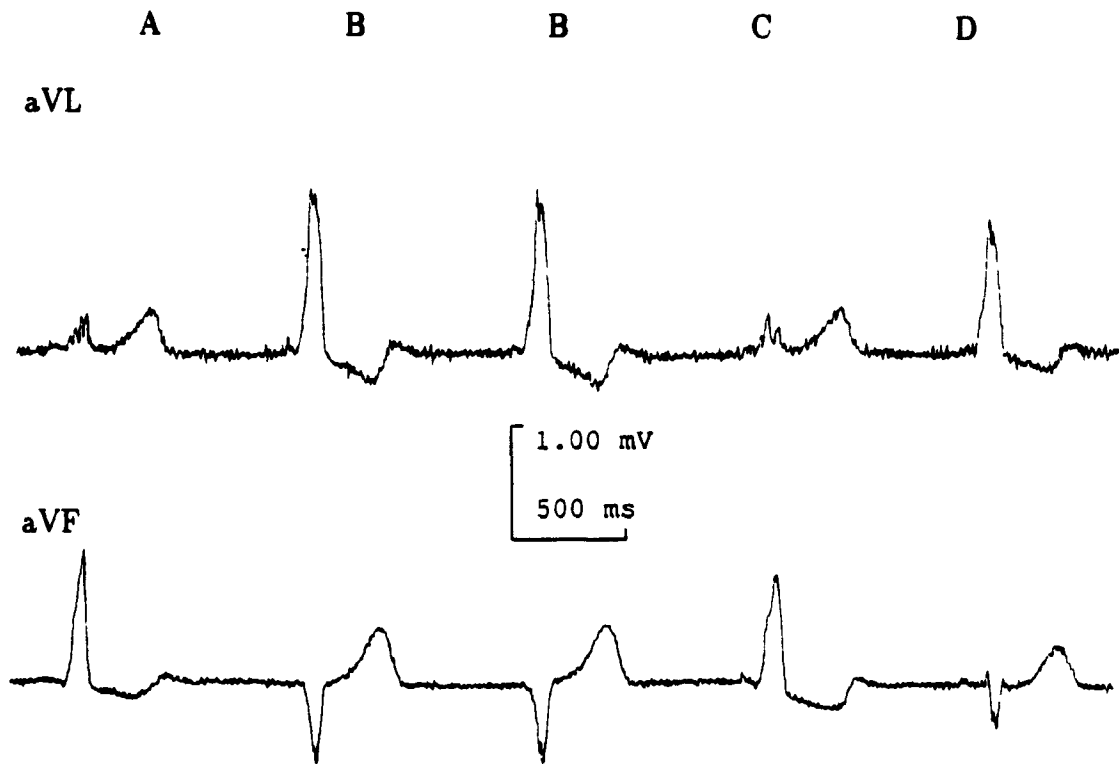


Figure F.1: Raw data traces of leads aVL and aVF.
This sequence of beats contains four different complexes, labelled A, B, C, and D. Beat couplets A and C, and B and D, have similar ventricular complexes. However, none of these are identical.

precordial lead V_2 , is presented in Figure F.2, for all 4 beat types. They are presented in the same sequence as in Figure F.1.

From the isopotential maps, as well as a 12-lead ECG derived from the BSPM data, it was determined that 2 different P-wave types were recorded. Beats A and B had one type, while beats C and D had another. This is most apparent by following the zero isopotential contour line in the first row of maps of Figure F.2. P-wave maximum isocontour plots of beats C and D are consistent with a pacemaker complex located along the sulcus terminalis and superior vena cava-right atrial junction in the upper posterior right atrium [110], and are typical atrial depolarisation BSP maps (see Chap. 4 and references [103,104,105,183]). The P-wave maps for beats A and B are not typical atrial depolarisation distributions, suggesting an alternative right atrial pacemaker site [110].

Ventricular complex maps for each of these 4 beats are shown at three different times after δ -wave onset (Fig F.2). δ -wave onset was defined as the very first instance in the isocontour maps where there was evidence of pre-excitation. In all 4 cases, this onset was signalled by the emergence of an area of positive potentials on the right anterior torso, inconsistent with atrial activity. The positive area in the early δ -wave maps (second row of maps in Fig. F.2) developed from this initial indication of pre-excitation. The δ -wave onset patterns were not stable, evolving into the maps seen in the third row (Fig. F.2). In all cases, a general distribution of positive potentials on the left-lateral chest wall (center of maps), and negative potentials on the right side (4th row, Fig. F.2) persisted to the end of ventricular depolarisation. Throughout the ventricular depolarisation complex (rows 2-4), similarities are seen between beat pairs A and C, and beats B and D.

Following schemes such as Benson et al. [75], the isopotential patterns displayed in the 3rd row of Figure F.2 suggest that the ventricular pre-excitation complexes of beats A and C correspond to right anterior AP locations. Equivalently, beats B and D are most consistent with right lateral pathways.

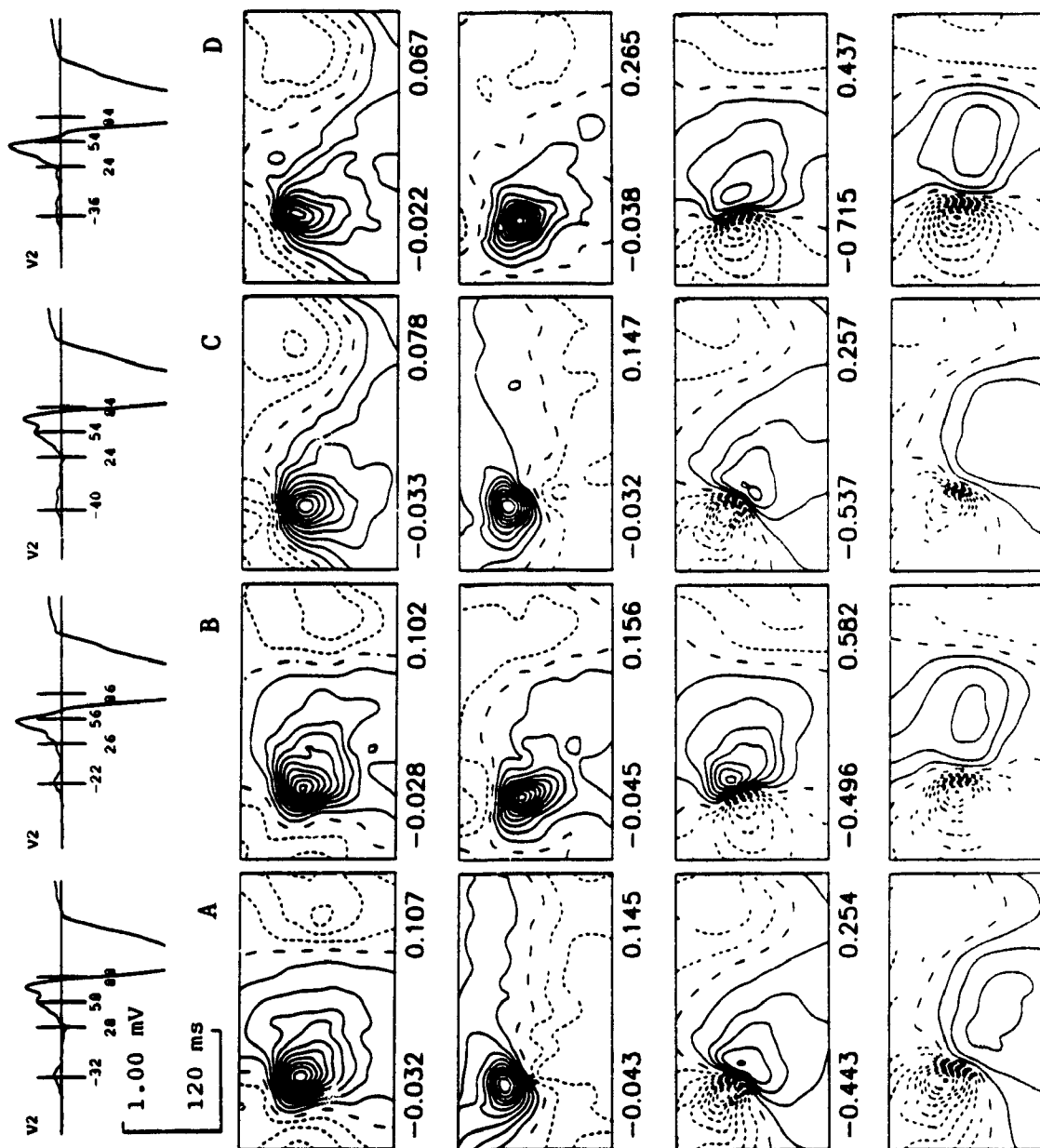


Figure F.2: BSPM isocontour plots of 4 different beats for subject DI189. Precordial lead V_2 is first plotted for each beat type (A, B, C, D). Below each lead V_2 are plotted 4 maps at maximum P-wave activity and for 3 times during ventricular activation via the accessory pathways for each beat type. The times of these maps, relative to δ -wave onset, are indicated in each V_2 trace. Extrema values plotted below each map are in mV.

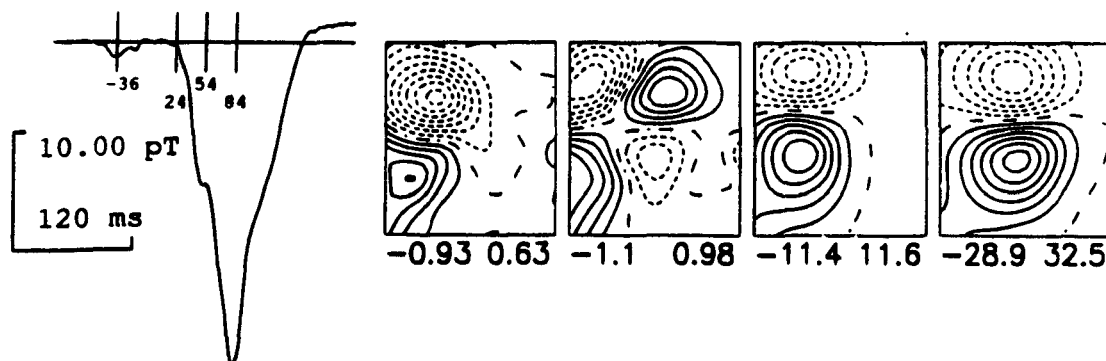


Figure F.3: MFM isocontour plots of beat D for subject DI189. MFM grid point B2 is plotted, along with 4 maps during the P wave and ventricular complex. Map times are indicated in MCG trace B2. Magnetic field extrema are in units of pT, with the positive field (solid lines) corresponding to the field pointing into the body.

F.3.2 MFM data

In the MFM data, we were not able to create averages of both types B and D, since type B was not frequent enough. A map of type D was obtained, and is presented in Figure F.3.

F.4 Discussion

During EPS 2 accessory atrio-ventricular pathways were found, and successfully interrupted with RF ablation therapy. The 2 sites corresponded to a right anterior (RA) and a right postero-lateral (RPL) (Gallagher [150] sites 2, and midway between 3 and 4). In combination with the two different atrial pacemaker sites, these 2 AP produced 4 different cardiac complexes. With a careful analysis of the BSPM patterns, it is possible to determine the contributions each of these components make to the different complexes recorded. In the following discussion, the 2 different ventricular complexes will be referred to as δ_1 (beats A and C) and δ_2 (beats B and D).

Both the timing of the onset of the δ waves relative to the P-wave maxima, and the BSPM distributions of the δ waves provide the evidence necessary to explain

each of the 4 cardiac complexes recorded. First of all, pre-excitation onset for beat types A and C (δ_1) occurs at 32 ms and 40 ms and for beats B and D (δ_2) at 22 ms and 36 ms, relative to P-wave maximum. The later onset of the δ_1 complexes in beats A and C suggests that these beats are the result of pre-excitation via a single accessory connection. The shorter pre-excitation onset times of δ_2 suggest that the propagation wavefront reaches the location of the AP responsible for δ_2 first. If this AP does not conduct, the wavefront moves on to the second, more distant AP (δ_1), and pre-excitation is then initiated. Hence, pre-excitation via a single accessory pathway generated the δ_1 complex. Finally, the localisation of the BSPM δ_1 maps to a right anterior pathway corresponds exactly with the location of one of the ablated sites, supporting the conclusion that the ventricular complexes of beats A and C result from pre-excitation via a single RA pathway.

The finding for δ_1 does not determine whether or not the δ_2 complex results from one or two accessory connections. Though close to a right postero-lateral location, the assignment of δ_2 based on the BSPM patterns, to a right lateral site is not accurate. In fact, the right lateral pattern probably emerges because of the combined effect of an anterior and a posterior location, suggesting that δ_2 results from concurrent pre-excitation via the two known pathways. Figure F.4 summarises the probable timing of the atrial and early ventricular pre-excitation events, in each of the 4 beat types. With the first atrial pacemaker site, the 2 pre-excitation complexes form the cardiac complexes labelled A and B. Under the action of another pacemaker location, the same 2 pre-excitation complexes result in two additional beats (C and D), which are only slightly different from A and B.

One may argue that the δ_2 complex could also reflect pre-excitation via a single (RPL) accessory pathway. This would require that both pathways conduct intermittently, but due to the independence of the 2 AP, this situation would result in a third type of ventricular pre-excitation complex. Two of these complexes would be due to excitation via each pathway, plus a third would reflect a random, but highly probable, simultaneous pre-excitation event. In combination with the 2 pacemaker

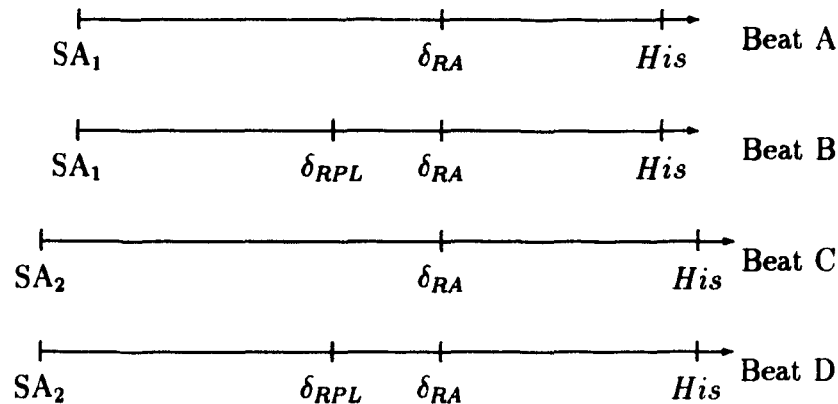


Figure F.4: Sketch of timing of events in the 4 pre-excitation complexes. The relative times when the excitation wavefront reached particular locations for each combination are indicated, relative to the AP's (δ waves). The scales are not accurate, since some events cannot be determined (e.g. His-onset). Each combination would result in a slightly different ventricular complex, at δ -wave onset, because of interfering atrial components, then later because of fusion from activation via the normal conduction pathway. (SA_1 , SA_2 =pacemaker complexes 1 and 2, δ_{RA} = right anterior AP, δ_{RPL} =right postero-lateral AP, His =His bundle)

sites, this scenario would then result in a total of 6 different cardiac complexes.

The slight differences found between each of the two ventricular complex pairs δ_1 (A and C) and δ_2 (B and D) result from two factors not yet discussed: atrial potentials during δ -wave onset and fusion of pre-excitation potentials with excitation via the His-Purkinje system (HPS). During onset of pre-excitation, the 2 different pacemaker sites will result in small differences in the maps. It was found that the actual δ -wave onset occurs during late atrial depolarisation in all 4 cases. The P-R intervals were all less than 60 ms, while a normal P-wave duration itself is >90 ms (reference [103,110] and Chapter 3). Duchosal et al. [167] found that this extremely premature pre-excitation was common in right-sided accessory pathways. Atrial depolarisation and repolarisation potentials (and magnetic fields) associated with the 2 different pacemaker sites will combine with early pre-excitation events to create small differences in the combination maps. The atrial potentials will primarily affect the

low-level minimum potentials in the δ -wave onset maps (e.g. Fig. F.2 at ~ 25 ms).

Ventricular excitation via the usual A-V conduction system (HPS) is expected sometime after onset of pre-excitation, resulting in a fusion complex. The two different pacemaker sites will again contribute to create different fusion patterns, through the relationship of the S-A node and A-V node. The two S-A nodes have different wave propagation times to the A-V node, resulting in different onset of ventricular activation via the normal pathway, independent of the onset of pre-excitation.

The MFM data was aligned relative to the average of beats D, using the 3 ECG leads recorded simultaneously. These 3 leads also provided confirmation of the beat type actually present in the MFM. The magnetic field maps were plotted to correspond to the same times as Figure F.2, hence the first map represents atrial depolarisation. This agrees with typical atrial depolarisation magnetic field maps. In the next map, the multipolar pattern suggests the presence of 2 distinct sources, probably atrial repolarisation and δ -wave onset. However, the presence of two concurrently active sites of pre-excitation might also produce a multipolar MFM pattern, because of the higher spatial resolution of the magnetic recording system, as compared to BSPM. The two extrema on the left side of this map, are continuous with the single dipole patterns in the following 2 maps, supporting the hypothesis that the second map contains both atrial repolarisation and pre-excitation dipoles.

F.5 Conclusion

Two different accessory A-V pathways were identified at RF-ablation. From analysis of body surface potential maps and the timing of the onset of pre-excitation relative to atrial activation, it was determined that a right anterior connection consistently contributed to ventricular pre-excitation. However, a right postero-lateral pathway conducted only intermittently. When both pathways contributed to pre-excitation, the resultant BSPM incorrectly reflected a right lateral connection.

Two separate atrial pacemaking complexes have been found to contribute to the

formation of slightly different ventricular pre-excitation complexes via two mechanisms. The first results from the different potential distributions arising from changes in the atrial excitation wavefronts originating in the 2 sites. Finally, two fusion patterns will follow from the differing delays between onset of atrial activity and conduction through the His-Purkinje system, even for pre-excitation via the same pathway(s). This combination of two pacemaking sites and two accessory A-V pathways produced four distinct heart complexes.

Bibliography

- [1] A. D. Waller. A demonstration on man of electromotive changes accompanying the heart's beat. *J. Physiol. London*, 8:229, 1887.
- [2] G. Baule and R. McFee. Detection of the magnetic field of the heart. *Am. Heart J.*, 55:95, 1963.
- [3] M.J.R. Lamothe. Detection of His-Purkinje system spatial features in magnetocardiograms. Master's thesis, Dalhousie University, 1987.
- [4] Abraham Peper. *The recording of His-Purkinje potentials at the body surface*. PhD thesis, U. of Amsterdam, 1990.
- [5] G. Stroink, C. Purcell, F. Brauer, and B. Blackford. An eddy-current shielded room with a partially closed entrance. *Il Nuovo Cimento*, 2D(2):195-202, April 1983.
- [6] R.B. Merritt, C. J. Purcell, and G. Stroink. Uniform magnetic field produced by three, four and five square coils. *Rev. Sci. Instrum.*, 54:879-882, 1983.
- [7] B. Brown. Improvements in a biomagnetic measurement system. Master's thesis, Dalhousie University, 1980.
- [8] J.E. Zimmerman. SQUID instruments and shielding for low level magnetic measurements. *J. Apply. Phys*, 48:702, 1977.
- [9] G.L. Romani, S.J. Williamson, and L. Kaufman. Biomagnetic instrumentation. *Rev. Sci. Instrum.*, 53(12):1815-1845, 1982.
- [10] M.J. Peters. *The detection of bioelectric sources within the heart using a SQUID sensor*. PhD thesis, Technical Univ. of Twente, 1981.
- [11] E. Lepeshkin. *Modern Electrocardiography*, volume 1. Williams and Wilkins, Baltimore, 1951.
- [12] J. Liebman, R. Plonsey, and Y. Rudy. *Pediatric and Fundamental Electrocardiography*. Martinus Nijhoff Publishing, Boston, 1987.
- [13] E.J. Berbari. High-resolution electrocardiography. *CRC Critical Reviews in Biomedical Engineering*, 16(1):67-103, 1988.
- [14] D.M. Mirvis. *Body Surface Electrocardiographic Mapping*. Kluwer Academic Publishers, Boston, 1988.

- [15] Peter W MacFarlane and T.D. Veitch Lawrie. *Comprehensive Electrocardiology: Theory and Practice in Health and Disease*. Pergamon Press, Inc., New York, 1989.
- [16] G. Stroink and C. MacAulay. Thermal noise generated by an eddy current shielded room. *Rev.Sci. Instrum.*, 57:658–660, 1986.
- [17] G. Stroink, M. Kouwenhoven, T.J. Montague, and B.M. Horáček. Magneto-cardiographic and body surface potential mapping in an Al-shielded room. In *Proc. 13th. Can. Med. and Biol. Eng. Conf.*, pages 231–232, 1987.
- [18] B.M. Horáček, W.J. Eifler, H. Gewirtz, R. Helppi, P.B. Macaulay, J.D. Sherwood, E.R. Smith, J. Tiberghien, and P.M. Rautaharju. An automated system for body-surface potential mapping. In H.G. Ostrow and K.L. Ripley, editors, *Computers in Cardiology*, pages 399–407. IEEE Computer Society, Long Beach, Calif., 1977.
- [19] C.E. MacAulay. The interrelationship of the eegs and the mcgs as determined by signal analysis. Master's thesis, Dalhousie University, 1984.
- [20] C.J. Purcell. *A comparison of electric and magnetic body surface mapping using single moving dipole inverse solutions*. PhD thesis, Dalhousie University, 1988.
- [21] H.K. Wolf, P.J. MacInnis, S. Stock, R.K. Helppi, and P.M. Rautaharju. Computer analysis of rest and exercise electrocardiograms. *Comput. Biomed. Res.*, 5:329–346, 1972.
- [22] H.K. Wolf, P.J. MacInnis, S. Stock, R.K. Helppi, and P.M. Rautaharju. Computer analysis of rest and exercise electrocardiograms. *Comp. Biom. Res.*, 5:329–346, 1972.
- [23] R.S. MacLeod. *Percutaneous Transluminal Coronary Angioplasty as a Model of Cardiac Ischemia: Clinical and Modelling Studies*. PhD thesis, Dalhousie University, 1990.
- [24] G. Stroink. Cardiomagnetic imaging. In B.L. Zaret, L. Kaufman, A.S. Berson, and R.A. Dunn, editors, *Frontiers of Cardiovascular Imaging*, pages 161–177. Raven Press, New York, 1993.
- [25] J.C. Sylven, B.M. Horáček, C.A. Spencer, G.A. Klassen, and T.J. Montague. Qt interval variability on the body surface. *J. Electrocardiology*, 17(2):179–188, 1984.
- [26] Richard F. Santopietro. The origin and characterization of the primary signal, noise, and interference sources in the high frequency electrocardiogram. *Proc. IEEE*, 65(5):707–713, 1977.

- [27] A.S. Berson and H.V. Pipberger. The low frequency response of electrocardiographs, a frequent source of recording errors. *Am. Heart J.*, 71(6):779-789, June 1966.
- [28] G.D. Dawson. *Journal of Phys.*, 115:2P, 1951.
- [29] H.H. Ros, A.S.M. Koeleman, and T.J. van der Akker. The technique of signal averaging and its practical application in the separation of atrial and His-Purkinje activity. In V. Hombach and H. Hilger, editors, *Signal Averaging Technique in Clinical Cardiology*, pages 3-14, New York, 1981. Shottauer Verlag.
- [30] R. Mehra and N. El-Sherif. Signal averaging of electrocardiographic potentials: A review. *Acup. Electrother. Res., Int. J.*, 7:133-155, 1982.
- [31] H. Riekkinen and P. Rautaharju. Body position, electrode level, and respiration effects on the Frank lead electrocardiogram. *Circulation*, 53:40-45, 1976.
- [32] P.M. Rautaharju, P.J. MacInnis, J.W. Warren, H.K. Wolf, P.M. Rykers, and H.P. Calhoun. Methods of ECG interpretation in the Dalhousie program; NO-VACODE ECG classification procedures for clinical trials and population health surveys. *Meth. Inform. Med.*, 29:362-374, 1990.
- [33] F.N. Wilson, A.G. Macleod, and P.S. Barker. *The Distribution of the Currents of Action and of Injury Displayed by Heart Muscle and Other Excitable Tissues*. University of Michigan Press, Ann Arbor, Michigan, 1933.
- [34] M.S. Spach, R.C. Barr, G.A. Serwer, J.M. Kootsey, and E.A. Johnson. Extracellular potentials related to intracellular action potentials in the dog Purkinje system. *Circ. Res.*, 30:505-19, 1972.
- [35] M.S. Spach and R.C. Barr. Origin of epicardial ST-T wave potentials in the intact dog. *Circ. Res.*, 39:475-87, 1976.
- [36] M.S. Spach, W.T. Miller III, E. Miller-Jones, R.B. Warren, and R.C. Barr. Extracellular potentials related to intracellular action potentials during impulse conduction in anisotropic canine cardiac muscle. *Circ. Res.*, 45:188-204, 1979.
- [37] W.T. Miller III and D.B. Geselowitz. Simulation studies of the electrocardiogram I. the normal heart. *Circ. Res.*, 43:301-15, 1978.
- [38] D.B. Geselowitz and W.T. Miller III. A bidomain model for anisotropic cardiac muscle. *Ann. Biomed. Eng.*, 117:191-206, 1983.
- [39] R.K. Hobbie. The electrocardiogram as an example of electrostatics. *Am. J. Physics*, 41:824-831, 1973.
- [40] R. Plonsey and R.C. Barr. *Bioelectricity: A Quantitative Approach*. Plenum Press, 1988.

- [41] D. Cohen and H. Hosaka. Magnetic field produced by a current dipole. *J. of Electrocardiology*, 4:409–417, 1976.
- [42] D. B. Geselowitz. On bioelectric potentials in an inhomogeneous volume conductor. *Biophys J.*, 29:1–11, 1967.
- [43] A. C. L. Barnard, I. M. Duck, and M. S. Lynn. The application of electromagnetic theory to electrocardiology 1: Derivation of the integral equations. *Biophys J.*, 7:443–462, 1967.
- [44] D. B. Geselowitz. On the magnetic field generated outside an inhomogeneous volume conductor by internal current sources. *IEEE Trans. Magn.*, MAG-6:346–347, 1970.
- [45] B.M. Horáček. Digital model for studies in magnetocardiography. *IEEE Trans. Magn.*, Mag-9(3):440–444, September 1973.
- [46] Y. Yamashita. Theoretical studies on the inverse problem in electrocardiography and the uniqueness of the solution. *IEEE Trans. Biomed. Eng.*, BME-29:719, 1982.
- [47] J. Sarvas. Basic mathematical and electromagnetic concepts of the biomagnetic inverse problem. *Phys. Med. Biol.*, 32(1):11–22, 1987.
- [48] B.M. Horáček. *The Effect on Electrocardiographic Lead Vectors of Conductivity Inhomogeneities in the Human torso*. PhD thesis, Dalhousie University, 1971.
- [49] R.C. Barr, T.C. Pilkington, J.P. Boineau, and M.S. Spach. Determining surface potentials from current dipoles, with application to electrocardiography. *IEEE Trans. Biomed. Eng.*, BME-13:88–92, 1966.
- [50] M. S. Lynn and W. P. Timlake. The use of multiple deflations in the numerical solution of singular systems of equations with applications to potential theory. *SIAM J. of Numer. Anal.*, 5(2):303–322, June 1968.
- [51] A. Heringa, D.F. Stegeman, G.J.H. Uijen, and J.P.C. de Weerd. The solution of electrical field problems in physiology. *IEEE Trans. on Biomed. Eng.*, BME-29(1):34–42, January 1982.
- [52] S.J. Williamson and L. Kaufman. Biomagnetism. *J. Mag. Mag. Materials*, 22(2):129–202, 1981.
- [53] C. Purcell, R. Lamothe, G. Stroink, and B.M. Horáček. Towards a magnetic inverse solution. In *13th Canadian Medical and Biological Engineering Conference*, pages 179–180, Halifax, Nova Scotia, June 1987. CMBES.
- [54] C. Purcell, G. Stroink, and B.M. Horáček. Magnetic inverse solution using a homogenous torso model. In *Proceedings of Ninth Annual Conference. IEEE/Engineering in Medicine and Biology Society*, November 1987.

- [55] T.F. Oostendorp and A. van Oosterom. Source parameter estimation in inhomogeneous volume conductors of arbitrary shape. *IEEE Trans. Biomed. Eng.*, BME-36:382-91, 1989.
- [56] C.J. Purcell and G. Stroink. Moving dipole inverse solutions using realistic torso models. *IEEE Trans. Biomed. Eng.*, BME-38:82-4, 1991.
- [57] IMSL Inc., Houston, Texas. *IMSL Library Reference Manual*, 8th edition, 1980.
- [58] G. Baule and R. McFee. The magnetic heart vector. *Am. Heart J.*, 79:223, 1970.
- [59] S. Rush. On the independence of magnetic and electric body surface recordings. *IEEE Trans. Biomed. Eng.*, BME-22(3):157-67, 1975.
- [60] L.V. Corbin and A.M. Scher. *Circ. Res.*, 41:58-, 1977.
- [61] J.P. Wikswo and J.P. Barach. Possible sources of new information in the magnetocardiogram. *J. Theor. Biol.*, 95:721-729, 1982.
- [62] F. Grynszpan and D.B. Geselowitz. Model studies of the magnetocardiogram. *Biophysical Journal*, 13:911-24, 1973.
- [63] B.N. Cuffin and D. Cohen. Magnetic fields of a dipole in special volume conductor shapes. *IEEE Trans. Biomed. Eng.*, BME-24(4):372-381, July 1977.
- [64] B.M. Horáček. Numerical model of an inhomogeneous human torso. *Adv. Cardiology*, 10:51-57, 1974.
- [65] B. M. Horáček, C. Purcell, R. Lamothe, R. Merritt, C. Kafer, S. Periyalwar, S. Dey, L. J. Leon, and G. Stroink. The effect of torso geometry on magnetocardiographic isofield maps. *Phys. Med. Biol.*, 32(1):121-124, 1987.
- [66] C.J. Purcell, G. Stroink, and B.M. Horáček. Effect of Torso Boundaries on Electric Potential and Magnetic Field of a Dipole. *IEEE Trans. Biomed. Eng.*, 35(9):671-678, 1988.
- [67] A.E. Becker, R.H. Anderson, M.R.C. Path, D. Durrer, and H.J.J. Wellens. The anatomical substrates of Wolff-Parkinson-White syndrome: A clinicopathologic correlation in seven patients. *Circulation*, 57:870-879, 1978.
- [68] L.J. Leon and B.M. Horáček. Computer model of excitation and recovery in the anisotropic myocardium: I. Rectangular and cubic arrays of excitable elements. *J. Electrocardiology*, 24:1-15, 1991.
- [69] J. Nenonen, J.A. Edens, L.J. Leon, and B.M. Horáček. Computer model of propagated excitation in the anisotropic human heart: I. implementation and algorithms. In K. Ripley and A. Murray, editors, *Computers in Cardiology*, pages 545-548. IEEE Computer Society Press, Los Alamitos, CA, 1991.

- [70] J. Nenonen, J.A. Edens, L.J. Leon, and B.M. Horáček. Computer model of propagated excitation in the anisotropic human heart: II. simulations of extracardiac fields. In K. Ripley and A. Murray, editors, *Computers in Cardiology*, pages 217–220. IEEE Computer Society Press, Los Alamitos, CA, 1991.
- [71] R.M. Gulrajani, H. Pham-Huy, R.A. Nadeau, P. Savard, J. de Guise, R.E. Primeau, and F.A. Roberge. Application of the single moving dipole inverse solution to the study of the Wolff-Parkinson-White syndrome in man. *J. Electrocardiology*, 17:271–288, 1984.
- [72] J. Nenonen, C.J. Purcell, B.M. Horáček, G. Stroink, and T. Katila. Magneto-cardiographic functional localization using a current dipole in a realistic torso. *IEEE Trans. Biomed. Eng.*, BME-38:658–64, 1991.
- [73] P. Weismuller, K. Abraham-Fuchs, S. Scheinder, P. Richter, M. Kochs, and V. Hombach. Magnetocardiographic non-invasive localization of accessory pathways in the Wolff-Parkinson-White syndrome by a multichannel system. *Eur. Heart J.*, 13:616–622, 1992.
- [74] H. Tsunakawa, G. Nishiyama, Y. Kusahana, and K. Harumi. Determination of the site of the accessory pathway in wpw syndrome by an electrocardiographic inverse solution. *Jpn. Heart J.*, 31:777–787, 1990.
- [75] D.W. Benson Jr., R. Sterba, J.J. Gallagher, A. Walston, and M.S. Spach. Localization of the site of ventricular preexcitation with body surface maps in patients with Wolff-Parkinson-White syndrome. *Circulation*, 65:1259–1268, 1982.
- [76] L.G. Horan, N.C. Flowers, and G.S. Sohi. A dynamic electrical record of the pathway of human His bundle activation from surface mapping. *Circ. Res.*, 50(1):47–54, January 1982.
- [77] R.R. Fenici, M. Masselli, S.N. Erné, and H.D. Hahlbohm. Magnetocardiographic mapping of the P-R interval phenomena in an unshielded hospital laboratory. In H. Weinberg, G. Stroink, and T. Katila, editors, *Biomagnetism: Applications and Theory*, pages 137–141, New York, August 1984. Fifth World Conference on Biomagnetism, Pergamon Press.
- [78] B.J. ten Voorde, M.J. Peters, G. Stroink, and R.L. van der Wieken. High resolution magnetic mapping of PR-interval phenomena of normal subjects. *Med. & Biol. Eng. & Comput.*, 26:130–135, 1988.
- [79] C. MacAulay, G. Stroink, and B.M. Horáček. Analysis of MCG spatial maps during the PR-interval. *Med. & Biol. Eng. & Comp.*, 23(SUPPL.2):1479–1480, 1985.
- [80] R. Lamothe, G. Stroink, and M.J. Gardner. High-resolution magnetocardiographic studies of the PR-interval. In *13th Canadian Medical and Biological Engineering Conference*, pages 177–178, Halifax, Nova Scotia, June 1987. CMBES.

- [81] J. Nenonen, T. Katila, M. Leinio, J. Montonen, M. Makijarvi, and P. Siltanen. Magnetocardiographic functional localization using current multipole models. *IEEE Trans. Biomed. Eng.*, BME-38:648-57, 1991.
- [82] R.L. Lux, A.K. Evans, M.J. Burgess, R.F. Wyatt, and J.A. Abildskov. Redundancy reduction for improved display and analysis of body surface potential maps, I: Spatial compression. *Circ. Res.*, 49(1):186-196, July 1981.
- [83] A.K. Evans, R.L. Lux, M.J. Burgess, R.F. Wyatt, and J.A. Abildskov. Redundancy reduction for improved display and analysis of body surface potential maps, II: Temporal compression. *Circ. Res.*, 49(1):197-202, July 1981.
- [84] C. Baumgartner, W.W. Sutherling, and D.S. Barth. Spatiotemporal modeling of somatosensory evoked magnetic fields. In S.J. Williamson, M. Hoke, G. Stroink, and M. Kotani, editors, *Advances in Biomagnetism*, pages 161-164. Plenum Press, New York, 1990.
- [85] C. Baumgartner, W.W. Sutherling, S. Di, and D.S. Barth. Multiple source modeling of the human epileptic spike complex in the magnetoencephalogram. In S.J. Williamson, M. Hoke, G. Stroink, and M. Kotani, editors, *Advances in Biomagnetism*, pages 299-302. Plenum Press, New York, 1990.
- [86] R.R. Douglas and L.J. Rogers. Comparative factor analysis models for an empirical study of EEG data. *Int. J. Neurosci.*, 18:211-226, 1983.
- [87] R. Lamothe and G. Stroink. Orthogonal expansions: Their applicability to signal extraction in electrophysiological mapping data. *Med. Biol. Eng. Comp.*, 29:522-28, 1991.
- [88] G.H. Golub and C. Reinsch. Singular value decomposition and least squares solutions. *Numer. Math.*, 14:403-420, 1970.
- [89] G. Golub and W. Kahan. Calculating the singular values and pseudo-inverse of a matrix. *J. SIAM Numer. Anal.*, 2(2):205-224, 1965.
- [90] W.H. Press, B.P. Flannery, S.A. Teukolsky, and W.T. Vetterling. *Numerical Recipes: The Art of Scientific Computing*. Cambridge Univ. Press, 1987.
- [91] J.T. Tou and R.C. Gonzalez. *Pattern Recognition Principles*. Addison-Wesley Publishing Company, Inc., U.S.A., 1974.
- [92] J.J. Gerbrands. On the relationship between SVD, KLT and PCA. *Pattern Recognition*, 14(1-6):375-381, 1981.
- [93] R. Lamothe, G. Stroink, and C.J. Kafer. Evaluation of techniques used to extract His-Purkinje system spatial distributions. In S.J. Williamson, M. Hoke, G. Stroink, and M. Kotani, editors, *Advances in Biomagnetism*, pages 357-360. Plenum Press, New York, 1990.

- [94] R. Lamothe, C. Purcell, and G. Stroink. Magnetocardiographic and body surface potential detection of spatial features of the human His-Purkinje system. In *Proceedings of the 9th Annual Conference of the IEEE Engineering in Medicine and Biology Society*, pages 172–173, Boston, USA, November 1987. IEEE.
- [95] D.E. Farrell, J. Tripp, and R. Norgren. Non-invasive information of the P-R segment of the cardiac cycle: An assessment of the clinical potential of the electric and magnetic methods. *Proc. SPIE*, 167, 1978.
- [96] D.E. Farrell, J.H. Tripp, and R. Norgren. Magnetic study of His-Purkinje conduction system in man. *IEEE Trans. Biomed. Eng.*, BME-27(7):345–350, July 1980.
- [97] R.R. Fenici, G.L. Romani, and R. Leoni. Magnetic measurements and modelling for the investigation of the human-heart conduction system. *Il Nuovo Cimento*, 2D(2):280–290, April 1983.
- [98] R.R. Fenici, M. Masselli, L. Lopez, and F. Sabetta. First simultaneous magnetocardiographic and invasive recordings of the P-R interval electrophysiological phenomena in man. *Med. & Biol. Eng. & Comp.*, suppl.2(23):1483–1484, August 1985.
- [99] R. Fenici, M. Masselli, L. Lopez, and F. Sabetta. Simultaneous magnetocardiographic mapping and invasive electrophysiology to evaluate the accuracy of the equivalent current dipole inverse solution for the localization of human cardiac sources. *New Trends in Arrhythmias*, II(2):357–371, 1986.
- [100] R.M. Gulrajani, H. Pham-Huy, R.A. Nadeau, P. Savard, J. DeGuise, R. Primeau, and F.A. Roberge. Application of the single moving dipole inverse solution to the study of the Wolff-Parkinson-White syndrome in man. *J. Electrocardiol.*, 17(3):271–288, 1984.
- [101] M.S. Spach, R.C. Barr, R.B. Warren, D.W. Benson, A. Walston, and S.B. Edwards. Isopotential body surface mapping in subjects of all ages: Emphasis on low-level potentials with analysis of the method. *Circulation*, 59(4):805–821, April 1979.
- [102] A. Takeuchi, K. Watanabe, M. Katayama, M. Nomura, Y. Nakaya, and H. Mori. Magnetic field of atrial depolarisation. *Medical Progress through Technology*, 14:73–80, 1989.
- [103] D. Stilli, E. Musso, P. Barone, P. Ciarlini, E. Macchi, F. Regoliosi, L. Dei Cas, C. Manca, O. Visioli, M. Bo, and B. Taccardi. Newer data on the configuration and variability ranges of body surface maps in a sample of normal subjects. *J. Electrocardiology*, 21(1):1–14, 1988.
- [104] B. Taccardi. Body surface distribution of equipotential lines during atrial depolarization and ventricular repolarization. *Circ. Res.*, 19(5):865–878, November 1966.

- [105] D.M. Mirvis. Body surface distribution of electrical potential during atrial depolarization and repolarization. *Circulation*, 62(1):167-173, July 1980.
- [106] D.M. Mirvis and J.L. Wilson. Determination of the spatial and intensity properties of atrial repolarization potentials in the dog. *J. Electrocardiology*, 19(2):99-108, 1986.
- [107] M. Saarinen, P. Siltanen, P.J. Karp, and T.E. Katila. The normal electrocardiogram: I Morphology. *Annals of Clinical Research*, 10(Suppl. 21):1-43, 1978.
- [108] M. Sumi, A. Takeuchi, M. Katayama, Y. Fukuda, M. Nomura, K. Fujino, M. Murakami, Y. Nakaya, and H. Mori. Magnetocardiographic P Waves in normal subjects and patients with mitral stenosis. *Japanese Heart J.*, 27(5):621-633, September 1986.
- [109] A. Takeuchi, K. Watanabe, M. Nomura, S. Ishihara, M. Sumi, M. Murakami, K. Saito, Y. Nakaya, and H. Mori. The P-wave in the magnetocardiogram. *J. Electrocardiology*, 21(2):161-167, 1988.
- [110] J.P. Boineau, T.E. Canavan, R.B. Schuessler, M.E. Cain, P.B. Corr, and J.L. Cox. Demonstration of a widely distributed atrial pacemaker complex in the human heart. *Circulation*, 77(6):1221-1237, 1988.
- [111] M.S. Spach, D. King, R.C. Barr, D.E. Boaz, M.N. Morrow, and S. Herman-Giddens. Electrical potential distribution surrounding the atria during depolarization and repolarization in the dog. *Circ. Res.*, 24:857-873, 1969.
- [112] T.N. James and L. Sherf. P waves, atrial depolarization and pacemaking site. In R.C. Schant, editor, *Advances in Electrocardiography*, pages 13-39. Grune and Stratton, New York, 1972.
- [113] M.J. Janse and R. H. Anderson. Specialized internodal atrial pathways fact or fiction? *Europ. J. Cardiol.*, 2:117-136, 1974.
- [114] M.S. Spach and J.M. Kootsey. The nature of electrical propagation in cardiac muscle. *Am. J. Physiol.*, 244:H3-H22, 1983.
- [115] M.S. Spach, M. Lieberman, J.G. Scott, R.C. Barr, E.A. Johnson, and J.M. Kootsey. Excitation sequences of the atrial septum and the av node in isolated hearts of the dog and rabbit. *Circ. Res.*, 29:156-172, 1971.
- [116] R. Plonsey. Capability and limitations of electrocardiography and magnetocardiography. *IEEE Trans. Biomed. Eng.*, BME-19:239-44, 1972.
- [117] H.H. Hecht and C.E. Kossmann. atrioventricular and intraventricular conduction. Revised nomenclature and concepts. *Am. J. Cardiol.*, 31:232-244, 1973.

- [118] B.J. Scherlag, S.H. Lau, R.H. Helfant, W.D. Berkowitz, E. Stein, and A.N. Damato. Catheter technique for recording His bundle activity in man. *Circulation*, 39:13–18, January 1969.
- [119] E.J. Berbari, R. Lazzara, P. Samet, and B.J. Scherlag. Noninvasive technique for detection of electrical activity during the P-R segment. *Circulation*, 48:1005–1013, November 1973.
- [120] N.C. Flowers, R.C. Hand, P.C. Orander, C.B. Miller, M.O. Walden, and L.G. Horan. Surface recording of electrical activity from the region of the bundle of His. *Am. J. Cardiol.*, 33:384–389, 1974.
- [121] E.J. Berbari, P. Lazzara, and B.J. Scherlag. The effects of filtering the his-purkinje system electrocardiogram. *IEEE Trans. Biomed. Engr.*, BME-26(2):82–85, 1979.
- [122] R. Fenici, G.L. Romani, S. Barbanera, P. Zeppilli, P. Carelli, and I. Modena. High resolution magnetocardiography. *G. Ital. Cardiol.*, 10:1366–1370, 1980.
- [123] H.E. Lorenzana, P.B. Pipes, M.P. Zaitlin, and D. James. A study of the P-R segment in the human magnetocardiogram. In H. Weinberg, G. Stroink, and T. Katila, editors, *Biomagnetism: Applications and Theory*, pages 142–147, New York, August 1984. Fifth World Conference on Biomagnetism, Pergamon Press.
- [124] M. Leinio, J. Montonen, M. Makijarvi, K. Makiniemi, J. Nenonen, T. Katila, and P. Siltanen. ECG and MCG studies on the His-Purkinje activity in a case of congenital heart block. In S.J. Williamson, M. Hoke, G. Stroink, and M. Kotani, editors, *Advances in Biomagnetism*, pages 377–380. Plenum Press, New York, 1990.
- [125] M. Makijarvi, R. Maniewski, I. Derka, J. Puurtinen, T. Katila, and P. Siltanen. High-resolution MCG study on heart conduction system. *Med. & Biol. Eng. & Comp.*, suppl.2(23):1485–1486, August 1985.
- [126] A. Peper, R. Jonges, T.G. Losekoot, and C.A. Grimbergen. Recording of surface His-Purkinje potentials. *Med. Biol. Eng. Comp.*, 23(4):365–376, July 1985.
- [127] Y. Zhuravlev, A. Lipovich, A. Matlashov, E. Godik, and Y. Gulyaev. Dynamic magnetic study of the heart conduction system. In S.J. Williamson, M. Hoke, G. Stroink, and M. Kotani, editors, *Advances in Biomagnetism*, pages 353–356. Plenum Press, New York, 1990.
- [128] R. Lamothe and G. Stroink. Orthogonal expansions of electrophysiological data leading to significant loss of information. In *Proc. 12th. Ann. Conf. IEEE Eng. Med. & Biol. Soc.*, Philadelphia, USA, November 1990.
- [129] J. Jie and G. Schoffa. Die nichtinvasive Registrierung der His-Bündel-Potentiale mit zeitlicher und räumlicher Mittelung. *Z. Kardiol.*, 77:358–365, 1988.

- [130] G.K. Massing and T.N. James. Anatomical configuration of the His bundle and bundle branches in the human heart. *Circulation*, 53:609, 1976.
- [131] J. Widran and M. Lev. The dissection of the atrioventricular node, bundle and bundle branches in the human heart. *Circulation*, 4:863-867, 1951.
- [132] C.J. Kafer. Characterizing his-purkinje system signals observed at the body surface. *J. Electrocardiology*, 24(3):221-14, 1991.
- [133] C.J. Kafer. *Characteristics of Electrocardiographic and Magnetocardiographic Recordings of Human His-Purkinje Activity Investigated by Means of a Computer Model*. PhD thesis, Dalhousie University, 1988.
- [134] A. Peper, R. Jonges, T.G. Losekoot, and C.A. Grimbergen. Separation of His-Purkinje potentials from coinciding atrium signals: Removal of the P-wave from the electrocardiogram. *Med. Biol. Eng. Comp.*, 20:195-201, July 1985.
- [135] E.J. Berbari, S.M. Collins, Y. Salu, and R. Arzbaecher. Orthogonal surface lead recordings of His-Purkinje activity: Comparison of actual and simulated waveforms. *IEEE Trans. Biomed. Eng.*, BME-30(3):160-167, March 1983.
- [136] S.N. Ern , R.R. Fenici, H.-D. Hahlbohm, H.P. Lehmann, and Z. Trontelj. Beat to beat surface recording and averaging of His-Purkinje activity in man. *J. Electrocardiology*, 16(4):355-362, 1983.
- [137] J. Toyama, C. Satoh, T. Watanabe, I. Kodama, and K. Yamada. Diverse characteristics in potential waveform of His-Purkinje system - experimental and simulation studies. *Jap. Circ. J.*, 52:188-196, 1988.
- [138] A. Mohammad-Djafari, F. Heron, R. Duperdu, and J. Perrin. Noninvasive recording of the His-Purkinje system electrical activity by a digital system design. *J. Biomed. Engng.*, 3:147-152, 1981.
- [139] S.N. Ern , R.R. Fenici, H.-D. Hahlbohm, J. Korsukewitz, H.P. Lehmann, and Y. Uchikawa. Magnetocardiographic study of the PR segment of normals. In H. Weinberg, G. Stroink, and T. Katila, editors, *Biomagnetism: Applications and Theory, Proceedings of 5th International Conference on Biomagnetism*, pages 132-136, Vancouver, Canada, August 1984.
- [140] D.E. Farrell, J.H. Tripp, and C.L. VanDoren. High resolution cardiomagnetism. In S.N. Ern , H.D. Halhbohm, and H. L bbig, editors, *Biomagnetism*, pages 273-282, New York, May 1981. Third International Workshop, Walter de Gruyter.
- [141] S. Barbanera, P. Carelli, R. Leoni, and G.L. Romani. Biomagnetic measurements in unshielded, normally noisy environments. In S.N. Ern , H.D. Halhbohm, and H. L bbig, editors, *Biomagnetism*, pages 139-149, New York, May 1981. Third International Workshop, Walter de Gruyter.

- [142] R.R. Fenici, G.L. Romani, M. Masselli, and I. Modena. Magnetocardiographic recording of the His-Purkinje system activity in man. *Japanese Heart Journal*, 23:-728-730, 1982.
- [143] R.R. Fenici, G.L. Romani, and S.N. Ern . High-resolution magnetic measurements of human cardiac electrophysiological events. *Il Nuovo Cimento*, 2D(2):231-247, April 1983.
- [144] J.L. Patrick, D.W. Hess, J.H. Tripp, and D.E. Farrell. The magnetic field produced by the conduction system of the human heart. *Il Nuovo Cimento*, 2D(2):255-265, April 1983.
- [145] G.L. Romani and R. Fenici. Study of the human heart conduction system by the biomagnetic method. *Atherosclerosis Reviews*, 10:81-88, 1983.
- [146] S.N. Ern , H.P. Lehmann, M. Masselli, and Y. Uchikawa. Modelling of the his-purkinje heart conduction system. In H. Weinberg, G. Stroink, and T. Katila, editors, *Biomagnetism: Applications and Theory*, pages 126-131, New York, August 1984. Fifth World Conference on Biomagnetism, Pergamon Press.
- [147] G.E.P. Box and G.M. Jenkins. *Time Series Analysis Forecasting and Control*. Holden-Day Series in time series analysis, Holden-Day, Amsterdam, 1970.
- [148] E.J. Berbari. Recording from ventricular conduction system. In John G. Webster, editor, *Encyclopedia of Medical Devices and Instrumentation*, pages 291-314. John Wiley & Sons, New York, 1988.
- [149] N.C. Flowers. Body-surface His-bundle electrocardiography. In Peter W. MacFarlane and T.D. Veitch Lawrie, editors, *Comprehensive Electrocardiology: Theory and Practice in Health and Disease*, pages 1053-1062. Pergamon Press, Inc., New York, 1989.
- [150] J.J. Gallagher, E.L.C. Pritchatt, W.C. Sealy, J. Kasell, and A.G. Wallace. The preexcitation syndromes. *Prog. Cardiovasc. Dis.*, 20:-285-327, 1978.
- [151] F.R. Cobb, Blumenstein S.D., W.C. Sealy, J.P. Boineau, G.S. Wagner, and A.G. Wallace. Successful surgical interruption of the bundle of Kent in a patient with Wolff-Parkinson-White syndrome. *Circulation*, 38:1018-29, 1968.
- [152] W.C. Sealy, B.G. Hattler Jr., Blumenstein S.D., and F.R. Cobb. Surgical treatment of Wolff-Parkinson-White syndrome. *Ann. Thorac. Surg.*, 8:1-11, 1969.
- [153] M.M. Scheinman, F. Morady, D.S. Hess, and R. Gonzalez. Catheter-induced ablation of the atrioventricular junction to control refractory supraventricular arrhythmias. *JAMA*, 248:851-55, 1982.

- [154] J.J. Gallagher, R.H. Svenson, J.J. Kasell, and et al. Catheter technique for closed-chest ablation of the atrioventricular conduction system: a therapeutic alternative for the treatment of refractory supraventricular tachycardia. *N. Engl. J. Med.*, 306:194-200, 1982.
- [155] W.M. Jackman, X. Wang, K.J. Friday, C.A. Roman, K.P. Moulton, K.J. Beckman, J.H. McClellan, N. Twidale, H.A. Hazlitt, M.I. Prior, P.D. Margolis, J.D. Calame, E.D. Overholt, and R. Lazzara. Catheter ablation of accessory atrioventricular pathways (Wolff-Parkinson-White syndrome) by radiofrequency current. *N. Engl. J. Med.*, 324:1605-11, 1991.
- [156] S. Yuan, P. Blomstrom, S. Pehrson, and B. Olsson. Localization of cardiac arrhythmias: conventional noninvasive methods. *Int. J. Cardiac Imaging*, 7:193-205, 1991.
- [157] T. Iwa and T. Magara. Correlation between localization of accessory conduction pathway and body surface maps in the Wolff-Parkinson-White syndrome. *Jap. Circulation J.*, 45:1192-1198, 1981.
- [158] T. Iwa, M. Kawasuji, T. Misaki, T. Iwase, and T. Magara. Localization and interruption of accessory conduction pathway in the Wolff-Parkinson-White syndrome. *J. Thorac. Cardiovasc. Surg.*, 80:271-279, 1980.
- [159] L. De Ambroggi, B. Taccardi, and E. Macchi. Body-surface maps of heart potentials: Tentative localization of pre-excited areas in forty-two Wolff-Parkinson-White patients. *Circulation*, 54:251-263, 1976.
- [160] W.D. Benson Jr. BSM in cardiac arrhythmias. In J. Liebman, R. Plonsey, and Y. Rudy, editors, *Pediatric and Fundamental Electrocardiography*, chapter 18. Martinus Nijhoff Publishing, Boston, 1987.
- [161] S. Kamakura, K. Shimomura, T. Ohe, M. Matsuhisa, and H. Toyoshima. The role of initial minimum potentials on body surface maps in predicting the site of accessory pathways in patients with Wolff-Parkinson-White syndrome. *Circulation*, 74:89-96, 1986.
- [162] M. Dubuc, R. Nadeau, G. Tremblay, T. Kus, F. Molin, and P. Savard. Pace mapping using body surface potential maps to guide catheter ablation of accessory pathways in patients with Wolff-Parkinson-White syndrome. *Circulation*, 87:135-143, 1993.
- [163] R.R. Fenici, M. Masselli, L. Lopez, and F. Sabetta. First simultaneous mcg and invasive kent bundel localization in man. *New Trends in Arrhythmias*, 1:455, 1985.
- [164] T. Katila, R. Maniewski, M. Makijarvi, J. Nenonen, and P. Siltanen. On the accuracy of source localisation in cardiac measurements. *Phys. Med. Biol.*, 32:125-131, 1987.

- [165] W. Moshage, S. Achenbach, A. Weikl, K. Gohl, K. Abraham-Fuchs, S. Schneider, and K. Bachmann. Progress in biomagnetic imaging of heart arrhythmias. *Frontiers in Eur. Radiology*, 8:1–19, 1991.
- [166] R.A. Nadeau, P. Savard, G. Faugère, M. Shenasa, P. Pagé, R.M. Gulrajani, R.A. Guardo, and R. Cardinal. Localization of pre-excitation sites in the Wolff-Parkinson-White syndrome by body surface potential mapping and a single moving dipole representation. In R. Th. van Dam and A. van Oosterom, editors, *Electrocardiographic Body Surface Mapping*, chapter 12. Martinus Nijhoff Publishing, Boston, 1986.
- [167] P.W. Duchosal, L. DeRoy, and J. Odier. Time relationship of the P-delta segment in the Wolff-Parkinson-White syndrome. *J. Electrocardiology*, 11:47–56, 1978.
- [168] R. Lemery, S.C. Hammill, D.L. Wood, G.K. Danielson, H.T. Mankin, M.J. Osborn, B.J. Gersh, and D.R. Holmes Jr. Value of the resting 12 lead electrocardiogram and vectorcardiogram for locating the accessory pathway in patients with the Wolff-Parkinson-White syndrome. *Br. Heart J.*, 58:324–32, 1987.
- [169] F.F. Rosenbaum, H.H. Hecht, F.N. Wilson, and F.D. Johnston. The potential variations of the thorax and the esophagus in anomalous atrioventricular excitation (Wolff-Parkinson-White syndrome). *Am. Heart J.*, 29:281–326, 1945.
- [170] C. Giorgi, R. Nadeau, P. Savard, M. Shenasa, P.L. Pagé, and R. Cardinal. Body surface isopotential mapping of the entire QRST complex in the Wolff-Parkinson-White syndrome. Correlation with the location of the accessory pathway. *Am. Heart J.*, 121:1445–1453, 1991.
- [171] J. Liebman, J.A. Zeno, B. Olshansky, A.S. Geha, C.W. Thomas, Y. Rudy, R.W. Henthorn, M. Cohen, and A.L. Waldo. Electrocardiographic body surface potential mapping in the Wolff-Parkinson-White syndrome: Non-invasive determination of the ventricular insertion sites of accessory atrioventricular connections. *Circulation*, 83:886–901, 1991.
- [172] M. Makijarvi, J. Nenonen, M. Leinio, J. Montonen, L. Toivonen, M. Nieminen, T. Katila, and P. Siltanen. Localization of accessory pathways in Wolff-Parkinson-White syndrome by high-resolution magnetocardiographic mapping. *J. Electrocardiology*, 25:143–155, 1992.
- [173] R. Fenici, G. Melillo, A. Cappelli, C. De Luca, and M. Masselli. Magnetocardiographic localization of Kent bundles. In S.J. Williamson, M. Hoke, G. Stroink, and M. Kotani, editors, *Advances in Biomagnetism*, pages 365–368. Plenum Press, New York, 1990.
- [174] Rok Hren. The effect of inhomogeneities on electrocardiographic and magnetocardiographic inverse solutions: Application in the localization of ventricular pre-excitation sites. Master's thesis, Daihousie University, 1993.

- [175] Frank H. Netter. *The Ciba Collection of Medical Illustrations: Volume 5 - Heart*. CIBA, F.F. Yonkman (Ed.), 1987.
- [176] G. Stroink, L.S. Greek, P. Elliott, and J. Nenonen. Is there a need for individualized torso models in magnetic inverse solutions? In M. Hoke, S.N. Ern , Y.C. Okada, and G.L. Romani, editors, *Biomagnetism: Clinical Aspects*, pages 813-817. Elsevier Science Publishers, The Netherlands, 1992.
- [177] K. Forsman, J. Nenonen, C. Purcell, and G. Stroink. Biomagnetic inverse solution with a realistic torso model. In M. Hoke, S.N. Ern , Y.C. Okada, and G.L. Romani, editors, *Biomagnetism: Clinical Aspects*, pages 819-823. Elsevier Science Publishers, The Netherlands, 1992.
- [178] T.J. van den Akker, H.H. Ros, H.G. Goovaerts, and H. Schneider. Real-time method for noninvasive recording of His Bundle activity of the electrocardiogram. *Comp. Biomed. Res.*, 9:559-569, 1976.
- [179] N. Alperin and D. Sadeh. An improved method for on-line averaging and detecting of ECG waveforms. *Comp. Biomed. Res.*, 19:193-202, 1986.
- [180] E.I. Jury. *Theory and Application of the Z-Transform Method*. John Wiley & Sons, Inc, USA, 1964.
- [181] J.E. Opfer, Y.K. Yeo, J.J. Pierce, and L.H. Rorden. A superconducting second-derivative gradiometer. *IEEE Trans. Magn.*, MAG-9:536-539, 19.
- [182] P. Carelli, I. Modena, and G.L. Romani. Detection coils. In S.J. Williamson, G.L. Romani, L. Kaufmann, and I. Modena, editors, *Biomagnetism: An Interdisciplinary Approach*, pages 85-99. Plenum Press, New York, 1983.
- [183] D.M. Mirvis. Atrial depolarization and repolarization. In David M. Mirvis, editor, *Body Surface Electrocardiographic Mapping*, pages 77-86. Kluwer Academic Publishers, Boston, 1988.